

THE UNIVERSITY OF CALGARY

**FULL-WAVE ANALYSES OF MULTI-LAYER
MICROSTRIP TRANSMISSION LINE
DISCONTINUITIES**

BY

Ming Yang

A DISSERTATION

SUBMITTED TO THE FACULTY OF GRADUATE STUDIES
IN PARTIAL FULFILLMENT OF THE REQUIREMENTS FOR THE
DEGREE OF DOCTOR OF PHILOSOPHY

DEPARTMENT OF ELECTRICAL AND COMPUTER
ENGINEERING

CALGARY, ALBERTA

AUGUST, 1993

© Ming Yang 1993



National Library
of Canada

Acquisitions and
Bibliographic Services Branch

395 Wellington Street
Ottawa, Ontario
K1A 0N4

Bibliothèque nationale
du Canada

Direction des acquisitions et
des services bibliographiques

395, rue Wellington
Ottawa (Ontario)
K1A 0N4

Your file Votre référence

Our file Notre référence

The author has granted an irrevocable non-exclusive licence allowing the National Library of Canada to reproduce, loan, distribute or sell copies of his/her thesis by any means and in any form or format, making this thesis available to interested persons.

L'auteur a accordé une licence irrévocable et non exclusive permettant à la Bibliothèque nationale du Canada de reproduire, prêter, distribuer ou vendre des copies de sa thèse de quelque manière et sous quelque forme que ce soit pour mettre des exemplaires de cette thèse à la disposition des personnes intéressées.

The author retains ownership of the copyright in his/her thesis. Neither the thesis nor substantial extracts from it may be printed or otherwise reproduced without his/her permission.

L'auteur conserve la propriété du droit d'auteur qui protège sa thèse. Ni la thèse ni des extraits substantiels de celle-ci ne doivent être imprimés ou autrement reproduits sans son autorisation.

ISBN 0-315-88654-4

Canada

Name MING YANG

Dissertation Abstracts International is arranged by broad, general subject categories. Please select the one subject which most nearly describes the content of your dissertation. Enter the corresponding four-digit code in the spaces provided.

Electronics and Electrical Engineering

SUBJECT TERM

0544

SUBJECT CODE

U·M·I

Subject Categories

THE HUMANITIES AND SOCIAL SCIENCES

COMMUNICATIONS AND THE ARTS

Architecture 0729
Art History 0377
Cinema 0900
Dance 0378
Fine Arts 0357
Information Science 0723
Journalism 0391
Library Science 0399
Mass Communications 0708
Music 0413
Speech Communication 0459
Theater 0465

EDUCATION

General 0515
Administration 0514
Adult and Continuing 0516
Agricultural 0517
Art 0273
Bilingual and Multicultural 0282
Business 0688
Community College 0275
Curriculum and Instruction 0727
Early Childhood 0518
Elementary 0524
Finance 0277
Guidance and Counseling 0519
Health 0680
Higher 0745
History of 0520
Home Economics 0278
Industrial 0521
Language and Literature 0279
Mathematics 0280
Music 0522
Philosophy of 0998
Physical 0523

Psychology 0525
Reading 0535
Religious 0527
Sciences 0714
Secondary 0533
Social Sciences 0534
Sociology of 0340
Special 0529
Teacher Training 0530
Technology 0710
Tests and Measurements 0288
Vocational 0747

LANGUAGE, LITERATURE AND LINGUISTICS

Language
General 0679
Ancient 0289
Linguistics 0290
Modern 0291
Literature
General 0401
Classical 0294
Comparative 0295
Medieval 0297
Modern 0298
African 0316
American 0591
Asian 0305
Canadian (English) 0352
Canadian (French) 0355
English 0593
Germanic 0311
Latin American 0312
Middle Eastern 0315
Romance 0313
Slavic and East European 0314

PHILOSOPHY, RELIGION AND THEOLOGY

Philosophy 0422
Religion
General 0318
Biblical Studies 0321
Clergy 0319
History of 0320
Philosophy of 0322
Theology 0469

SOCIAL SCIENCES

American Studies 0323
Anthropology
Archaeology 0324
Cultural 0326
Physical 0327
Business Administration
General 0310
Accounting 0272
Banking 0770
Management 0454
Marketing 0338
Canadian Studies 0385
Economics
General 0501
Agricultural 0503
Commerce-Business 0505
Finance 0508
History 0509
Labor 0510
Theory 0511
Folklore 0358
Geography 0366
Gerontology 0351
History
General 0578

Ancient 0579
Medieval 0581
Modern 0582
Black 0328
African 0331
Asia, Australia and Oceania 0332
Canadian 0334
European 0335
Latin American 0336
Middle Eastern 0333
United States 0337
History of Science 0585
Law 0398
Political Science
General 0615
International Law and
Relations 0616
Public Administration 0617
Recreation 0814
Social Work 0452
Sociology
General 0626
Criminology and Penology 0627
Demography 0938
Ethnic and Racial Studies 0631
Individual and Family
Studies 0628
Industrial and Labor
Relations 0629
Public and Social Welfare 0630
Social Structure and
Development 0700
Theory and Methods 0344
Transportation 0709
Urban and Regional Planning 0999
Women's Studies 0453

THE SCIENCES AND ENGINEERING

BIOLOGICAL SCIENCES

Agriculture
General 0473
Agronomy 0285
Animal Culture and
Nutrition 0475
Animal Pathology 0476
Food Science and
Technology 0359
Forestry and Wildlife 0478
Plant Culture 0479
Plant Pathology 0480
Plant Physiology 0817
Range Management 0777
Wood Technology 0746
Biology
General 0306
Anatomy 0287
Biostatistics 0308
Botany 0309
Cell 0379
Ecology 0329
Entomology 0353
Genetics 0369
Limnology 0793
Microbiology 0410
Molecular 0307
Neuroscience 0317
Oceanography 0416
Physiology 0433
Radiation 0821
Veterinary Science 0778
Zoology 0472
Biophysics
General 0786
Medical 0760

EARTH SCIENCES

Biogeochemistry 0425
Geochemistry 0996

Geodesy 0370
Geology 0372
Geophysics 0373
Hydrology 0388
Mineralogy 0411
Paleobotany 0345
Paleoecology 0426
Paleontology 0418
Paleozoology 0985
Palynology 0427
Physical Geography 0368
Physical Oceanography 0415

HEALTH AND ENVIRONMENTAL SCIENCES

Environmental Sciences 0768
Health Sciences
General 0566
Audiology 0300
Chemotherapy 0992
Dentistry 0567
Education 0350
Hospital Management 0769
Human Development 0758
Immunology 0982
Medicine and Surgery 0564
Mental Health 0347
Nursing 0569
Nutrition 0570
Obstetrics and Gynecology 0380
Occupational Health and
Therapy 0354
Ophthalmology 0381
Pathology 0571
Pharmacology 0419
Pharmacy 0572
Physical Therapy 0382
Public Health 0573
Radiology 0574
Recreation 0575

Speech Pathology 0460
Toxicology 0383
Home Economics 0386

PHYSICAL SCIENCES

Pure Sciences

Chemistry
General 0485
Agricultural 0749
Analytical 0486
Biochemistry 0487
Inorganic 0488
Nuclear 0738
Organic 0490
Pharmaceutical 0491
Physical 0494
Polymer 0495
Radiation 0754
Mathematics 0405
Physics
General 0605
Acoustics 0986
Astronomy and
Astrophysics 0606
Atmospheric Science 0608
Atomic 0748
Electronics and Electricity 0607
Elementary Particles and
High Energy 0798
Fluid and Plasma 0759
Molecular 0609
Nuclear 0610
Optics 0752
Radiation 0756
Solid State 0611
Statistics 0463

Applied Sciences

Applied Mechanics 0346
Computer Science 0984

Engineering

General 0537
Aerospace 0538
Agricultural 0539
Automotive 0540
Biomedical 0541
Chemical 0542
Civil 0543
Electronics and Electrical 0544
Heat and Thermodynamics 0348
Hydraulic 0545
Industrial 0546
Marine 0547
Materials Science 0794
Mechanical 0548
Metallurgy 0743
Mining 0551
Nuclear 0552
Packaging 0549
Petroleum 0765
Sanitary and Municipal 0554
System Science 0790
Geotechnology 0428
Operations Research 0796
Plastics Technology 0795
Textile Technology 0994

PSYCHOLOGY

General 0621
Behavioral 0384
Clinical 0622
Developmental 0620
Experimental 0623
Industrial 0624
Personality 0625
Physiological 0989
Psychobiology 0349
Psychometrics 0632
Social 0451



Nom _____

Dissertation Abstracts International est organisé en catégories de sujets. Veuillez s.v.p. choisir le sujet qui décrit le mieux votre thèse et inscrire le code numérique approprié dans l'espace réservé ci-dessous.

SUJET



CODE DE SUJET

Catégories par sujets

HUMANITÉS ET SCIENCES SOCIALES

COMMUNICATIONS ET LES ARTS

Architecture	0729
Beaux-arts	0357
Bibliothéconomie	0399
Cinéma	0900
Communication verbale	0459
Communications	0708
Danse	0378
Histoire de l'art	0377
Journalisme	0391
Musique	0413
Sciences de l'information	0723
Théâtre	0465

ÉDUCATION

Généralités	515
Administration	0514
Art	0273
Collèges communautaires	0275
Commerce	0688
Économie domestique	0278
Éducation permanente	0516
Éducation préscolaire	0518
Éducation sanitaire	0680
Enseignement agricole	0517
Enseignement bilingue et multiculturel	0282
Enseignement industriel	0521
Enseignement primaire	0524
Enseignement professionnel	0747
Enseignement religieux	0527
Enseignement secondaire	0533
Enseignement spécial	0529
Enseignement supérieur	0745
Évaluation	0288
Finances	0277
Formation des enseignants	0530
Histoire de l'éducation	0520
Langues et littérature	0279

Lecture	0535
Mathématiques	0280
Musique	0522
Orientation et consultation	0519
Philosophie de l'éducation	0998
Physique	0523
Programmes d'études et enseignement	0727
Psychologie	0525
Sciences	0714
Sciences sociales	0534
Sociologie de l'éducation	0340
Technologie	0710

LANGUE, LITTÉRATURE ET LINGUISTIQUE

Langues	
Généralités	0679
Anciennes	0289
Linguistique	0290
Modernes	0291
Littérature	
Généralités	0401
Anciennes	0294
Comparée	0295
Médiévale	0297
Moderne	0298
Africaine	0316
Américaine	0591
Anglaise	0593
Asiatique	0305
Canadienne (Anglaise)	0352
Canadienne (Française)	0355
Germanique	0311
Latino-américaine	0312
Moyen-orientale	0315
Romane	0313
Slave et est-européenne	0314

PHILOSOPHIE, RELIGION ET THÉOLOGIE

Philosophie	0422
Religion	
Généralités	0318
Clergé	0319
Études bibliques	0321
Histoire des religions	0320
Philosophie de la religion	0322
Théologie	0469

SCIENCES SOCIALES

Anthropologie	
Archéologie	0324
Culturelle	0326
Physique	0327
Droit	0398
Économie	
Généralités	0501
Commerce-Affaires	0505
Économie agricole	0503
Économie du travail	0510
Finances	0508
Histoire	0509
Théorie	0511
Études américaines	0323
Études canadiennes	0385
Études féministes	0453
Folklore	0358
Géographie	0366
Gérontologie	0351
Gestion des affaires	
Généralités	0310
Administration	0454
Banques	0770
Comptabilité	0272
Marketing	0338
Histoire	
Histoire générale	0578

Ancienne	0579
Médiévale	0581
Moderne	0582
Histoire des noirs	0328
Africaine	0331
Canadienne	0334
États-Unis	0337
Européenne	0335
Moyen-orientale	0333
Latino-américaine	0336
Asie, Australie et Océanie	0332
Histoire des sciences	0585
Loisirs	0814
Planification urbaine et régionale	0999
Science politique	
Généralités	0615
Administration publique	0617
Droit et relations internationales	0616
Sociologie	
Généralités	0626
Aide et bien-être social	0630
Criminologie et établissements pénitentiaires	0627
Démographie	0938
Études de l'individu et de la famille	0628
Études des relations interethniques et des relations raciales	0631
Structure et développement social	0700
Théorie et méthodes	0344
Travail et relations industrielles	0629
Transports	0709
Travail social	0452

SCIENCES ET INGÉNIERIE

SCIENCES BIOLOGIQUES

Agriculture	
Généralités	0473
Agronomie	0285
Alimentation et technologie alimentaire	0359
Culture	0479
Élevage et alimentation	0475
Exploitation des pâturages	0777
Pathologie animale	0476
Pathologie végétale	0480
Physiologie végétale	0817
Sylviculture et faune	0478
Technologie du bois	0746
Biologie	
Généralités	0306
Anatomie	0287
Biologie (Statistiques)	0308
Biologie moléculaire	0307
Botanique	0309
Cellule	0379
Écologie	0329
Entomologie	0353
Génétique	0369
Limnologie	0793
Microbiologie	0410
Neurologie	0317
Océanographie	0416
Physiologie	0433
Radiation	0821
Science vétérinaire	0778
Zoologie	0472
Biophysique	
Généralités	0786
Médicale	0760

Géologie	0372
Géophysique	0373
Hydrologie	0388
Minéralogie	0411
Océanographie physique	0415
Paléobotanique	0345
Paléocécologie	0426
Paléontologie	0418
Paléozoologie	0985
Palynologie	0427

SCIENCES DE LA SANTÉ ET DE L'ENVIRONNEMENT

Économie domestique	0386
Sciences de l'environnement	0768
Sciences de la santé	
Généralités	0566
Administration des hôpitaux	0769
Alimentation et nutrition	0570
Audiologie	0300
Chimiothérapie	0992
Dentisterie	0567
Développement humain	0758
Enseignement	0350
Immunologie	0982
Loisirs	0575
Médecine du travail et thérapie	0354
Médecine et chirurgie	0564
Obstétrique et gynécologie	0380
Ophtalmologie	0381
Orthophonie	0460
Pathologie	0571
Pharmacie	0572
Pharmacologie	0419
Physiothérapie	0382
Radiologie	0574
Santé mentale	0347
Santé publique	0573
Soins infirmiers	0569
Toxicologie	0383

SCIENCES PHYSIQUES

Sciences Pures

Chimie	
Généralités	0485
Biochimie	0487
Chimie agricole	0749
Chimie analytique	0486
Chimie minérale	0488
Chimie nucléaire	0738
Chimie organique	0490
Chimie pharmaceutique	0491
Physique	0494
Polymères	0495
Radiation	0754
Mathématiques	
Physique	
Généralités	0605
Acoustique	0986
Astronomie et astrophysique	0606
Électronique et électricité	0607
Fluides et plasma	0759
Météorologie	0608
Optique	0752
Particules (Physique nucléaire)	0798
Physique atomique	0748
Physique de l'état solide	0611
Physique moléculaire	0609
Physique nucléaire	0610
Radiation nucléaire	0756
Statistiques	0463

Sciences Appliquées Et Technologie

Informatique	0984
Ingénierie	
Généralités	0537
Agricole	0539
Automobile	0540

Biomédicale	0541
Chaleur et thermodynamique	0348
Conditionnement (Emballage)	0549
Génie aérospatial	0538
Génie chimique	0542
Génie civil	0543
Génie électronique et électrique	0544
Génie industriel	0546
Génie mécanique	0548
Génie nucléaire	0552
Ingénierie des systèmes	0790
Mécanique navale	0547
Métallurgie	0743
Science des matériaux	0794
Technique du pétrole	0765
Technique minière	0551
Techniques sanitaires et municipales	0554
Technologie hydraulique	0545
Mécanique appliquée	0346
Géotechnologie	0428
Matières plastiques (Technologie)	0795
Recherche opérationnelle	0796
Textiles et tissus (Technologie)	0794

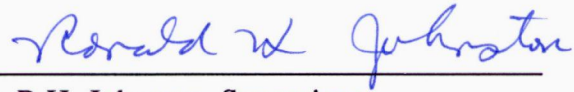
PSYCHOLOGIE

Généralités	0621
Personnalité	0625
Psychobiologie	0349
Psychologie clinique	0622
Psychologie du comportement	0384
Psychologie du développement	0620
Psychologie expérimentale	0623
Psychologie industrielle	0624
Psychologie physiologique	0989
Psychologie sociale	0451
Psychométrie	0632

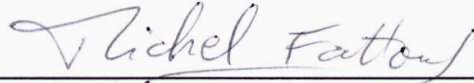


THE UNIVERSITY OF CALGARY
FACULTY OF GRADUATE STUDIES

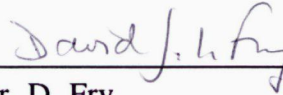
The undersigned certify that they have read, and recommend to the Faculty of Graduate Studies for acceptance, a thesis entitled, "Full-Wave Analyses of Multi-Layer Microstrip Transmission Line Discontinuities", submitted by Ming Yang in partial fulfillment of the requirements for the degree of Doctor of Philosophy.



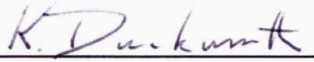
Dr. R.H. Johnston, Supervisor
Dept. of Electrical and Computer Engineering



Dr. M. Fattouche
Dept. of Electrical and Computer Engineering



Dr. D. Fry
Dept. of Physics and Astronomy



Dr. K. Duckworth
Dept. of Geology & Geophysics



Dr. L. Chow, External Examiner
Dept. of Elect. & Comp. Engg.
University of Waterloo

Date: Sept. 27 '93

Abstract

In this dissertation, full-wave analysis techniques are used to analyze the behavior of microstrip transmission line discontinuities. The full-wave analysis method takes advantage of the closed-form 2-D spectral domain Green's functions, together with the application of the moment method (MoM), to solve the electromagnetic integral equations.

A generalized spectral domain Green's function is derived, which can be used to analyze multilayer, multistrip, and vertical conductor structures. The asymptotic behavior of the Green's function is also studied.

Infinite microstrip transmission lines in multilayer dielectric layers are studied. The frequency dependent propagation constant and characteristic impedance can be obtained, using a generalized analysis algorithm.

Several typical microstrip transmission line discontinuities are analyzed and measured from low operating frequencies up to cut-off frequencies. These circuits include: 1-D discontinuities (open, gap), 2-D discontinuities (corner), vertical half wave dipoles, and 3-D discontinuities (shorting via). Good agreement has been observed between results in this research and measurements and/or publications by other researchers. Some useful conclusions have been drawn.

Also in this dissertation, a microstrip discontinuity de-embedding measurement technique (using non-time-domain network analyzers) is developed. This technique enables one to use a multiline calibration to determine the properties of the transitions that surround the discontinuity being measured. Then the S-parameters of the discontinuity are determined.

Acknowledgements

I would like to express my sincere gratitude to my supervisor Dr. R.H. Johnston for his constant guidance, encouragement, and support throughout the whole program.

I also wish to thank professors and supporting staff in the Department of Electrical and Computer Engineering, University of Calgary, for their help during my study.

Some measurements were made using network analyzers of Novatel Communication Inc., Communication Research Centre of Canada (CRC), and TRlabs. I would like to express my appreciation.

I am indebted to wife, Yiping (Donna), who is always patient and encouraging, Without her constant support, help, and hard work, I could not have finished this dissertation.

Finally, I wish to thank all of my friends, fellow students, and all the other people around me, whose names are impossible to be all listed here, for their various help.

Dedication

To my wife Yiping (Donna)

and

our daughter Chenchen (Joanna)

and son Yangyang (Steven)

Table of Contents

Approval Page	ii
Abstract	iii
Acknowledgements	iv
Dedication	v
Table of Contents	vi
List of Tables	x
List of Figures	xi
List of Symbols	xv
1 Introduction	1
2 Generalized Dyadic Green's Functions	12
2.1 Mathematical Definitions	15
2.1.1 Green's Functions	15
2.1.2 Dyadic Green's Functions	17
2.1.3 Spectral Domain Analyses	19
2.2 Theory	21
2.3 Generalization of the Dyadic Green's Functions	36
2.3.1 Signal Flow Graphs for TE and TM waves	36
2.3.2 Layer Removal— Total and Partial	39
2.3.3 Transmission Matrices Method	43
2.4 Example: Single Substrate layer	45
2.5 Asymptotic Expressions	48
2.6 Dyadic Green's Functions for a Magnetic Dipole	52
2.6.1 Derivation	53
2.6.2 Boundary Conditions on the Slot and Aperture	57
3 Infinite Line Analysis	59
3.1 Formulation	60
3.1.1 Electric Field	62
3.1.2 The Characteristic Equation for k_e	63

3.1.3	The Characteristic Impedance	65
3.1.4	Galerkin's Procedure and Moment Method	68
3.2	Numerical Techniques	69
3.2.1	Basis Functions	69
3.2.2	Numerical Quadrature	71
3.2.3	Complex Root Searching	74
3.3	Results	75
3.3.1	Convergence Tests	75
3.3.2	Calculated and Measured Propagation Constants	76
3.3.3	Calculated Characteristic Impedance	77
3.3.4	A Note on the Choice of the Basis Functions	77
4	The Open 1-D Discontinuities	94
4.1	Formulation	95
4.1.1	Current expansion — Basis Functions	95
4.1.2	Testing Procedure	97
4.2	Numerical Considerations	99
4.2.1	Traveling Wave Decomposition	99
4.2.2	Step-Up Procedure	100
4.3	Matrix Formulation	102
4.3.1	Derivation	102
4.3.2	The Toeplitz Matrix	106
4.4	Results	107
4.4.1	Comparison of the Two Galerkin's Procedures	107
4.4.2	Convergence Test	109
4.4.3	Comparison with the Measurement	111
5	The Gap 1-D Discontinuities	125
5.1	Formulation	126
5.1.1	Basis and Testing Functions	126
5.1.2	Matrix Formulation	128
5.2	Results	130
5.2.1	Convergence Test	130
5.2.2	S-parameters as a Function of Frequency	135
5.2.3	S-parameters as a Function of Gap Distance	142
5.3	Measurement	146
5.4	Discussions	151

6	2-D Discontinuity — Corner	154
6.1	Theory	155
6.1.1	Current on the Microstrip Surface	155
6.1.2	Numerical Considerations	158
6.1.3	The Matrix Formulation	162
6.2	Results	165
6.2.1	Convergence Test	165
6.2.2	Corner Circuit Parameters as Functions of Frequency	168
7	Vertical Dipole Analyses	173
7.1	Theory	173
7.1.1	Circuit Discussions	173
7.1.2	Matrix Formulation	175
7.1.3	Consideration on Diagonal elements	177
7.2	Results	179
7.2.1	Results from SDA	179
7.2.2	Results from the Spatial Domain Method	180
7.2.3	Comparison of the Green's Functions	180
8	3-D Discontinuity — Shorting Via	188
8.1	Theory	189
8.1.1	Circuit Discussions	189
8.1.2	Matrix Formulation	191
8.2	Results	196
8.2.1	Convergence Test	196
8.2.2	Frequency Response of the Short Circuit	197
9	Measurement of Microstrip Discontinuities	201
9.1	Formulations	203
9.1.1	DUT Circuit and Its Signal Flow Graph	203
9.1.2	Through Lines as Standards	205
9.1.3	Multi-line Nonlinear Least Square Error De-embedding Techniques	208
9.2	Results	209
9.2.1	Untermination	209
9.2.2	De-embedding of the DUT	213
9.3	Other De-embedded Discontinuities	216
9.3.1	Open	216
9.3.2	Short	217
9.3.3	Zero Length Transmission Line	217

9.4	Conclusions on the Multi-Line Method	220
9.5	De-embedding with Time-Domain Network Analyzers	221
10	Conclusions	224
	Bibliography	232
A	Comparison of Decomposed and Undecomposed Traveling Wave Functions	250
B	Conversion of the 2-D Spectral Domain Green's Function into the Sommerfeld Integral	252

List of Tables

3.1	Comparison of the current coefficients by two basis functions ($N = 2$) ($W = .025''$, $h = .025''$, $\epsilon_r = 9.8$).	79
3.2	Comparison of the current coefficients by two basis functions ($N = 3$) ($W = .025''$, $h = .025''$, $\epsilon_r = 9.8$).	80
7.1	G_{zz} values calculated using two different methods (freq = 3GHz, $\epsilon_r =$ 1, $a = .5\text{mm}$, off-set = $.0005\text{mm}$).	182

List of Figures

2.1	The generalized geometry of multilayer structures.	23
2.2	Generalized signal flow graph for multilayer structures.	30
2.3	Determination of the inputs to the generalized signal flow graph. . . .	32
2.4	A microstrip crossover in a multilayer structure.	38
2.5	A layer represented by a signal flow graph block.	39
2.6	Signal flow graph after total layer removal.	42
2.7	Illustration of partial layer removal.	43
2.8	Transmission matrices for layers and interfaces.	44
2.9	Signal flow graph of a grounded substrate-air (two-layer) structure. .	46
3.1	A microstrip transmission line in a multilayer structure.	61
3.2	Deformation of the integration path into the complex domain.	81
3.3	Convergence test for a single layer substrate transmission line ($W = .025"$, $h = .025"$, $\epsilon_r = 9.8$).	82
3.4	Convergence test for a double substrate transmission line ($W = .05"$, $h_1 = .01"$, $h_2 = .025"$, $\epsilon_{r1} = 2.2$, $\epsilon_{r2} = 9.8$).	83
3.5	Convergence test for a single layer substrate transmission line ($W = 8.99\text{mm}$, $h = 3.175\text{mm}$, $\epsilon_r = 2.55$).	84
3.6	Convergence test for a single layer substrate transmission line ($W = 37.0\text{mm}$, $h = 12.7\text{mm}$, $\epsilon_r = 2.40$).	85
3.7	$\sqrt{\epsilon_e}$ of a single layer substrate transmission line with measurement made by Fordham [69] ($W = .025"$, $h = .025"$, $\epsilon_r = 9.8$).	86
3.8	$\sqrt{\epsilon_e}$ of a double layer substrate transmission line with measurement made by Fordham [69] ($W = .05"$, $h_1 = .01"$, $h_2 = .025"$, $\epsilon_{r1} = 2.2$, $\epsilon_{r2} = 9.8$).	87
3.9	$\sqrt{\epsilon_e}$ of a single layer substrate transmission line with measurement made at TRILabs ($W = 8.99\text{mm}$, $h = 3.175\text{mm}$, $\epsilon_r = 2.55$).	88
3.10	$\sqrt{\epsilon_e}$ of a single layer substrate transmission line with measurement made at Novatel Communications, Inc. ($W = 37.0\text{mm}$, $h = 12.7\text{mm}$, $\epsilon_r = 2.40$).	89
3.11	Characteristic impedance of a single layer substrate transmission line ($W = .025"$, $h = .025"$, $\epsilon_r = 9.8$).	90
3.12	Characteristic impedance of a double layer substrate transmission line ($W = .05"$, $h_1 = .01"$, $h_2 = .025"$, $\epsilon_{r1} = 2.2$, $\epsilon_{r2} = 9.8$).	91
3.13	Characteristic impedance of a single layer substrate transmission line ($W = 8.99\text{mm}$, $h = 3.175\text{mm}$, $\epsilon_r = 2.55$).	92

3.14	Characteristic impedance of a single layer substrate transmission line ($W = 37.0\text{mm}$, $h = 12.7\text{mm}$, $\epsilon_r = 2.40$).	93
4.1	A microstrip transmission line open and gap discontinuities.	113
4.2	Basis functions for the open circuit.	114
4.3	Comparison of the two Galerkin's procedures for $ \Gamma $ for an open ended line (freq = 20GHz, $W = .60\text{mm}$, $h = .635\text{mm}$, $\epsilon_r = 9.9$).	115
4.4	Comparison of the two Galerkin's procedures for $\angle\Gamma$ for an open ended line (freq = 20GHz, $W = .60\text{mm}$, $h = .635\text{mm}$, $\epsilon_r = 9.9$).	116
4.5	Convergence test for the two Galerkin's procedures for $ \Gamma $ for an open ended line (freq = 10GHz, $W = .60\text{mm}$, $h = .635\text{mm}$, $\epsilon_r = 9.9$).	117
4.6	Convergence test for the two Galerkin's procedures for $\angle\Gamma$ for an open ended line (freq = 10GHz, $W = .60\text{mm}$, $h = .635\text{mm}$, $\epsilon_r = 9.9$).	118
4.7	Frequency response of convergence for modified Galerkin's procedure for $ \Gamma $ for an open ended line ($W = .60\text{mm}$, $h = .635\text{mm}$, $\epsilon_r = 9.9$).	119
4.8	Frequency response of convergence for modified Galerkin's procedure for $\angle\Gamma$ for an open ended line ($W = .60\text{mm}$, $h = .635\text{mm}$, $\epsilon_r = 9.9$).	120
4.9	Calculated reflection coefficient ($\angle\Gamma$) for an open ended line with mea- surement made by Gronau and Wolff [101] ($W = .60\text{mm}$, $h = .635\text{mm}$, $\epsilon_r = 9.9$).	121
4.10	Calculated reflection coefficient ($ \Gamma $) for an open ended line ($W =$ $.60\text{mm}$, $h = .635\text{mm}$, $\epsilon_r = 9.9$).	122
4.11	Calculated reflection coefficient ($ \Gamma $) for an open ended line: SDA and Touchstone ($W = 8.99\text{mm}$, $h = 3.175\text{mm}$, $\epsilon_r = 2.55$).	123
4.12	Calculated reflection coefficient ($\angle\Gamma$) for an open ended line: SDA and Touchstone ($W = 8.99\text{mm}$, $h = 3.175\text{mm}$, $\epsilon_r = 2.55$).	124
5.1	Basis functions for the gap circuit.	127
5.2	Comparisons of the three different transverse distributions ($ \Gamma $) (freq = 5GHz, $W = .508\text{mm}$, $s = .04\text{mm}$, $h = .508\text{mm}$, $\epsilon_r = 8.875$).	131
5.3	Comparisons of the three different transverse distributions ($ T $) (freq = 5GHz, $W = .508\text{mm}$, $s = .04\text{mm}$, $h = .508\text{mm}$, $\epsilon_r = 8.875$).	132
5.4	Comparisons of the three different transverse distributions ($\angle\Gamma$) (freq = 5GHz, $W = .508\text{mm}$, $s = .04\text{mm}$, $h = .508\text{mm}$, $\epsilon_r = 8.875$).	133
5.5	Comparisons of the three different transverse distributions ($\angle T$) (freq = 5GHz, $W = .508\text{mm}$, $s = .04\text{mm}$, $h = .508\text{mm}$, $\epsilon_r = 8.875$).	134
5.6	Reflection coefficient $ \Gamma $ as a function of frequency for a gap ($W =$ 8.99mm , $s = 2.0\text{mm}$, $h = 3.175\text{mm}$, $\epsilon_r = 2.55$).	136
5.7	Reflection coefficient $\angle\Gamma$ as a function of frequency for a gap ($W =$ 8.99mm , $s = 2.0\text{mm}$, $h = 3.175\text{mm}$, $\epsilon_r = 2.55$).	137

5.8	Transmission coefficient $ T $ as a function of frequency for a gap ($W = 8.99\text{mm}$, $s = 2.0\text{mm}$, $h = 3.175\text{mm}$, $\epsilon_r = 2.55$).	138
5.9	Transmission coefficient $\angle T$ as a function of frequency for a gap ($W = 8.99\text{mm}$, $s = 2.0\text{mm}$, $h = 3.175\text{mm}$, $\epsilon_r = 2.55$).	139
5.10	Power loss as a function of frequency for a gap ($W = 8.99\text{mm}$, $s = 2.0\text{mm}$, $h = 3.175\text{mm}$, $\epsilon_r = 2.55$).	141
5.11	Reflection coefficient $ \Gamma $ as a function of the gap size (freq = 10GHz, $W = 8.99\text{mm}$, $h = 3.175\text{mm}$, $\epsilon_r = 2.55$).	143
5.12	Reflection coefficient $\angle \Gamma$ as a function of the gap size (freq = 10GHz, $W = 8.99\text{mm}$, $h = 3.175\text{mm}$, $\epsilon_r = 2.55$).	144
5.13	Transmission coefficient $ T $ as a function of the gap size (freq = 10GHz, $W = 8.99\text{mm}$, $h = 3.175\text{mm}$, $\epsilon_r = 2.55$).	145
5.14	Transmission coefficient $\angle T$ as a function of the gap size (freq = 10GHz, $W = 8.99\text{mm}$, $h = 3.175\text{mm}$, $\epsilon_r = 2.55$).	146
5.15	Power loss as a function of the gap size (freq = 10GHz, $W = 8.99\text{mm}$, $h = 3.175\text{mm}$, $\epsilon_r = 2.55$).	147
5.16	The reflection phases from port 1 and port 2 ($W = 8.99\text{mm}$, $s = 2.0\text{mm}$, $h = 3.175\text{mm}$, $\epsilon_r = 2.55$).	150
6.1	A microstrip corner and its PWS function covered area.	156
6.2	Magnitude convergence test for a corner (freq = 3GHz, $W_1 = W_2 = .508\text{mm}$, $h = 1.016\text{mm}$, $\epsilon_r = 10.2$).	166
6.3	Phase convergence test for a corner (freq = 3GHz, $W_1 = W_2 = .508\text{mm}$, $h = 1.016\text{mm}$, $\epsilon_r = 10.2$).	167
6.4	Frequency response of $ S_{11} $ for a corner ($W_1 = W_2 = .508\text{mm}$, $h = 1.016\text{mm}$, $\epsilon_r = 10.2$).	168
6.5	Frequency response of $\angle S_{11}$ for a corner ($W_1 = W_2 = .508\text{mm}$, $h = 1.016\text{mm}$, $\epsilon_r = 10.2$).	169
6.6	Frequency response of $ S_{21} $ for a corner ($W_1 = W_2 = .508\text{mm}$, $h = 1.016\text{mm}$, $\epsilon_r = 10.2$).	170
6.7	Frequency response of $\angle S_{21}$ for a corner ($W_1 = W_2 = .508\text{mm}$, $h = 1.016\text{mm}$, $\epsilon_r = 10.2$).	171
7.1	A vertical wire in a multilayer structure.	174
7.2	PWS functions on a vertical dipole.	183
7.3	Magnitude of the current on a dipole by SDA (freq = 3GHz, $a = .5\text{mm}$, $L = 50\text{mm}$).	184
7.4	Phase of the current on a dipole by SDA (freq = 3GHz, $a = .5\text{mm}$, $L = 50\text{mm}$).	185

7.5	Magnitude of the current on a dipole by spatial domain method (Harrington's method [41]) (freq = 3GHz, a = .5mm, L = 50mm).	186
7.6	Phase of the current on a dipole by spatial domain method (Harrington's method [41]) (freq = 3GHz, a = .5mm, L = 50mm).	187
8.1	Microstrip with a shorting via.	189
8.2	Attached mode due to the current flow on the via.	192
8.3	Convergence test of the reflection coefficient ($\angle\Gamma$) (freq = 2GHz, W = 2mm, h = 1mm, a = .1W, $x_p = -5$ mm, $y_p = 0$ mm, $\epsilon_r = 2.5$).	195
8.4	Convergence test of the reflection coefficient ($ \Gamma $) (freq = 2GHz, W = 2mm, h = 1mm, a = .1W, $x_p = -5$ mm, $y_p = 0$ mm, $\epsilon_r = 2.5$).	196
8.5	Frequency response of the reflection coefficient ($ \Gamma $) for a shorting via (W = 2mm, h = 1mm, a = .1W, $x_p = -5$ mm, $y_p = 0$ mm, $\epsilon_r = 2.5$).	198
8.6	Frequency response of the reflection coefficient ($\angle\Gamma$) for a shorting via (W = 2mm, h = 1mm, a = .1W, $x_p = -5$ mm, $y_p = 0$ mm, $\epsilon_r = 2.5$).	199
9.1	A microstrip discontinuity (corner) embedded in microstrip lines.	204
9.2	Signal flow graph for discontinuity measurement circuit.	205
9.3	Through lines with different lengths as standards.	206
9.4	Signal flow graph for the through line standards.	207
9.5	Im(γ) of the intervening transmission line (W = 37.0mm, h = 12.7mm, $\epsilon_r = 2.4$).	210
9.6	S-parameters of the coax-microstrip transition obtained with three standard lines.	211
9.7	Comparison of 3-line and 2-line untermination of the coax-microstrip transition.	212
9.8	Comparison of a corner's de-embedded $ S_{11} $ with measured data (W ₁ = W ₂ = 37.0mm, h = 12.7mm, $\epsilon_r = 2.4$).	214
9.9	Comparison of a corner's de-embedded $ S_{21} $ with measured data (W ₁ = W ₂ = 37.0mm, h = 12.7mm, $\epsilon_r = 2.4$).	215
9.10	Comparison of an open circuit reflection: de-embedded and measured (W = 37.0mm, h = 12.7mm, $\epsilon_r = 2.4$).	216
9.11	Comparison of a short circuit reflection: de-embedded and measured (W = 37.0mm, h = 12.7mm, $\epsilon_r = 2.4$).	218
9.12	Magnitude of zero length transmission line S-parameters (W = 37.0mm, h = 12.7mm, $\epsilon_r = 2.4$).	219
9.13	Phase of zero length transmission line S-parameters (W = 37.0mm, h = 12.7mm, $\epsilon_r = 2.4$).	220

List of Symbols

α	Attenuation constant of the transmission line.
β	Phase constant of the transmission line.
γ	Propagation constant, defined as $\alpha + j\beta$.
f	Frequency.
ω	Angular frequency, $\omega = 2\pi f$.
σ	Conductivity of the dielectric material.
ϵ_0	Permittivity of the free-space.
ϵ_{ri}	Relative permittivity of the dielectric material for layer i .
ϵ_i	Defined as $\epsilon_0\epsilon_{ri}$.
μ_0	Permeability of the free-space.
λ_0	Electromagnetic wavelength in free-space.
λ_x, λ_y	Fourier-domain variables in Cartesian coordinates.
λ	$\lambda = \sqrt{\lambda_x^2 + \lambda_y^2}$.
k_i	Wave number for layer i , defined as $\omega\sqrt{\epsilon_i\mu_0}$.
k_e	Effective propagation constant of transmission line.
q_i	$q_i = \sqrt{\lambda_x^2 + \lambda_y^2 - k_i^2}$.
a	Radius of the conductor pins or dipoles.
h	Thickness of the single-layer dielectric substrate.
j	$j = \sqrt{-1}$.
s	Size of a gap in a microstrip transmission line.
ae_1, ae_2	E_z^\mp Inputs to a multi-layer structure by an electric Herizian dipole.
ah_1, ah_2	H_z^\mp Inputs to a multi-layer structure by an electric Herizian dipole.
be_1, be_2	E_z^\mp Inputs to a multi-layer structure by a magnetic Herizian dipole.
bh_1, bh_2	H_z^\mp Inputs to a multi-layer structure by a magnetic Herizian dipole.
D	Thickness of the dielectric layers.
$[I]$	Current coefficient matrix to be determined in the moment method.
PWS	Piece-Wise-Sinusoidal current mode.
SDA	Spectral Domain Analysis.
L	Length of the vertical conductors.
W	Width of microstrips.
$[Z]$	Matrix for the reactions between basis and testing functions.
$[V]$	Matrix for the reactions between input and testing functions.
\mathbf{n}	Normal vector pointing from medium 1 to medium 2.
\mathbf{E}	Electric field intensity.
\mathbf{H}	Magnetic field intensity.
\mathbf{J}_s	Surface electric current density.

$\mathbf{J}_{\text{ms}}, \mathbf{M}_{\text{s}}$	Surface magnetic current density.
$G_{\mu\nu}$	The Green's function in μ direction due to a dipole in ν direction.
$\tilde{G}_{\mu\nu}$	The Fourier domain counterpart of $G_{\mu\nu}$.
R	Reflection coefficient of a network, same as s_{11} .
T	Transmission coefficient of a network, same as s_{21} .
Z_0	Characteristic impedance of transmission line.
Γ	Reflection coefficient or S_{11} of a network.
∇	Nabla operator, $\nabla = \mathbf{a}_x \frac{\partial}{\partial x} + \mathbf{a}_y \frac{\partial}{\partial y} + \mathbf{a}_z \frac{\partial}{\partial z}$.

Chapter 1

Introduction

The spectral-domain analysis (SDA) method can be attributed to Sommerfeld, who first derived the Green's functions for electromagnetic (EM) field due to Hertz dipoles in stratified media, and summarized his work in his book [1]. The Green's functions that Sommerfeld obtained were in integral form and are known today as the Sommerfeld integral. They are the exact spatial domain Green's functions expressed in integral form, which usually have to be evaluated numerically. This integral form of Green's functions are in fact the inverse Fourier transforms of the spectral domain Green's functions used in the spectral domain analysis [2].

Sommerfeld's technique was used in the analysis of microstrip line circuits by Yamashita and Mittra [3], and later further developed by Denlinger [4] and Itoh et al [5]-[9].

The spectral domain method is actually a Fourier-transformed version of the more general integral equation method applied to microstrip line and other printed circuits in layered structures, which can be used to analyze a wide range of printed circuits, such as aperture-coupled lines [10], microstrip-slotline and microstrip-microstrip transitions [11][12], cross and T junctions [13], strip crossovers [14], meander lines [15],

microstrip filters [16][17], non-uniform transmission lines [18], coplanar waveguide (CPW) elements [19], wires [20], and multiconductor transmission lines [21], in layered dielectric structures. The dielectric layers are assumed to be infinitely large in the horizontal directions. The medium for each layer is assumed to be homogeneous and isotropic (uniaxially/biaxially anisotropic media maybe included [22][23][24]), with finite relative permittivity ϵ_r , finite relative permeability μ_r (magnetic dielectrics [25][26]), and finite conductivity σ .

The integral equation method is a full-wave method: waves radiated into free space (space wave) and launched into the layered medium (surface wave) are included. Compared to the finite element method, the integral method does not require large computer memories, and open structures can be analyzed as easily as closed ones. There are two kinds of integral equations: the electric field integral equation (EFIE) and the magnetic field integral equation (MFIE), where the electric field and magnetic field, respectively, are expressed as a convolution between the appropriate Green's function and the current source. It was shown in [27] that MFIE fails for zero-volume embedded conductors. Since this dissertation deals with zero-thickness strips, the EFIE will be used.

A Green's function is determined by the composition of the physical structure, the electromagnetic (EM) properties of each layer involved, and the specifications of the source and the field: the locations of them in the structure, the orientations of the vector quantities, and their natures (electric or magnetic). It is one of the

basic building blocks in the integral equation method. If one inversely transforms (evaluates) the Sommerfeld integral Green's function back into the spatial domain, and uses it in the rest of the analysis, then this is the spatial domain integral equation method. This method does not require the basis functions for the moment method to have closed form Fourier transform. Therefore, it is flexible, and very suitable for odd shaped circuits. However, since there is usually no analytic solution to the inverse transform, one has to find a way to deal with the spatial domain Green's function. A straight forward but costly method is to calculate and tabulate the Green's function. A more effective way is to use approximate expressions. Good approximation work has been achieved to get closed form expressions for the spatial domain Green's function in references [28],[29] and [30], for example. Using the complex image method, Chow et al have obtained closed form Green's functions that give an error of only $.1 \sim 0.5\%$ with a few terms [31][32].

The spectral domain analysis (SDA) method does not use the inverse transform of the Green's function. Instead, it uses the transforms the basis and the testing functions of the moment method in the Fourier domain as well. Therefore, it is suitable for analysis of circuits with conductors of simple shapes. The main advantages of SDA method are that one works with the non-integral form Green's function which is the exact analytic solution to the Helmholtz equation, and that the Green's function can be generalized to accommodate multilayer, multistrip structures, without approximations. The main drawbacks of the SDA method is that heavy mathematical manipulations are involved, and it is computationally time costly, because usually

the double improper integrals have to be evaluated numerically.

The Green's function plays an important role in the analysis. It is the electric or magnetic field produced by an infinitesimal (point) electric or magnetic current source (Hertz dipole). The total field can then be determined by convolving (integrating) the Green's function with the real source distribution. Since the Green's function describes the electromagnetic system of the structure, its application is not restricted to transmission line type circuits. Microstrip antennas, for instance, can be analyzed using the Green's function [33]-[36], where the layer thickness and dielectric constants can be adjusted to improve the antenna performance. The coupling between the antenna elements through surface waves in the media, as well as space waves, can be calculated [37][38]. Radiation and surface wave losses can be distinguished from each other [39]. The EM waves from slot radiators and the field distribution in semiconductors can also be analyzed [40][41].

In most cases, the distribution of the source is not known a priori, and it has to be determined in the analysis. This is a very practical problem. In this dissertation various structures of microstrip circuits are analyzed, where none of the current distributions are assumed to be known. Instead, they are determined in the course of the analysis. The technique used to determine the unknown current distribution is the method of moments (MoM).

The moment method is a powerful tool for solving linear integral-differential

equations, such as the deterministic problem

$$L(f) = g \quad (1.1)$$

where L is a linear operator, f is the unknown solution function, and g is the function resulted from the application of L on f . In the moment method, the unknown function f (in our analysis, the current distribution function) is replaced by an approximate function f^a which is a linear combination of a series of known functions (basis), the coefficients of which are to be determined in the process:

$$f^a = \sum_n \alpha_n f_n \quad (1.2)$$

Here, the moment method uses a finite number of terms (functions) to represent an unknown function. Thus the original problem becomes

$$\delta + \sum_n \alpha_n L(f_n) = g \quad (1.3)$$

where δ is the error due to the introduction of f^a . Another series of functions, called weighting functions or testing functions, w_m , in the range of L , is used to take the inner product with Equation 1.3. The moment method lets the inner product $\langle w_m, \delta \rangle$ be zero. Comparing Equation 1.3 with the original problem Equation 1.1, it is noted that by letting inner product $\langle w_m, \delta \rangle$ be zero, MoM approximates the exact solution f with f^a in a sense that it equates the projections of $L(f)$ and $L(f^a)$ on $\mathcal{J}(w_m)$, where $\mathcal{J}(w_m)$ is the space spanned by the w_m . Since the error δ is orthogonal to the projections (inner product is zero), it is of second order, and the moment method solution minimizes the error δ [42]. If the dimension of the linearly

independent basis functions is greater than the dimension of the solution space, the moment method solution is exact.

The moment method is not only used in the spectral domain, it is also widely used in the spatial domain, where the domain of the basis functions can be more flexible (see [43], for instance).

In this dissertation, a generalized Green's function is first derived in Chapter 2. It is generalized in that all the electric and magnetic field components generated by an infinitesimal, electric or magnetic dipole (Hertz dipole), can be calculated in the spectral domain for any multilayer structure. In other words, this Green's function can be used in the analysis of all kinds of layered structures. The electromagnetic (EM) waves generated by the Hertz dipole is decomposed into TM and TE waves with respect to the normal direction (z) of the layers, in the spectral domain. The propagation of the TE and TM waves within the structure is represented with a signal flow graph, which has not been used in this context in literature. Based on the transmission line theory and the signal flow graph manipulations, two layer removal methods are developed, which make the evaluation of the Green's function faster.

Chapter 3 deals with the analysis of infinitely long microstrip transmission lines. This analysis determines the effective propagation constant k_e (or equivalently, the effective dielectric constant ϵ_e), and the characteristic impedance Z_0 , the two most important calculated parameters for any transmission line. This step is important

and necessary, because the other chapters will have to make use of the infinite line analysis.

The propagation constant calculation is quite straight forward. First a current on the strip, with assumed transverse magnitude profile, travels down the strip with an unknown propagation constant. The tangential electric field due to this current is obtained by convolving the assumed current with the generalized Green's function and then this tangential electric field is set to be zero on the surface of the strip (boundary condition). The inner product between this tangential field and the assumed current is taken to enforce the boundary condition. The inner product is still zero, because the tangential field and the testing current are complementarily zero (Galerkin's procedure of moment method). This results in a characteristic integral equation, the root being the unknown effective propagation constant k_e . This method can be used to analyze microstrip transmission lines in any kind of multilayer structures, because the generalized Green's function is employed which takes care of the properties of the structures.

Four sets of electric current basis functions are used and the results are compared. Useful conclusions on the choice of the basis current functions are given.

The calculation of the characteristic impedance Z_0 involves the computation of the transmitted power as well as the total current on the strip. The total current can be determined in the propagation constant calculation, where the moment method is used to determine the coefficients of the current basis functions. The power can be

obtained by integrating the Poynting vector over the transversal plane, whose normal is to the direction of the current flow. A generalized Poynting vector function for multilayered structures is derived for the calculation of the characteristic impedance of microstrip transmission lines.

Chapter 4 and 5 cover the analyses of 1-D microstrip discontinuities: opens and gaps, so called because they have changes in only one of the three dimensions, in this case the transmission direction. Away from the discontinuity, the current on the strip is assumed to be a traveling wave, with the propagation constant obtained from the infinite line analysis. A unit traveling wave is incident from $-\infty$, and the reflected wave is from $x = 0$ back to $-\infty$ with the same propagation constant but with the opposite sign. The amount of the reflected traveling wave, R , the reflection coefficient, is an unknown to be determined. In the vicinity of the discontinuity, the current distribution is not expected to be well organized traveling waves. Therefore, the current at the discontinuity is locally expanded into a series of roof-top functions. The linear combination of these roof-top functions, together with the incident and the reflected traveling wave, represent the true current distribution on the strip. The roof-top functions can be either triangle functions or piece-wise-sinusoidal (PWS) functions. The latter has been found to be more convergent, because the reconstructed current is smoother [44]. Studies by other researchers have shown [4][45] that the transverse current is only of significance for very wide strips. For most practical microstrip transmission lines the magnitude of the transverse current is usually -20~-40 dB below the longitudinal current.

If the discontinuity is an open, only the reflected wave and local current basis have to be determined. If the circuit is a gap, there are also transmission and local current on the coupled branch which are also unknowns to be determined. These two analyses, however, are very similar to each other. The modified Galerkin's procedure is applied to determine current distribution. It is noted that at locations away from the discontinuity, the traveling wave mode causes the boundary conditions to be automatically satisfied. This is because the traveling wave is obtained from the infinite line analysis, and at locations far away from the discontinuities, the transmission line behaves like an infinitely long line. Thus, the testing functions are needed only in the region of the discontinuity, where boundary conditions have to be enforced. Two Galerkin's procedures are compared, which validate the local need of the boundary condition enforcement at the discontinuities. Also, a step-up convergence test procedure is suggested, which increases the number of the basis functions one by one, while the convergence of the algorithm is monitored.

Chapter 6 deals with the analysis of the 2-D discontinuity. Corners of microstrip transmission lines are analyzed. As 2-D implies, the configuration of the line changes in both the x and the y directions. At the discontinuity, the current can flow in either direction. This area is segmented into small rectangles, and x and y direction currents on these small cells are assumed. The magnitudes of these currents are determined by the moment method, which converts the electric field integral equation (EFIE) into linear equations, the unknowns being the magnitudes of the current basis functions; and the elements in the coefficient matrix of the linear equation are the reactions

(inner products) between current basis functions (PWS and traveling wave functions) and testing functions (all PWS functions) (For exact Galerkin's procedure they are the same). Unlike the 1-D analysis, where only one element in the dyadic Green's functions, G_{xx} , is used, the 2-D analysis makes use of G_{xx} , G_{yy} , G_{xy} , and G_{yx} . Good agreement has been achieved between this analysis and the one by Harokopos et al [46].

The spectral domain analysis technique as it applies to circuits with vertical objects (3-D) is given in Chapter 7 and 8, where a vertical half-wavelength dipole and a via-shortened microstrip transmission line are analyzed. This analysis involves the use of the Green's functions for a vertical Hertz dipole. The combined use of vertical Green's functions with horizontal ones makes possible the analysis of virtually all layered structures with strips and vertical wires. If current expansion included the transverse current, better agreement with the measurement should be achieved. In that case, all nine elements in the Green's function dyad will have to be used.

The de-embedding measurement of the microstrip discontinuities is discussed in Chapter 9, where two de-embedding techniques are presented. The first one makes use of redundancy (with multi-through-line references) measurements to reduce the random error due to the non-uniformity of the connectors, lines and discontinuities, and least-squared-error de-embedding results are obtained. This method does not need a time-domain loaded network analyzer, and the random errors can be reduced to a minimum with multiple reference through lines and DUT (device under test)

circuits. The second de-embedding technique takes advantage of the time-domain feature of an automatic network analyzer. It needs only one reference line and the required data processing is substantially reduced. Both techniques have been used in the research and have proved to be effective.

Finally, the conclusion is presented in Chapter 10, where a brief summary is given on the research of the spectral domain technique in this dissertation. Future work is suggested to simplify and speed up the analysis method, to make it more useful.

All fields and currents involved in this dissertation are assumed to be harmonically time dependent, and a factor of $e^{j\omega t}$ is assumed throughout and is suppressed in the equations.

Chapter 2

Generalized Dyadic Green's Functions

Green's function plays an important role in integral equation techniques. By definition, a Green's function is the response of a linear system to an impulse (δ) input. In this dissertation, specifically speaking, the response is the electromagnetic field; the input is an elementary current source, which can be either an electric or a magnetic Hertz dipole; and the linear system is the multilayered dielectric structure in which microstrips and/or vertical conductors are embedded. Most Green's functions used in literature are only the field components involved in the analysis for the specific structures (usually a one or two dielectric layer structure). In this chapter, derivation of a generalized Green's function is made, which can be used to express any of the electromagnetic field components, for arbitrary multilayered structures. The point source can be either an electric or a magnetic Hertz dipole.

The generalized Green's function gives the electromagnetic field response to a point source in an arbitrary horizontally large, stratified dielectric structure. The analysis of the microstrip circuits, which is presented here in this dissertation, makes heavy use of the Green's functions. The generalization of the Green's functions in effect enables the analysis of multilayer, multistrip analysis.

Dyadic Green's functions are concise representations of vector-input, vector-output systems. For our analyses, they are the relationships between vector electromagnetic fields and vector elementary source currents. For instance, G_{xy} is the electric field in the x direction due to a Hertz dipole in the y direction. In a matrix representation of the dyadic Green's function, G_{xy} is just one of nine elements in a 3×3 matrix. The δ current vector is related to the vector electric or magnetic field by the dyadic Green's function.

Generalization of the Green's function to accommodate multilayer, multistrip structures are performed by Das et al [47], Itoh et al [8][9], and others [48][49][50], in various ways. Some of them, [8], for instance, uses quasi-TEM approximation to derive generalized Green's functions for shielded structures. Most of these analyses make use of magnetic vector potentials.

Layered medium Green's function can be either in the spatial domain or in the spectral domain. The exact analytic expression in the spatial domain is the famous Sommerfeld integral [1]. The spatial domain integral equation analysis has some advantages: it is easier for one to work in the physical world because EM waves and electric current are physical phenomena and the circuits involved are all finite in size, one does not have to switch back and forth between the two domains, less manipulation is required, and numerical work will be easier because the spectral domain method usually requires evaluation of infinite integrals. It is also easier to analyze odd shaped discontinuities even with lumped elements in the spatial domain [51]. To

make spatial domain analysis feasible one has to derive the spatial domain Green's function. The starting point of most of the derivations is the Sommerfeld integral, the exact Green's function. Some spatial domain Green's functions were derived for specific type of circuits, by Alanen and Lindell [28], Barkeshli et al [29] and Aksun and Mittra[30], for instance. The complex image method has been used by Chow et al to get approximate spatial domain Green's functions [52][53][54][31][32]. In [31], the closed form Green's function of a point charge in multilayered media was derived. In [32], the Green's function of a horizontal electric dipole in layered dielectrics between two ground planes was derived, which was used in the analyses of coplanar waveguide with air bridge [55] and multiconductor transmission lines [56]. The use of complex images can give the Green's functions an error of $.1 \sim 0.5\%$ with a few terms.

In this chapter, a generalized spectral domain dyadic Green's function is derived. The expressions obtained are in closed form and are the exact solutions to the Helmholtz equations. This spectral domain Green's function can represent all the Green's functions that are frequently encountered in planar structure analyses, as long as the media are homogeneous and isotropic. It can be used for arbitrary multilayer, multistrip, and vertical wire configurations. It is rigorous in that the losses due to space-wave radiation and surface-wave generation are included in the expressions. The power losses to the dissipative dielectric layers and the imperfect ground plane can also be included. The function itself is implemented in a C++ language program, and is easy to evaluate. The calculated response quantities can

be any of the electric or magnetic field components (E_x , E_y , E_z , H_x , H_y , and H_z), and the input can be either an electric or a magnetic current Hertz dipole in any orientation.

The EM waves are decomposed into TE and TM waves (modes) with respect to the z direction (the normal direction of the layer planes). The propagation of the TE and TM waves within the structure is represented with signal flow graphs. A fast evaluation algorithm using layer removal method is developed. The asymptotic behavior as the arguments (the spectral domain variables λ) become large is also studied and the expressions are derived.

2.1 Mathematical Definitions

2.1.1 Green's Functions

The Green's function method is very powerful in solving linear partial differential equations. It can be applied to a large group of electromagnetic problems. Theoretically, it is the response to an elementary point source, and the final solution to the given source is the convolution between Green's function and the real source distribution function.

Suppose a linear inhomogeneous equation has the following form:

$$\mathcal{L}U(\vec{r}) = f(\vec{r}) \quad (2.1)$$

where \mathcal{L} represents a linear integral-differential operator, $U(\vec{r})$ is the unknown solution function and $f(\vec{r})$ is the input. Now, instead of solving Equation 2.1 directly, Green's function method tries to solve a related auxiliary equation as follows:

$$\mathcal{L}G(\vec{r}) = \delta(\vec{r}) \quad (2.2)$$

where $G(\vec{r})$ is called the Green's function, and $\delta(\vec{r})$ is the impulse function, which is also called the Dirac function. $\delta(\vec{r})$ is used to represent an elementary input. The boundary conditions and other parameters about the system are the same as the original problem. In other words, only the input function is replaced by the impulse function.

If the solution G to Equation 2.2 exists and is known, then the solution to the original Equation 2.1, $U(\vec{r})$, can be obtained through the following expression:

$$U(\vec{r}) = \iiint f(\vec{r}')G(\vec{r} - \vec{r}')dv' \quad (2.3)$$

where the volume integration is conducted over the region (v') where the source $f(\vec{r}')$ is defined. This integrates all the contributions of $f(\vec{r}')$ onto $U(\vec{r})$ as governed by $G(\vec{r} - \vec{r}')$.

If the original integral-differential equation Equation 2.1 deals with the relationship between an electromagnetic field component U and a current source distribution f (either electric or magnetic current), the solution G to the auxiliary Equation 2.2 is the associated Green's function and the impulse source is a Hertz dipole. The original equation is called the Helmholtz equation, which is derived from Maxwell's

equations. If only electric current is the source, the equation takes the form

$$\nabla \times \nabla \times \mathbf{E} - k^2 \mathbf{E} = -j\omega\mu \mathbf{i}_s \quad (2.4)$$

where ∇ is the Nabla operator, k is the wave number of the medium, ω is the angular frequency, \mathbf{E} is the vector electric field intensity, and \mathbf{i}_s is a vector current source.

Equation 2.4 is a vector-input, vector-output equation. It is noted that a current source in one direction can cause a electric field in all three directions, and that a electric field in one direction can have contributions from the current source in all three direction. To apply the scalar Equation 2.3, one has to write as many as nine such integrals to have a complete representation of the vector electric field generated by a vector current source. It is very inconvenient to write these scalar equations. The problem can be eased by using the dyadic representation of the Green's functions.

2.1.2 Dyadic Green's Functions

A dyad is a group of quantities, which is in this context refers to the relationship between a pair of vectors. The use of this terminology makes it easier to understand the application of dyadic Green's functions in our analysis. In this dissertation, a dyad is used to represent the relationship between a vector source and a vector field. The source is either an electric or a magnetic current filament (Hertz dipole), while the field is either an electric or a magnetic field excited by the source.

The dyadic representation of the Green's function simplifies the notations, and emphasizes the relationship between each pair of the field and the current vector elements. For example, if one needs to express the relationship between a vector electric current and its electric field, a nine-element dyadic Green's can be used. The elements in a dyadic Green's function, however, have to be derived in the usual way.

In the stratified structures we are dealing with, a dyadic Green's function is a function of the coordinates of the source Hertz dipole (x', y', z') and the field (x, y, z) , known as the source point and field point, respectively. The orientations of the source and the field vector are all included in the dyad.

Using a dyadic representation, an elementary electric field $d\mathbf{E}$ can be written as the product between the dyadic Green's function $\vec{\mathbf{G}}(x, y, z|x', y', z')$ and an elementary current $d\mathbf{J}$ as

$$d\mathbf{E}(x, y, z) = \vec{\mathbf{G}}(x, y, z|x', y', z') \cdot d\mathbf{J}(x', y', z') \quad (2.5)$$

This can be expressed more explicitly in matrix form as

$$\begin{bmatrix} dE_x(x, y, z) \\ dE_y(x, y, z) \\ dE_z(x, y, z) \end{bmatrix} = \begin{bmatrix} G_{xx} & G_{xy} & G_{xz} \\ G_{yx} & G_{yy} & G_{yz} \\ G_{zx} & G_{zy} & G_{zz} \end{bmatrix} \cdot \begin{bmatrix} dJ_x(x', y', z') \\ dJ_y(x', y', z') \\ dJ_z(x', y', z') \end{bmatrix} \quad (2.6)$$

In Equation 2.6, each elementary field component is clearly expressed to be dependent upon all the elementary current components. Conversely, each current element has contributions to all field elements, which means that if the source is only in one direction, one can still expect a field in all directions. From this equation it is also

seen that a dyad in Cartesian coordinate system has nine elements. However, in practical planar circuit analysis, after some simplifications, assumptions, and mathematical preprocessing, usually only one or two of the nine elements will be used.

The integral form of Equation 2.5 is the spatial domain electric field integral equation (EFIE):

$$\mathbf{E}(x, y, z) = \iiint \vec{\mathbf{G}}(x, y, z | x', y', z') \cdot \mathbf{J}(x', y', z') dx' dy' dz' \quad (2.7)$$

where the current \mathbf{J} is usually the unknown and is determined in the analysis as the boundary conditions for the electric field \mathbf{E} are applied on the conductor surfaces.

2.1.3 Spectral Domain Analyses

The dyadic Green's functions referred to hereafter can be used to represent any of the following combinations of source and field:

- Electric field due to an electric current Hertz dipole.
- Electric field due to a magnetic current Hertz dipole.
- Magnetic field due to an electric current Hertz dipole.
- Magnetic field due to a magnetic current Hertz dipole.

The 2-D Fourier transform of a spatial function into its spectral form is given by Stinson, for instance, as [57].

$$\tilde{\vec{G}}(\lambda_x, \lambda_y, z, x', y', z') = \frac{1}{4\pi^2} \iint \vec{G}(x, y, z | x', y', z') e^{-j\lambda_x(x-x')} e^{-j\lambda_y(y-y')} dx dy \quad (2.8)$$

while the inverse transform is defined as

$$\vec{G}(x, y, z | x', y', z') = \iint \tilde{\vec{G}}(\lambda_x, \lambda_y, z, x', y', z') e^{j\lambda_x(x-x')} e^{j\lambda_y(y-y')} d\lambda_x d\lambda_y \quad (2.9)$$

Note that the coordinates x and y have been transformed into the spectral domain variables λ_x and λ_y , respectively. The vertical coordinate z remains intact. This is because the structure is assumed to be infinite in the horizontal directions, and layered in the vertical (z) direction.

The advantages of using the spectral domain analysis are that the Green's functions are exact solutions to Helmholtz equation, and it is easy to generalize the analysis into multilayer, multistrip structures. The original problem is in the spatial domain, which is physically easy to view and understand. However, it is usually easier to solve the problem in the spectral domain. For instance, to solve Equation 2.2, one has to deal with a δ function in the spatial domain. So far there are only a few special cases where simple analytical Green's function solutions can be obtained for this kind of problem. If transformed into the spectral domain, the δ function simply becomes a constant, which is easier to handle. In addition, transforming from the spatial domain into the spectral domain also converts differential and integral operations into simple algebraic operations, which further simplifies the problem. For

instance, in the spectral domain, the Helmholtz equation for Green's function G_{xx} becomes [58]

$$(\lambda_x^2 + \lambda_y^2 - k^2)G_{xx} - \frac{\partial^2}{\partial z^2}G_{xx} = -j\frac{1}{4\pi^2}\omega\mu_0 \quad (2.10)$$

If the Hertz dipole is at an interface between two adjacent layers, all the layers are source-free. If the Hertz dipole is within a layer, then an imaginary interface can be purposely defined in the plane where the Hertz current dipole resides. This imaginary interface divides that layer into two layers, and makes all layers source-free. Now the Hertz dipole is at an interface, and can be accounted for in the application of the boundary conditions over that interface. The Helmholtz equations are now homogeneous (zero on the right-hand side) in all the layers. The spectral domain solutions are simply two exponential functions of z with two constants to be determined with solutions in other layers. With the application of boundary conditions on all the interfaces between the dielectric layers, the field due to this Hertz dipole can be obtained, which is known as the spectral domain Green's function.

2.2 Theory

The generalized structure to be analyzed is shown in Figure 2.1. The total number of layers is n , with the Hertz dipole residing between k th and $(k + 1)$ th layers. No matter whether the Hertz dipole resides in a physical interface, the plane in which it resides is always defined as an interface. This insures that all layers are source-free. The inputs to the structure due to this Hertz dipole will be determined later using

boundary conditions.

For any specific circuits, the number of dielectric layers, their thickness, and their dielectric constants should be known to the user. If there is no slot in the structure, only electric field and electric current are involved. The current distribution on the conductors is unknown. The electric field generated by a Hertz dipole in the place of the unknown electric current has to be determined first, where the electric field by definition is the Green's function. In the circuit analysis the Green's function is convolved with the unknown current distribution on the conductor surface, to get the expression for the total electric field. With the enforcement of the boundary conditions for the electric field on the conductor surface, and the application of the moment method, the true current distribution can be determined. The Hertz dipole has to be in the plane where the strip is embedded, hence the location of the Hertz dipole is known in the derivation of the Green's function.

Now that we have defined the source to be at an interface, all the regions within the layers become source-free, which makes possible in layer i , for instance, the following spectral domain solutions (Green's functions) to the Helmholtz equations:

$$\tilde{\mathbf{G}}_i(\lambda_x, \lambda_y, z) = \tilde{\mathbf{G}}_i^+(\lambda_x, \lambda_y) e^{-q_i z} + \tilde{\mathbf{G}}_i^-(\lambda_x, \lambda_y) e^{+q_i z} \quad (2.11)$$

$$\tilde{\mathbf{H}}_i(\lambda_x, \lambda_y, z) = \tilde{\mathbf{H}}_i^+(\lambda_x, \lambda_y) e^{-q_i z} + \tilde{\mathbf{H}}_i^-(\lambda_x, \lambda_y) e^{+q_i z} \quad (2.12)$$

where electric fields $\tilde{\mathbf{G}}_i^\pm(\lambda_x, \lambda_y)$ and magnetic fields $\tilde{\mathbf{H}}_i^\pm(\lambda_x, \lambda_y)$ are to be determined together with the fields in other layers, and $q_i = \sqrt{\lambda_x^2 + \lambda_y^2 - k_i^2}$, where $k_i^2 = \omega^2 \mu \epsilon_i$.

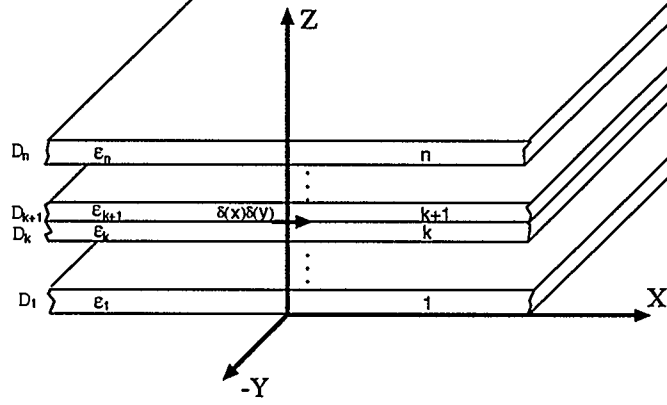


Figure 2.1: The generalized geometry of multilayer structures.

It is noted that the sign of the square root

$$q_i = \sqrt{\lambda_x^2 + \lambda_y^2 - k_i^2}$$

is carefully determined to denote the direction of the propagation of the spectral wave. For the open structures, the infinitely thick layers should only have outward bound waves, which decrease as an exponential function of z .

Obviously the final determination of the Green's function in the structure involves the enforcement of the boundary conditions for electric and magnetic fields at each interface. The use of transverse-electric (TE) and transverse-magnetic (TM) modes makes the derivation systematic and very efficient.

It is known that electromagnetic waves can be decomposed into TE and TM modes that depend only on longitudinal electric and magnetic fields, respectively, and

TE and TM waves do not couple to each other as they cross a dielectric interface [59]. This means that one can process TE and TM modes separately in the structure and superposition them at the final stage. The advantage of this decomposition is that one can apply transmission line and microwave network theory in the determination of the EM fields.

In the stratified structures, due to their uniformity in the horizontal directions, the wave traveling upward and downward in the z direction can be decomposed into TE (which depends on H_z) and TM (which depends on E_z) waves, also known as LSM and LSE modes [60]. Therefore, all the field components can be expressed in terms of the longitudinal-to- z components H_z and E_z , Where the TE wave is totally determined by H_z , and the TM wave is totally determined by E_z .

There are traveling waves in both $+z$ and $-z$ directions due to the reflection and the transmission at the layer interfaces. Therefore, in each layer, there are TE and TM waves traveling in both the $+z$ and the $-z$ directions. So by solving for H_{zi}^+ , H_{zi}^- , E_{zi}^+ , and E_{zi}^- one can determine the total electric and magnetic fields in the z direction in a layer i . The other field components can be determined from the electric and magnetic field in the z direction. Therefore, the most important step in obtaining the Green's functions is to determine the four unknown longitudinal fields in the layer of the field point.

As a matter of fact, the decomposition of the fields in the stratified media into TM and TE takes E_z and H_z as potentials [61]. There are numerous choices for

the potentials. It is quite often a personal choice as to which potentials to use. The most commonly used ones are the magnetic vector potential \vec{A} , and the electric vector potential \vec{F} . One can choose to use different combinations of elements from \vec{A} and \vec{F} . For instance, there are Hertz-Debye potentials, Sommerfeld potentials, and transverse potentials. There are also mixed potentials which makes use of scalar potentials, as well as vector ones. Each set of these potentials has their own features, some lead to better numerical convergence; some are easy to handle; some give good symmetry of revolution. Mosig in [62] briefly introduces and compares the different potentials. His conclusion as to which choice is easier and more systematic for layered structure is that it is advisable to use the longitudinal field components E_z and H_z , or components of Hertz vector potentials which are in fact different from longitudinal fields by a constant factor. This is because, although the computation of the potentials is possible, the boundary condition across the layer interfaces have a simpler formulation with longitudinal field potentials; the other field expressions are easier to write; and the integral equation is easier to formulate. The most convenient part is that one can use EM wave knowledge directly in the formulation. For instance, the boundary condition can be formulated as soon as the field expression is obtained—one does not have to derive the boundary conditions for the potentials. Also the integral equations are concise and its physical meaning is clear.

The boundary conditions for the dielectric interfaces are that the tangential electric and magnetic field have to be continuous across the interface, unless electric or magnetic current sources exist at the interface. It is known already that the only

source we are dealing with is the Hertz dipole.

Since the δ function current (the Hertz dipole) is located at an interface, and has been transformed into a constant in the spectral domain, the Hertz dipole at the interface can be easily accounted for in the application of the boundary conditions. The spectral domain boundary conditions due to the existence of the Hertz dipole at

$$x = 0, \quad y = 0$$

are derived as follows below.

In the spatial domain, at the boundary where a surface current exists, the following boundary conditions apply

$$\mathbf{n} \times (\mathbf{H}_2 - \mathbf{H}_1) = \mathbf{J}_s \quad (2.13)$$

$$\mathbf{n} \times (\mathbf{E}_2 - \mathbf{E}_1) = -\mathbf{J}_{ms} \quad (2.14)$$

where \mathbf{J}_s and \mathbf{J}_{ms} are the surface electric and magnetic current densities, respectively, and \mathbf{n} is the unit normal vector pointing from medium 1 to medium 2. If there is only an x directed electric Hertz dipole at the interface, for instance, all field components are continuous across this interface except for H_y , which becomes

$$H_{y1} - H_{y2} = \delta(x)\delta(y) \quad (2.15)$$

By taking the 2-D Fourier transformation of the equation it becomes

$$\tilde{H}_{y1} - \tilde{H}_{y2} = \frac{1}{4\pi^2} \quad (2.16)$$

Thus the boundary conditions at the interface where the dipole resides show that all tangential field components should be continuous except for \tilde{H}_y .

At all the other interfaces the tangential fields (\tilde{E}_x , \tilde{E}_y , \tilde{H}_x , and \tilde{H}_y) are continuous, because there are no sources at those interfaces.

As the multilayer structure is defined to be infinite in the x and y directions, it is layered only in the vertical (z) direction. The top and bottom layer, each of which has only one side facing the rest of the structure, are called boundary layers. The outer side of a boundary layer faces a termination, which is the boundary of the whole structure. For any structure there are two terminations, the top one and the the bottom one. A termination has no thickness. It is described by its reflection properties to TE and TM waves, which are usually jointly determined by the dielectric properties of the boundary layers and that of the materials attached to the outer sides of the boundary layers. These terminations give the relationship between the incident and the reflected TE and TM waves. Examples of these terminations are

1. a match where there are no reflected waves (leaving waves only, $|\Gamma| = 0$).
2. a perfect conducting plate where the reflected wave has the same amplitude as the incident wave and the phase is either 0° (TM) or 180° (TE).
3. any other known value of reflection coefficient ($|\Gamma| \leq 1$) that can determine the reflected wave.

Free space is considered as a layer for an open structure. However, no layer can be specified as being infinitely thick. A practical way to treat any infinite layer thickness is to give it a very large value, say, 10 meters for an inch thick circuit, for instance. This thickness is irrelevant for propagation and S-parameter computations, as long as the reflection of the termination is set to be zero. For characteristic impedance computation, however, the layer thickness is important because the electromagnetic power flow has to be computed over a specified structure region in a plane whose normal is in the same direction as the transmission line. A perfect conductor termination is the most common for microstrip structures, where all incident TE and TM waves are reflected. If the ground plane is not a perfect conductor, an equivalent surface impedance can be used to determine the reflected TE and TM wave [63].

If the structure has n layers total, with the possibility that the two outermost ones are semi-infinite, there are $(n - 1)$ interfaces and 2 terminations. The unknowns in solving for the Green's functions are the z direction electric and magnetic fields in each layer. To determine the total electric field E_{zi} in the z direction in layer i one needs both E_{zi}^+ and E_{zi}^- to be determined. The same is true for H_{zi} . Therefore in each layer one has to determine four unknowns. The total number of unknowns is therefore $n \times 4$. When enforcing the boundary conditions, each interface can give four independent equations, resulting from boundary conditions for E_x , E_y , H_x , and H_y across the interface, respectively. The interfaces then can give $(n - 1) \times 4$ equations. The terminations can uniquely determine the reflected E_z (TM) and H_z (TE) in the

boundary layers. Then the terminations can give another 4 (2 for each termination) equations. There are now in total $n \times 4$ equations for $n \times 4$ unknowns. Thus the solutions to the problem are unique.

Since one can decompose the traveling wave into TE and TM components, which do not couple to each other in the structure, one can respectively determine the desired field components by the TE and TM waves, and superposition them at the final stage. The propagation of TE and TM modes within layered structures are very similar to that of EM waves in a circuit where networks are linked with transmission lines. In the layered structure, TE and TM modes get partly reflected and partly transmitted at the dielectric interfaces, which suggests that an interface acts like a network for microwave signals; within the layers the TE and TM waves travel with the spectral domain propagation constant q_i as $e^{\pm q_i z}$, which is like the propagation of microwave signals in a transmission line, with spatial propagation constant β ($e^{\pm j\beta z}$). Due to these similarities, the behavior of the TE and TM waves within a layered structure can be treated as microwave signals in a cascaded network interlinked with transmission lines, where signal flow graphs can be used to present an accurate conceptual and mathematical picture.

The topology of the signal flow graph, which is determined by the structure and the location of the Hertz dipole, is the same for both TE and TM waves, as shown in Figure 2.2. The branches between nodes in Figure 2.2 show that the TE and TM waves are transmitted and reflected at interfaces, and propagate within the layers

from one interface to another. The network parameters describing the interfaces and the terminations, and the inputs to the signal flow graph, are different for TE and TM waves, as expected. At each interface, if the TE and TM waves traveling to $+z$

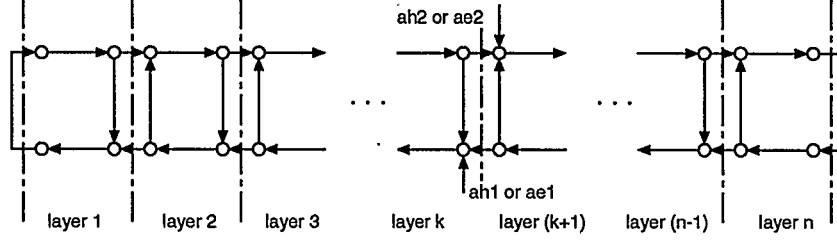


Figure 2.2: Generalized signal flow graph for multilayer structures.

direction are incident from medium 1 to medium 2, the transmission and reflection coefficients are

$$T_{TE}^{1 \rightarrow 2} = \frac{2 q_1}{q_1 + q_2} \quad (2.17)$$

$$\Gamma_{TE}^{1 \rightarrow 2} = \frac{q_1 - q_2}{q_1 + q_2} \quad (2.18)$$

$$T_{TM}^{1 \rightarrow 2} = \frac{2 q_1 \epsilon_1}{q_1 \epsilon_2 + q_2 \epsilon_1} \quad (2.19)$$

$$\Gamma_{TM}^{1 \rightarrow 2} = \frac{q_1 \epsilon_2 - q_2 \epsilon_1}{q_1 \epsilon_2 + q_2 \epsilon_1} \quad (2.20)$$

where

$$T_{TE}^{1 \rightarrow 2} = \frac{H_{z2}^+}{H_{z1}^+},$$

$$\Gamma_{TE}^{1 \rightarrow 2} = \frac{H_{z1}^-}{H_{z1}^+},$$

$$T_{TM}^{1 \rightarrow 2} = \frac{E_{z2}^+}{E_{z1}^+},$$

and

$$\Gamma_{TM}^{1 \rightarrow 2} = \frac{E_{z1}^-}{E_{z1}^+}.$$

If the TE and TM waves are incident from medium 2 to medium 1 (in this case, the incident wave is traveling in the $-z$ direction), the subscripts and superscripts “1” and “2” in the expressions above would be exchanged and thus another four expressions result. Therefore, for each interface in Figure 2.2, there are four network parameters (two reflections and two transmissions) for each of the TE and TM waves. For the waves that travel within the layers, the branches between the interfaces are simply exponential functions, as $e^{-q_i D_i}$ in layer i , for instance, where D_i is the thickness of layer i .

The four parameters ah_1 , ah_2 , ae_1 , and ae_2 in Figure 2.2 are the inputs to the networks, which are excited by the Hertz dipole at the dielectric interface between layers k and $(k+1)$. ah_1 and ah_2 are H_z^- in the $-z$ direction and H_z^+ in the $+z$ direction, respectively (TE modes). ae_1 and ae_2 are E_z^- in the $-z$ direction and E_z^+ in the $+z$ direction, respectively (TM modes).

The values of the four parameters ah_1 , ah_2 , ae_1 , and ae_2 are determined by solving the problem shown in Figure 2.3, where the radiation into two semi-infinite half spaces with different dielectric constants, by a Hertz dipole residing at the interface is solved for. This Hertz dipole launches $ah_2(H_z^+)$ and $ae_2(E_z^+)$ to the upper space, and $ah_1(H_z^-)$ and $ae_1(E_z^-)$ to the lower space. Their expressions are obtained simultaneously as the boundary conditions for the tangential electric and magnetic

field are applied at the interface. These inputs are in fact the TE and TM modes that the Hertz dipole launches into the structure. If there is no other interfaces than the one in which the Hertz dipole is embedded, the total longitudinal field distribution will be expressed with these four inputs with spectral domain propagation constants q_k and q_{k+1} . However, we are dealing with a layered structure, where the TE and TM modes are bounced back and forth between layer interfaces, which changes the “initial” longitudinal field distribution by the four inputs. Therefore signal flow graph shown in Figure 2.2 has to be solved.

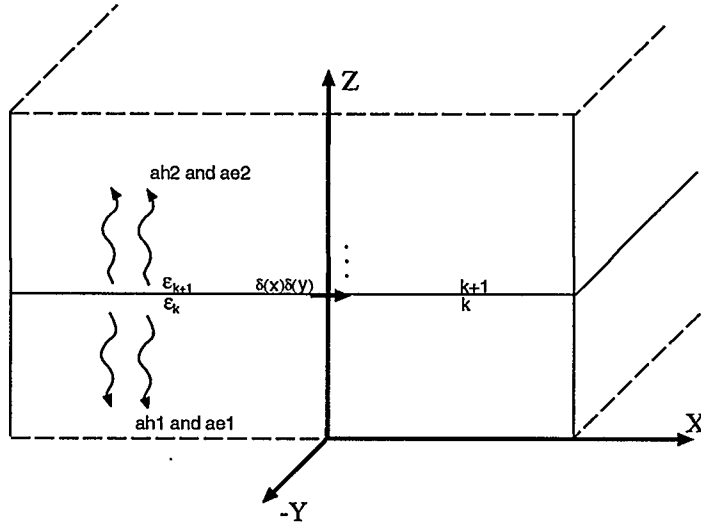


Figure 2.3: Determination of the inputs to the generalized signal flow graph.

The four inputs ah_1 , ah_2 , ae_1 , and ae_2 as determined for an x directed Hertz dipole are:

$$ah_1 = \frac{-j}{4\pi^2} \frac{\lambda_y}{q_k + q_{k+1}} \quad (TE) \quad (2.21)$$

$$ah_2 = \frac{-j}{4\pi^2} \frac{\lambda_y}{q_k + q_{k+1}} \quad (TE) \quad (2.22)$$

$$ae_1 = \frac{1}{4\pi^2\omega} \frac{\lambda_x q_{k+1}}{q_k \epsilon_{k+1} + q_{k+1} \epsilon_k} \quad (TM) \quad (2.23)$$

$$ae_2 = \frac{-1}{4\pi^2\omega} \frac{\lambda_x q_k}{q_k \epsilon_{k+1} + q_{k+1} \epsilon_k} \quad (TM) \quad (2.24)$$

where $\epsilon_i = \epsilon_0 \epsilon_{ri}$.

The expressions for the inputs by y and z Hertz directed dipoles are obtained with the same method as in the determination of the inputs by the x directed Hertz electric dipole. The inputs to the generalized signal flow graph Figure 2.2 for the y directed electric dipole are:

$$ah_1 = \frac{j}{4\pi^2} \frac{\lambda_x}{q_k + q_{k+1}} \quad (TE) \quad (2.25)$$

$$ah_2 = \frac{j}{4\pi^2} \frac{\lambda_x}{q_k + q_{k+1}} \quad (TE) \quad (2.26)$$

$$ae_1 = \frac{1}{4\pi^2\omega} \frac{\lambda_y q_{k+1}}{q_k \epsilon_{k+1} + q_{k+1} \epsilon_k} \quad (TM) \quad (2.27)$$

$$ae_2 = \frac{-1}{4\pi^2\omega} \frac{\lambda_y q_k}{q_k \epsilon_{k+1} + q_{k+1} \epsilon_k} \quad (TM). \quad (2.28)$$

The inputs for the z directed electric dipole are:

$$ah_1 = 0 \quad (TE) \quad (2.29)$$

$$ah_2 = 0 \quad (TE) \quad (2.30)$$

$$ae_1 = \frac{-j\lambda^2}{8\pi\omega q_k \epsilon_k} \quad (TM) \quad (2.31)$$

$$ae_2 = \frac{-j\lambda^2}{8\pi\omega q_k \epsilon_k} \quad (TM) \quad (2.32)$$

where $\lambda^2 = \lambda_x^2 + \lambda_y^2$.

It is noted that an interface has zero thickness and therefore a vertical electric Hertz dipole will have its two ends in different layers. This poses a problem here, as it is hard to determine the TM mode (there is no TE mode [62]) excited by such a vertical dipole at the interface. In all other other cases, where tangential dipoles are at the interface between two different dielectric layers, the inputs can be verified with a moving dipole method, where same results are obtained when the dipole is moved into the interface plane from either side of it. However, different TM mode inputs are obtained when a vertical dipole is moved, from different sides, into the plane of the interface between different dielectric layers.

The cause to this problem is not very clear yet. It is probably due to the fact the dipole is lying across the interface, and therefore probably excessive charge accumulates at the interface. Since no charge source is assumed in our analysis, there is an inconsistency in the field obtained.

To avoid this problem in dealing with vertical wire circuits, the source point is kept in a homogeneous dielectric material, i.e. at an interface between two same dielectric layers. When determining the field produced by a vertical Hertz dipole next to the interface, a zero thickness imaginary layer is inserted between the dipole and the layer with different dielectric constant. That is why $ae_1 = ae_2$ for the z directed Hertz dipole.

Now that all the branches and the inputs in the generalized signal flow graph in Figure 2.2 are given, the longitudinal field components at any location in the structure can be determined by solving this signal flow graph. Once the longitudinal field components are obtained, the tangential components can be determined as well according to the following expressions [64]:

$$\tilde{G}_{xi} = \frac{-j}{\lambda_x^2 + \lambda_y^2} [+\lambda_x q_i (\tilde{E}_{zi}^+ - \tilde{E}_{zi}^-) + j \omega \mu \lambda_y (\tilde{H}_{zi}^+ + \tilde{H}_{zi}^-)] \quad (2.33)$$

$$\tilde{G}_{yi} = \frac{+j}{\lambda_x^2 + \lambda_y^2} [-\lambda_y q_i (\tilde{E}_{zi}^+ - \tilde{E}_{zi}^-) + j \omega \mu \lambda_x (\tilde{H}_{zi}^+ + \tilde{H}_{zi}^-)] \quad (2.34)$$

$$\tilde{H}_{xi} = \frac{+j}{\lambda_x^2 + \lambda_y^2} [-\lambda_x q_i (\tilde{H}_{zi}^+ - \tilde{H}_{zi}^-) + j \omega \epsilon_i \lambda_y (\tilde{E}_{zi}^+ + \tilde{E}_{zi}^-)] \quad (2.35)$$

$$\tilde{H}_{yi} = \frac{-j}{\lambda_x^2 + \lambda_y^2} [+\lambda_y q_i (\tilde{H}_{zi}^+ - \tilde{H}_{zi}^-) + j \omega \epsilon_i \lambda_x (\tilde{E}_{zi}^+ + \tilde{E}_{zi}^-)] \quad (2.36)$$

Since the field components (both the longitudinal and the tangential) we obtained here are excited by a Hertz dipole in the structure, they are by definition the Green's functions. For a Hertz dipole in each of the three directions (x , y , and z), one can obtain three electric (magnetic) field components, which in effect are three electric (magnetic) Green's functions. All nine different such electric (magnetic) Green's functions can be obtained. Thus a complete dyadic electric (magnetic) Green's function due to an electric Hertz dipole can be obtained.

2.3 Generalization of the Dyadic Green's Functions

2.3.1 Signal Flow Graphs for TE and TM waves

Signal flow graph Figure 2.2 is used to represent the generalized multilayered structure. This representation can be used for all the structures that have homogeneous dielectric layers infinite in the x and y directions, a category into which almost all microstrip layered structures such as single-layer or multilayer, lossy or lossless, open or grounded terminations fall. For any structure, the known quantities include the number of layers, their thickness and dielectric constants, the locations and the orientations of the source and the field, and the termination of the structure. It is noted that shape and size of the strip being investigated, however, is not part of the Green's functions. We are only looking at the field due to an elementary current (Hertz dipole) in the place of current carrying conductor surface. The signal flow graph in Figure 2.2 is used to get such Green's functions. For any specific circuit, the locations of the strips and wires are used to determine the locations of source and field points. As soon as the Green's function is obtained, it will be used in the analysis of any circuits that have the same structure and the same source and field locations, using the spectral domain integral electric field equation (IEFE) technique and the moment method.

There are several ways of solving the signal flow graph in Figure 2.2. One of them is to use the linear equation method, where the values at all nodes are obtained

simultaneously. This method involves the manipulation of the coefficient matrix, and therefore it takes significant amount of CPU time. Since one only needs the values at a pair of specific nodes that corresponds to the observation point (field point), transmission matrix method can be used where layers are viewed as transmission lines and interfaces are viewed as two-port networks. This method, although faster than the linear equation method, is still considered slow because S-parameter matrices have to be converted to transmission matrices, and matrix multiplication will have to be performed.

The recursive technique is a easy and time efficient method, because the time taken for the solution of the signal flow graph increases only linearly with the number of layers. In addition, the recursive method can be performed either numerically or analytically. This method takes advantage of the topology of the generalized signal flow graph, which behaves like a number of two-port networks cascaded together.

For microstrip analysis purposes, it is almost always true that one should determine the tangential electric fields E_x and E_y in the plane where the Hertz dipole resides. Sometimes, however, there are some other locations where the fields need to be determined. If one wants to analyze a multimicrostrip structure, in order to apply the boundary conditions, one has to, for each of the strips, determine the electric tangential field due to the currents on all the other strips (mutual reaction), as well as the electric tangential field due to the current on this strip itself (self reaction).

For instance, Figure 2.4 shows a microstrip crossover which is usually used in

monolithic microwave integrated circuits, VLSI, and microstrip antenna feed circuits [65]. To analyze it, one has to determine the tangential electric fields on strip B due to current on both strip A and B, and vice versa. Thus a pair of integral equations result, which can be solved by numerical methods such as the moment method.

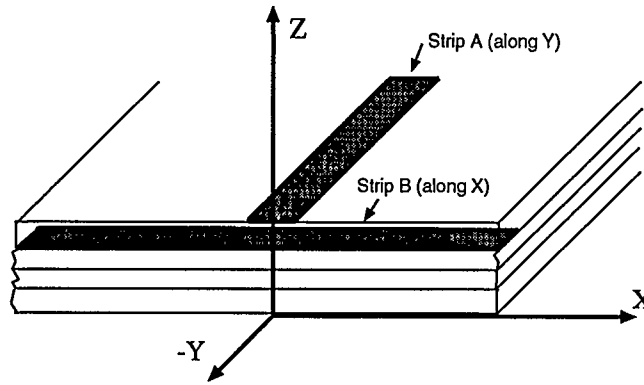


Figure 2.4: A microstrip crossover in a multilayer structure.

Generally speaking, one can determine the Green's function for a structure with the following quantities given:

1. the number of layers n ;
2. the thickness D and the dielectric parameters ϵ_r , μ_r , and σ (or loss tangent) of each layer;
3. the two terminations on top and at the bottom of the structure;

4. the location k and the orientation of the current dipole; and
5. the location m and the orientation of the observation point.

The locations where field intensities are of interest can be represented by a pair of nodes (a port) shown in Figure 2.2, and the field can be determined recursively by layer removal, or transmission matrices methods, as will be shown (Here it is assumed $m \geq k$, which does not result in a loss of generality).

2.3.2 Layer Removal— Total and Partial

From the generalized signal flow graph representation Figure 2.2 it is noted that each layer is represented by a section of the graph, as shown in Figure 2.5. The whole structure is built up with such two-port blocks, with some modifications for the boundary layers.

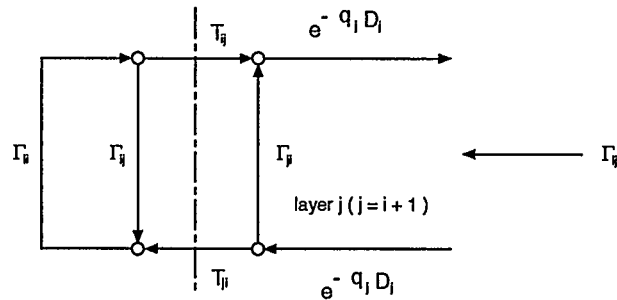


Figure 2.5: A layer represented by a signal flow graph block.

The source point is where the inputs are located, i.e. the interface between layer k and layer $(k + 1)$. The observation (field) points can be any where in the signal flow graph, which are where the nodal values have to be determined. Since not all the nodes in Figure 2.2 are of interest in the analysis, one can just represent the portion of the signal flow graph beyond the observation point with an effective reflection, which can be obtained by a method which we named total layer removal. This removal procedure starts from the outermost (boundary) layer, which in fact is the simplification of the signal flow graph [66].

In transmission line theory, the input reflection coefficient can be obtained by starting from the load, calculating and including each component's effect on the line as the driving point moves to the input end. By analogy with transmission line theory and signal flow graph theory, the effective reflection coefficient at the observation point can be obtained by the following method:

1. starting from the termination at the outermost layer (layer 1), calculate the reflection coefficient Γ_{l1} , which is the input reflection coefficient if one looks into layer 1 from the right side of it;
2. apply this Γ_{l1} to the interface between layers 1 and 2, as load reflection coefficient, and remove layer 1 conceptually (total removal, because layer 1 is no longer needed in the following derivation);
3. the reflection coefficient looking into layer 2 from its right side can be obtained

- by solving signal flow graph shown in Figure 2.5, where $i = 1$ and $j = 2$.
4. repeat step 2 and step 3—each time solve the signal flow graph shown in Figure 2.5, and remove the layer that is no longer needed—until the excitations (interface between layers k and $(k + 1)$) are reached, where the effective reflection coefficient Γ_{lk} is obtained. This Γ_{lk} represents the effect of all the layers removed beyond the observation point.
 5. the same layer removal procedure is applied on the other side of the excitations in Figure 2.2, where the observation point is located at interface between layers m and $(m + 1)$ ($m \geq k$). Due to the existence of the observation point one can only do total layer removal until the pair of nodes that correspond to observation point is reached.

In this recursive layer removal procedure, each layer is treated only once. The time needed to process the signal flow graph is proportional to the number of layers in the structure.

After the total layer removal procedure is carried out, the signal flow graph is reduced in size, and consequently the evaluation time is reduced. Figure 2.6 shows the signal flow graph after the total layer removal. Nodes b^+ and b^- should not be removed because that is where H_z and E_z are to be determined (observation point). However, in this case one can still partially remove each layer recursively from the observation point until one reaches the source interface. The partial layer removal is

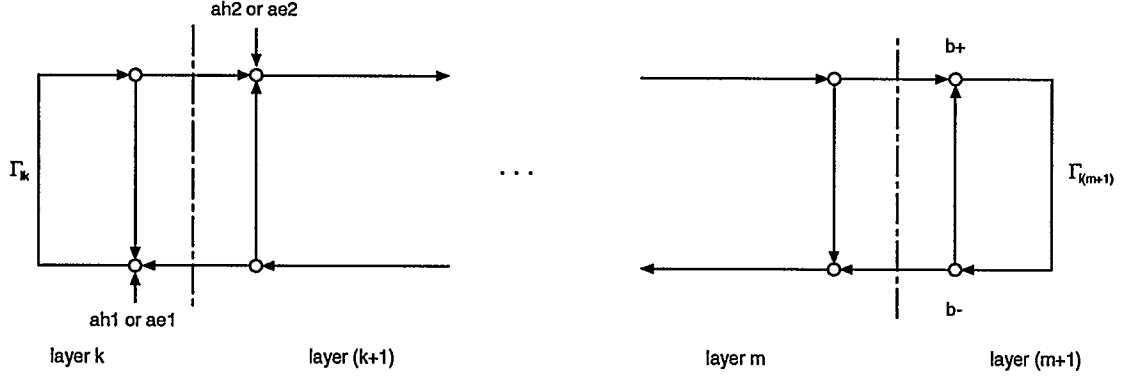


Figure 2.6: Signal flow graph after total layer removal.

in fact a signal flow graph simplification procedure and is illustrated in Figure 2.7.

As one can see, after some simple manipulations of the signal flow graph, each layer can be converted into a transfer branch and a reflection branch. The transfer branches from all the layers can be accumulated (multiplied) to get the total transfer function from the excitation point to the observation point. The reflection branch of the outer section is treated as a load reflection Γ_l for the inner section, which is used similarly to the total layer removal procedure. The layers are not totally removed, since the observation point nodes are still there. The process only simplifies the graph in a recursive procedure, and thus we named it partial layer removal.

The layer removal idea is also used in the calculation of the characteristic impedance in the infinite transmission line analysis, where a generalized Poynting vector function is formulated in the spectral domain. This generalization of multilayer

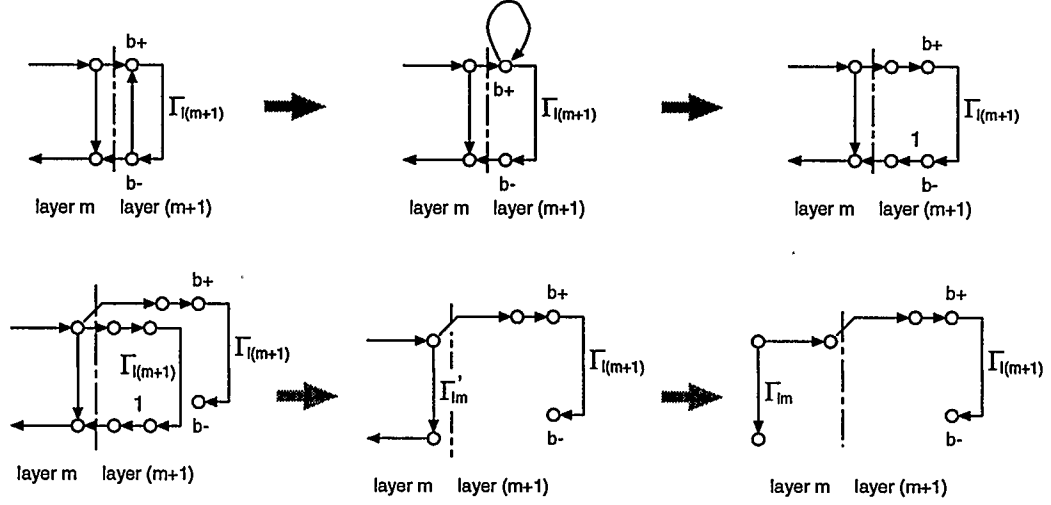


Figure 2.7: Illustration of partial layer removal.

Poynting function enables the calculation of transmitted power along the line, and thus the characteristic impedance can be computed.

2.3.3 Transmission Matrices Method

This method is very simple and straight forward. As shown in Figure 2.2, the whole structure is represented by a chain of two-port networks cascaded together with transmission lines. It is noted that the signal flow paths (branches) in this signal flow graph are the similar to the scattering parameters in microwave network theory. A scattering parameter matrix can be easily converted into an ABCD matrix, or a transmission matrix. Therefore shown in Figure 2.8 all the layers and interfaces are represented with transmission matrices. It is noted that in such a combined network

where transmission lines are between the scattering networks, the transmission lines also have to be treated as networks and expressed with transmission matrices.

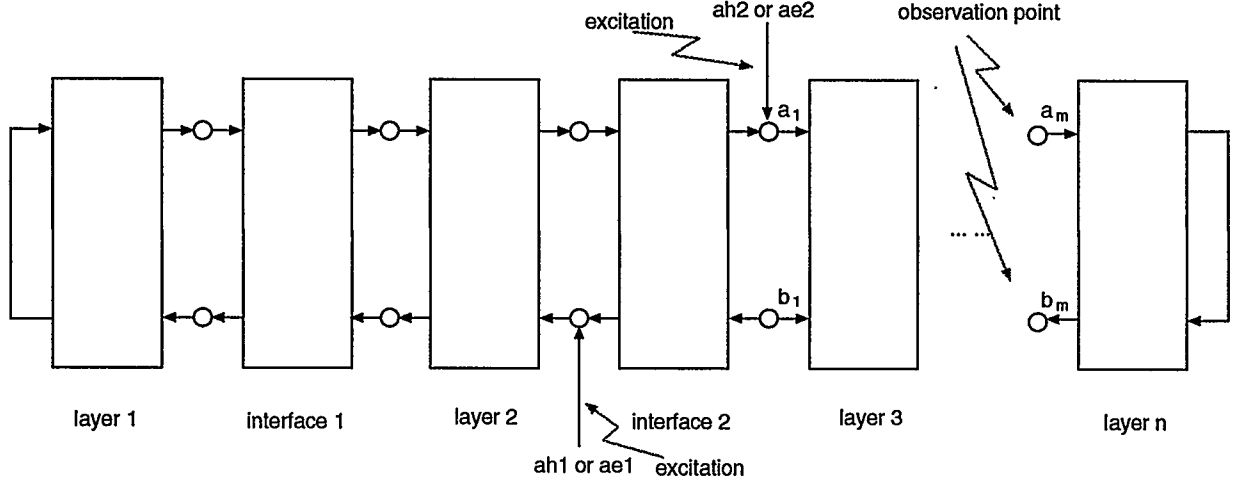


Figure 2.8: Transmission matrices for layers and interfaces.

To solve this network problem, one has to

1. first multiply the transmission matrices together on each side of the excitation interface to determine the effective reflection coefficients on each side of the excitation interface (in this example, interface 2). This simplifies the signal flow graph and consequently the signal fed into and reflected from the observation point side, a_1 and b_1 , can be determined;
2. if there are m transmission matrices between the excitation interface and the observation point (in this example, the observation point is located at the interface between layers $(n-1)$ and n), then the forward and backward longitudinal

fields a_m and b_m are

$$\begin{bmatrix} a_m \\ b_m \end{bmatrix} = [T_m] \cdots [T_3] [T_2] [T_1] \begin{bmatrix} a_1 \\ b_1 \end{bmatrix}.$$

Thus the signal flow graph is solved, and the Green's function can be obtained. This method, however, takes relatively more computer time than layer removal method, because matrix conversions and multiplications are involved. Also, unlike the layer removal method, where layers are just treated as simple transmission lines, layers here are treated as networks, and have to be manipulated like interfaces. From this comparison, it is believed that the layer removal method is a better candidate for the determination of the longitudinal field components. Therefore, the layer removal method is used in the following analysis, and is implemented in the computer program.

2.4 Example: Single Substrate layer

As an example for the determination of the Green's function, we now use the generalized spectral domain Green's function to determine G_{xx} and G_{xy} for a single substrate layer, conductor-backed structure, with the x directed electric Hertz dipole at the substrate-air interface. Figure 2.9 shows the signal flow graph of this structure. It has to be pointed out that, as far as our definition is concerned, this structure has two layers, a dielectric layer and an air layer, although almost all other literature refers to it as a one layer structure. The reflection coefficients at a perfect conducting

surface are 1 for the TM wave, and -1 for the TE wave. The thickness of the air layer is assumed to be D for the moment. Later it will be shown that D does not contribute to the final expression, due to the fact that there is no reflection from the air-side termination. From Figure 2.9, it is easy to determine the longitudinal

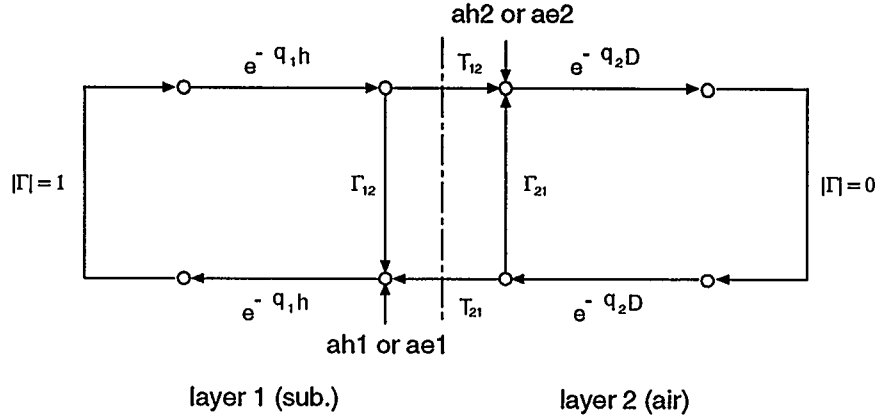


Figure 2.9: Signal flow graph of a grounded substrate-air (two-layer) structure.

components \tilde{H}_{z1}^+ , \tilde{H}_{z1}^- , \tilde{E}_{z1}^+ , and \tilde{E}_{z1}^- as follows:

$$\tilde{H}_{z1}^- = \frac{ah_1}{1 + \Gamma_{12}^{TE} e^{-2q_1 h}}, \quad (2.37)$$

$$\tilde{H}_{z1}^+ = \frac{-ah_1 e^{-2q_1 h}}{1 + \Gamma_{12}^{TE} e^{-2q_1 h}}, \quad (2.38)$$

$$\tilde{E}_{z1}^- = \frac{ae_1}{1 - \Gamma_{12}^{TM} e^{-2q_1 h}}, \quad (2.39)$$

and

$$\tilde{E}_{z1}^+ = \frac{ae_1 e^{-2q_1 h}}{1 - \Gamma_{12}^{TM} e^{-2q_1 h}}, \quad (2.40)$$

where Γ_{12}^{TM} and Γ_{12}^{TE} are given in Equation 2.20 and Equation 2.18, respectively, and ah_1 and ae_1 are given in Equation 2.21 and Equation 2.23, respectively.

Substituting the expressions given above into Equation 2.33 and Equation 2.34, one can obtain the following expressions of the Green's function at the substrate-air interface due to an x directed Hertz electric dipole at the same interface:

$$\tilde{G}_{xx} = \frac{-jZ_0}{4\pi^2 k_0 \lambda^2} \left[\frac{k_0^2 \lambda_y^2}{D_e(\lambda)} - \frac{q_1 q_2 \lambda_x^2}{D_m(\lambda)} \right] \sinh(q_1 h) \quad (2.41)$$

$$\tilde{G}_{yx} = \frac{jZ_0 \lambda_x \lambda_y}{4\pi^2 k_0 \lambda^2} \left[\frac{k_0^2}{D_e(\lambda)} + \frac{q_1 q_2}{D_m(\lambda)} \right] \sinh(q_1 h) \quad (2.42)$$

where

$$D_e(\lambda) = q_1 \cosh(q_1 h) + q_2 \sinh(q_1 h)$$

$$D_m(\lambda) = q_1 \sinh(q_1 h) + q_2 \epsilon_r \cosh(q_1 h)$$

$$q_i = \sqrt{\lambda^2 - k_i^2}$$

$$\lambda^2 = \lambda_x^2 + \lambda_y^2$$

and

$$Z_0 = \sqrt{\frac{\mu_0}{\epsilon_0}}$$

As expected, the air thickness D is not in the final expressions of the Green's function. These formulae are proved to be the same as those obtained by other researchers[11]. $D_e(\lambda)$ and $D_m(\lambda)$ are the characteristic equations for TM and TE surface modes in the structure. Their zeros are the poles in the Green's function expressions. The poles from $D_e(\lambda)$ give rise to the TM modes and the poles from $D_m(\lambda)$ give rise to the TE modes. The treatment of these poles are discussed later.

2.5 Asymptotic Expressions

The integral equation method makes use of the Green's function to describe the field generated by a current source. The derivation of the exact expressions of the spectral domain dyadic Green's functions is given above. The spatial domain Green's function can be obtained by taking the inverse Fourier transform of its spectral domain counterpart. The resultant Green's function in the spatial domain is also a generalized one in describing the multilayer, multistrip structure. It can be tabulated or, for the single layer case, written as asymptotic expression in the spatial domain [29]. The spatial domain Green's function is more flexible and suitable for the analysis of odd conductor shapes.

In the spectral domain, it's very important to have the asymptotic expressions for the Green's function, because improper integration is involved. The exact Green's function derived in this chapter is mainly used in the integration over the region near the origin (λ_x and λ_y are small). The evaluation itself, although theoretically and mathematically exact, takes a lot of computer time. In fact, more than 95% of the computation time is used for the numerical integration. To alleviate this problem, the number of computations requiring the exact Green's function should be kept to a minimum. One way of doing it is to use the exact value of Green's function only around the origin, where some poles are in the integration path and hence the behavior of the integrand is hard to predict. For regions where the function arguments are large, approximate expressions can be used. As the arguments (λ_x

and λ_y) become large, the Green's function will follow an asymptotic behavior, with the magnitude decreasing as the arguments increase. This is true for most of the elements in the dyadic Green's function. Some elementary Green's functions in the dyad increase with the arguments. In this case, an imaginary layer is defined between the source and the field points, whose thickness approaches to zero (see Chapter 7). The asymptotic expressions are usually in simple analytic forms, and therefore are easier and less time consuming to manipulate and compute. This suggests that one should use the asymptotic expressions in the numerical integration when the arguments are large, to get faster evaluations or even closed form integrations for the tail contributions.

It is easy to derive the asymptotic expressions for single layer or double layer structures, as can be found in the literature [11][13]. In multilayer cases, however, the asymptotic expressions are not readily available, due to the general nature of the structures. However, this does not mean that there is no asymptotic expressions for multilayer Green's functions. It is shown that there are asymptotic expressions for multilayer Green's functions. The price to pay is that it takes a larger argument (λ) value to get the same accuracy as in single layer cases.

As seen in the signal flow graph representation in Figure 2.2, each layer acts as a segment of a transmission line in the spectral domain. But they are not exactly transmission lines. The difference here is: as the TE or the TM waves travel across the layer, the magnitude of the waves decreases exponentially in the spectral domain.

The branches that correspond to the wave transmission in the layers in Figure 2.2 are all exponential functions of q . In layer i , for instance, this signal flow branch is $e^{-q_i D_i}$, where D_i is the layer thickness and $q_i = \sqrt{\lambda_x^2 + \lambda_y^2 - k_i^2}$. When λ_x or λ_y are large, the branch becomes exponentially small. This means that the signal strength that reaches the next interface decreases exponentially with λ_x and λ_y . The amount that is reflected back is even smaller (double path). Also it is noted that, unless terminated with perfect conductor plane, the next interface does not give full reflections. As λ_x or λ_y gets larger and larger, the Hertz dipole receives less and less reflected wave, and it is more and more as if the Hertz dipole is placed between two infinitely thick layers. A big advantage of this feature is that it enables one to derive asymptotic expressions for the multilayer Green's function. Basically, the method here is to treat a multilayer structure as one with two infinitely thick layers as the argument becomes very large, because when λ becomes large, the reflected wave from the next interface becomes exponentially small, and thus can be neglected.

Therefore, the asymptotic expressions are based on the conditions

$$q_i = \sqrt{\lambda^2 - k_i^2} \approx \lambda$$

and

$$e^{-2q_k D_k}, e^{-2q_{k+1} D_{k+1}} \approx 0$$

where the D 's are the thickness of the two adjacent layers at the Hertz dipole.

Under these conditions, the following asymptotic expressions can be drawn:

For the x directed electric dipole

$$G_{xx} \approx \frac{j}{4\pi^2\omega(\epsilon_k + \epsilon_{k+1})} \left(\frac{2\lambda_x^2}{\lambda} - \frac{(k_k^2 - k_{k+1}^2)\lambda_y^2}{\lambda^3} \right) \quad (2.43)$$

and

$$G_{yx} \approx \frac{j\lambda_x\lambda_y}{4\pi^2\omega(\epsilon_k + \epsilon_{k+1})} \left(\frac{2}{\lambda} + \frac{(k_k^2 - k_{k+1}^2)}{\lambda^3} \right) \quad (2.44)$$

and for the y directed electric dipole

$$G_{xy} \approx \frac{j\lambda_x\lambda_y}{4\pi^2\omega(\epsilon_k + \epsilon_{k+1})} \left(\frac{2}{\lambda} + \frac{(k_k^2 - k_{k+1}^2)}{\lambda^3} \right) \quad (2.45)$$

and

$$G_{yy} \approx \frac{j}{4\pi^2\omega(\epsilon_k + \epsilon_{k+1})} \left(\frac{2\lambda_y^2}{\lambda} - \frac{(k_k^2 - k_{k+1}^2)\lambda_x^2}{\lambda^3} \right) \quad (2.46)$$

Note that they are actually exact Green's functions for a structure with two infinitely thick dielectric layers. As stated above, the asymptotic expressions are derived based on the condition that the dipole is radiating into two infinite dielectric hemispheres, in the spectral domain. Other dyadic elements' asymptotic expressions can be derived analogously.

It should be noted that these asymptotic expressions are for the Green's functions only. The integrands in the calculation of the matrix elements in the moment method usually are the product of the Green's function, the base function, and the testing function, all in the spectral domain. To get a closed form analytical integration of the tail contribution, one also has to determine the asymptotic expressions for the base and the testing functions. Also noted is that the above asymptotic expressions are for

the cases where the source and the field are in the same plane in the structure. If they are not in the same plane, as in the analysis of multistrip circuits, the asymptotic expression can be simply assumed to be zero, because it decreases exponentially with λ .

2.6 Dyadic Green's Functions for a Magnetic Dipole

In the previous sections in this chapter, electric and magnetic Green's functions for electric Hertz dipole have been derived. The electric and magnetic fields (Green's functions) generated by the Hertz dipole can be obtained by solving the signal flow graph shown in Figure 2.2, which can determine the longitudinal electric and magnetic fields. These are the following elements of the spectral domain dyadic Green's functions

$$\tilde{G}_{zx}, \tilde{G}_{zy}, \tilde{G}_{zz}, \tilde{H}_{zx}, \tilde{H}_{zy}, \text{ and } \tilde{H}_{zz},$$

where $\tilde{G}_{z\nu}$ are z directed electric Green's functions due to ν directed Hertz dipole, and $\tilde{H}_{z\nu}$ are z directed magnetic Green's functions due to ν directed Hertz dipole.

The tangential (to the horizontal plane) components can be derived from the longitudinal components, using Equation 2.33 through Equation 2.36. Therefore, a complete set of electric and a complete set of magnetic dyadic Green's functions of electric Hertz dipole can be determined.

There are also dyadic Green's functions for the magnetic Hertz dipole. To general-

ize the Green's functions in our program, a magnetic dipole dyadic Green's functions for multilayered structures are also derived.

2.6.1 Derivation

In the analysis of slot transmission lines and aperture microstrip antennas, where there are openings in infinitely large sheet conductors, magnetic current is usually involved. In this case, although the conductor with opening(s) is infinitely large, it can not be treated as a ground plane, because planar grounds do not have any openings. The Green's functions for a structure that has a ground plane with openings are very difficult to derive, because the assumption that the structure is horizontally homogeneous and infinite is no longer valid.

It is also impossible to use the moment method to determine the electric current on the infinite conductor surface with openings.

To alleviate these difficulties, the electric field on the slot that is tangential to the plane, instead of the electric current on the conductor sheet, is used as the source. This is because the tangential electric field is nonzero only on the slot, a small, finite area. The tangential electric field can be treated as a magnetic current, by the equivalence principle [59]

$$\mathbf{M}_s = \hat{n} \times \mathbf{E}_s,$$

A physical magnetic current does not exist. As one can see, we are only using the

tangential electric field as a magnetic current, because in the Maxwell's equations, the tangential electric field on the surface that encloses the region of interest behaves like the magnetic current source on it. Although a mathematical assumption, the magnetic current can greatly simplify the derivation and the analysis, because the principle of duality (to electric current) can be applied now. An elementary tangential electric field is viewed by this equivalence principle as an elementary magnetic current source (magnetic Hertz dipole). The electromagnetic field generated by this elementary source is the Green's function for a magnetic Hertz dipole.

If the tangential electric fields on the slot are already known, which means the distribution of the magnetic current is known, then the radiated field on each side of the sheet due to this known source can be computed separately on both sides, using the equivalence principle (to get the magnetic current) and the Green's function for a magnetic dipole. This Green's function is convolved with this known magnetic current distribution to get the total field.

If the tangential electric field (or equivalently, the magnetic current) on the slot is unknown, such as in the cases of a slot line or aperture antenna analysis, the moment method should be used to determine the field distribution. First the distribution of the magnetic current is expanded according to the basis functions over the slot; then the assumed magnetic current is convolved with the Green's function for the magnetic dipole to get the total tangential magnetic field on each side of the slot; thirdly an equation between the tangential magnetic field on both side of the slot is

formed; finally the inner products are taken between the equation and the testing functions defined on the slot and a system of linear equations result. The solutions to the equations are the magnetic current distribution. The boundary condition that is enforced over the slot is that the tangential magnetic field be continuous.

For any analyses of the slot lines, the aperture antennas, or like circuits, a magnetic Green's function has to be formulated. It can be derived as follows:

1. The original problem is the radiation from an infinitely large conductor sheet with an aperture. The electric current occurs everywhere on the sheet except in the aperture, while the magnetic current (tangential electric field) is nonzero only in the aperture.
2. To consider the radiation within an enclosed region, all the tangential fields on the surface that enclose the region are viewed as sources, and are sufficient to determine the field in the region (uniqueness theorem). The field outside the region can be assumed to be zero.
3. Now consider an imaginary, infinitely large, planar conductor sheet brought into close proximity with the apertured conductor from outside of the area of interest. This imaginary sheet will short out all of the electric current on the apertured sheet (or it may be explained as the image of the electric current canceling out the real current). The magnetic current in the aperture, however, remains intact. The introduction of the infinitely large conductor

sheet is allowed because nothing enters the region of interest and the other side of the aperture has been assumed to have zero field. The change that this step introduces is that, now the problem is the radiation by the magnetic current in the presence of the infinitely large conductor sheet, while the old problem was the radiation by both electric and magnetic currents without the planar conductor.

4. The remaining source in the region of interest is the magnetic current residing infinitely close to an infinitely large planar conductor. Since the conductor has no apertures on it, it can be viewed as a ground plane.
5. Now consider the radiation by an elementary magnetic current in the slot, the Green's function for a magnetic Hertz dipole. Note the structure that the magnetic Hertz dipole "sees" is not exactly the same as the physical one. The original structure has been divided into two halves. The number of layers for the Green's function on the different sides may be different, and the inputs are always next to the ground. This is not the same as for the electric Green's function.
6. Determination of the inputs to the altered structure are obtained by using the theorem of duality. As an example, the inputs due to an x directed magnetic dipole are

$$be_1 = \frac{j}{4\pi^2} \frac{\lambda_y}{q_k + q_{k+1}} \quad (TM) \quad (2.47)$$

$$be_2 = \frac{j}{4\pi^2} \frac{\lambda_y}{q_k + q_{k+1}} \quad (TM) \quad (2.48)$$

$$bh_1 = \frac{1}{4\pi^2\omega} \frac{\lambda_x q_{k+1}}{q_k\mu_{k+1} + q_{k+1}\mu_k} \quad (TE) \quad (2.49)$$

$$bh_2 = \frac{-1}{4\pi^2\omega} \frac{\lambda_x q_k}{q_k\mu_{k+1} + q_{k+1}\mu_k} \quad (TE) \quad (2.50)$$

where $\mu_i = \mu_0\mu_{ri}$. In practice, one can let $q_k = q_{k+1}$ and the distance between the dipole and ground plane be zero, and use the general signal flow graph Figure 2.2 and other relevant equations to get the final magnetic Green's function expressions.

2.6.2 Boundary Conditions on the Slot and Aperture

The boundary conditions for the openings on an infinite conductor sheet are not the same as that for strip problems. As one can see, the continuity of the tangential field across any interfaces should be enforced. One does not have to be concerned about the tangential electric field, because it has been considered as the magnetic current at the slot. Its continuity is guaranteed as the same magnetic current is assumed on both sides of the slot. The tangential magnetic field, however, has to be considered. The boundary condition here is that the tangential magnetic field has to be continuous across the slot [11][67]. It should be noted that one does not have to consider the boundary conditions over the slot and aperture until working on specific circuits, and this subsection is not part of the derivation of the Green's functions for a magnetic Hertz dipole.

All the other properties of the magnetic Green's function are similar to the electric

one. No further derivation will be performed here, since in this dissertation, slot configurations are not given further consideration.

Chapter 3

Infinite Line Analysis

Infinite line analysis is important in that it determines the characteristic impedance and the propagation constant of the microstrip transmission line, which are the two most basic and important parameters of a transmission line. Further microstrip circuit analyses will use these determined parameters.

In this chapter, the current distribution on the microstrip is determined by applying the full-wave analysis with the moment method (Galerkin's procedure). The number of dielectric layers is arbitrary, the structure being described by the generalized multilayer Green's function as derived in Chapter 2. For sub/super dielectric layer structures, frequency compensation is possible by properly choosing the thickness and the dielectric constants of the layers. This is useful if transmission lines with low dispersion are required.

The current is assumed to be varying along the transmission line with $e^{-jk_e x}$ dependence, with k_e , the effective propagation constant, to be determined. It is also assumed that the current has longitudinal (along the strip) components only, because any transverse contributions have been proved to be very small ($< -20 \sim -40dB$) and can be neglected, if the width of the strip is not very wide[4][45]. Also,

the transverse directed current, if any, will be odd function over the width of the strip [68]. This odd function will not have significant contribution to the field until the strip width is significant in terms of the wavelength.

Several combinations of current expansion are tested, and good agreement with measurement is observed. Some useful conclusions are drawn.

The characteristic impedance of the transmission lines is also studied. Based on the ideas in the generalization of the Green's functions, a generalized transmitted power computation algorithm is developed. Using this algorithm, one can determine the characteristic impedance of a strip line in a multilayer structure.

3.1 Formulation

This formulation derives the algorithm for the calculation of the effective propagation constant k_e , and the characteristic impedance Z_0 .

Full-wave analyses of infinite microstrip transmission lines on single or double layer dielectric have been carried out by some researchers (see [4][5][69], for instance). Most of them have obtained very good results for the propagation constants. Hashimoto derived a closed form expression for Z_0 for single layer microstrip lines [70]. In this chapter the generalized multilayer Green's function is used to compute the effective dielectric constant for microstrip transmission lines. Another important function—the generalized multilayer Poynting vector function—is derived

and implemented into a C++ program. This makes possible the analysis of virtually any kind of infinite microstrip transmission lines, which is especially meaningful for analyzing monolithic microwave integrated circuits (MMIC) and microstrip antennas, where the structures are often multilayer and multistrip with lossy dielectric media.

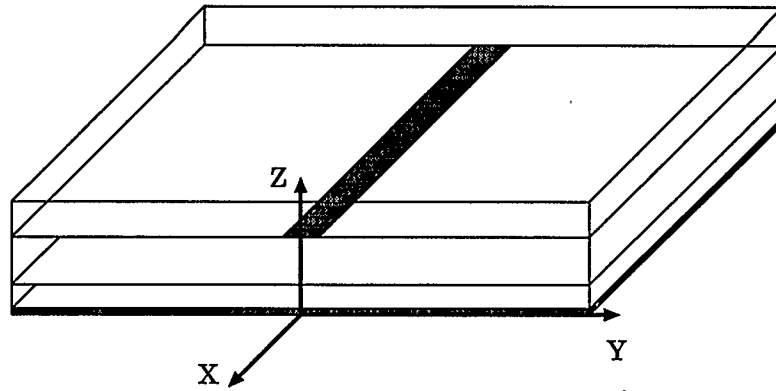


Figure 3.1: A microstrip transmission line in a multilayer structure.

The physical structure and the coordinate system used in this chapter are shown in Figure 3.1. There are n layers in the structure. The infinite microstrip resides at an interface between two layers and stretches from $x = -\infty$ to $x = +\infty$. The input wave is incident from $x = -\infty$ and propagates to $x = +\infty$.

3.1.1 Electric Field

If the current vector on the strip is assumed to have a longitudinal component only, i.e. no y direction current exists, then the current can be expressed as

$$J_x(x', y') = \begin{cases} I_x(y')e^{-jk_e x'} & \text{on strip surface} \\ 0 & \text{otherwise} \end{cases} \quad (3.1)$$

where $I_x(y')$ is the transverse (to the microstrip line) distribution of the current, and k_e is the effective propagation constant of the wave along the strip to be determined in this chapter. $I_x(y')$ can be assumed to be the constant distribution across the width of the strip, or the Maxwellian distribution, or further expanded in term of the Maxwellian-cosine basis functions. All of these distributions are examined and compared in the following sections. The results are found to be in very close agreement with each other.

The electric field at (x, y) due to the current in Equation 3.1 is

$$E_x(x, y) = \iint G_{xx}(x, y|x', y')J_x(x', y')dx'dy' \quad (3.2)$$

Note that only E_x is given in Equation 3.2. This is because

1. E_z is not applicable in enforcing the boundary conditions on the strip; and
2. A mathematical pre-manipulation shows that E_y becomes irrelevant (zero contribution) as the moment method is applied, due to the symmetry of $I_x(y')$.

Equation 3.2 is the Pocklington integral equation [71] applied to the microstrip analysis [72].

3.1.2 The Characteristic Equation for k_e

The application of the boundary conditions on the surface of the strip, along with the use of the Green's function and the current distribution assumption, gives rise to the characteristic equation for the propagation constant k_e . Usually the strip is assumed to be a perfect conductor. Nonperfect conductor strips, however, can also be accounted for by employing surface impedance boundary conditions[73].

Assuming that the strip is a perfect conductor, then boundary conditions on the strip surface specify that all tangential electric fields should be zero. If we constrain x and y to the surface of the strip, then the boundary conditions give the expression

$$0 = \iint G_{xx}(x, y|x', y') J_x(x', y') dx' dy' \quad (3.3)$$

for

$$-\infty < x < +\infty, -\frac{W}{2} < y < +\frac{W}{2}.$$

G_{xx} does not have a closed form expression in the spatial domain. When transferred into the spectral domain, however, the Green's function can be expressed in a closed form (see Chapter 2). G_{xx} then can be expressed as

$$G_{xx}(x, y|x', y') = \iint \tilde{G}_{xx}(\lambda_x, \lambda_y) e^{j\lambda_x(x-x')} e^{j\lambda_y(y-y')} d\lambda_x d\lambda_y \quad (3.4)$$

Substituting Equation 3.4 into Equation 3.3, we get

$$0 = \iiint \tilde{G}_{xx}(\lambda_x, \lambda_y) e^{j\lambda_x(x-x')} e^{j\lambda_y(y-y')} d\lambda_x d\lambda_y J_x(x', y') dx' dy' \quad (3.5)$$

for

$$-\infty < x < +\infty, -\frac{W}{2} < y < +\frac{W}{2} .$$

Substituting Equation 3.1 into the above equation, We get

$$0 = \iiint \tilde{G}_{xx}(\lambda_x, \lambda_y) e^{j\lambda_x(x-x')} e^{j\lambda_y(y-y')} d\lambda_x d\lambda_y I_x(y') e^{-jk_e x'} dx' dy' \quad (3.6)$$

for

$$-\infty < x < +\infty, -\frac{W}{2} < y < +\frac{W}{2} .$$

Interchanging the integration order and performing the integrations with respect to the variables x' , y' , and λ_x , the following equation results

$$0 = \int \tilde{G}_{xx}(k_e, \lambda_y) \tilde{I}_x(\lambda_y) e^{-jk_e x} e^{-j\lambda_y y} d\lambda_y \quad (3.7)$$

for

$$-\infty < x < +\infty, -\frac{W}{2} < y < +\frac{W}{2}$$

where

$$\tilde{I}_x(\lambda_y) = \int I_x(y') e^{-j\lambda_y y'} dy' ,$$

which is the 1-D Fourier transform of I_x (with a factor of $1/(2\pi)$ different from the definition in Chapter 2).

Equation 3.7 states that the electric field on the strip surface is zero (boundary condition for the conductor surface). To solve this equation, however, an inner

product has to be taken and evaluated. This is because Equation 3.7 also depends on y . The inner product is between the tangential electric field and the current that generates the field (Galerkin's procedure):

$$\langle E_x, J_x^* \rangle = \int E_x J_x^* dy = \int \tilde{G}_{xx}(k_e, \lambda_y) \tilde{I}_x^2(\lambda_y) d\lambda_y = 0 \quad (3.8)$$

where J^* is the complex conjugate of J .

Since the electric tangential field and the electric current are complementarily zero (one is non-zero only where the other is zero), the inner product is still zero but the specifications for the valid areas in Equation 3.7 can be removed.

Equation 3.8 is the characteristic equation for the determination of the propagation constant k_e of infinitely long microstrip transmission lines. From this equation it is noted that the Green's function G_{xx} plays a very important role in describing the whole structure. The generalized Green's function includes all the possibilities of practical structures, and hence makes possible the analysis of microstrip lines in multilayer structures.

3.1.3 The Characteristic Impedance

Another important parameter for a transmission line is the characteristic impedance Z_0 , which, in case of TEM wave transmission line, is defined as the ratio of the traveling voltage wave to the traveling current wave. In microstrip configurations, however, a definition for a traveling voltage becomes problematic, since there is no

TEM traveling voltage wave.

Using a method similar to analyzing the propagation constant k_e , where a macroscopic effect of the waves is taken into account, the characteristic impedance can be defined by looking at the average power being transmitted. The definition thereby takes the form [74]

$$Z_0 = \frac{2P_{av}}{I_x^2} \quad (3.9)$$

where P_{av} is the average power traveling in $+x$ direction and I_x is the total current flowing on the strip. This definition for the characteristic impedance makes use of the quantities that can be determined relatively easily and accurately in the full-wave analysis. The current can be obtained from the effective propagation constant analysis using the moment method; the power transmitted along the line is obtained from the integration of the Poynting vector. In time-harmonic case this power is defined as

$$P_{av} = (1/2) \text{Re} \iint (E_y H_z^* - E_z H_y^*) dy dz \quad (3.10)$$

where the integrand is the average Poynting vector over a plane perpendicular to the direction of the propagation.

Direct evaluation of Equation 3.10 is almost impossible, because field intensity values are required all over the plane, thus the inverse transform will have to be performed everywhere. Fortunately Parseval's theorem [75] can be used [74] to simplify the procedure:

$$P_{av} = \pi \text{Re} \iint (\tilde{E}_y \tilde{H}_z^* - \tilde{E}_z \tilde{H}_y^*) dz d\lambda_y \quad (3.11)$$

The following field components are needed in the integrand:

$$\tilde{E}_y = 2\pi\tilde{G}_{yx}(-k_e, \lambda_y)\tilde{I}_x(\lambda_y)$$

$$\tilde{E}_z = 2\pi\tilde{G}_{zx}(-k_e, \lambda_y)\tilde{I}_x(\lambda_y)$$

$$\tilde{H}_z^* = 2\pi\tilde{H}_{zx}^*(-k_e, \lambda_y)\tilde{I}_x^*(\lambda_y)$$

$$\tilde{H}_y^* = 2\pi\tilde{H}_{yx}^*(-k_e, \lambda_y)\tilde{I}_x^*(\lambda_y)$$

Since the z dependence of the integrand is of the exponential type, the spatial integration with respect to z in Equation 3.11 can be accomplished in closed form. This greatly reduces the evaluation time.

A generalized version of this evaluation is developed. First the closed form expression for the spatial integration is derived similarly to the derivation of the generalized Green's function. Then the average power is obtained by numerically integrating the remaining part of the integrand in Equation 3.11, in the spectral domain.

The generalized spatial integration is briefly described as follows. By examining the integrand in Equation 3.11, it is not difficult to find that the integrand dependences on variable z are simply hyperbolic functions, which consist of exponential functions of z . Note that all field components can be derived from the longitudinal electric and magnetic fields, E_z and H_z , which are the superposition of their $+z$ and $-z$ traveling wave members. Therefore it is obvious that in each layer the integrand can be expressed as linear combinations of E_z^+ , E_z^- , H_z^+ , and H_z^- . All these four

components are exponentially varying with z . Their linear combinations and products are still z exponential. Thus the integrand can be integrated in closed form layer by layer. The determination of those z direction components are similar to the generalization of the Green's function.

It should be noted that, since z components vary exponentially with q_i and the latter increases with λ_y , care must be taken not to take any positive exponential in the integrand, otherwise numerical instability occurs. For instance, if the thickness of layer i is D_i and $E_z^-(z)$ is equal to A at $z = 0$ and B at $z = D_i > 0$, and since this wave travels in $-z$ direction it should be $e^{q_i z}$ dependent. One should use, in the analytical integrand expression, $E_z^-(z) = B e^{-q_i(D_i - z)}$, instead of $E_z^-(z) = A e^{q_i z}$, because the latter grows exponentially as λ_y becomes large when the numerical integration with respect to λ_y is performed. ($q_i = \sqrt{\lambda_x^2 + \lambda_y^2 - k_i^2}$).

3.1.4 Galerkin's Procedure and Moment Method

The moment method is a very powerful tool in solving integral-differential equations. The basic idea is to expand the unknown function in terms of a series of known functions, called basis functions, with the complex magnitude of each one to be determined. This results in the linear combination of the basis functions in the place of the unknown function in the original integral-differential equation; another series of known functions, called testing functions, are then used to take inner products one by one with the altered integral-differential equation, which results in a system

of linear equations for the unknown complex magnitudes. Thus the moment method converts the integral-differential equation into a system of linear equations. The solutions to the latter form an approximated solution to the original problem.

Galerkin's procedure is a special case of the moment method, in which the testing function series are chosen to be the same as the expansion functions. Since Galerkin's procedure uses only one set of expansion functions, and has good convergence behavior, it has become one of the most widely used procedures. This procedure has proved to be a good choice in the infinite line analysis and its modified version is used in the following chapters (in some of the following chapters the Galerkin's procedure has been modified to obtain better numerical convergence).

3.2 Numerical Techniques

3.2.1 Basis Functions

Before the moment method can be applied, the transverse expansion series for the electric current on the strip, $I_x(y')$, has to be determined. There are four sets of basis functions that are frequently used in the literature. All of them are examined and compared in the analysis. They are

1. Constant distribution (one term only):

$$I_x(y') = \begin{cases} \frac{1}{W} & \text{for } |y'| \leq \frac{W}{2} \\ 0 & \text{otherwise} \end{cases} \quad (3.12)$$

2. Maxwellian distribution (one term only):

$$I_x(y') = \begin{cases} \frac{2}{\pi W} \frac{1}{\sqrt{1-(\frac{2y'}{W})^2}} & \text{for } |y'| \leq \frac{W}{2} \\ 0 & \text{otherwise} \end{cases} \quad (3.13)$$

3. Maxwellian-cosine distribution (N terms, method 1):

$$I_x(y') = \begin{cases} \sum_{n=1}^N \frac{2}{\pi W} \frac{I_n}{\sqrt{1-(\frac{2y'}{W})^2}} \cos[\frac{(n-1)\pi y'}{W}] & \text{for } |y'| \leq \frac{W}{2} \\ 0 & \text{otherwise} \end{cases} \quad (3.14)$$

4. Maxwellian-cosine distribution (N terms, method 2):

$$I_x(y') = \begin{cases} \sum_{n=1}^N \frac{2}{\pi W} \frac{I_n}{\sqrt{1-(\frac{2y'}{W})^2}} \cos[\frac{(n-1)2\pi y'}{W}] & \text{for } |y'| \leq \frac{W}{2} \\ 0 & \text{otherwise} \end{cases} \quad (3.15)$$

The uniform transverse distribution is the simplest. It is not the faithful representation of the physical current distribution. But it is found in the analysis that it gives fast convergence and fairly good results, compared to the more complicated ones. The single term Maxwellian is better than the uniform one, because it has two poles at the edges of the strip which reflect the static nature of the transverse distribution.

The multiterm basis functions can reconstruct the current distribution in detail. It should be pointed out, about the two multiterm basis, that (1) the two multiterm

Maxwellian-cosine methods reduce to Maxwellian distribution when N is chosen to be one; and (2) method 2 is actually just a subset of method 1. H-Y Yang [76] used method 2 to determine the current distribution. However, as will be shown later, the contribution of the terms omitted from method 1 (the even numbered terms in method 1) should not be neglected, because each even numbered term's magnitude is usually nearly an order of magnitude higher than that of the following odd numbered term. Therefore, for a multiple term current expansion, method 1 is preferred.

3.2.2 Numerical Quadrature

In all the cases above, improper integrations are required to evaluate the inner product, which forms the elements of the matrix in the linear equations. It has the general form of

$$Z_{ij} = \int_0^\infty \tilde{G}_{xx}(k_e, \lambda_y) \tilde{I}_{xi}^*(\lambda_y) \tilde{I}_{xj}(\lambda_y) d\lambda_y \quad (3.16)$$

Most of the integration is done with numerical integration (numerical quadrature) techniques in the spectral domain. There are singularities corresponding to the TE and TM surface waves [77] along the real axis, if the medium is lossless [78][79]. If the medium is lossy, the singularities will be no longer on the real axis. Instead, they are located in the fourth quadrant of the complex λ plane [80].. For single or even double layered structures, it is possible to determine the locations of these singularities by numerically solving a pair of transcendental equations [81][82]. In that case one can use pole extraction techniques to get their contribution (residues)

from those poles [83], and have a real axis integration with Cauchy principal integral, or use steepest descent path method to finish the numerical integration [84]. For multilayered structures, where the transcendental equations for TE and TM waves are even more complicated, the locations of the singularities can be very difficult to determine, and therefore no reliable and efficient numerical methods can be used to accurately locate them. All we know about these singularities is that they lie between $[k_0, k_0\sqrt{\max(\epsilon_{ri})}]$ [47]. There are also infinite number of leaky wave poles [85], which need be taken care of. But as long as the integration path does not cross the branch cut, no leaky wave poles will be caught in the numerical integration [86][87][88]. It has been pointed out in [44] that for a conductor-backed single layer structure, the solution k_e to the characteristic Equation 3.8 is always greater than the highest possible TM or TE surface modes, and therefore there is no risk of encountering a pole along the integration path if the solution k_e is approached from $\lambda_x > k_e$. However, for multilayered general structures and in cases of discontinuities, there is the possibility that poles will be encountered [89]. To avoid encountering singularities, the integration path is deformed into the complex domain [57], as path 2 shown in Figure 3.2. The integration along path 2 is the same as along path 1, because there is no singularities in the area enclosed by path 1 and path 2, and by Cauchy's theorem [90], the loop integration should be zero.

A branch cut is introduced at $\pm k_0$ if the structure is open. If, on the other hand, the structure is closed by top and bottom ground planes, no branch cut is needed, because the EM waves are trapped in the structure [32].

When the path is off the real axis, the integrand increases exponentially; therefore care must be taken as how far the path should be deformed in the imaginary part. For single layered structures, H-Y Yang found [91] that the maximum of $\text{Im}(\lambda_x)$ and $\text{Im}(\lambda_y)$ should be $.02h$, where h is the layer thickness. For multilayer structures, it is even harder to determine the amount of deformation. It is determined with trial-and-error in this dissertation.

The integration from 0 to ∞ is accomplished in two parts: $[0, Q]$ and $[Q, \infty]$. The first interval gives the main contribution. The contribution from the second interval is less significant, and is called the “tail” contribution. For the first interval, the integration is performed numerically using the Romberg or Gaussian-Legendre quadrature techniques; for the second interval, where for a converged integration the contribution is not as big as that from $[0, Q]$, the asymptotic expressions are used to evaluate the tail contribution.

Q is adaptively determined by the computer program. The program is first given a subinterval length for numerical quadrature, over which a 96-point Gaussian-Legendre quadrature [92] is performed; then the program moves forward in $+\lambda_y$ direction by such a subinterval and performs the Gaussian-Legendre quadrature again; this step is repeated as the program integrates over one such a subinterval after another. The results from these subinterval integrals are summed up to get the total integral. When the contribution from a new subinterval integration is found to be less than a pre-set percentage of the total integral, the numerical process is trun-

cated, and the upper limit of the numerical quadrature Q is passed to the asymptotic expressions. The tail contribution is calculated as the integral of the asymptotic expression over $[Q, \infty)$.

3.2.3 Complex Root Searching

The solution to the characteristic equation for k_e is a complex value for k_e that makes the equation equal to zero. There is no input or excitation to the equation, i.e. the equation is homogeneous. The solution is found when the determinant of the coefficient matrix is zero or less than a given small value. This can be achieved by an iterative root searching process. If there is no loss in the dielectric layer or the strip, a simple Newton's method or interval-halving should suffice, because the solution is real for lossless transmission lines. For the general solution, however, a complex root searching algorithm should be employed to compute both the phase velocity and the attenuation for the transmission line. It is found that Muller's three-point method is an efficient root searching algorithm. It can be used for complex root, as well as real root searching, and it converges relatively quickly. Usually a convergence can be reached in less than five searches.

3.3 Results

3.3.1 Convergence Tests

The convergence of the infinite line analysis algorithm is tested on several microstrip transmission lines. As shown in this section, the convergence can be reached for just two basis functions, i.e. $N = 2$. Results from $N > 2$ are virtually identical (i.e. overlapping on the converged curve).

The basis functions for the current expansion are either uniform or method 1, as listed in Section 3.2.1, method 2 will be used later for comparison in the following sections.

Figure 3.3 through Figure 3.6 show the convergence of the propagation delay factors of four different transmission lines. The assumption of the uniform transverse current distribution is a reasonable one since the calculated square root of the effective dielectric constants (the propagation delay factors, $\sqrt{\epsilon_e}$) are very close to the converged values. The Maxwellian distribution, however, is a better assumption, because it has poles at the two edges of the strip which reflects the transversely static nature of the longitudinal electric current on the strip (a pole at the edge of the strip is called the edge condition). Actually, when $N = 1$, it is the exact solution if the strip is in a homogeneous medium space [4][93].

3.3.2 Calculated and Measured Propagation Constants

Figure 3.7 shows the comparison of the computed square root of the effective dielectric constant $\sqrt{\epsilon_e}$ for a single layer alumina microstrip transmission line with the measurements made by Fordham[69]. The agreement between the measurements and the computations is very good.

The algorithm is also applied to multilayer structures. As shown in Figure 3.8, a two layer microstrip transmission line is analyzed. The substrate is alumina and duroid. The relative permittivity of the bottom layer is 2.2, and the top one is 9.8. Again the agreement between the measured data in [69] and the computed data is very good.

I also made measurements of the propagation for some lines. Figure 3.9 and Figure 3.10 show the square root of the effective dielectric constants $\sqrt{\epsilon_e}$ of transmission lines printed on single layer substrates. The first measurement (Figure 3.9) was made on a HP network analyzer at TRLabs, and the second one (Figure 3.10) was at Novatel Communications, Inc.. There are some big discrepancies between the measurement and the analysis in Figure 3.9. This is due to the nonidentical construction of the circuits and the reference lines, and the noise in the measurements. The measurement techniques and the data analysis method are described in Chapter 9.

3.3.3 Calculated Characteristic Impedance

The characteristic impedances of these four microstrip transmission lines are also calculated. These results are shown in Figure 3.11 through Figure 3.14.

The results from the quasi-static analysis are also plotted for the single-layer microstrip transmission lines [94]. There is no quasi-static data available for multilayer transmission lines. The big advantage of the SDA method is that it be used to analyze multilayer structures. Measurement of Z_0 is a difficult issue. Getsinger suggested three measurement techniques for the determination of Z_0 [95]. They seemed to work reasonably well at relatively low frequencies. It is known that the characteristic impedance of microstrip has very strong frequency dependence, which makes the modeling of the coax-microstrip transition difficult at high frequencies. Since there is a lack of reliable methods and standards, no measurements of Z_0 and ϵ_e have been attempted at high frequencies.

3.3.4 A Note on the Choice of the Basis Functions

As listed in Section 3.2.1, four basis functions were proposed. The results from three of them (#1 ~ #3) have been used. Very close agreement has been achieved with observations for the propagation constant and the characteristic impedance calculations. Method 2 (#4) is a subset of the more complicated method 1. In other words, terms 1, 2, 3, 4 ... in method 2 are terms 1, 3, 5, 7 ... in method

1. The even numbered terms in method 1 are omitted in method 2. Method 2 has also been tried in the analysis. As expected, the results are in reasonable agreement with those obtained with other basis functions, because the first term, which is the most important one, is retained. Good agreement comes from the fact that the parameters computed are not very sensitive to the choice of the basis functions and the main terms (the first ones) of these two methods are the same. Since method 2 is a subset of method 1, one may wonder if the terms omitted by method 2 are really insignificant. The best way to compare the difference is to apply these two methods to the same circuit and investigate the results.

The comparison was made on one of the four circuits, with $\epsilon_r = 9.8$, $h = w = .025$ ". The current distribution coefficients from the application of these two methods are tabulated in Table 3.1 (for $N = 2$) and Table 3.2 (for $N = 3$). It should be noted that since there is no input to the system of the infinitely long transmission lines, a set of the solutions to the characteristic equations are still solutions if they are all multiplied by a common factor. Therefore the magnitudes of the first terms of these two methods are both given a 1.0 to normalize the results.

It is noted from these two tables that the terms omitted by method 2 are not insignificant. Take $f = 1.000\text{GHz}$ as an example. If $N = 2$ (two terms are used), the magnitude of the second term is .2423 for method 1, and .1032 for method 2. Remember the second term in method 2 is the third term in method 1, which is not included if $N = 2$ and the second term in method 1 is not included in method 2.

freq. (GHz)	method 1 I_2	method 2 I_2
1.000	.2423	.1032
3.000	.2420	.1034
5.000	.2453	.1047
7.000	.2522	.1071
9.000	.2615	.1105
11.00	.2746	.1156
13.00	.2907	.1211
15.00	.3078	.1271
17.00	.3263	.1335
19.00	.3459	.1403
21.00	.3680	.1472
23.00	.3901	.1543
25.00	.4131	.1616
27.00	.4367	.1689

Table 3.1: Comparison of the current coefficients by two basis functions ($N = 2$) ($W = .025''$, $h = .025''$, $\epsilon_r = 9.8$).

This means that method 2 has omitted a term which is .2423 in magnitude, and has included a less important (.1032 in magnitude) term. As a rule of thumb, the finite terms used in any numerical algorithm should be able to best represent the reality. If only two terms are used, these two terms should be the two most significant parts in the function represented.

The same phenomenon is observed in Table 3.2 where the magnitudes of the terms in method 1 are generally larger than those in method 2. This means that method 1 can more faithfully represent the current distribution on the strip surface. Theoretically this means that in order for the moment method to converge fast and

freq. (GHz)	method 1		method 2	
	I_2	I_3	I_2	I_3
1.000	.2939	-.0231	.0896	-.0294
3.000	.2922	-.0223	.0911	-.0261
5.000	.3009	-.0247	.0906	-.0298
7.000	.3081	-.0247	.0932	-.0297
9.000	.1855	.0338	.0960	-.0318
11.00	.3356	-.0262	.1000	-.0331
13.00	.3621	-.0309	.1047	-.0345
15.00	.4049	-.0415	.1104	-.0352
17.00	.4048	-.0331	.1152	-.0385
19.00	.4298	-.0349	.1222	-.0379
21.00	.4589	-.0377	.1270	-.0425
23.00	.4900	-.0410	.1332	-.0445
25.00	.5151	-.0414	.1396	-.0461
27.00	.4993	-.0251	.1465	-.0470

Table 3.2: Comparison of the current coefficients by two basis functions ($N = 3$) ($W = .025''$, $h = .025''$, $\epsilon_r = 9.8$).

effectively to the true solution, one has to use a basis functions set that is as complete and realistic as possible.

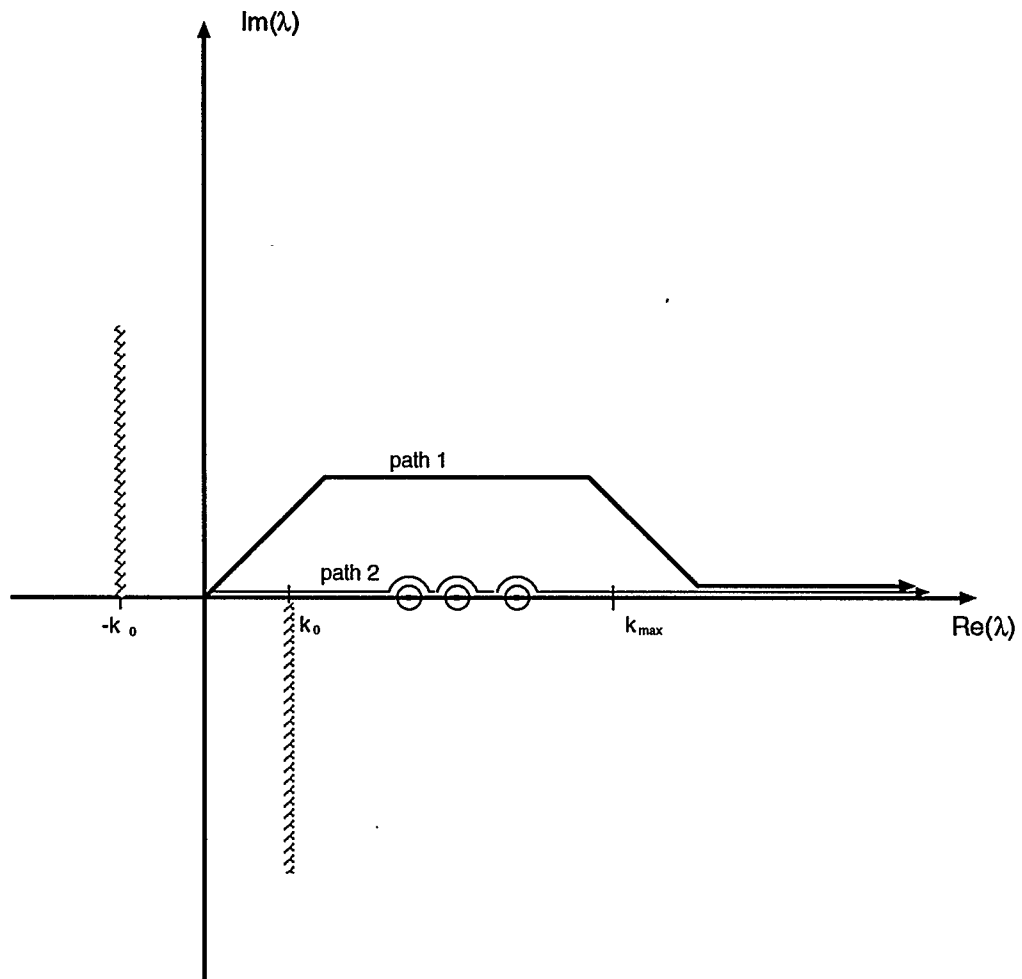


Figure 3.2: Deformation of the integration path into the complex domain.

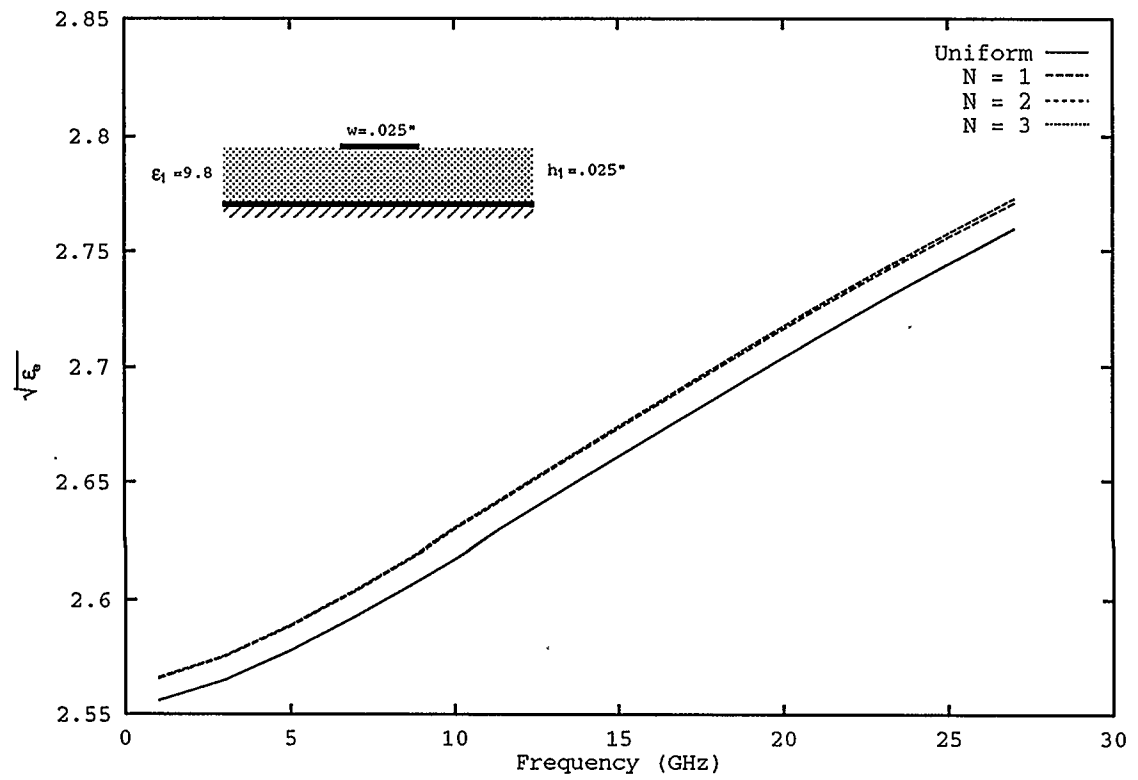


Figure 3.3: Convergence test for a single layer substrate transmission line ($W = .025''$, $h = .025''$, $\epsilon_r = 9.8$).

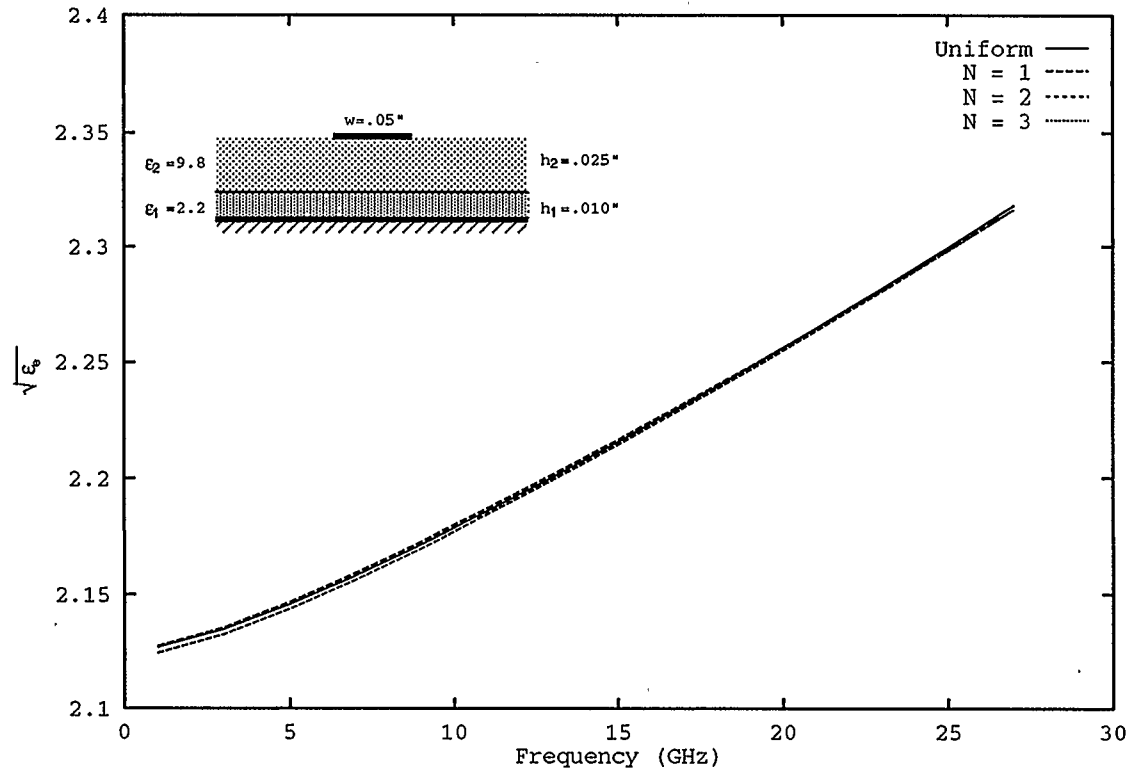


Figure 3.4: Convergence test for a double substrate transmission line ($W = .05''$, $h_1 = .01''$, $h_2 = .025''$, $\epsilon_{r1} = 2.2$, $\epsilon_{r2} = 9.8$).

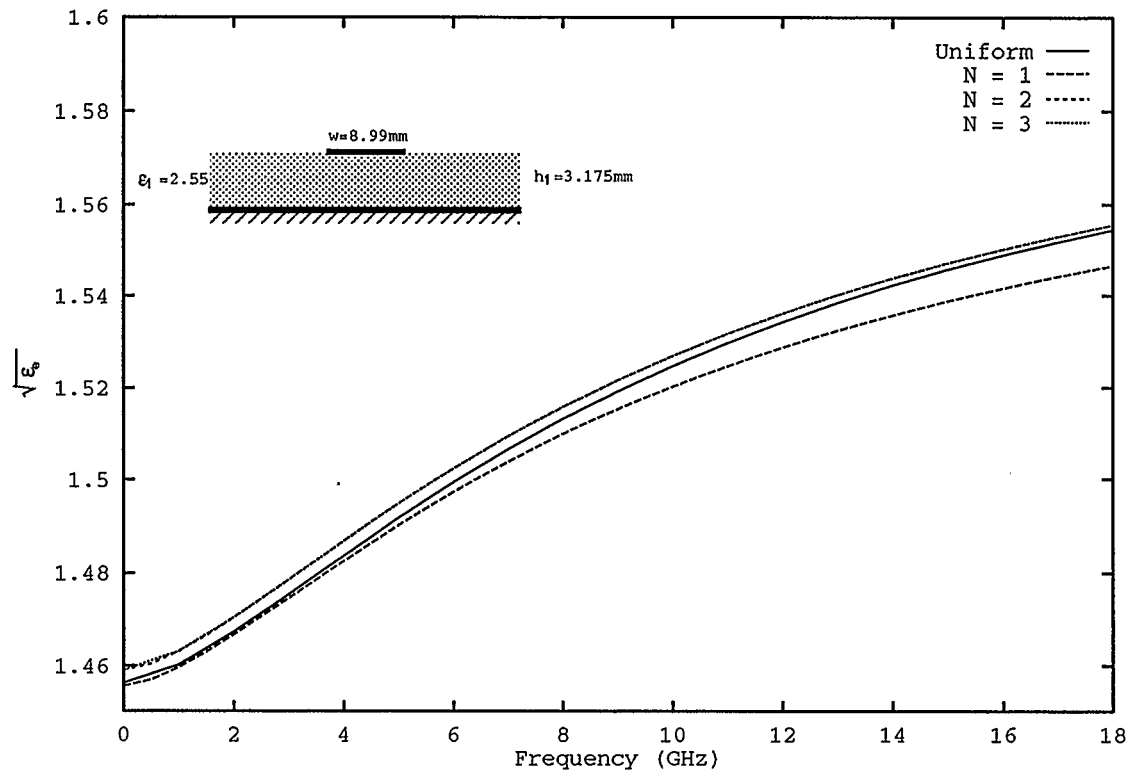


Figure 3.5: Convergence test for a single layer substrate transmission line ($W = 8.99\text{mm}$, $h = 3.175\text{mm}$, $\epsilon_r = 2.55$).

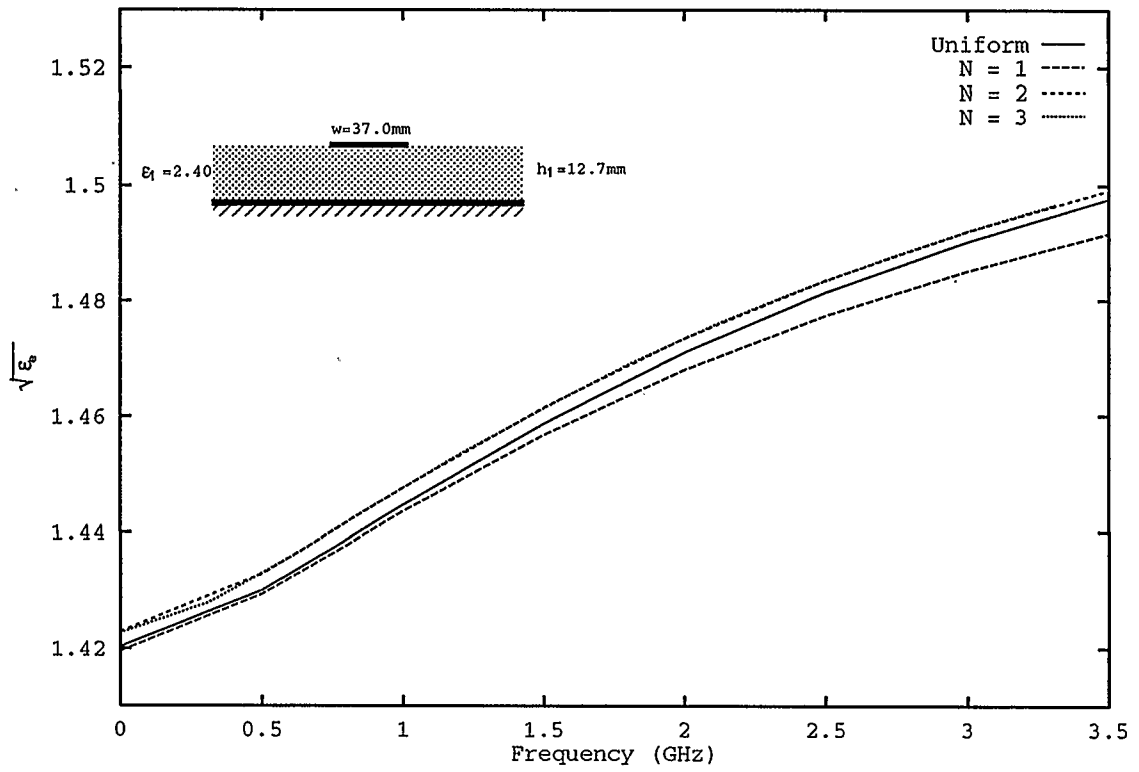


Figure 3.6: Convergence test for a single layer substrate transmission line ($W = 37.0\text{mm}$, $h = 12.7\text{mm}$, $\epsilon_r = 2.40$).

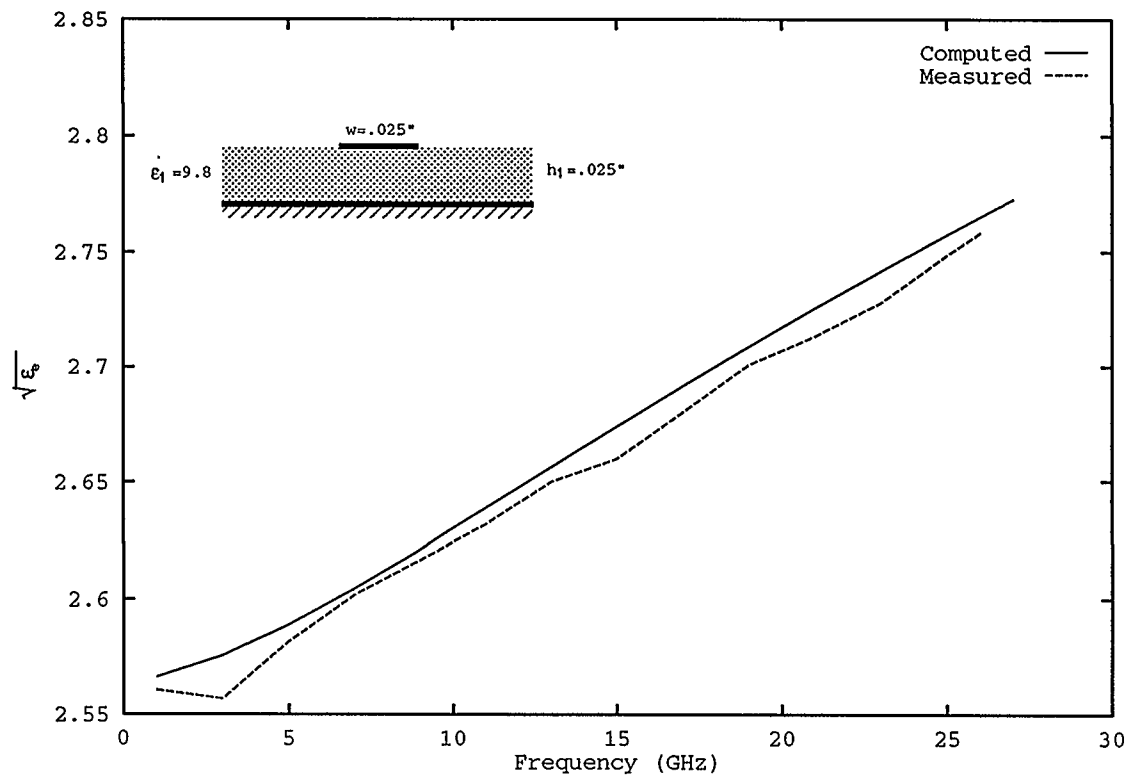


Figure 3.7: $\sqrt{\epsilon_e}$ of a single layer substrate transmission line with measurement made by Fordham [69] ($W = .025''$, $h = .025''$, $\epsilon_r = 9.8$).

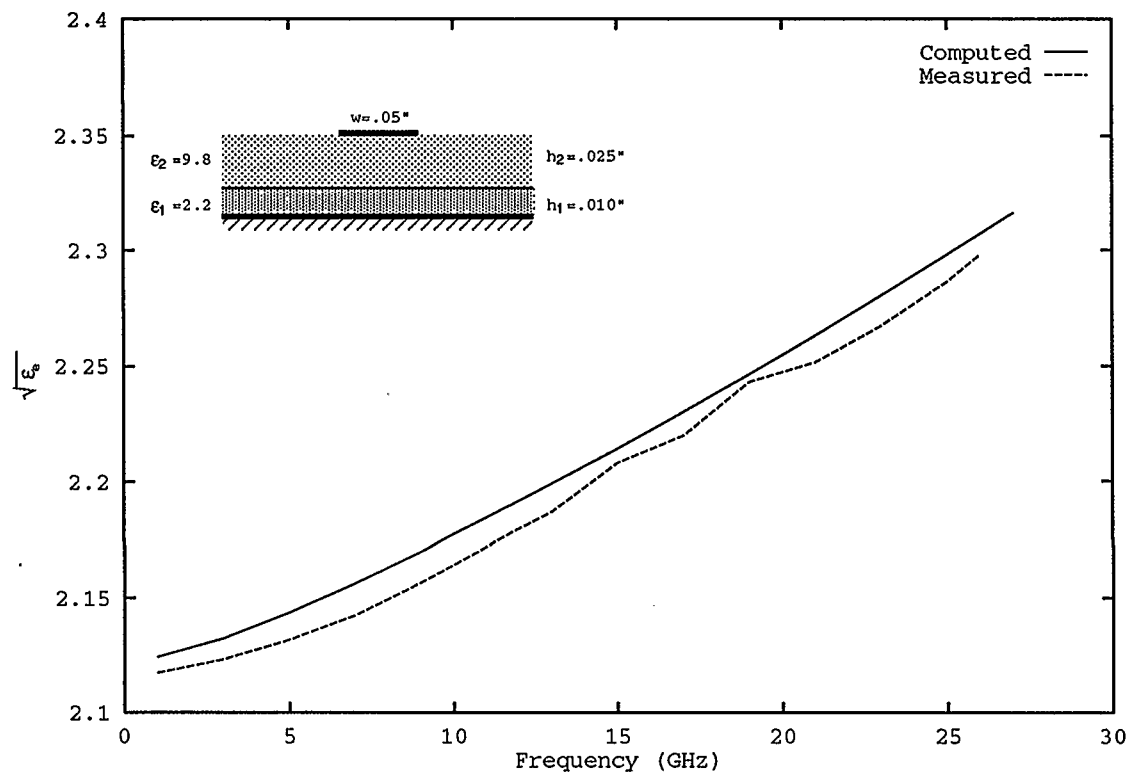


Figure 3.8: $\sqrt{\epsilon_e}$ of a double layer substrate transmission line with measurement made by Fordham [69] ($W = .05''$, $h_1 = .01''$, $h_2 = .025''$, $\epsilon_{r1} = 2.2$, $\epsilon_{r2} = 9.8$).

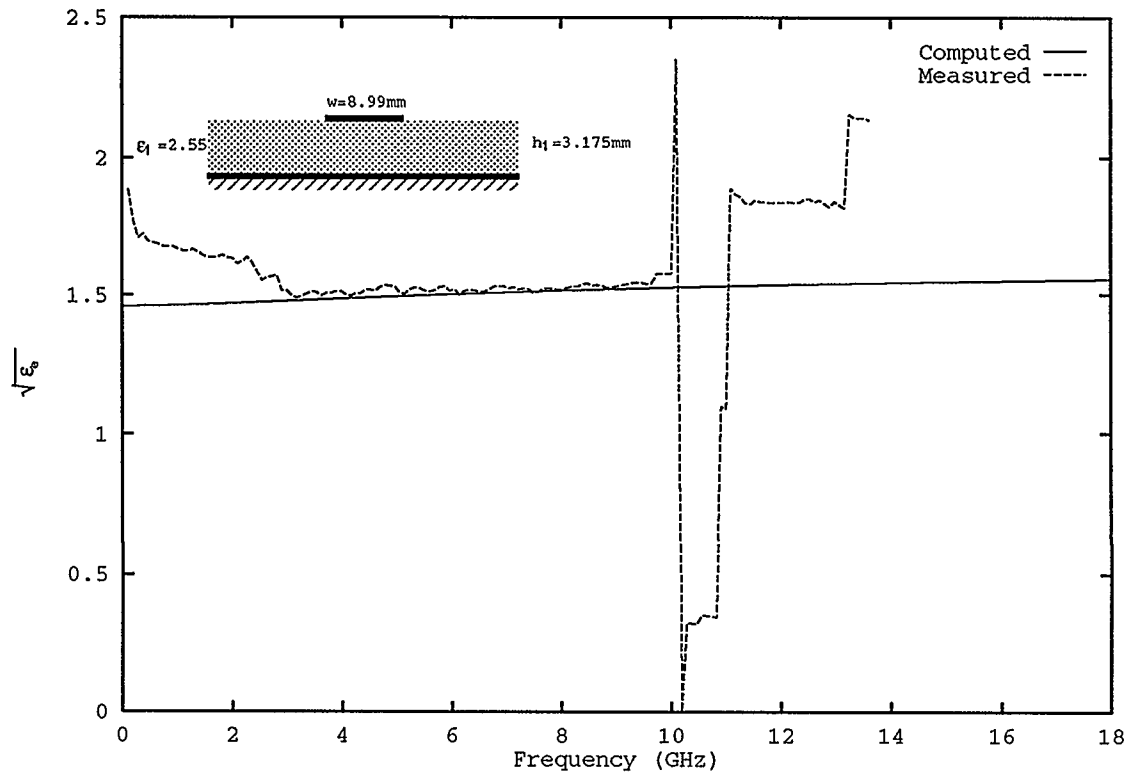


Figure 3.9: $\sqrt{\epsilon_e}$ of a single layer substrate transmission line with measurement made at TRLabs ($W = 8.99\text{mm}$, $h = 3.175\text{mm}$, $\epsilon_r = 2.55$).

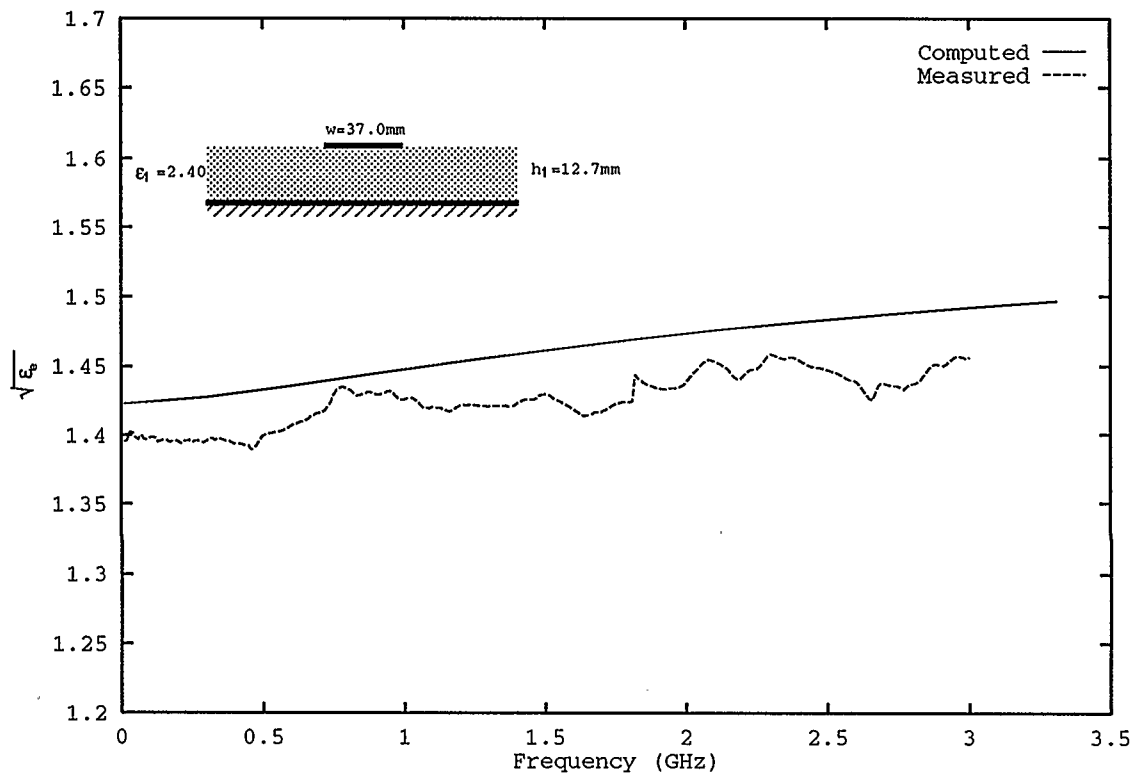


Figure 3.10: $\sqrt{\epsilon_e}$ of a single layer substrate transmission line with measurement made at Novatel Communications, Inc. ($W = 37.0\text{mm}$, $h = 12.7\text{mm}$, $\epsilon_r = 2.40$).

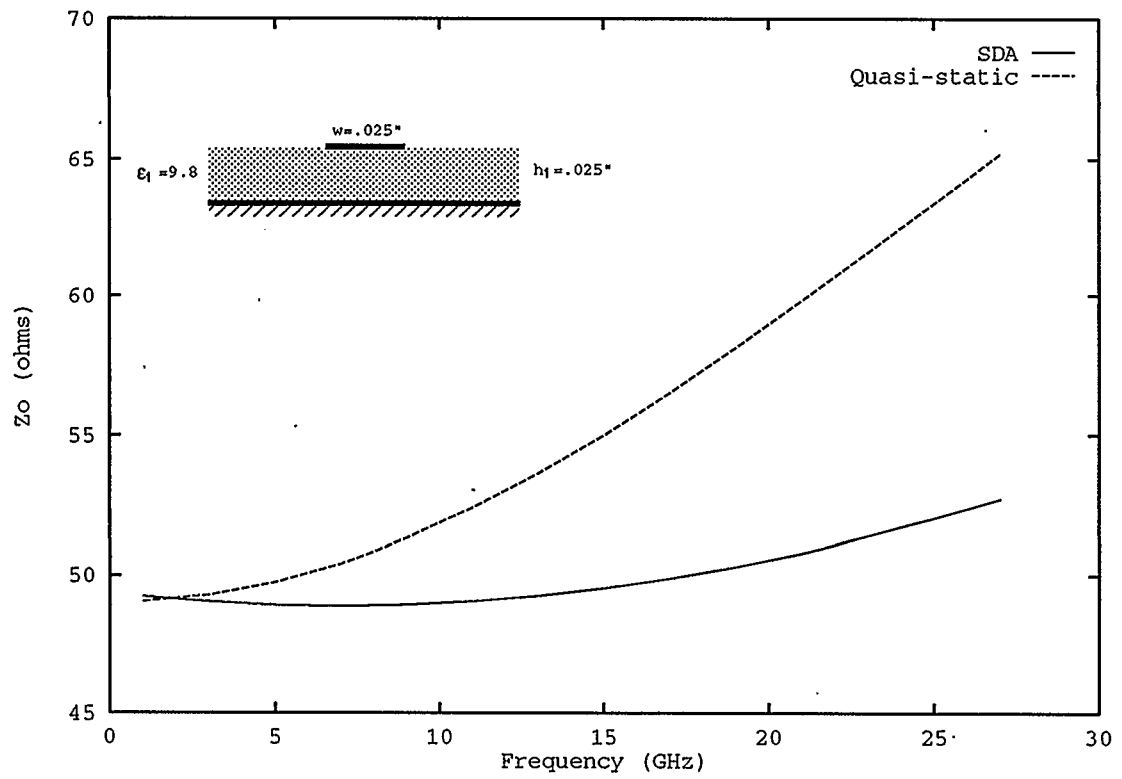


Figure 3.11: Characteristic impedance of a single layer substrate transmission line ($W = .025''$, $h = .025''$, $\epsilon_r = 9.8$).

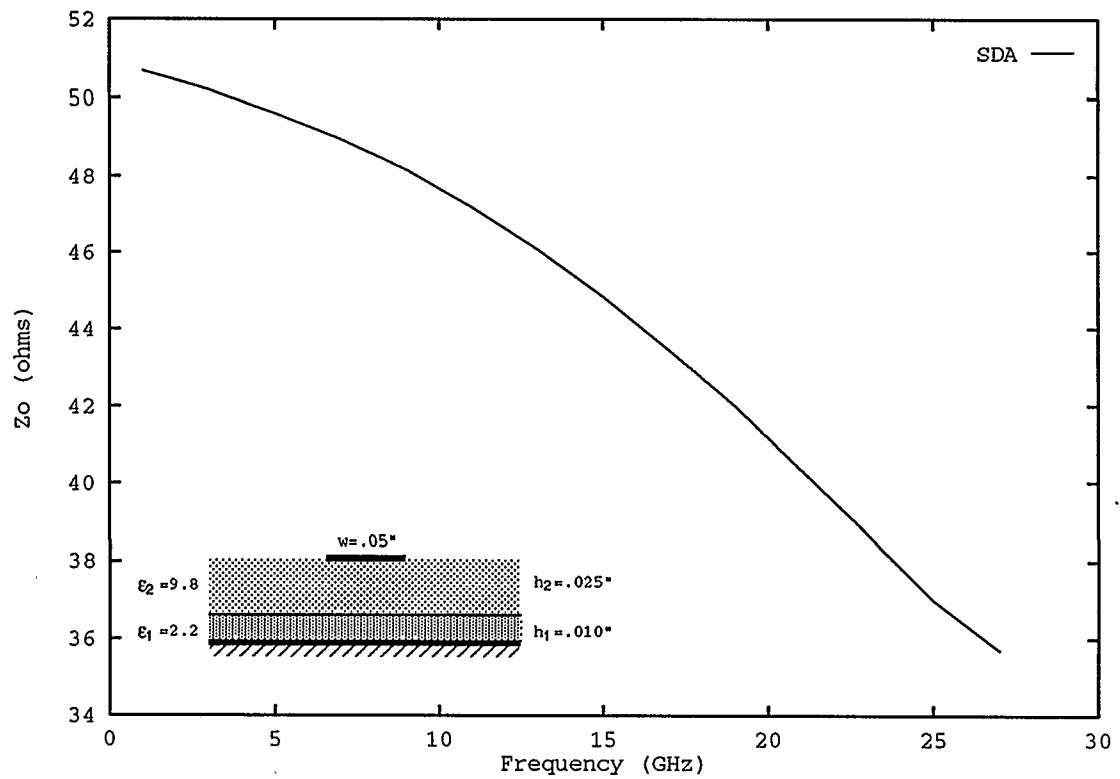


Figure 3.12: Characteristic impedance of a double layer substrate transmission line ($W = .05''$, $h_1 = .01''$, $h_2 = .025''$, $\epsilon_{r1} = 2.2$, $\epsilon_{r2} = 9.8$).

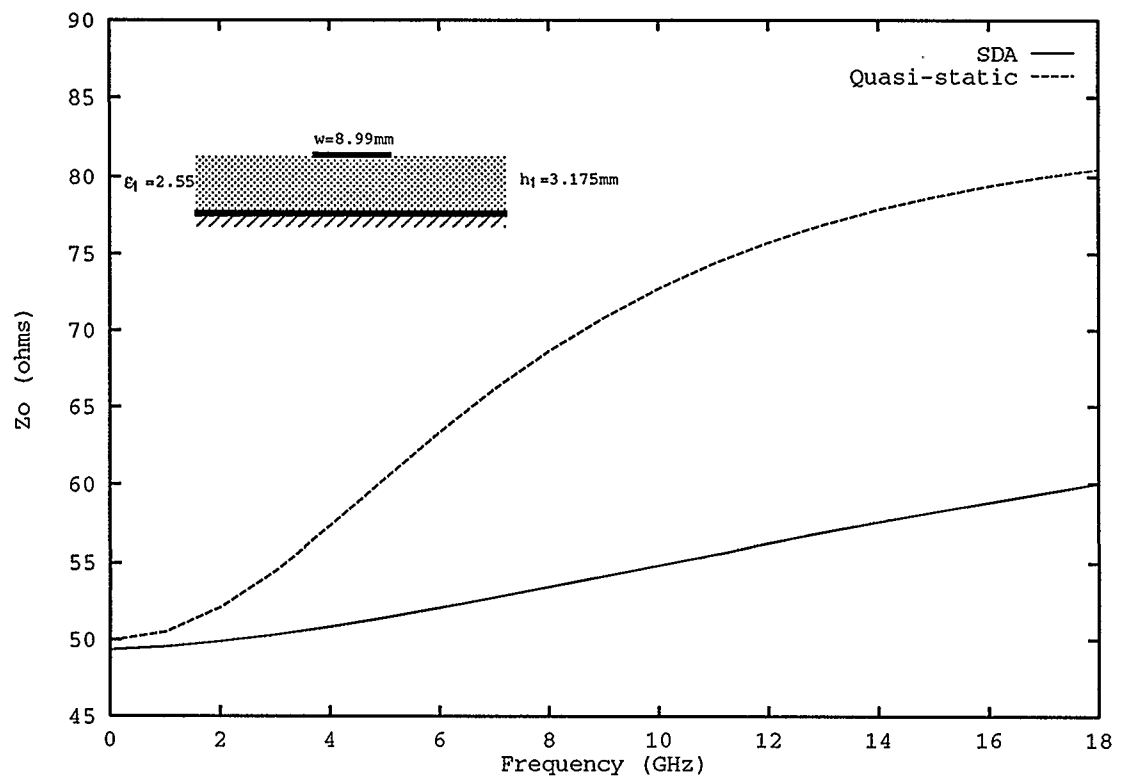


Figure 3.13: Characteristic impedance of a single layer substrate transmission line ($W = 8.99\text{mm}$, $h = 3.175\text{mm}$, $\epsilon_r = 2.55$).

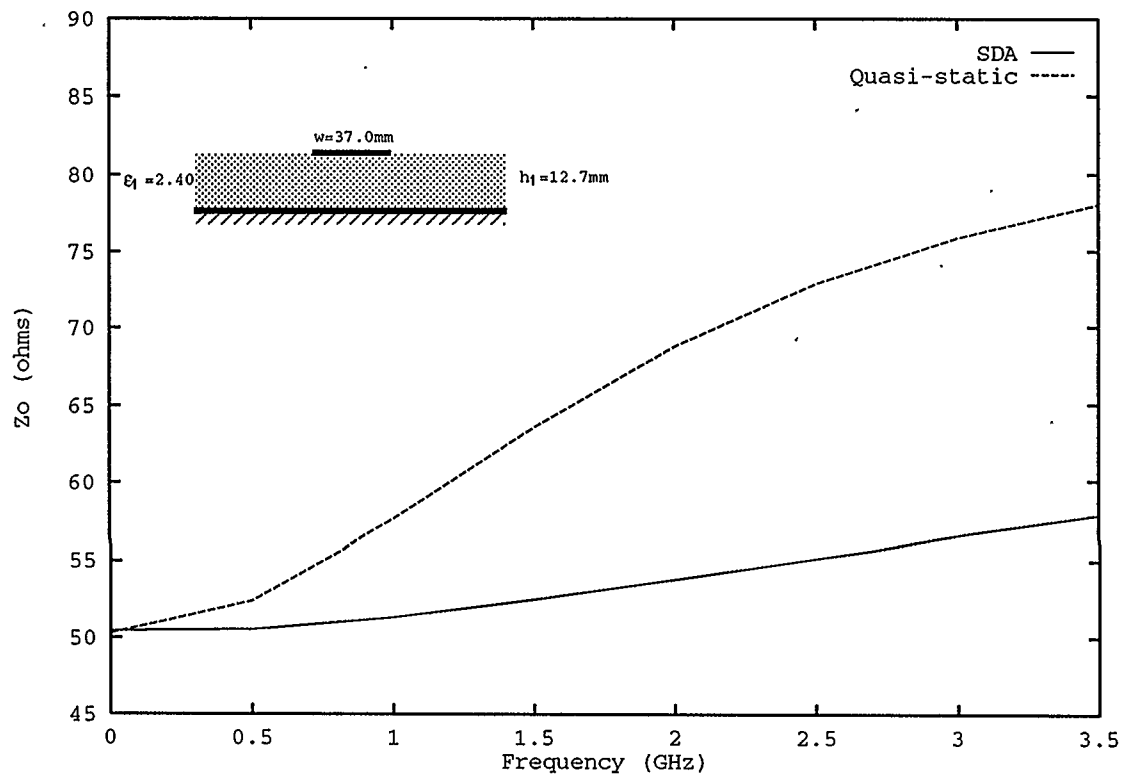


Figure 3.14: Characteristic impedance of a single layer substrate transmission line ($W = 37.0\text{mm}$, $h = 12.7\text{mm}$, $\epsilon_r = 2.40$).

Chapter 4

The Open 1-D Discontinuities

One dimensional microstrip transmission line discontinuities (hereafter referred to as 1-D discontinuities) include opens and gaps. They are so named because the geometry of the strip changes in only one dimension. See Figure 4.1.

The analysis of 1-D discontinuities involves that of the semi-infinite transmission lines, and the local behavior of the current at the discontinuity. Therefore the analysis is more complicated than that of the infinite line, but still simpler than other discontinuities, such as corners, and Tees, etc.

Opens can be used as tuning elements in filters, or as feeders to microstrip radiating patches [96].

In this chapter, the formulae for the analysis of open circuits and some examples are given. Good agreement with measurements and/or other published results are achieved. The analysis of the gaps is similar and is carried out in the next chapter.

4.1 Formulation

4.1.1 Current expansion — Basis Functions

Since an open is a combination of a semi-infinite line and an open end, the basis functions have to reflect this geometry. One common way of analyzing this sort of circuit is to make the length of the transmission line finite and truncate it after several guided wavelengths from the discontinuity [44]. A more reasonable method is to keep the line the way it is, and apply a combination of infinite line and local subdomain analysis.

At the open end discontinuity, high order modes are expected to be generated, and consequently the current distribution there will no longer be sinusoidal. To represent the local current distribution at the open end of the transmission line, a series of subdomain piecewise-sinusoidal (PWS) basis functions is used. At a location far from the open end, the electric current behaves as if it is on an infinite line, and thus the traveling wave base function is also used on the whole strip surface.

Although it is quite arbitrary in the choice of the basis and testing functions in the moment method [42], it is advisable to choose the basis functions that can smoothly reconstruct the true current distribution. Smoothness means the differentiability of the basis functions should be as high as possible. Askun and Mittra [97] point out that the differentiability in the direction of the current flow is more important than in the orthogonal direction.

If the width of the strip is not electrically wide (with respect to the wavelength of the wave), as is the case for most practical transmission lines, the current that flows transversely (with respect to the direction of the transmission) can be neglected [4]. Therefore the current on the strip is assumed to flow in the x (longitudinal) direction only. Since it is a surface current over the strip, the current distribution is a function of both x and y , although it flows in the x direction only.

The transverse variation profile of the longitudinal current (the x direction current) is also determined from the infinite line analysis. The moment method is used here to determine the current distribution at the open end, and the current magnitude and phase of the reflected wave on the strip far away from the discontinuity.

The chosen basis functions are shown as follows:

$$f_i(x', y') = \begin{cases} f_x(y')P(x' - x_i) & i = 1, 2, \dots, N. \quad \text{at the open end area} \\ f_x(y')e^{jk_e x'} & i = N + 1 \quad \text{on whole strip surface} \end{cases} \quad (4.1)$$

where $f_x(y')$ is the transverse distribution of the current, assumed to be Maxwellian, and k_e is the effective propagation constant of the wave along the strip, determined by the infinitely long line analysis in Chapter 3; and $P(x' - x_i)$ is the piecewise-sinusoidal subdomain function defined as

$$P(x' - x_i) = \begin{cases} \frac{\sin k_e(d - |x' - x_i|)}{\sin k_e d} & \text{for } |x' - x_i| \leq d \\ 0 & \text{otherwise} \end{cases} \quad (4.2)$$

The PWS function is a roof-top function shown in Figure 4.2(a). The half length of the PWS functions d ($d = |x_i - x_{i+1}|$) is determined by a trial-and-error method.

The smaller the d , the smoother the reconstructed current distribution, but the longer the computer time and the more such functions that are needed to reach a convergence. On the other hand, if d is too large, the basis functions will not be able to reconstruct the current distribution faithfully, and convergence is hard to reach. It is found that by letting $d = 0.03\lambda_e$ one can obtain satisfactory convergence without losing detail in the current distribution. The total number of PWS functions required depends on the convergence of the moment method. Therefore, PWS functions are placed into the line one by one starting from the open end. The total number of PWS's is increased as the convergence of the reflection coefficient is monitored. As soon as convergence is reached, the numerical analysis is finished. This dynamic procedure is elaborated on later in this chapter.

4.1.2 Testing Procedure

In the moment method, a series of testing functions has to be selected to form the inner products with the given equation where the unknown solution function has been expressed as a linear combination of the basis function series. Each testing function, when taking the inner product with the equation, gives a linear equation, the coefficients of the basis functions being the unknowns. This whole testing procedure results in a system of linear equations. The resultant solution is a least squared error average of the true solution [42][98].

The testing functions are applied in conjunction with the enforcement of the

boundary conditions on the transmission strips. The boundary conditions can be enforced only in the region where the testing functions are defined. Therefore the selection of the testing functions is very important. If the testing functions are chosen to be the same as the basis functions, it is called Galerkin's procedure (or Galerkin's method). There are two versions of Galerkin's procedure usually used in the spectral domain analysis method, the exact one and the modified one [44][76]. The exact one, so called because it uses the whole set of the basis function as the testing functions, which include the traveling wave function as well. The modified procedure uses the testing series to be all local PWS functions. The exact one tries to enforce the boundary condition all over the strip, including the semi-infinite strip because the traveling wave is used as a testing function. Since the traveling wave function is obtained from the infinite line analysis, the boundary condition of zero tangential electric field on the strip surface is automatically met at the area far away from the open end. This is because the strip distant from the open end is locally an infinite line—the field due to the current at the open end can be neglected. Therefore it is suggested that more attention should be paid to the open end area when enforcing the boundary conditions. Thus the testing functions should all be defined around the open end. Apparently the PWS functions are the best candidates. The procedure that results is a modified Galerkin's procedure. Since the PWS functions are local to the open end only, the modified method meets the requirement that boundary condition should be enforced there.

Both exact and modified Galerkin's procedures are tested and compared in the

analysis in this chapter.

Numerical results show that the modified Galerkin's procedure is less oscillatory as the number of the basis functions increases, and thus converges faster than the exact one. The reason behind this phenomenon is obviously that, as stated above, away from the open end, boundary conditions are self met due to the use of traveling wave basis functions, and the modified Galerkin's procedure emphasizes the need to enforce the boundary conditions at the open end.

4.2 Numerical Considerations

4.2.1 Traveling Wave Decomposition

The PWS basis functions are shown in Figure 4.2(a) (note that they are not drawn to scale). They are used to construct the high mode current distribution at the open end. Away from the open end, the local current distribution should be the same as if the strip is infinitely long. The traveling wave base function is used to represent the current away from the open end. It is decomposed into a sine and a cosine function, using Euler's formula [44]:

$$e^{\pm j k_e x'} = \cos(k_e x') \pm j \sin(k_e x') \quad (4.3)$$

This decomposition is not simply to get a different mathematical expression. The

defined region for the cosine function has been altered. The sine wave goes from $-\infty$ to 0 in x , while the cosine wave goes from $-\infty$ to $-\lambda_e/4$ (see Figure 4.2(b)).

The decomposition results from the consideration of the convergence. As shown in Chapter 3, the matrix element Z_{ij} always takes the form of a double integration of the product of the Green's function, the base function f_i , and the testing function f_j , all in the spectral domain. It is not difficult to obtain the transform of the traveling wave $e^{\pm jk_e x'}$ over $x' \in (-\infty, 0]$. Some researchers [44][99] have pointed out that the decomposition is necessary to get rid of the non-zero end current of the cosine function. Actually, non-zero end current is not a problem, because a half-PWS function can be placed at $x' = 0$ to cancel it out. It is found that a decomposition has to be performed to obtain better convergence, because the transforms of the sine and the cosine functions decrease with λ_x^{-2} , while the transform of the exponential function varies with λ_x^{-1} only.

The comparison of the transforms of decomposed and undecomposed traveling wave basis functions can be found in Appendix A.

4.2.2 Step-Up Procedure

The numerical procedure is very time consuming. Some parameters have to be determined by trial-and-error. In practice, some of them do not have to be changed once appropriate values are found. The half length of the PWS function d , for

instance, has to be determined before any matrix elements can be calculated. It is a trade-off between computer time and accuracy. The smaller the d , the more PWS functions that have to be placed in a given area, and thus the more faithful the re-construction of the current, and of course, the more the computer time that will be required. It is found that choosing d to be $.03\lambda_e$ is a reasonable trade-off [100]. Once this is determined, it will be used in all the following analysis.

Another hard-to-decide parameter is the total number of the PWS functions in the moment method, or in other words, the order of the matrix. It is conceivable that the farther away a location is from the open end, the lower the magnitude of the PWS function there, because the high order mode currents set up by the discontinuity get attenuated some distance away from the open end.

The user is in more control if he can view the process of the convergence. A step-up procedure is therefore suggested here which increases the number of the PWS functions one at a time. The convergence is printed as the function of the number of the total PWS. If convergence is reached, the user can terminate the program, or the program can do it automatically. By printing out the convergence progress, the program can let the user monitor how the program works, making it easier to debug the program. This step-up procedure can be quite easily realized by writing a shell script file on UNIX system. In addition, if the computer breaks down during the analysis, only one matrix element will be lost, because all the previous runs have already finished and the reusable datum have already been saved. The user

can restart the process from where it was abnormally terminated very easily. The program will only compute whatever it can not find in the data bank.

It is found that a total coverage of $.5 \sim .7$ guided wavelength gives convergence of a few percent variation or less. This length is equivalent to approximately a total of $20 \sim 25$ PWS functions.

4.3 Matrix Formulation

4.3.1 Derivation

The moment method is used to determine the current distribution by the following procedure. First the tangential electric field is formulated from the Green's function and the assumed current distribution, as follows

$$E_x = \iint G_{xx}(J_x^I - \Gamma J_x^R + \sum_{n=1}^N I_n f_n) dx' dy' \quad (4.4)$$

where J_x^I is the input current source incident from $x' = -\infty$ with unit magnitude; J_x^R is the reflected wave from the open whose magnitude Γ is to be determined, and the function is different from the incident wave only for the sign of k_e ; and f_n 's are the PWS functions, whose magnitudes I_n are also to be determined.

As soon as the tangential electric field is formulated, the next thing to do is to determine the testing functions. The choice of testing functions determines where

and how the boundary condition on surface of the strip is enforced. I have used both exact and modified Galerkin's procedures. For the modified procedure the testing functions are all PWS. Since there are $N + 1$ unknown magnitudes (N PWS's and one Γ) but only N PWS's, another PWS has to be added. This one is chosen to be one more step from the last base PWS function, bridging the PWS basis and the pure traveling wave areas($x_i = (N + 1)d$). In this configuration, the area covered by the testing PWS functions is larger than that covered by the basis PWS functions, by half the length of a PWS function.

The final matrix forms of the moment method are shown in Equation 4.5 and 4.6, respectively, that is

$$\begin{bmatrix} [Z_{pp}^{N \times N}] & [Z_{pR}^{N \times 1}] \\ [Z_{Rp}^{1 \times N}] & [Z_{RR}^{1 \times 1}] \end{bmatrix} \begin{bmatrix} [I_p^{N \times 1}] \\ \Gamma \end{bmatrix} = - \begin{bmatrix} [V_{pI}^{N \times 1}] \\ [V_{RI}^{1 \times 1}] \end{bmatrix} \quad (4.5)$$

for the exact Galerkin's procedure, and

$$\begin{bmatrix} [Z_{pp}^{(N+1) \times N}] & [Z_{pR}^{(N+1) \times 1}] \end{bmatrix} \begin{bmatrix} [I_p^{N \times 1}] \\ \Gamma \end{bmatrix} = - \begin{bmatrix} [V_{pI}^{(N+1) \times 1}] \end{bmatrix} \quad (4.6)$$

for the modified Galerkin's procedure.

It is noted that the only difference between the two equations is the last row in the matrix, which results from the different choice of the last testing function, a traveling wave or a PWS function.

The matrix elements are defined as follows:

$$Z_{pp}^{mn} = \int_{-\infty}^{+\infty} \int_{-\infty}^{+\infty} \tilde{G}_{xx}(\lambda_x, \lambda_y) \tilde{F}_x^2(\lambda_y) \tilde{P}_x^2(\lambda_x) \cos[d(m-n)\lambda_x] d\lambda_x d\lambda_y \quad (4.7)$$

$$Z_{pR}^m = \int_{-\infty}^{+\infty} \int_{-\infty}^{+\infty} \tilde{G}_{xx}(\lambda_x, \lambda_y) \tilde{F}_x^2(\lambda_y) \tilde{P}_x(\lambda_x) \tilde{R}_x(\lambda_x) e^{-md\lambda_x} d\lambda_x d\lambda_y \quad (4.8)$$

$$Z_{Rp}^n = Z_{pR}^n \quad (4.9)$$

$$Z_{RR} = \int_{-\infty}^{+\infty} \int_{-\infty}^{+\infty} \tilde{G}_{xx}(\lambda_x, \lambda_y) \tilde{F}_x^2(\lambda_y) \tilde{R}_x^2(\lambda_x) 2j \cos\left(\frac{\pi}{2k_e} \lambda_x\right) d\lambda_x d\lambda_y \quad (4.10)$$

$$V_{pI}^m = \int_{-\infty}^{+\infty} \int_{-\infty}^{+\infty} \tilde{G}_{xx}(\lambda_x, \lambda_y) \tilde{F}_x^2(\lambda_y) \tilde{P}_x(\lambda_x) \tilde{V}_x(\lambda_x) e^{-md\lambda_x} d\lambda_x d\lambda_y \quad (4.11)$$

and

$$V_{RI} = 2 \int_{-\infty}^{+\infty} \int_{-\infty}^{+\infty} \tilde{G}_{xx}(\lambda_x, \lambda_y) \tilde{F}_x^2(\lambda_y) \tilde{R}_x(\lambda_x) \tilde{V}_x(\lambda_x) d\lambda_x d\lambda_y \quad (4.12)$$

where

$$\tilde{P}_x(\lambda_x) = \frac{2k_e}{\sin(k_e d)} \frac{\cos(k_e d) - \cos(\lambda_x d)}{\lambda_x^2 - k_e^2}, \quad (4.13)$$

$$\tilde{F}_x^2(\lambda_y) = J_0\left(\frac{W}{2}\lambda_y\right), \quad (4.14)$$

$$\tilde{R}_x(\lambda_x) = \left(e^{\frac{j\pi\lambda_x}{2k_e}} + j\right) \int_{-\infty}^0 \sin(k_e x) e^{-jk_e x} dx, \quad (4.15)$$

$$\tilde{V}_x(\lambda_x) = \left(e^{\frac{j\pi\lambda_x}{2k_e}} - j\right) \int_{-\infty}^0 \sin(k_e x) e^{-jk_e x} dx, \quad (4.16)$$

and

$$\int_{-\infty}^0 \sin(k_e x) e^{-jk_e x} dx = \frac{k_e}{\lambda_x^2 - k_e^2} + \frac{j\pi}{2} [\delta(\lambda_x + k_e) - \delta(\lambda_x - k_e)]. \quad (4.17)$$

The function $\tilde{G}_{xx}(\lambda_x, \lambda_y)$ is the spectral domain Green's function which is obtained from Chapter 2. Since it is generalized, this analysis is applicable to multilayer microstrip opens. One only has to change the description of the structure and the width of the strip to analyze a microstrip in a new structure.

The δ functions in the last expression shown above should not cause any problems, because when substituted into the integrand, it samples λ_x at $\pm k_e$, and the rest of the integral is with respect to λ_y and should be zero, which is the root searching result in the infinite line analysis.

4.3.2 The Toeplitz Matrix

All the integrals for the elements above can be simplified into two semi-infinite integrals, and then transformed into polar integrals which consist of a finite integral and an infinite one. This can significantly reduce the time taken for evaluation of the integrals.

It is also noted that the submatrix $[Z_{pp}]$ is a Toeplitz matrix, which means that if the first row is known, the rest of the matrix can be determined by using the expression

$$Z_{i,j} = Z_{1,|i-j|+1} \quad (4.18)$$

This reduces a great amount of computation time. The fact that this matrix is Toeplitz comes from the layout and the numbering of the PWS functions along the line (Figure 4.2). From the element expression Equation 4.7 it is noted that the element values are determined by the distance between the two PWS functions involved.

The submatrix $[Z_{Rp}]$ is the same as $[Z_{pR}]$, thus the whole Z-matrix is symmetrical for the exact Galerkin's procedure, but asymmetrical for the modified one, due to the fact that the testing functions are not exactly the same as the basis functions.

4.4 Results

If one is concerned only with the circuit performance, then finding only the reflection coefficient is sufficient. However, the moment method analysis can reveal more information. The current distribution at the open is determined from the magnitudes of the PWS functions. If, for instance, a microstrip antenna is being analyzed, the current distribution is very important in determining the radiation pattern. Since this dissertation deals only with the circuit performance of the microstrip discontinuities, we shall restrict our considerations to the magnitude and the phase of the reflection coefficient and other network parameters.

4.4.1 Comparison of the Two Galerkin's Procedures

The results from the two Galerkin's procedures — the exact one and the modified one, are shown and compared in this subsection.

Figure 4.3 shows the convergence behaviors of the two procedures for an open circuit at 20GHz. The vertical axis is the magnitude of the reflection coefficient $|\Gamma|$ and the horizontal one is the number of PWS functions used. It is clear that the modified procedure is far better than the exact one, which converges much more quickly. The exact procedure, on the other hand, is still lightly oscillatory over the range of the analysis. After first a few trials ($N < 8$), the modified procedure gives stabilized results and reaches convergence as soon as the number of PWS's is over 8.

It is expected that many more PWS functions are required for the exact Galerkin's procedure to reach the same convergence, since the oscillation decays very slowly.

The critical number of PWS functions, where convergence starts, is readily explainable, if one takes a look at the traveling wave truncation at the open end. Recall that the cosine part of the traveling wave starts one quarter of an effective wavelength away from the open end, and the length of each PWS function is .03 of an effective wavelength. Eight PWS functions are just enough to cover the gap between the tip of the cosine wave and the open end, making the current continuous from the open end to $-\infty$.

It is noted that even for the modified Galerkin's procedure, there is still some residual oscillation about a stable value. This phenomenon can be due to the fact that the number of PWS functions is not large enough to totally cover all the high order mode area, or the size of each PWS function is not small enough to reconstruct the local current distribution in fine detail. As discussed before, this is simply a trade-off between the computation time and the accuracy. A better result can be obtained by having some after processing of the results. For instance, the average value in the oscillation can be extracted from the convergence plot, and can be taken as the final converged value.

Another comparison is made for the phase convergence of the reflection coefficient $\angle\Gamma$, shown in Figure 4.4. This is the same board at the same frequency as the one above. Although the modified Galerkin's procedure starts with very poor output for

the first few tests, it reaches the convergence very quickly and demonstrates good stability once it reaches convergence. The exact procedure, on the other hand, is again somewhat oscillatory.

From the two figures shown, it is clear that the modified Galerkin's procedure is a better choice, because the importance of the local boundary condition is emphasized. For locations far away from the open end the boundary condition is automatically met due to the choice of the traveling wave base function. It should be noted that the modified Galerkin's procedure provides poor output for the first a few tests, due to the small area covered by the PWS functions. As the number of PWS becomes large enough, the convergence is smooth and stable. This is understandable because the staggered cosine and sine combination (Figure 4.2) is not a real representation of the traveling waves $e^{\mp jkx}$. Many PWS functions and the staggered cosine and sine are required to obtain a full reconstruction of the traveling wave and the local current.

4.4.2 Convergence Test

The convergence test is always important, because this tells the user how the algorithm output varies as the number of the PWS's increases. The program should be terminated as soon as the pre-set convergence criteria is met, since any further effort is unnecessary.

Figure 4.5 and 4.6 show the convergence response of a microstrip open on a single board. The frequency is set to 10GHz. All the other parameters of the board are the same as in Figure 4.3. Also shown is the convergence behavior of the exact Galerkin's procedure. This is another demonstration that modified procedure is a better choice. Figure 4.5 shows that an accuracy of about .3% for the magnitude can be achieved if N is chosen to be around 20, or making the PWS coverage about $.5\lambda_e$. For the same PWS coverage, phase accuracy of less than 1° can be achieved (Figure 4.6).

As the frequency increases, the total number of the PWS's may have to be increased. This is understandable because the higher the frequency, the greater the high order mode waves with greater amplitudes, and consequently the farther they travel before vanishing. It should also be noted that the higher the frequency, the shorter the guided wavelength, and the smaller the covered area by the same number of PWS's.

These effects are shown in Figure 4.7 and 4.8, where the convergence of the magnitude and the phase are plotted. In these two figures, only the results from the modified Galerkin's procedure are plotted. As the frequency is increased from 5GHz to 25GHz, the magnitude and the phase become more and more oscillatory, which suggests that at high frequencies, more PWS functions should be employed in order to achieve high accuracy.

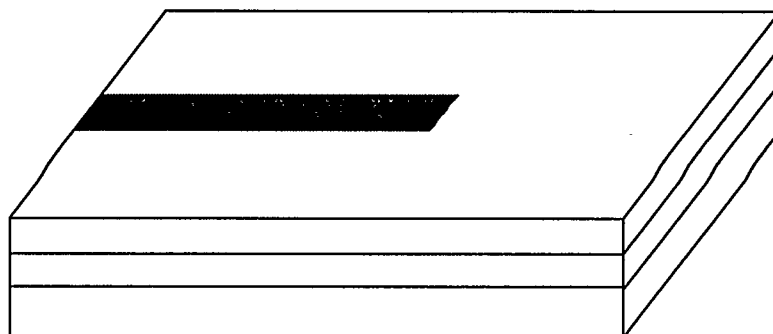
4.4.3 Comparison with the Measurement

Figure 4.9 plots the phase of the reflection coefficient for the same circuit together with the measurement made by Gronau and Wolff [101]. As the figure shows, the agreement is reasonably good. The magnitude of the reflection coefficient for this open circuit is plotted in Figure 4.10. Since measurement data is not available for the magnitude, only the calculated data is plotted.

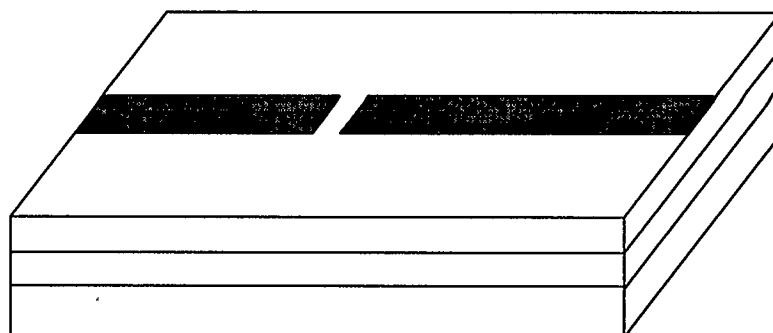
Results for another open circuit are plotted in Figure 4.11 and 4.12. The magnitude and its phase as a function of the frequency show trends similar to those shown by other circuits. It is clearly shown that the higher the frequency, the smaller the magnitude of the reflection, and the more negative its phase. This clearly demonstrates the effect of the radiation loss at the open end, and the so-called extension length (excess length) beyond the physical end of the line. Since the electrical size of the open end increases with the frequency, the return loss increases with the frequency. It should also be noted that the radiation loss includes the radiation into the medium as surface waves, as well as into the free space as space wave.

The calculations from Touchstone[102], a commercial circuit analysis package, are also plotted along with the results from this theory. Touchstone uses a model developed by Kirschning et al [103], with modifications, which is based on quasi-static analysis. Good agreement was obtained in Figure 4.12 over a reasonable frequency band. At very high frequencies, however, a significant discrepancy was observed. It is notable that Touchstone model failed to predict any change in the magnitude of

the reflection coefficient — it simply gave a constant unit magnitude as shown in Figure 4.11. This is due to the static nature of the model used in Touchstone, which does not fully account for the high frequency response of the circuit. Also notable is the phase change with frequency. Touchstone model simply predicts that the phase linearly decrease with frequency as shown in Figure 4.12, which is resulted from a fixed extension length. The SDA, on the other hand, gives a nonlinear change, which indicates that the excess length is not a fixed value.

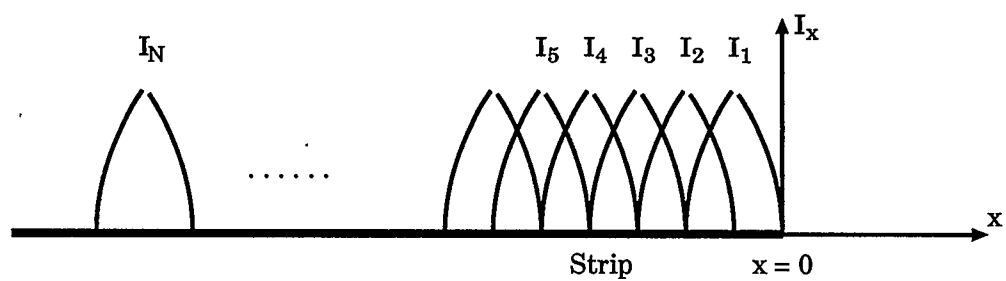


(a) Open

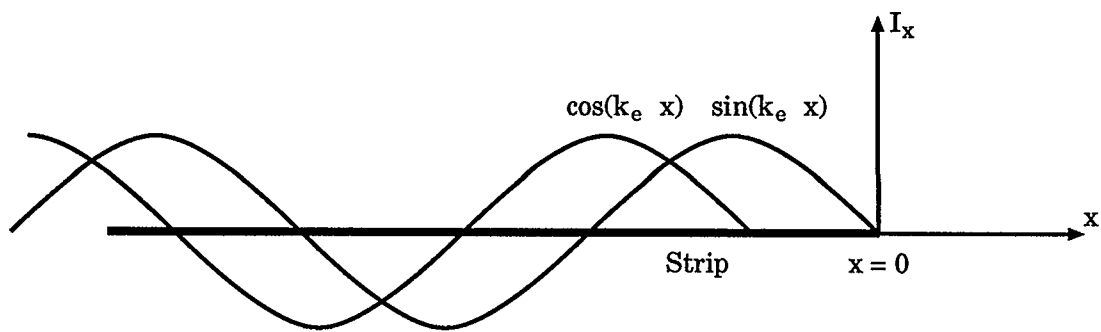


(b) Gap

Figure 4.1: A microstrip transmission line open and gap discontinuities.



(a) PWS Functions



(b) Traveling Wave Functions

Figure 4.2: Basis functions for the open circuit.

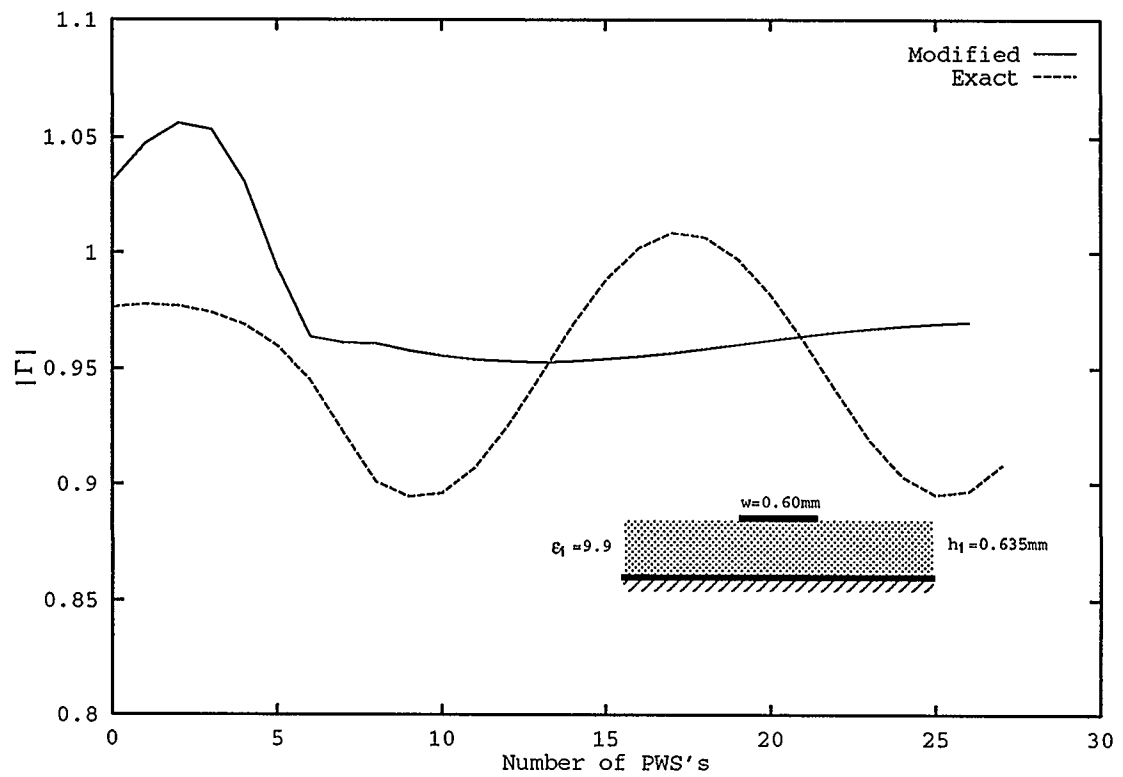


Figure 4.3: Comparison of the two Galerkin's procedures for $|\Gamma|$ for an open ended line (freq = 20GHz, $W = .60\text{mm}$, $h = .635\text{mm}$, $\epsilon_r = 9.9$).

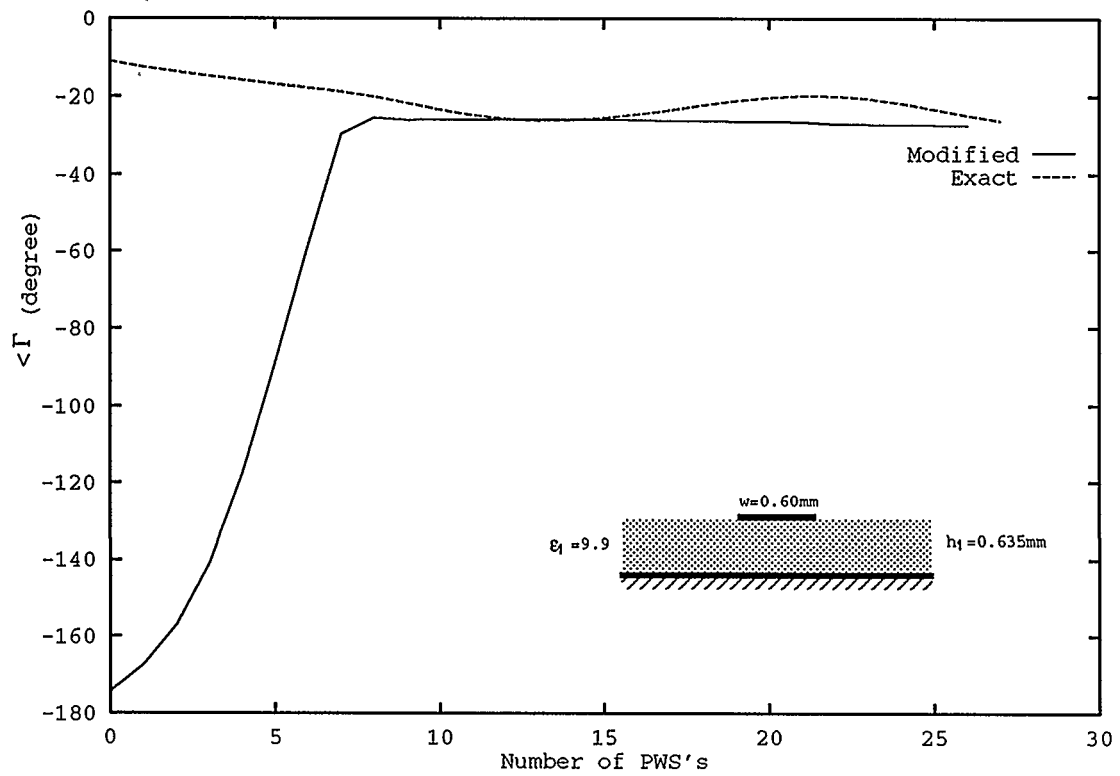


Figure 4.4: Comparison of the two Galerkin's procedures for $\angle\Gamma$ for an open ended line (freq = 20GHz, $W = .60\text{mm}$, $h = .635\text{mm}$, $\epsilon_r = 9.9$).

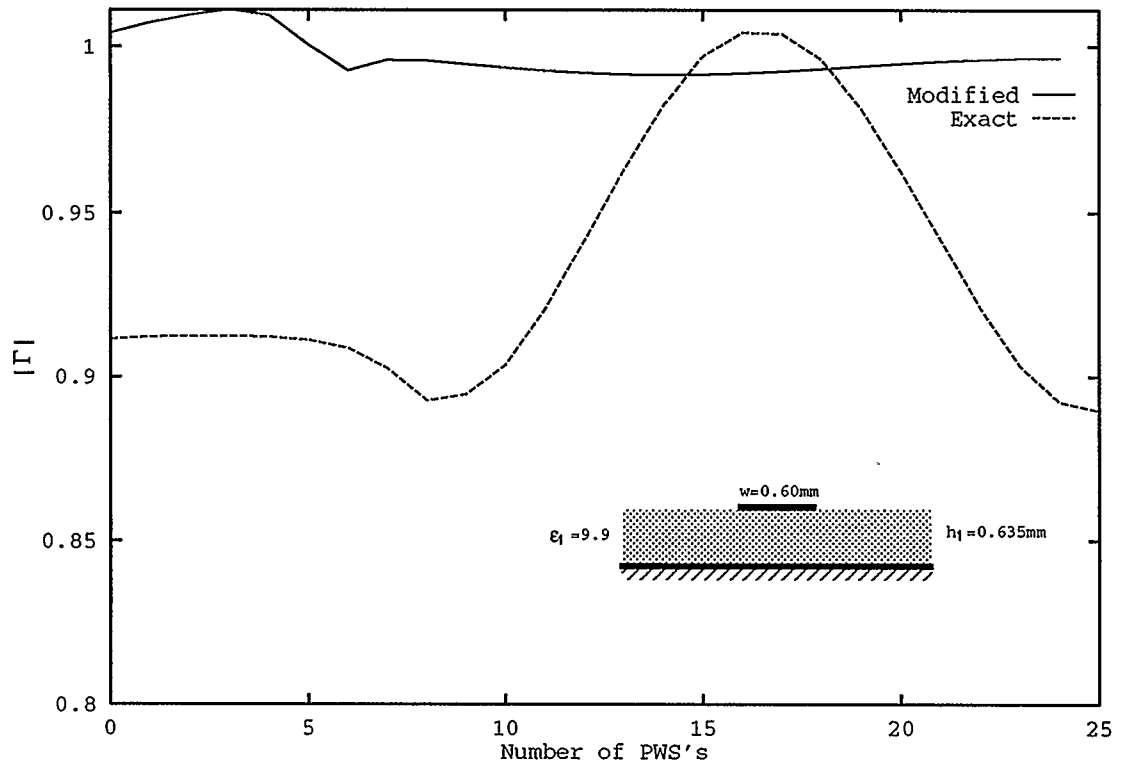


Figure 4.5: Convergence test for the two Galerkin's procedures for $|\Gamma|$ for an open ended line (freq = 10GHz, $W = .60\text{mm}$, $h = .635\text{mm}$, $\epsilon_r = 9.9$).

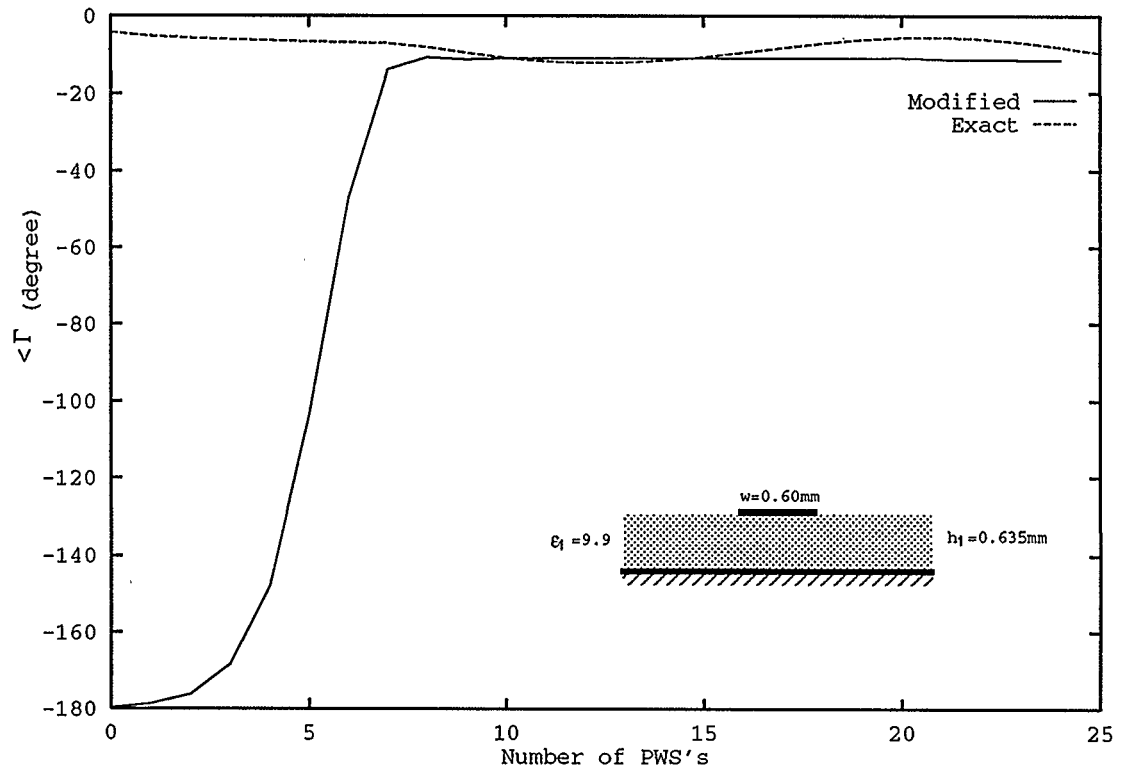


Figure 4.6: Convergence test for the two Galerkin's procedures for $\angle\Gamma$ for an open ended line (freq = 10GHz, $W = .60\text{mm}$, $h = .635\text{mm}$, $\epsilon_r = 9.9$).

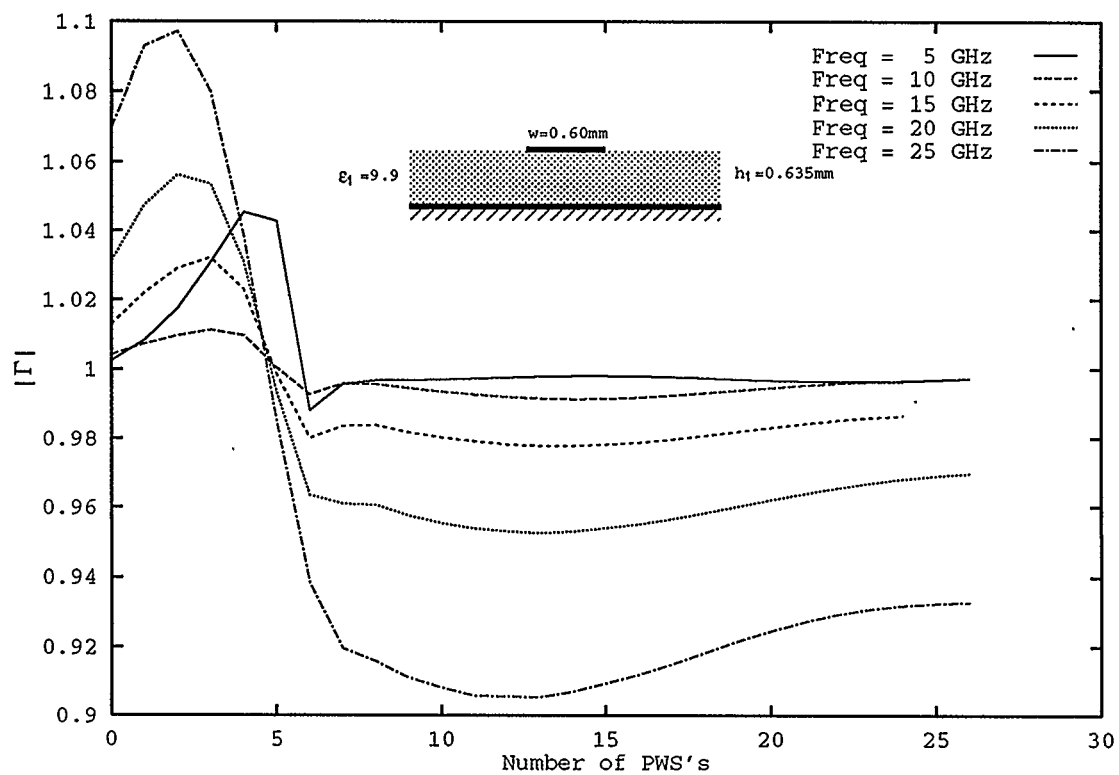


Figure 4.7: Frequency response of convergence for modified Galerkin's procedure for $|\Gamma|$ for an open ended line ($W = .60\text{mm}$, $h = .635\text{mm}$, $\epsilon_r = 9.9$).

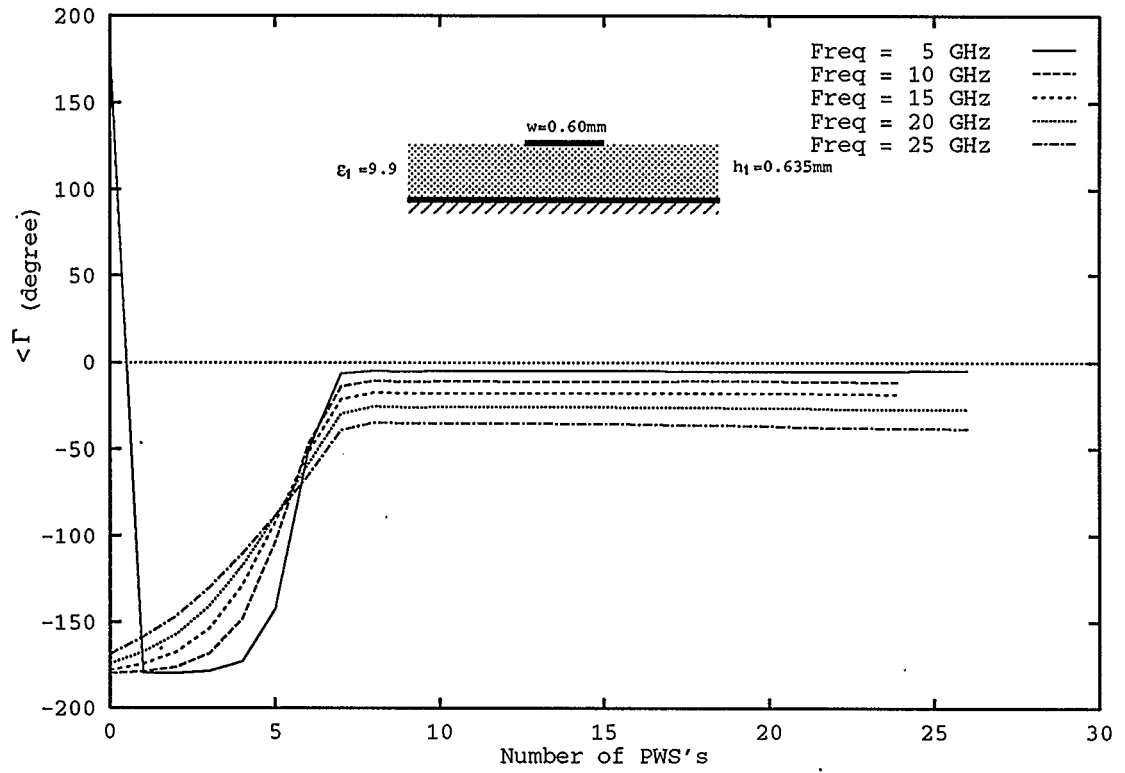


Figure 4.8: Frequency response of convergence for modified Galerkin's procedure for $\angle \Gamma$ for an open ended line ($W = .60\text{mm}$, $h = .635\text{mm}$, $\epsilon_r = 9.9$).

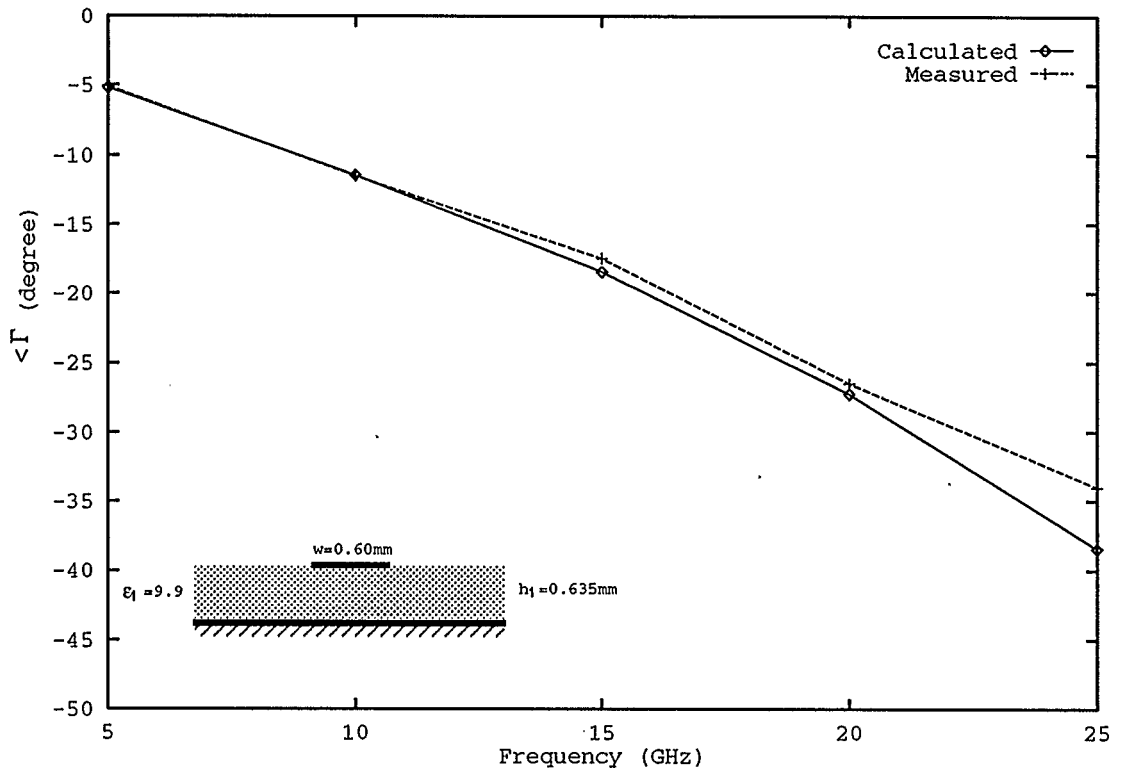


Figure 4.9: Calculated reflection coefficient ($\angle \Gamma$) for an open ended line with measurement made by Gronau and Wolff [101] ($W = .60\text{mm}$, $h = .635\text{mm}$, $\epsilon_r = 9.9$).

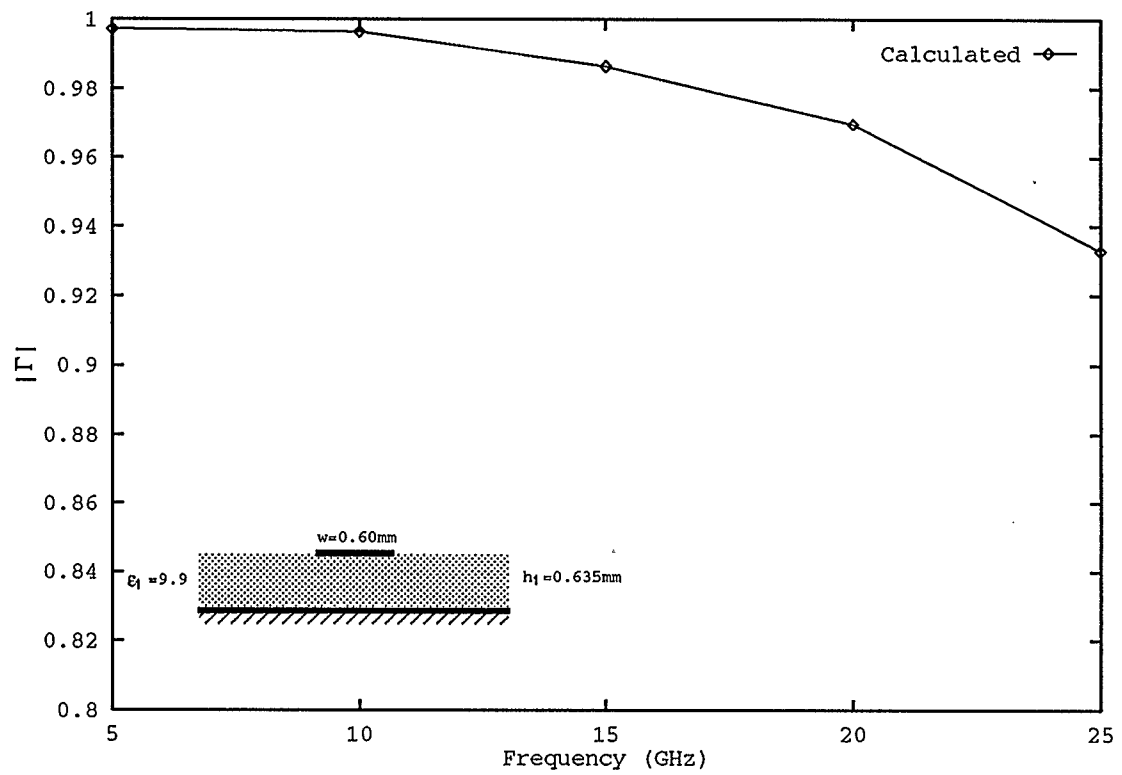


Figure 4.10: Calculated reflection coefficient ($|\Gamma|$) for an open ended line ($W = .60\text{mm}$, $h = .635\text{mm}$, $\epsilon_r = 9.9$).

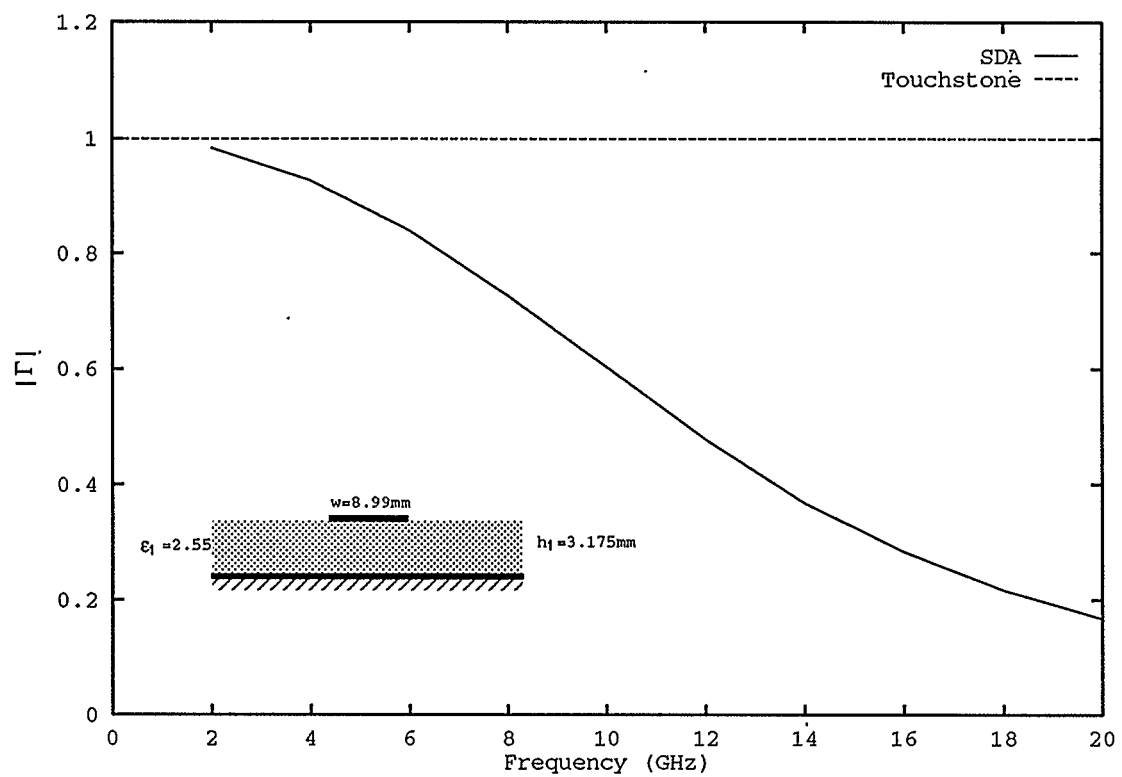


Figure 4.11: Calculated reflection coefficient ($|\Gamma|$) for an open ended line: SDA and Touchstone ($W = 8.99\text{mm}$, $h = 3.175\text{mm}$, $\epsilon_r = 2.55$).

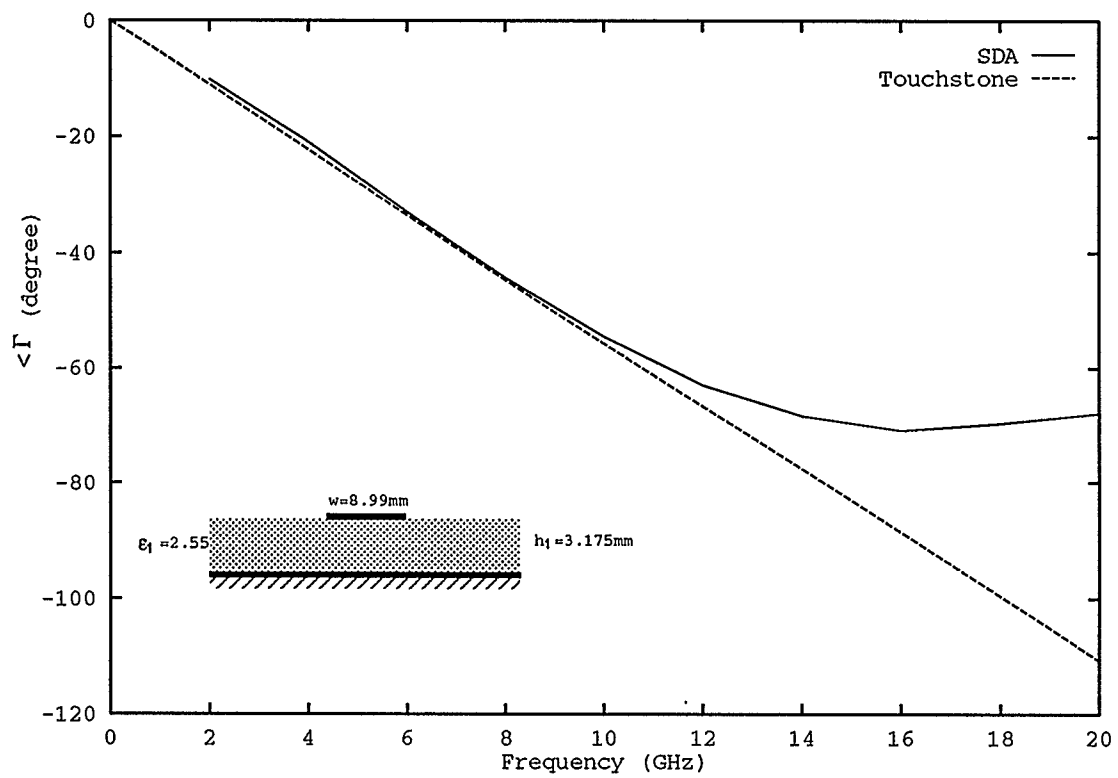


Figure 4.12: Calculated reflection coefficient ($\angle \Gamma$) for an open ended line: SDA and Touchstone ($W = 8.99\text{mm}$, $h = 3.175\text{mm}$, $\epsilon_r = 2.55$).

Chapter 5

The Gap 1-D Discontinuities

In this chapter, analysis of microstrip transmission line gap discontinuities is discussed. Since the analysis is similar to that of the microstrip open, the discussion will emphasize those features unique to the gap.

A microstrip transmission line gap is shown in Figure 4.1(b), in Chapter 4. The gap can be viewed as two opens face to face, with some distance between their open ends. Therefore, the analysis of a gap can then borrow the techniques used in the open circuit analysis.

Since a gap consists of two semi-infinite transmission lines and two open ends, more computation time is needed for gap analysis than for the open. Computation time is not doubled since the reactions between elements on each branch are the same and need not to be re-computed. The extra time needed is to calculate the reactions between the elements on opposite sides of the gap.

5.1 Formulation

5.1.1 Basis and Testing Functions

First, a traveling wave is incident from $x = -\infty$ to $x = 0$ on strip 1. It is partly reflected back to $x = -\infty$, and partly transmitted over the gap to the other side and travels on strip 2 to $x = +\infty$. In this case, there will be three traveling waves occurring on the strip, namely, incident f^I , reflection f^R , and transmission f^T .

Secondly, the current at the discontinuity is not distributed the same way as on the regular lines. High order modes are produced by the discontinuity. This irregularity will be accounted for by the PWS functions again. It is expected that the high order mode currents will disappear at points distant from the gap, thus the PWS functions will be restricted to the gap region only as shown in Figure 5.1. Also, the number of PWS functions is increased one by one until convergence is reached. (Note that Figure 5.1 is not drawn to scale)

As observed in Chapter 4, the modified Galerkin's procedure for the moment method has been found to be superior to the exact one. Thus in this chapter the modified Galerkin's procedure is used without further comparison. In the case of a gap analysis, the number of unknowns will be $(2 \times N) + 2$, where N is the number of PWS functions on each branch. So there are $(2 \times N)$ PWS plus 2 traveling wave (one reflection and one transmission) unknowns. The modified Galerkin's procedure needs two more testing functions to form a system of linear equations. They are

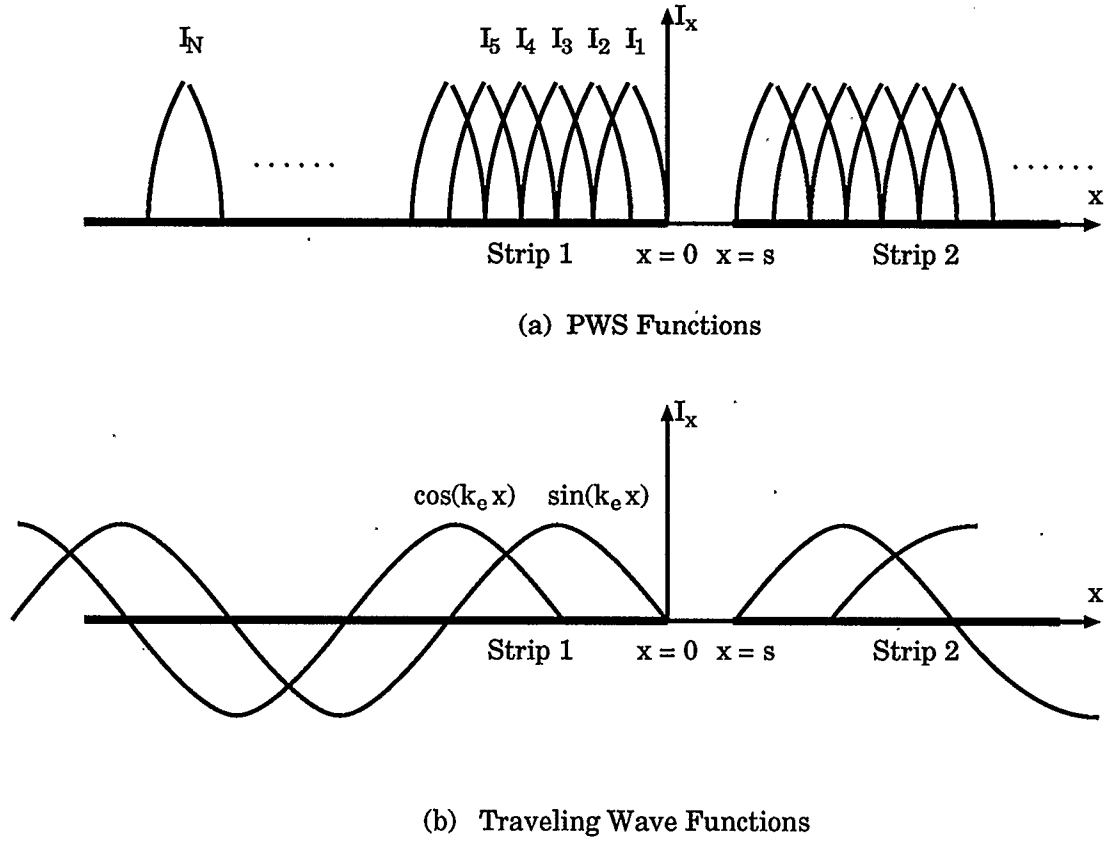


Figure 5.1: Basis functions for the gap circuit.

chosen to be PWS's as well which center at the edges of area covered by the basis PWS functions on each branch, respectively. This arrangement makes the testing area cover the basis PWS function area. The boundary conditions are thus enforced only in the gap region, as the traveling wave self-enforces the boundary condition on the regular lines away from the gap.

5.1.2 Matrix Formulation

Using the modified Galerkin's procedure, the matrix form of the moment method takes the form:

$$\begin{bmatrix} [Z_{pp}^{(N+1) \times N}] & [Z_{pR}^{(N+1) \times 1}] & [Z_{psp}^{(N+1) \times N}] & [Z_{pT}^{(N+1) \times 1}] \\ [Z_{psp}^{(N+1) \times N}] & [Z_{pT}^{(N+1) \times 1}] & [Z_{pp}^{(N+1) \times N}] & [Z_{pR}^{(N+1) \times 1}] \end{bmatrix} \begin{bmatrix} [I_{p1}^{N \times 1}] \\ \Gamma \\ [I_{p2}^{N \times 1}] \\ T \end{bmatrix} = - \begin{bmatrix} [V_{pI}^{(N+1) \times 1}] \\ [V_{psI}^{(N+1) \times 1}] \end{bmatrix} \quad (5.1)$$

One half of the above equation is from the open analysis, which in this equation are the two diagonal blocks of the coefficient matrix, and the top half of the voltage vector. The expressions for these matrix elements have been shown in Chapter 4, and will not be re-written here. It is noted that this formulation takes advantage of the fact that the two branches are of the same width, and therefore the reactions between the PWS's on one branch are the same as those on the other. The same is true for reactions between the PWS's and the traveling waves.

The rest of the equation is introduced for gap analysis. The remaining blocks of the coefficient matrix are the reactions among the PWS's and the traveling waves across the gap; the bottom half of the voltage vector are the reactions between the testing PWS functions on the output branch and the incident traveling wave. The matrix elements that are first introduced in this chapter are as follows (note that the

PWS's are symmetrically numbered from the gap):

$$Z_{psp}^{mn} = \int_{-\infty}^{+\infty} \int_{-\infty}^{+\infty} \tilde{G}_{xx}(\lambda_x, \lambda_y) \tilde{F}_y^2(\lambda_y) \tilde{P}_x^2(\lambda_x) \cos[(md + nd + s)\lambda_x] d\lambda_x d\lambda_y$$

$$Z_{pT}^m = \int_{-\infty}^{+\infty} \int_{-\infty}^{+\infty} \tilde{G}_{xx}(\lambda_x, \lambda_y) \tilde{F}_y^2(\lambda_y) \tilde{P}_x(\lambda_x) \tilde{T}_x(\lambda_x) e^{-(md+s)\lambda_x} d\lambda_x d\lambda_y$$

and

$$V_{psI}^m = \int_{-\infty}^{+\infty} \int_{-\infty}^{+\infty} \tilde{G}_{xx}(\lambda_x, \lambda_y) \tilde{F}_y^2(\lambda_y) \tilde{P}_x(\lambda_x) \tilde{V}_x(\lambda_x) e^{-(md+s)\lambda_x} d\lambda_x d\lambda_y$$

where again

$$\tilde{T}_x(\lambda_x) = (e^{\frac{-j\pi\lambda_x}{2k_e}} + j) \int_{-\infty}^0 \sin(k_e x) e^{-jk_e x} dx,$$

and

$$\int_{-\infty}^0 \sin(k_e x) e^{-jk_e x} dx = \frac{k_e}{\lambda_x^2 - k_e^2} + \frac{j}{2} [\delta(\lambda_x + k_e) - \delta(\lambda_x - k_e)].$$

The numerical procedure to obtain the matrix element values is the same as in Chapter 4, where a 2-D numerical integration is performed. Making careful observations of the properties of the matrices can save a lot of computer time. The reactions between PWS's in diagonal blocks $[Z_{pp}^{(N+1) \times N}]$ are Toeplitz, as pointed out in Chapter 4. Only the first row needs to be calculated. The cross-gap reactions $[Z_{psp}^{(N+1) \times N}]$ have a similar symmetry. Elements in this sub-matrix have the same value if they

are on a same line that is parallel to the cross diagonal line. So if the main diagonal and the next parallel sub-diagonal elements are known, the rest of the matrix can be determined, using the expression

$$Z_{i,j} = \begin{cases} Z_{(i+j)/2,(i+j)/2} & \text{if } (i+j) \text{ is even} \\ Z_{(i+j-1)/2,(i+j+1)/2} & \text{if } (i+j) \text{ is odd} \end{cases}$$

5.2 Results

5.2.1 Convergence Test

It is important to apply a convergence test for all numerical processes. In a manner similar to the microstrip open analysis, the gap analysis uses the step-up procedure to test for convergence. The number of the PWS basis functions on each side of the gap increases one by one from zero until convergence is reached.

In the previous chapters, the transverse distribution of the longitudinal current was chosen to be Maxwellian. This is based on the infinite line analysis. The uniform transverse distribution is easy to handle by it is not the reflection of the physical distribution [69]. The multiterm Maxwellian-cosine distributions are better because they reflect the static nature of the transverse distribution of the current. The transverse charge distribution is like in the static field case, where most charges are pushed to the edges of the strip by their electric field. The choice of the basis functions is in reality a trade-off between computer time and accuracy. It is found

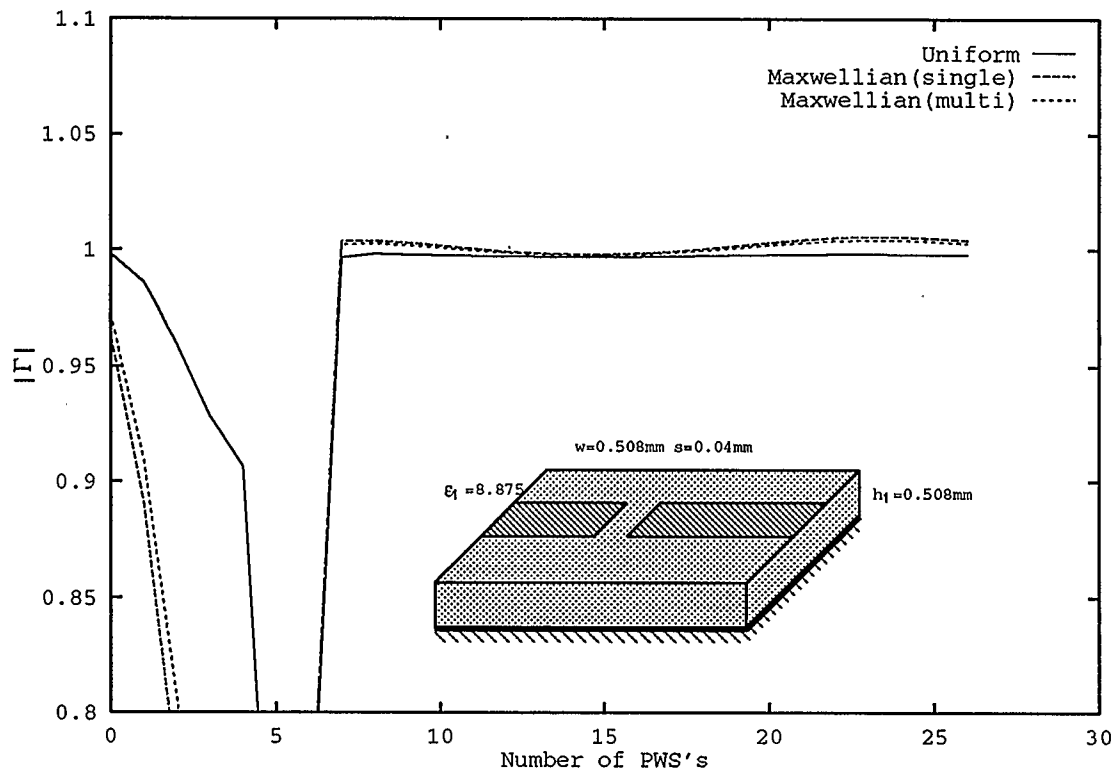


Figure 5.2: Comparisons of the three different transverse distributions ($|\Gamma|$) (freq = 5GHz, $W = .508\text{mm}$, $s = .04\text{mm}$, $h = .508\text{mm}$, $\epsilon_r = 8.875$).

that the uniform distribution is not in good agreement with the measurement, but the Maxwellian choice in most cases can faithfully give the correct answer. The question is, will this distribution still be good enough when applied to the 1-D discontinuity analysis? It is found to be true after the convergence investigation. As an example, the results from using three different transverse distributions are shown in Figure 5.2 through 5.5. The frequency is 5GHz. The gap distance is 0.04 mm, and the board

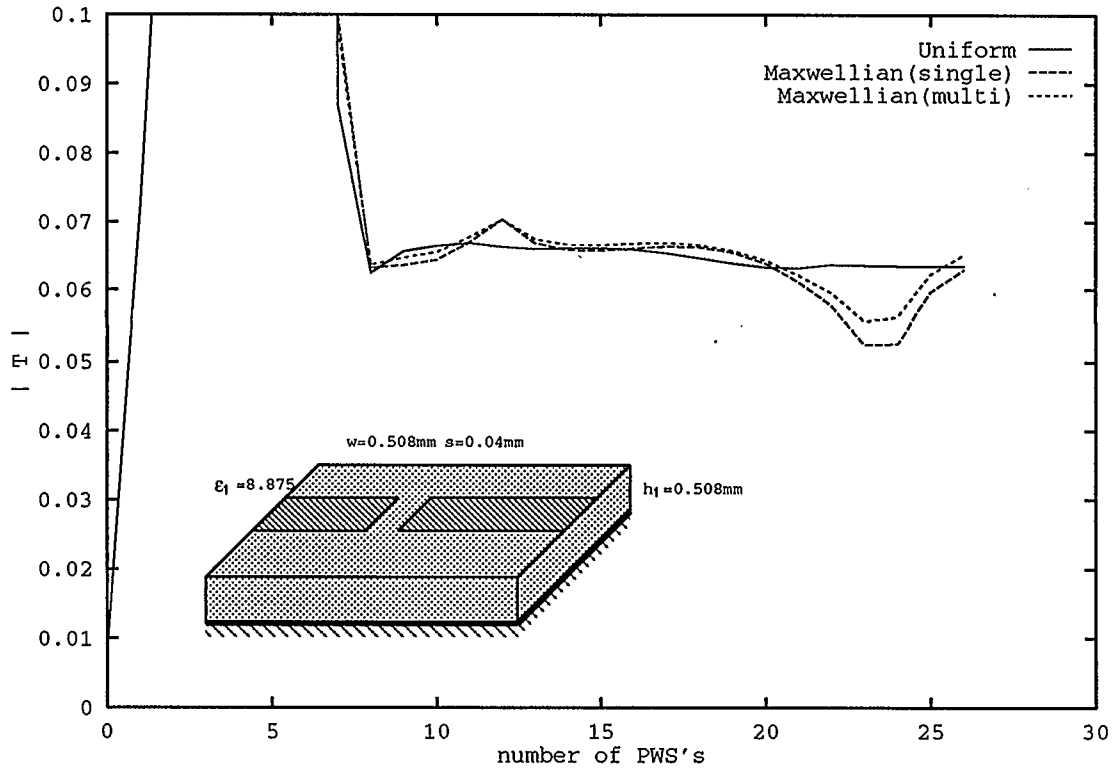


Figure 5.3: Comparisons of the three different transverse distributions ($|T|$) (freq = 5GHz, $W = .508\text{mm}$, $s = .04\text{mm}$, $h = .508\text{mm}$, $\epsilon_r = 8.875$).

parameters are shown in the figures.

It is noted from these figures that uniform distribution gives the best convergence (the least oscillatory curve), as far as results stability is concerned. However, care must be taken not to be fooled by this convergence, because this convergence is obtained based on a loose assumption — the uniform distribution (see Chapter 3). The other two distributions, single term and multiple term Maxwellian, agree with

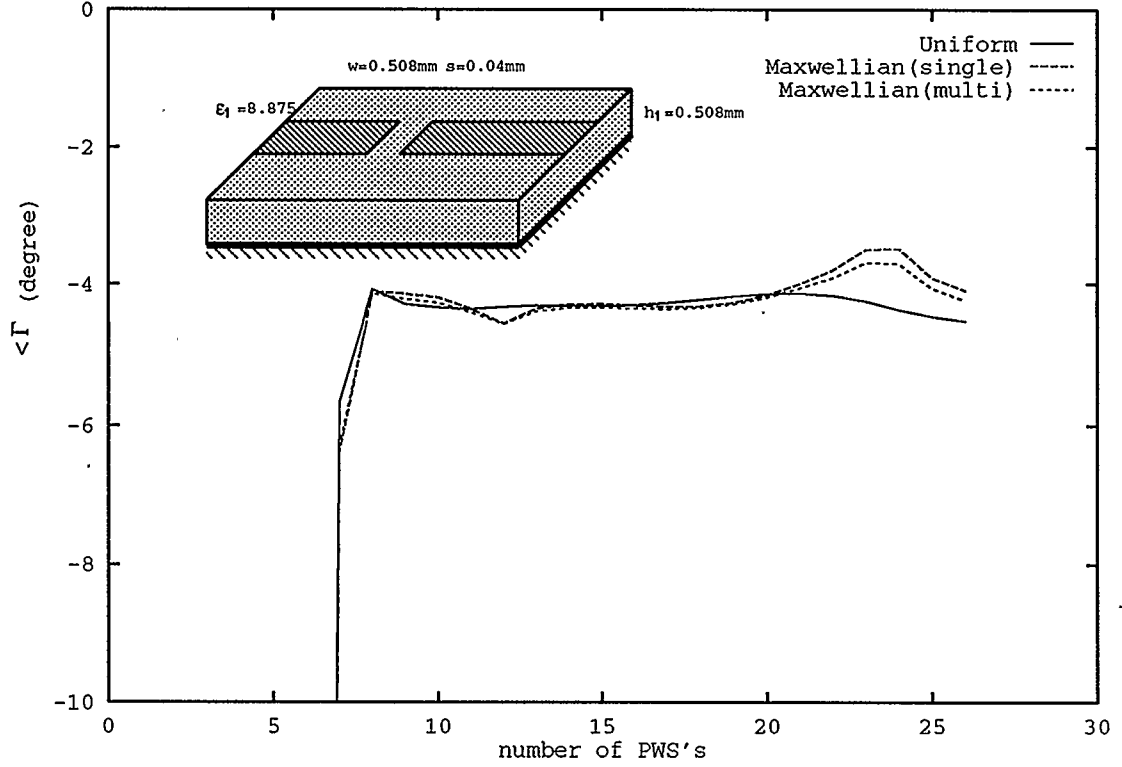


Figure 5.4: Comparisons of the three different transverse distributions ($\langle \Gamma \rangle$) (freq = 5GHz, $W = .508\text{mm}$, $s = .04\text{mm}$, $h = .508\text{mm}$, $\epsilon_r = 8.875$).

each other very well. They follow the same oscillating trend. Detailed plots show that the multiple term oscillates less in magnitude than the single term, indicating the multiple term is more accurate. On the whole, the Maxwellian is still a valid choice for the transverse distribution.

Using a single Maxwellian distribution and 26 PWS basis functions on each side of the gap, the accuracy of the magnitude of the reflection coefficient is better than

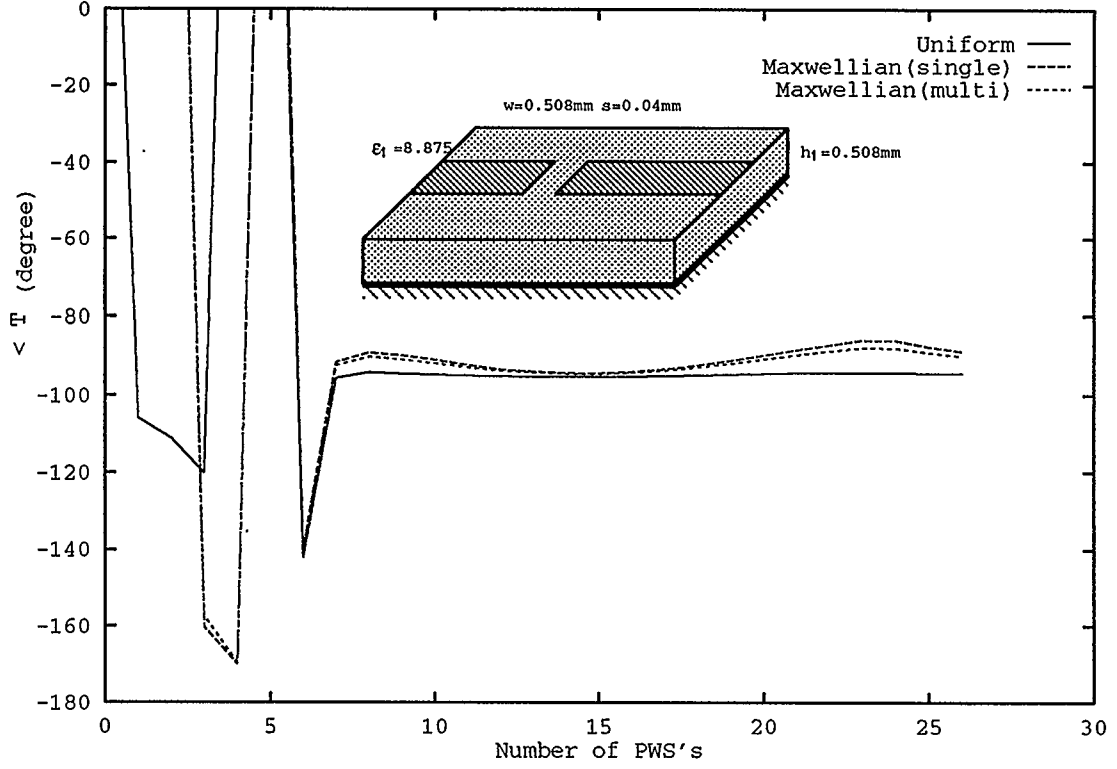


Figure 5.5: Comparisons of the three different transverse distributions ($\angle T$) (freq = 5GHz, $W = .508\text{mm}$, $s = .04\text{mm}$, $h = .508\text{mm}$, $\epsilon_r = 8.875$).

1% (Figure 5.2), the phase variation is less than 1° (Figure 5.4). For the transmission parameter S_{21} or T , the relative convergence is not as good as for the reflection. Its magnitude varies between 0.05 to 0.06 (Figure 5.3). This large relative variation is due to the fact that the magnitude of T is so small that it has less effect than the reflection coefficient in the convergence test process. In cases like this, where there is a nearly-zero parameter with some large ones, care must be taken to get

even convergence. One way of getting less varying T is to tighten the convergence criteria, but it will inevitably prolong the numerical process. A better way is to pre-magnify T by multiplying it with a large weighting factor to make T the same amplitude as Γ . When convergence is reached, both Γ and T will have the same relative variances.

Also noted in these figures, the gap changes the transmission properties significantly no matter how small the gap is. Even if the gap size is practically zero, there is still a discontinuity in current flow. A high frequency wave can be coupled over the gap and transmitted to the other end. The lower the frequency, the higher the reflection that is expected. This is shown in the following discussions.

5.2.2 S-parameters as a Function of Frequency

Figures 5.6 through 5.9 show the response of a microstrip transmission line gap as a function of frequency, together with our measured data. The gap size is chosen to be 2.0 mm. The frequency is spanned from 2GHz through 20GHz.

For the purpose of comparison, the calculated reflection coefficient for a pure open on the same board and with the same line width is also plotted along with the calculated and the measured gap response (Figure 5.6 and 5.7). Also plotted are the results obtained with Touchstone[102], which uses a gap model developed by Hammerstad [104].

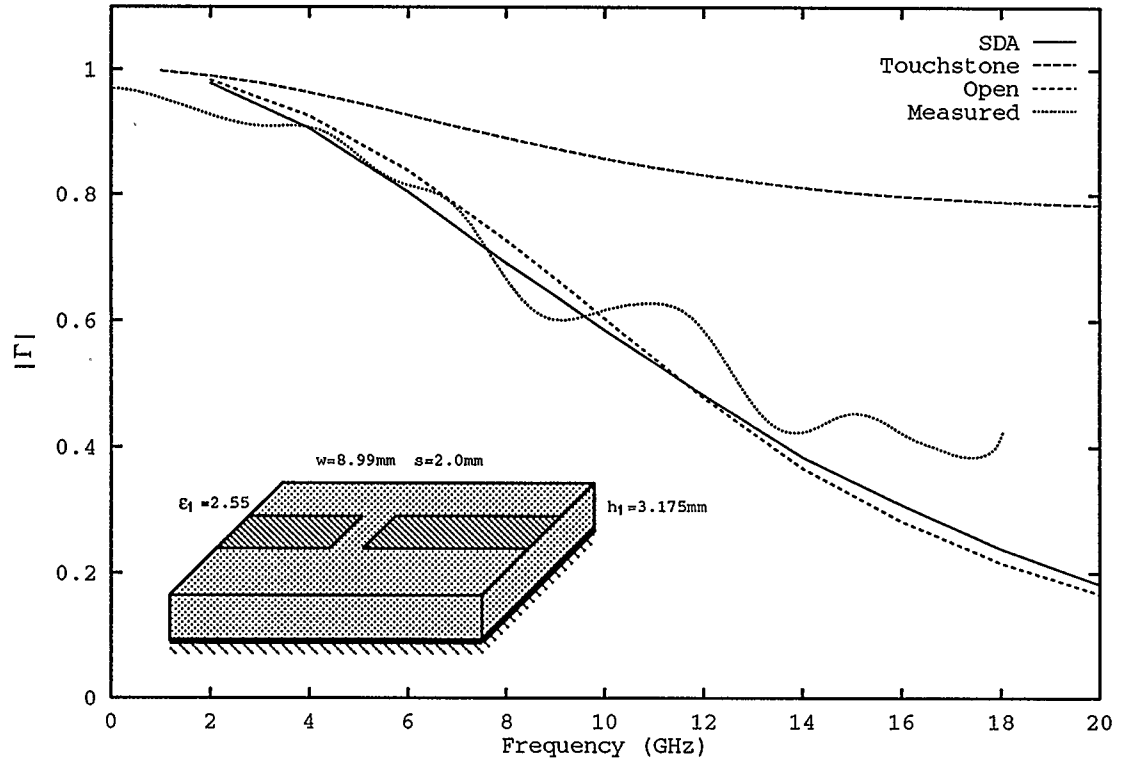


Figure 5.6: Reflection coefficient $|\Gamma|$ as a function of frequency for a gap ($W = 8.99\text{mm}$, $s = 2.0\text{mm}$, $h = 3.175\text{mm}$, $\epsilon_r = 2.55$).

For the magnitude of the reflection coefficient (Figure 5.6), the results from the open and gap analyses are very close to each other. The small discrepancies can be due to the presence and absence of the output branch. The SDA method results are shown to be very close to the measurement. It is noted that Touchstone predicts a stronger reflection than the SDA algorithm. This can be due to the fact that the model used in Touchstone is not a full-wave model and can not fully account for all

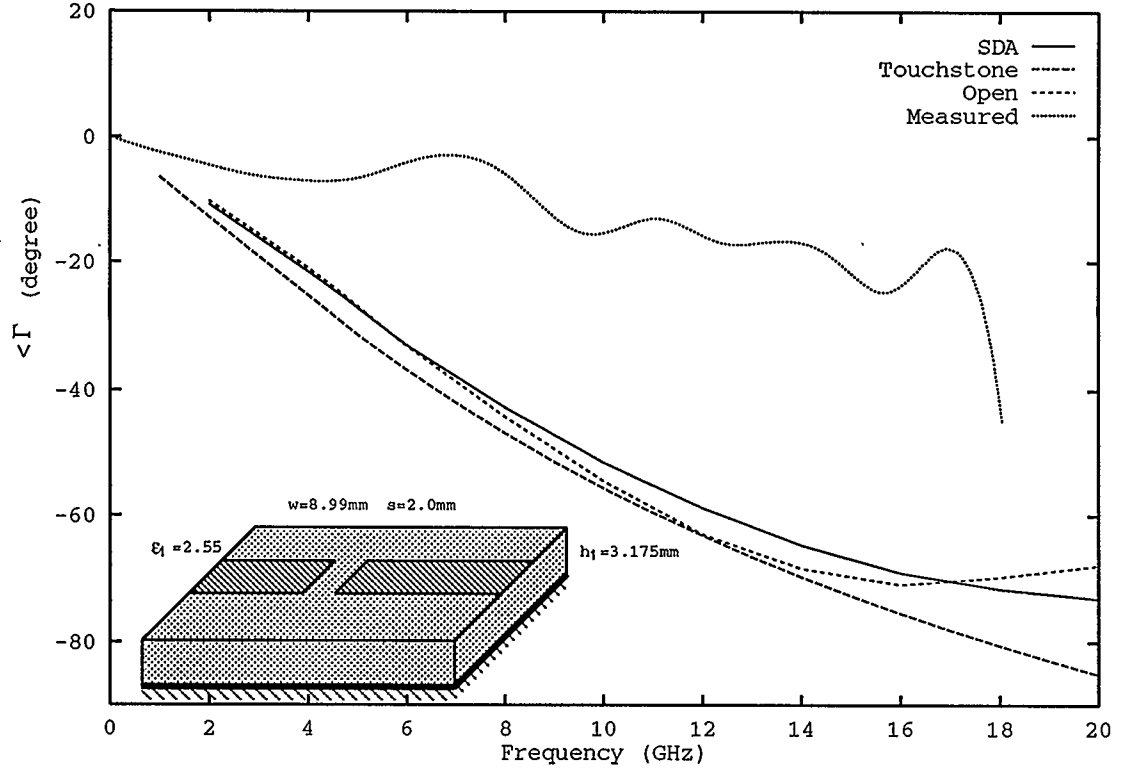


Figure 5.7: Reflection coefficient $\angle \Gamma$ as a function of frequency for a gap ($W = 8.99\text{mm}$, $s = 2.0\text{mm}$, $h = 3.175\text{mm}$, $\epsilon_r = 2.55$).

the EM wave behaviors. For instance, it is to be expected that any discontinuities will radiate power into the substrate and free-space, which results in lossy circuit model. However, Touchstone does not give any prediction of the power loss into free space and the substrate — its model is lossless. The difference as regards the power loss will be discussed and shown later.

The magnitude of the transmission $|T|$ (Figure 5.8) shows good agreement be-

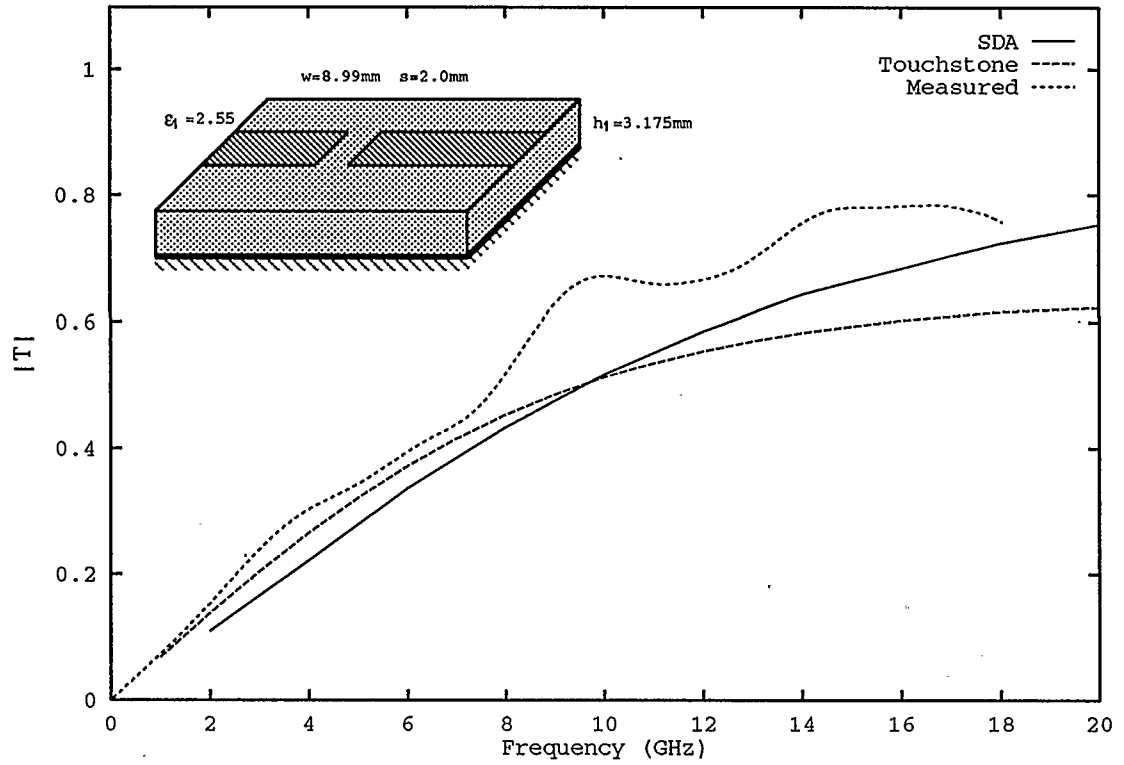


Figure 5.8: Transmission coefficient $|T|$ as a function of frequency for a gap ($W = 8.99\text{mm}$, $s = 2.0\text{mm}$, $h = 3.175\text{mm}$, $\epsilon_r = 2.55$).

tween this theory (SDA) and Touchstone, except that at very high frequencies (relative to the dimensions of the circuit) the discrepancy becomes significant (0.75/0.62 at 20GHz for this circuit). It is noted that the measured data closely follows the SDA simulation up to 18GHz, which is an indication that the SDA method works well for the gap analysis. The oscillation in the measured data can be due to the finite size of the substrate board, which can cause surface waves to be reflected back and

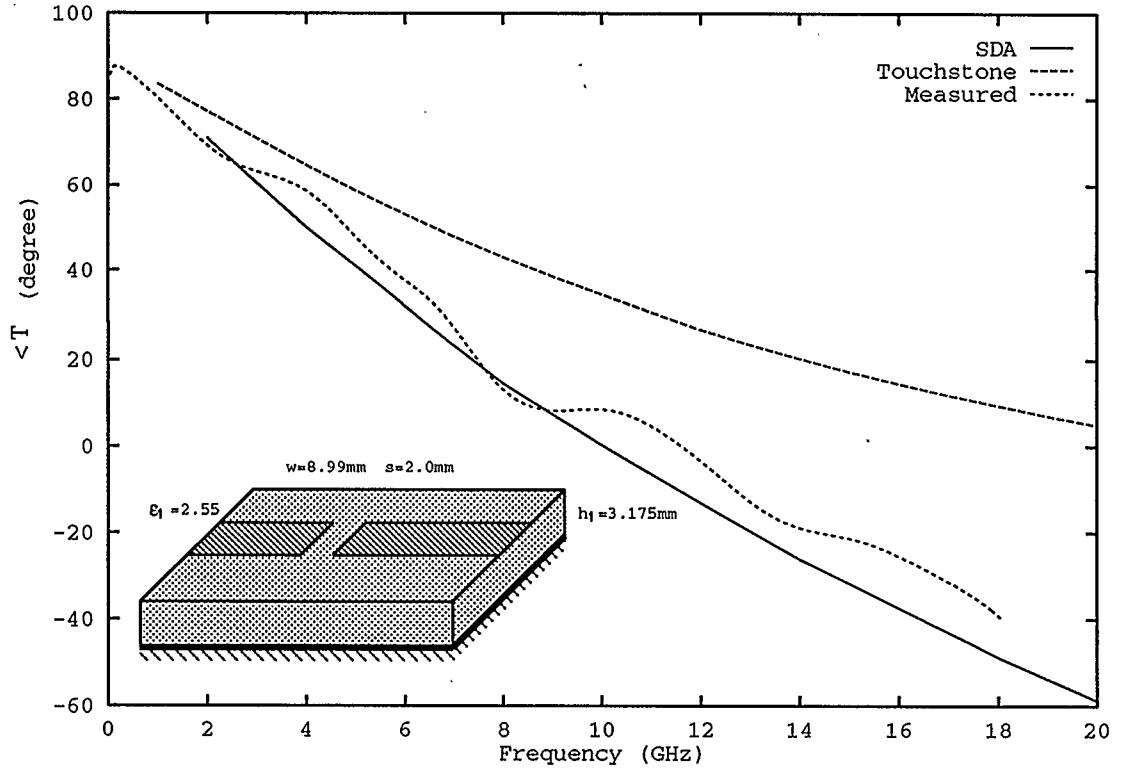


Figure 5.9: Transmission coefficient $\angle T$ as a function of frequency for a gap ($W = 8.99\text{mm}$, $s = 2.0\text{mm}$, $h = 3.175\text{mm}$, $\epsilon_r = 2.55$).

forth. These reflections can be either constructive or destructive. The measurement method will be discussed later.

As far as the phase is concerned, the spectral domain method and Touchstone give very close phase predictions for reflection coefficient. The reflection phases obtained with/without the output branch (gap/open) are close to each other (Figure 5.7). The measured reflection phase, however, is in poor agreement with the simulation.

This discrepancy is caused by the poor fabrication of the circuit. The measurement accuracy of the reflection depends on how much the two connector-microstrip transitions are similar to each other. See the following section for details about the measurement method.

For the transmission phase, a big discrepancy was observed between SDA and Touchstone predictions (Figure 5.9). The agreement between the measurement and SDA simulation, however, is very good. This further that the spectral domain method is a reliable analysis technique.

Figure 5.10 shows the relative power loss of the gap which is defined as

$$P_{loss} = 1 - |S_{11}|^2 - |S_{21}|^2$$

The SDA method predicts that there is power loss into the substrate and free space. the Touchstone model, on the other hand, fails to predict this loss. The SDA also predicts a non-monotonic change of the power loss with frequency. The power loss does not increase after 15GHz. Instead, it starts to decrease. An interpretation of this behavior is that as frequency gets higher, more and more high modes are created, which are launched into the substrate as surface waves. The surface waves are picked up by the strip on the other side of the gap. Therefore the total coupled power is increased, and the total power loss into the substrate and free-space is decreased.

It is notable that the discrepancies between the SDA method and the Touchstone model are not consistent. The magnitude of the transmission agrees very well, but

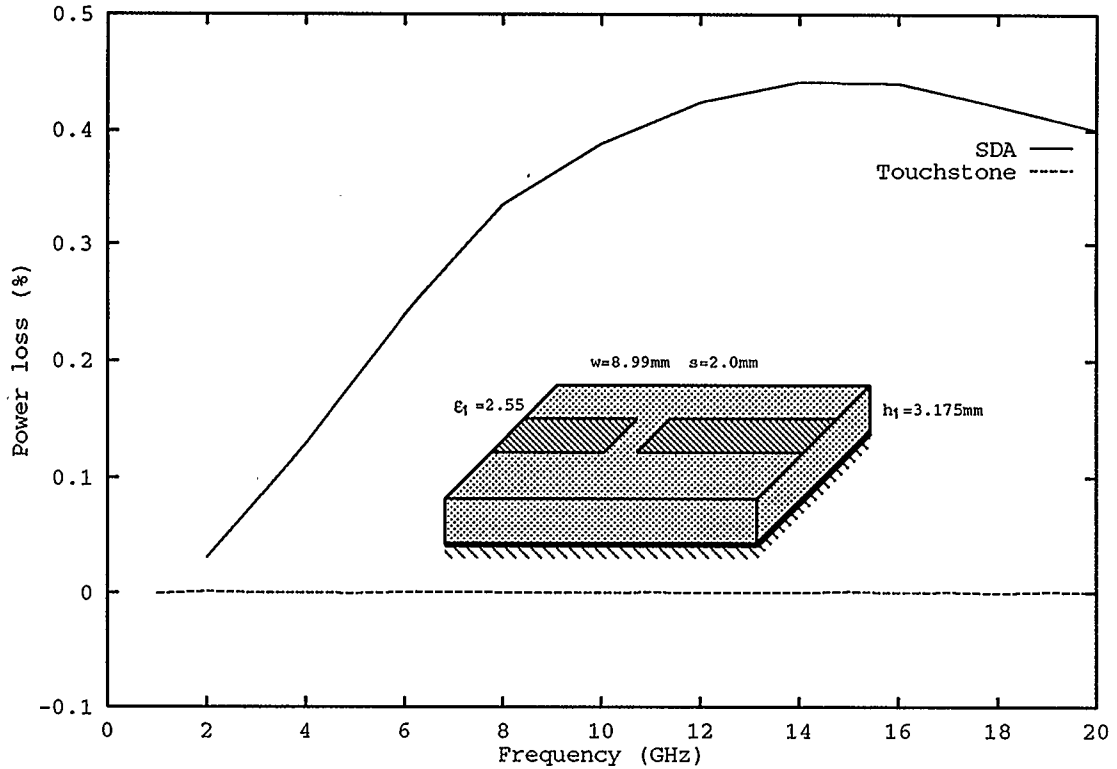


Figure 5.10: Power loss as a function of frequency for a gap ($W = 8.99\text{mm}$, $s = 2.0\text{mm}$, $h = 3.175\text{mm}$, $\epsilon_r = 2.55$).

that of the reflection does not. The reverse is true for the phase: the phase of the reflection agrees well, but that of the transmission has poor agreement. It is conceivable that the Touchstone models only emphasizes certain aspect of the problem (recall that, in the open circuit analysis, the Touchstone model failed to show any change of magnitude of the reflection with frequency but the phase prediction was very good). It is understandable that in the early days the microwave engineers were

mainly concerned with the phase of the reflection coefficient for an open circuit, and the power coupled across a gap for a gap circuit. Touchstone can only go so far to accommodate these needs. On the other hand, the spectral domain method is a full wave analysis, which uses rigorous formulation to cover all the aspects of the analysis. The power loss was accounted for as surface wave into the substrate and as space wave into free space. All the EM wave coupling mechanisms are inherently included in the spectral domain analysis. It is thus believed that the data obtained with the spectral domain method are more reliable.

5.2.3 S-parameters as a Function of Gap Distance

The behavior of the S-parameters is also analyzed as the size of the gap changes by varying the gap size from 0mm to 10mm. The transmission line width and the substrate height are the same as the circuit shown in Figure 5.6. The frequency was chosen to be 10GHz. The results are shown in Figure 5.11 through 5.14. Again, the results from Touchstone are plotted along with the measurement.

It is noted that, as far as the SDA analysis is concerned, zero gap size is not the same as no gap in an infinite transmission line. Zero gap size is an infinitely small gap, whereas no gap is an unbroken transmission line. For zero size gap, the current is not continuous, and the traveling wave on the other branch is coupled electromagnetically over the gap. Therefore, it is not a full transmission. The reflection is also non-zero.

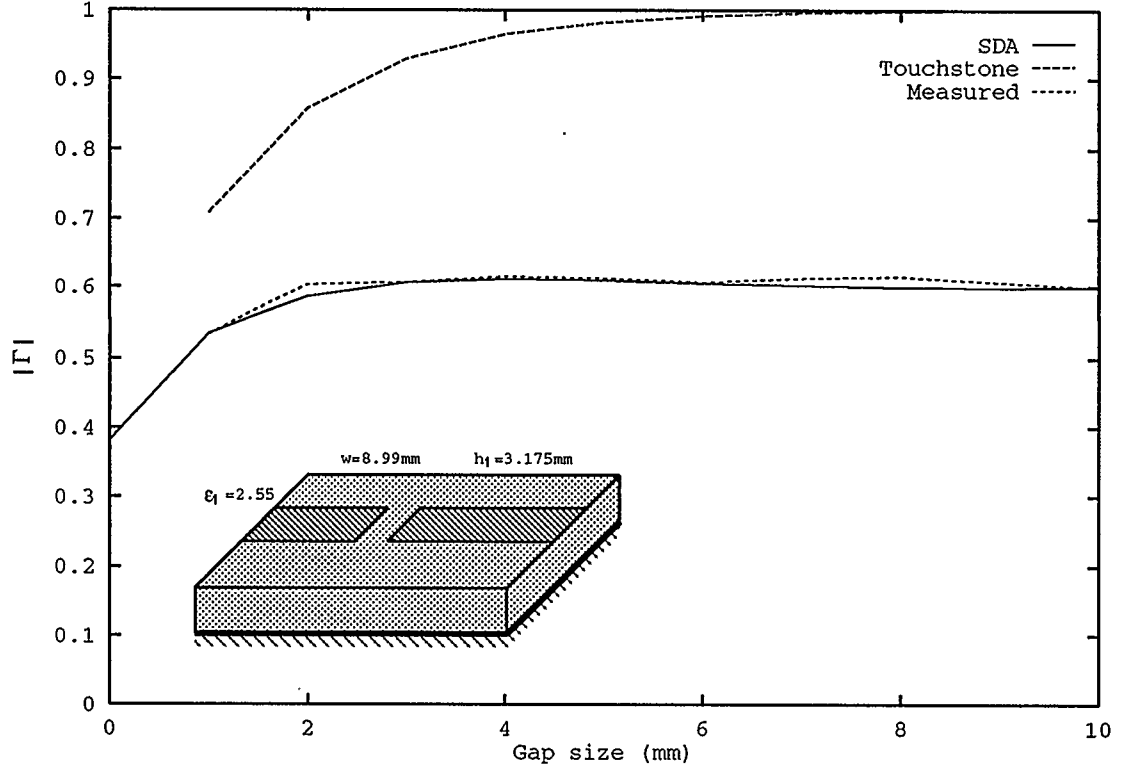


Figure 5.11: Reflection coefficient $|\Gamma|$ as a function of the gap size (freq = 10GHz, $W = 8.99\text{mm}$, $h = 3.175\text{mm}$, $\epsilon_r = 2.55$).

As the gap size increases, the reflection S-parameters of the gap tend to become constant values, which are found to be the values of the open circuit of the same line. This is a good way of verifying the algorithm, because the input branch virtually faces an open if the gap size becomes big enough.

Good agreements between the measurement and the analysis have been observed for $|\Gamma|$, $|T|$, and $\angle T$, except for $\angle \Gamma$, where big discrepancy is observed. Again, it is

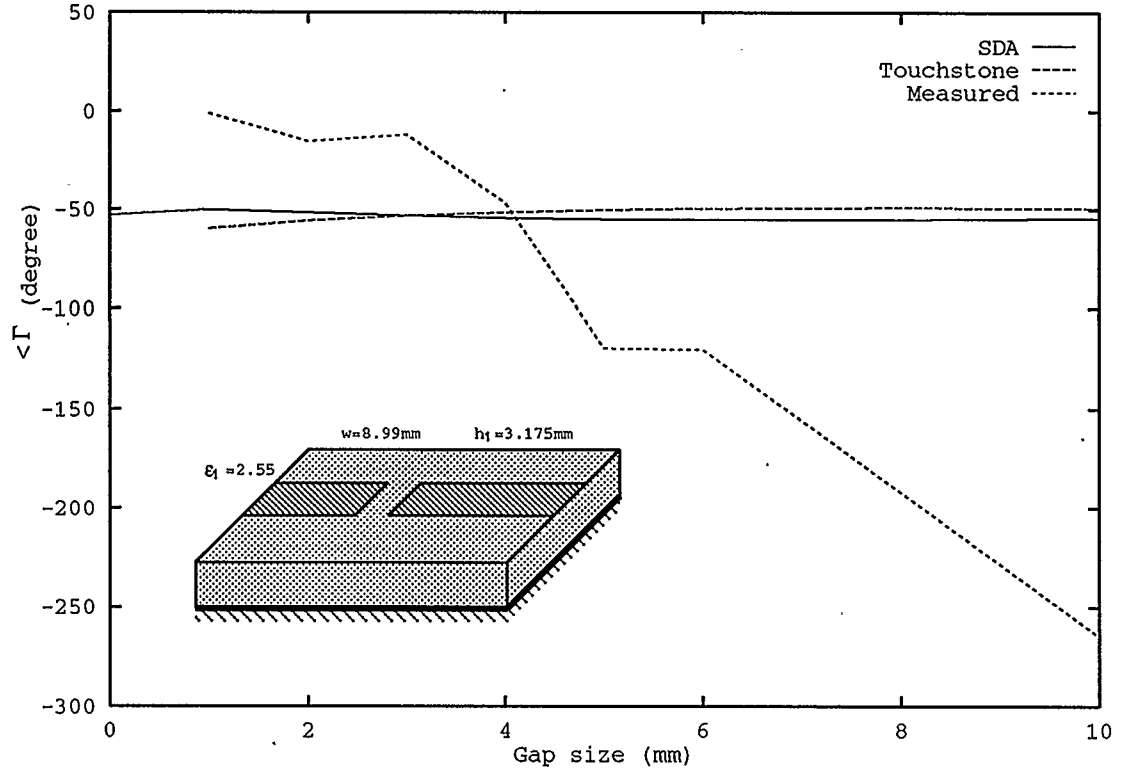


Figure 5.12: Reflection coefficient $\angle \Gamma$ as a function of the gap size (freq = 10GHz, $W = 8.99\text{mm}$, $h = 3.175\text{mm}$, $\epsilon_r = 2.55$).

probably due to the assumption in the measurement that the two transitions are the same. See the measurement section for further discussions.

The power loss of the gap is also shown as a function of its size in Figure 5.15. As is shown again, the Touchstone model failed to predict any power loss by the gap discontinuity, while the SDA gives a changing power loss. As expected, the power loss increases monotonically with the size of the gap. This is due to the fact

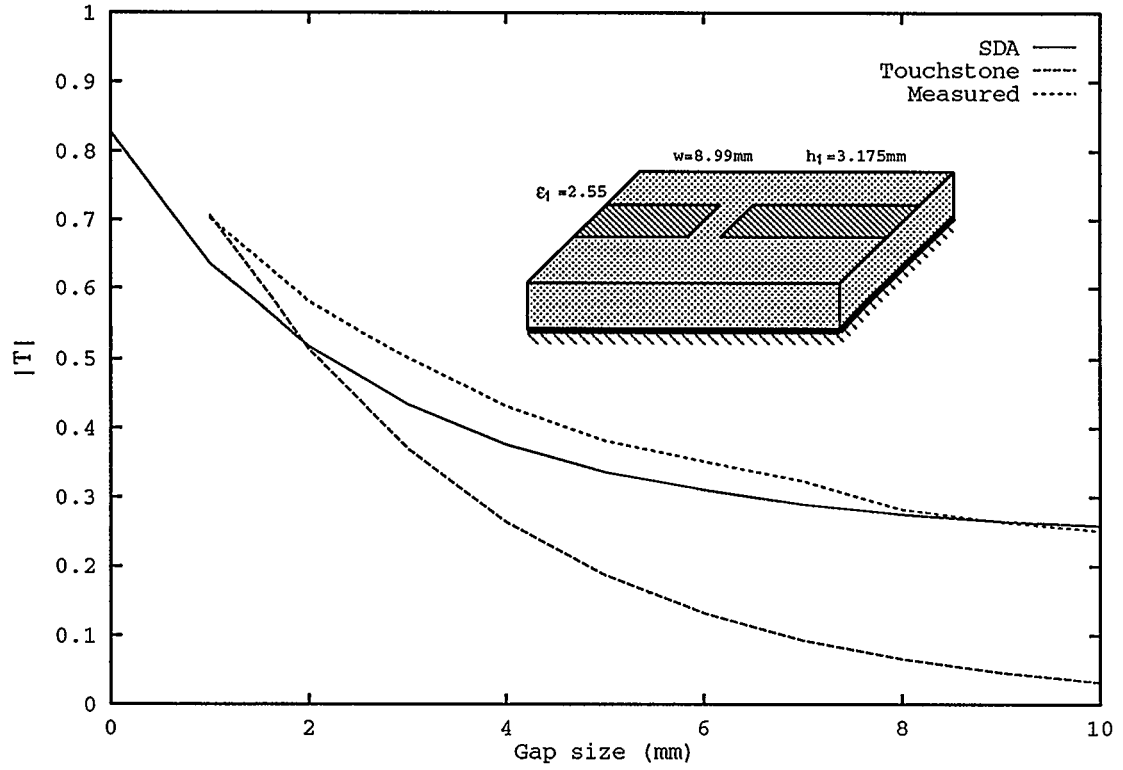


Figure 5.13: Transmission coefficient $|T|$ as a function of the gap size (freq = 10GHz, $W = 8.99\text{mm}$, $h = 3.175\text{mm}$, $\epsilon_r = 2.55$).

that as the gap becomes bigger, the reflection tends to be constant (open), but the power picked up by the coupled branch becomes smaller and smaller. Accordingly the fractional power loss is going to be larger and larger. At about 5GHz, the total power that is lost into the substrate and free space is about half of the total incident power.

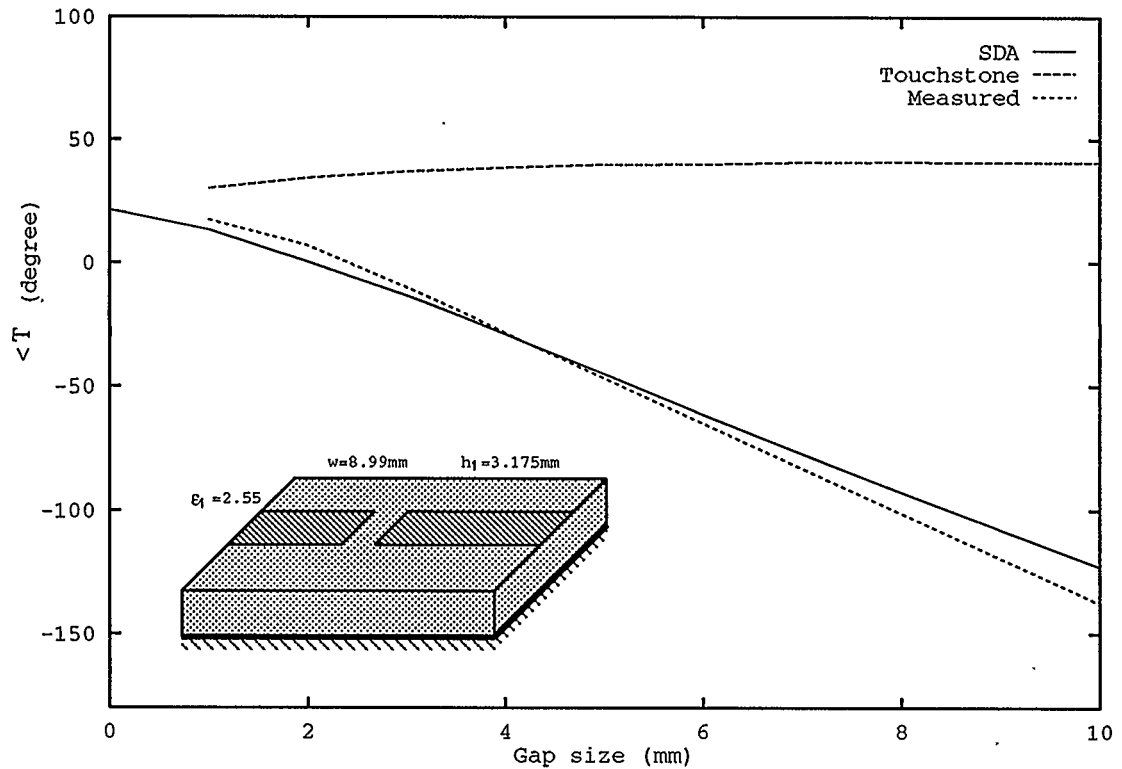


Figure 5.14: Transmission coefficient $\angle T$ as a function of the gap size (freq = 10GHz, $W = 8.99\text{mm}$, $h = 3.175\text{mm}$, $\epsilon_r = 2.55$).

5.3 Measurement

Full discussions on measurement can be found in Chapter 9. Since the agreement between the measurement and the analysis is not very good for $\angle T$ in this chapter, it is necessary to have a brief discussion here.

The measurement method here uses an automatic network analyzer with time-

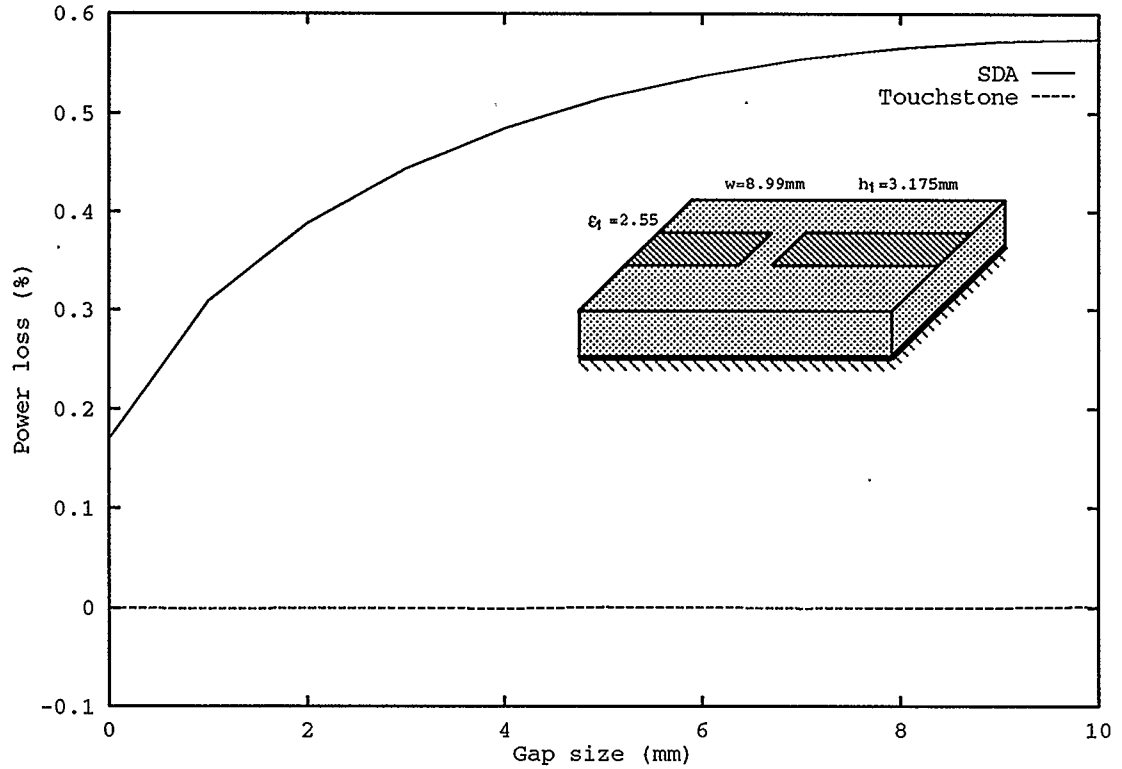


Figure 5.15: Power loss as a function of the gap size (freq = 10GHz, $W = 8.99\text{mm}$, $h = 3.175\text{mm}$, $\epsilon_r = 2.55$).

domain features. The time-domain feature is used to get one-pass travel of the signal, which greatly simplifies the processing of the measured data.

The measurement starts with a straight through line. A gap is later formed on the same board by cutting away a segment of the microstrip. The size of the gap can be increased gradually to get the measured data as a function of gap size. As can be seen, this method is destructive. The measurement can not be repeated, because

the original circuit will be destroyed in the measurement. Therefore, it is important to take each step carefully.

The straight microstrip line consists of two connector-to-strip transitions and a piece of microstrip, configured as connector1-taper1-strip-taper2-connector2. A tapered line is needed to form a smooth transition between the coaxial connector and the strip. The connector and the tapered line form the transition. Efforts have been made to fabricate the two transitions as similar as possible. The measurement procedure is described as follows:

1. With the network analyzer properly calibrated, the time-domain feature is used (time-domain gate is turned on) to measure a one-pass travel of the signal through the straight line. This measured quantity is S_{21}^{thru} which is expressed as

$$S_{21}^{thru} = S_{21}^{t_1} e^{-\gamma L} S_{21}^{t_2} \quad (5.2)$$

where γ is the propagation constant of the microstrip transmission line; t_1 and t_2 stand for transition 1 and transition 2, respectively; and L is the length of the microstrip line.

2. From the middle of the strip towards port 2, cut away a part of the strip to form a gap of size Δ . Now the configuration of the circuit is transition1-strip1-gap-strip2-transition2. With time-domain gate still on, measure S_{11}^m and S_{21}^m ,

which gives

$$S_{11}^m = (S_{21}^{t_1})^2 e^{-2\gamma L_1} S_{11}^{gap} \quad (5.3)$$

and

$$S_{21}^m = S_{21}^{t_1} e^{-\gamma L_1} S_{21}^{gap} e^{-\gamma L_2} S_{21}^{t_2} \quad (5.4)$$

Note that

$$2 \times L_1 = L$$

and

$$L_1 + L_2 = L - \Delta$$

3. Using the information obtained from Equation 5.2, the S-parameters of the gap can be obtained as

$$S_{11}^{gap} = \frac{S_{11}^m}{S_{21}^{thru}} \frac{S_{21}^{t_2}}{S_{21}^{t_1}} \quad (5.5)$$

and

$$S_{21}^{gap} = \frac{S_{21}^m}{S_{21}^{thru}} e^{-\gamma \Delta} \quad (5.6)$$

In the procedure shown above, γ in Equation 5.6 can be obtained either by multiline measurement (see Chapter 9), or by using numerical analysis (SDA). The

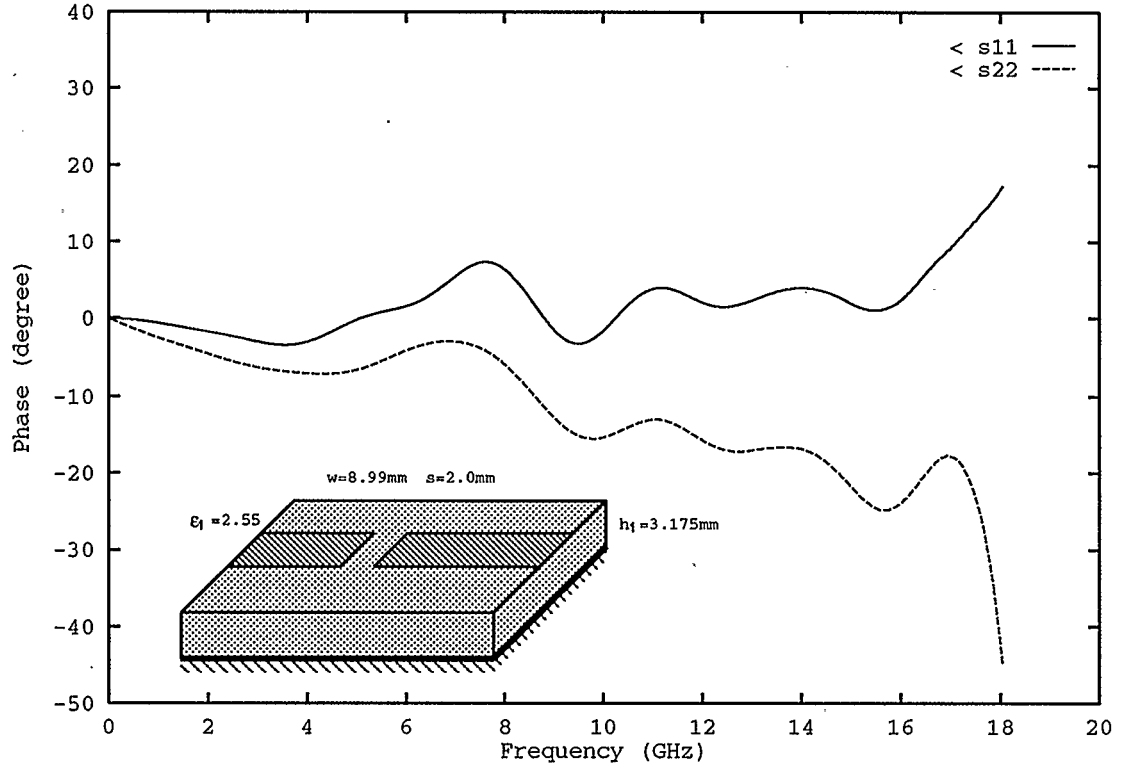


Figure 5.16: The reflection phases from port 1 and port 2 ($W = 8.99\text{mm}$, $s = 2.0\text{mm}$, $h = 3.175\text{mm}$, $\epsilon_r = 2.55$).

determination of S_{11}^{gap} in Equation 5.5, however, depends heavily on the similarity of the two transitions. If S_{21}^{t1} and S_{21}^{t2} are not equal to each other, error results. It is expected that their magnitudes are very close, but the phases can differ significantly, because at high frequencies, small length change can result in large phase change. That is why the agreement between the analysis and measurement is very good for $|\Gamma|$, but very poor for $\angle\Gamma$. This argument can be supported by the difference

between the two reflections looking into the circuit from port 1 and port 2, as shown in Figure 5.16, where the phase of port 2 has been compensated as if it faced the same length of the strip as the port 1.

Also noted in the measurement is in effect due to the finite size of the board, there is a cavity-like effect in the frequency response of the circuit parameters. This effect demonstrates an oscillation as the S-parameters change with frequency. This effect can be removed to some extent by smoothing the results.

5.4 Discussions

The gap analysis depicts a clear picture of how the electromagnetic wave behaves and reacts with electric current in a stratified medium. Electric current, which can only flow in a conductor, is the source of EM wave. In our case, the current carrying body is the conductor strip embedded in a multilayer structure. The EM wave and the current (conduction current, not displacement current) react to each other in the structure. The laws of the reactions between current and EM waves are Maxwell's equations, which govern how EM waves travel in the media, cross interfaces between layers, and reflect from conductors.

The reaction between the EM wave and the electric current converts one to the other. The Green's function determines how electric current generates an EM wave by giving the EM field generated by an infinitesimal electric current dipole (Hertz

dipole) in a specific multilayer structure. When we have a given electric current distribution (although it maybe an assumed one to start with), the total EM field can be determined by the convolution between the Green's function and the current distribution. The EM field generated by this assumed current distribution exists all over the structure. However, the electric current can only be carried on conductors, while the EM wave has to satisfy certain boundary conditions. These boundary conditions can be viewed as the requirement that the EM wave imposes upon its creator, the electric current on the strip. Hence now the question is what kind of electric current distribution can generate the right EM field in this structure that can meet the boundary condition on the strip?

The approximate solution is obtainable using the moment method. First, make some reasonable assumptions about the current distribution on the strip surface by choosing the right basis functions; then get the expression for the strip surface tangential electric field generated by the assumed current distribution; finally enforce the boundary condition on the strip surface by defining the testing functions that are non-zero only on the strip surface, and letting the inner products between the tangential field and these testing functions be zero.

To get a correct solution, one has to bear in mind that all conductor surfaces will carry induced current due to the influence of the EM wave. The induced current will also radiate to the structure thereby making a contribution to the whole EM field. Equilibrium will be reached when the total radiated field satisfies the boundary

conditions on all the conductor surfaces, i.e. the total tangential electric field be zero on the conductor surface. The current distribution at equilibrium is the unique solution to the problem.

In the microstrip gap circuit, the incident current radiates EM waves into the structure, which in turn induce currents on both input and output strips. The induced current also radiates into the structure, and also causing induced current on the strips. Equilibrium will be reached when the total radiated EM field has a zero tangential electric field on all the strip surfaces. Under this unique equilibrium, both input and output strips will have new current distributions other than the incident current. This determines the reflection and the transmission coefficients of the gap.

Chapter 6

2-D Discontinuity — Corner

Microstrip discontinuities are in various forms. According to their particular configurations, they can be divided into 1-D, 2-D, and 3-D three groups.

1-D discontinuities include opens and gaps, where the microstrip line has a change in only one dimension (in the wave traveling direction), either an abrupt end (open) or an absence of a segment of the strip (gap).

1-D discontinuities have been analyzed in the previous two chapters.

The 2-D group has more members, including the corner, the impedance step, the bend, the Tee, etc, which have changes in at least one lateral dimension. Actually, all arbitrarily shaped planar circuits should be regarded as 2-D. The current flow on the strip surface consequently has two directions, no matter how low the frequency is.

If there is a vertical conductor in the circuit, the discontinuity should be regarded as 3-D, because the introduction of the vertical conductor will cause the current flow on the strip surface to have both x and y directions, in addition to the vertical current flow (in z direction) on the vertical conductor, thus there will be current flow in all

three dimensions.

The 3-D discontinuity analysis will be carried out in Chapter 7 and 8.

In this chapter, the corner will be studied as an example of 2-D discontinuity analyses.

6.1 Theory

6.1.1 Current on the Microstrip Surface

A microstrip corner is shown in Figure 6.1. In this analysis, the input is assumed to be a traveling wave from $x = -\infty$, as in all the other analyses of the circuits with a semi-infinitely long transmission lines. At the corner, the incident wave is reflected and transmitted. The reflection produces a traveling wave back to $x = -\infty$ and the transmission produces a traveling wave to $y = -\infty$. The dielectric substrate is assumed again to be infinitely large, so that no horizontal boundary effects are present. This significantly simplifies the analysis, because the Green's function is derived based on this assumption, and subsequently the reaction between any two PWS functions will depend only on their relative vectorial separation. This assumption is valid for most practical cases, where the board is large compared with both the wavelength and the discontinuity itself. If for some circuits the board is small and the boundary effects have to be considered, in order to make sure the

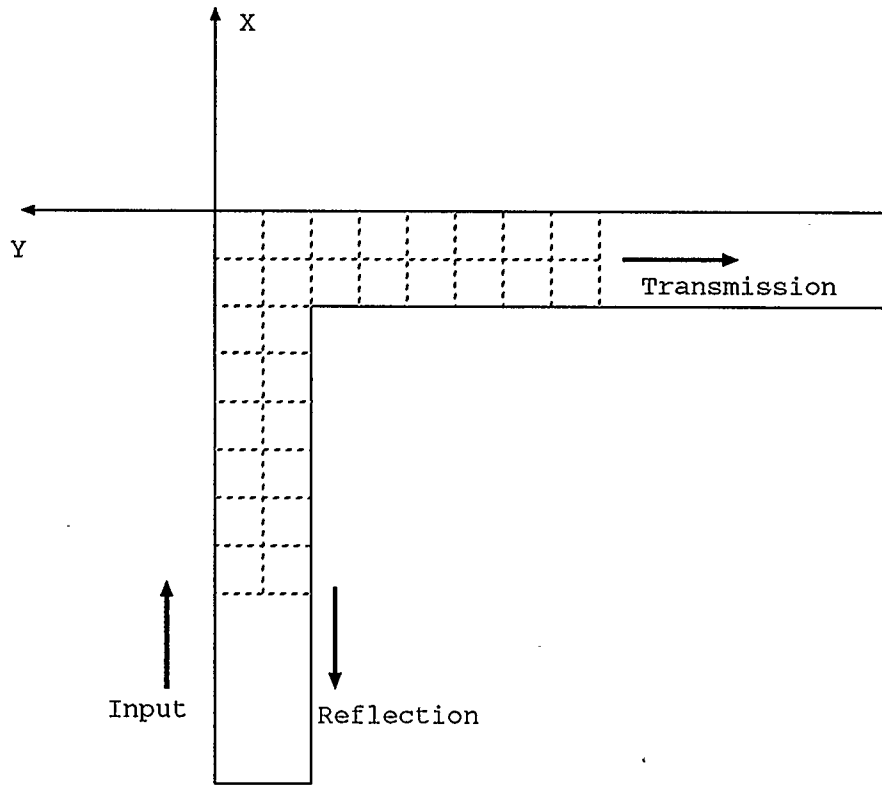


Figure 6.1: A microstrip corner and its PWS function covered area.

circuit work properly, an absorbing material may be applied to the boundary to remove the reflected waves. In this case, the discontinuity will behave as if the board is large.

The analysis in this chapter is similar to [99], except that (1) triangle functions are used as the basis in [99], whereas here PWS functions are used which have been proved to have a better convergence; and (2) multilayer Green's functions instead of single layer ones are employed, which can be used to analyze corners in multilayered

dielectric structures.

Unlike in the 1-D analyses, where the input and the reflected traveling waves are represented with functions that stretch over all the semi-infinite line, the traveling waves here are truncated to a finite size, to be an integer number of effective wavelengths. The reason for this truncation will be discussed later.

High order modes are generated by the non-transmission line nature of the corner. This effect is taken care of by the introduction of local current basis functions (using PWS functions). These functions are used to reconstruct the complicated current distribution at the corner and on the two transmission lines close to the corner. The magnitude of the high order modes decrease as they move away from the corner. The convergence is tested again as the area covered by the PWS functions expands .

The traveling waves are similar to those used in the microstrip open and gap analyses, which is staggered sine and cosine waves, except there is coordinate shift and rotation when representing the transmitted traveling wave (in y direction). The traveling wave functions have been truncated into finite size. The incident and the reflected traveling waves terminate at the far edge of the output strip ($x = 0$), overlapping with the output strip. Because the transverse edge condition of the strips (pole at the edge) at the corner area is not met, a uniform transverse distribution of the traveling wave is assumed. If, on the other hand, the Maxwellian distribution is used, one will have to use much smaller PWS functions to cancel the effect of the traveling wave's non-physical behavior (infinite amplitude) in the corner area. This

will take considerably longer computer time.

The transmission waves are defined to start at the far edge of the corner area ($y = 0$), which means that the traveling waves on the two branches overlap at the corner region. The PWS functions, still defined as one unit length (i.e. one segment) wide, and two units long, have both x and y directions. To account for the high order modes at the discontinuity, current in the transverse direction is expected to appear on the input and the output branches regardless of the operation frequency.

Since some transverse PWS functions are assumed to appear on the input and output strips, the transmission line has to be divided into at least two parts in the transverse direction. This is because a PWS function is defined to be two segments long. The number of transverse segments is determined automatically in the numerical process by checking on the electrical length of the width of the two strips.

6.1.2 Numerical Considerations

As shown in Figure 6.1, the area affected by high order modes is divided into small rectangles (cells). Depending on the strip width, the input strip is transversely divided into n_1 parts, and the output strip into n_2 parts. This local high order mode area is extended on each strip n_{ext} of the PWS functions. The number n_{ext} is to be increased one by one until convergence is reached.

It is noted that the reactions between the traveling waves and the testing functions

that are on different branches of the corner do not decrease rapidly as the distances separating them increase. This is due to the unphysical assumption that the lines are infinitely long. The field due to the contribution from the current on an infinitely long transmission line can be indefinite, if the propagation of the wave on the strip is slower than the speed of the wave in the horizontal direction on the same level without the strip. For example, a suspended strip with an infinitely thick dielectric superstrate has a propagation speed that lies between the wave speeds in the air and in the dielectric media; the horizontal wave speed without the strip, however, can be higher than the wave propagation speed on strip. If this is the case, an indefinite field can result at some lateral locations. This phenomenon has been briefly analyzed by Das[73]. In ordinary microstrip configurations, this is unlikely to happen. The decrease of the magnitude of the field in the lateral direction, however, is very slow. With the inclusion of the effects of the two δ -functions in Equation 4.17, it is possible to alleviate the problem. However, it is more convenient to use a finite sized traveling wave. The convergence can thus be improved.

The finite traveling wave is defined such that the sine and cosine waves are both an integer number of the effective wavelength long. Four or five of such wavelengths is found to be sufficient to give very good convergence. It has proved to be unnecessary to assume more such wavelengths because the electric field at the high order mode area due to the current at the far end is negligible. Since the cosine wave is one quarter of a wavelength retarded from the open end, it is terminated one quarter of a wavelength farther than the sine wave.

The MoM uses the modified Galerkin's method again in the determination of the current distribution. All of the x and y directed PWS functions are also used as testing functions. Since the two traveling waves are not to be used as the testing functions as in the case of the exact Galerkin's method, two more testing functions are needed to form a square matrix of reaction. These two testing functions, t_1 and t_2 , are chosen to be PWS functions as well. Their widths are the same as the widths of the two strips, respectively. t_1 is centered at the edge of the high order mode area covered by the basis PWS functions on the input branch. t_2 is similarly put on the output branch. In other words, these two testing functions bridge the local high order mode and pure traveling waves areas. This selection of location and type of the additional testing functions emphasizes the local nature of the boundary conditions and minimizes the number of function types dealt with in the program, because all the testing functions are now the PWS type. The moment method is therefore a modified Galerkin's procedure.

The integer numbers n_1 and n_2 are determined in such a way that under no circumstances should the cell size be larger than the predetermined value — $0.03\lambda_{ei}$. Take the input strip as an example: if the infinite line analysis reveals that the effective wavelength is λ_{e1} , then the number n_2 should be:

$$n_2 = \max(2, \lceil \frac{W_2}{0.03\lambda_{e1}} \rceil)$$

where the function $\lceil x \rceil$ represents the smallest integer that is greater than or equal to x , and W_2 is the width of the second strip (in the y direction). This guarantees

that the length of x direction PWS functions on input strip will not exceed $0.03\lambda_{e1}$.

As can be expected, the number of the basis functions is now greatly increased. Since the most time consuming part in the numerical process is filling up the matrix whose elements are reactions between basis or input functions and testing functions, care must be taken not to calculate any elements that are already known. For instance, if the two strip widths are the same, it is advantageous that one calculation be applied to more than one element. If the two strips are not the same width, there is still the possibility that the cells can be square after the partition. In this case the reactions between x direction functions will be the same as those between y direction functions. Also a time saving consideration is that the reaction on opposite sides of a traveling wave should have the same value, or at least they are different only in sign. In any case, the reactions are determined by the functions involved and the vectorial separation between them. If any symmetrical layout exists, or separation and function pattern matches with other known reactions, the known values can be used to fill up the element. The reactions obtained are therefore stored according to the relative vectorial separation of the two functions involved.

It is also possible to use this method to analyze fairly irregular shaped discontinuities [99]. For instance, Harokopus and Katehi [15] uses small cells to form a zigzag type mitered corner. There are also non-rectangular shaped basis functions which can be used to have a conformal representation of the mitered corner [105]. If a data bank is set up where the reactions for all the different separations are stored, then

all the matrix elements are known and the current distribution can be determined. Thus the circuit behavior is obtained. The main limitation is that the shape of the patch has to conform to certain discrete sizes.

6.1.3 The Matrix Formulation

Since there are both x and y direction currents and fields, it is expected that Green's functions G_{xx} , G_{xy} , G_{yx} , and G_{yy} are to be used, in determination of the total x and y direction electric field. However, no z direction dyadic elements of the Green's function are to be used, due to the fact that the circuit is planar.

Using the basis and the testing functions described above, the matrix form of the MoM can be derived as follows:

First, the total tangential electric fields generated by all the currents considered are (in the spatial domain)

$$E_x(x, y) = \iint (G_{xx} \sum I_x + G_{xy} \sum I_y) dx' dy' \quad (6.1)$$

and

$$E_y(x, y) = \iint (G_{yx} \sum I_x + G_{yy} \sum I_y) dx' dy' \quad (6.2)$$

where again the Green's functions are determined by the structure of the stratified media and the vertical location of the strip, but not by the shape of the strip.

According to the boundary conditions, these tangential fields have to be zero on

the strip surface. This is enforced by making the inner products of these fields with the testing functions defined on the strip surface and letting the inner products be zero. This step results in a system of linear equations, which in the matrix form is

$$\begin{bmatrix} [Z^{xx}] & [Z^{xy}] & [Z^{xR}] & [Z^{xT}] \\ [Z^{yx}] & [Z^{yy}] & [Z^{yR}] & [Z^{yT}] \\ [Z^{t1x}] & [Z^{t1y}] & [Z^{t1R}] & [Z^{t1T}] \\ [Z^{t2x}] & [Z^{t2y}] & [Z^{t2R}] & [Z^{t2T}] \end{bmatrix} \begin{bmatrix} [I^x] \\ [I^y] \\ R \\ T \end{bmatrix} = - \begin{bmatrix} [Z^{xI}] \\ [Z^{yI}] \\ Z^{t1I} \\ Z^{t2I} \end{bmatrix} \quad (6.3)$$

It is noted that the inner product is in a sense both vectorial and integral inner product. The vectorial product occurs when the directions of the two parts are at a right angle. The product is zero, e.g.

$$< E_x, I_y > = 0.$$

The integral product is defined as before in the other chapters, e.g.

$$Z_{i,j}^{xy} = \iint \tilde{G}_{xy} \tilde{I}_{yj} \tilde{I}_{xi} d\lambda_x d\lambda_y.$$

The last two equations in Equation 6.3 are from the inner products between the additional testing functions and the basis functions. On the right side of the equation are the reactions between the testing functions and the input, which is the incident traveling wave.

From Equation 6.3 it is observed that the input to the system, in our case the incident current wave, plays a key role in determining the whole current distribution.

The governing law here is the boundary condition on the strip: the total tangential electric field on the strip surface has to be zero. The incident current radiates into the structure causing induced current on the strip surface, which also radiates. The total current thus consists of the incident current (also called the impressed current [59]) and the induced current. The total current distribution can not be arbitrary — it has to be such that the total generated tangential fields on the strip surface are zero, the fields being determined jointly by the current distribution and the Green's function of the structure.

The moment method enforces the boundary condition on the strip surface by introducing the inner products between the generated fields and some functions non-zero only on the strip, and letting the inner products be zero. So there are two approximations in MoM: the first one is the expansion of the unknown solution function into a linear combination of a series of basis functions; and the second one is introduction of the inner products. The first approximation causes some loss of detail in the real current distribution; while the second one enforces the boundary condition in a piecewisely average sense. Since MoM only makes the integral (the inner product) zero, there can be some positive-negative cancellations in the integral region. Therefore, it is very important to have small size basis and testing functions, in order to have a valid analysis. Also, the selections of the basis and testing functions are important in obtaining good convergence. On the other hand, one has to bear in mind that small size basis functions increase the total number of unknowns, which takes more computer time to fill up the matrix. As pointed out before, this is a

trade-off between accuracy and speed.

6.2 Results

6.2.1 Convergence Test

The convergence of the algorithm is tested as the area covered by the local PWS functions expand. The number of PWS functions on each branch of the corner is increased as the variations of the reflection and transmission coefficients are monitored. When adding more PWS functions does not change the results much, convergence is reached since the PWS functions have covered sufficient part of the high order mode area.

The convergence test is carried out at the frequency of 3GHz. The circuit's parameters are shown in Figure 6.2 and 6.3, along with their convergence behavior as the number of the PWS functions increases. It is noted that the results start to converge after the PWS functions have filled up the areas not covered by the traveling wave modes, which is between the tip of the cosine function and the outer edge of the corner.

The frequency at which the convergence is tested is relatively low compared to the dimensions of the strip and the discontinuity. Therefore it is expected that the reflection is very small and the transmission is almost complete ($|T| \approx 1.0$). Also,

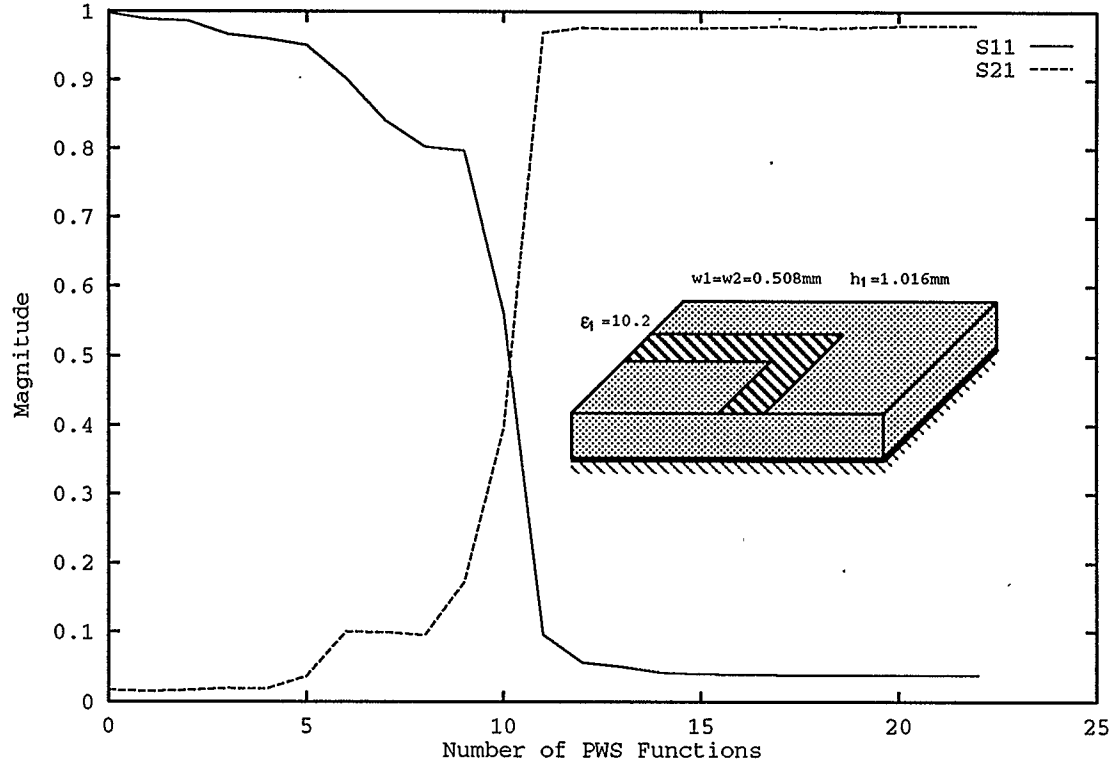


Figure 6.2: Magnitude convergence test for a corner (freq = 3GHz, $W_1 = W_2 = .508\text{mm}$, $h = 1.016\text{mm}$, $\epsilon_r = 10.2$).

the corner does not impose a large phase shift on the incident wave. The phase of the reflection suggests a strong imaginary part in the equivalent impedance at the corner. This can be explained as follows: at low frequency, the bent strip acts like a capacitance to ground on the input strip, whose susceptance is formed by the product of the frequency and the capacitance. Since the frequency also determines the susceptance, the reflection phase is to be expected to be between those of pure

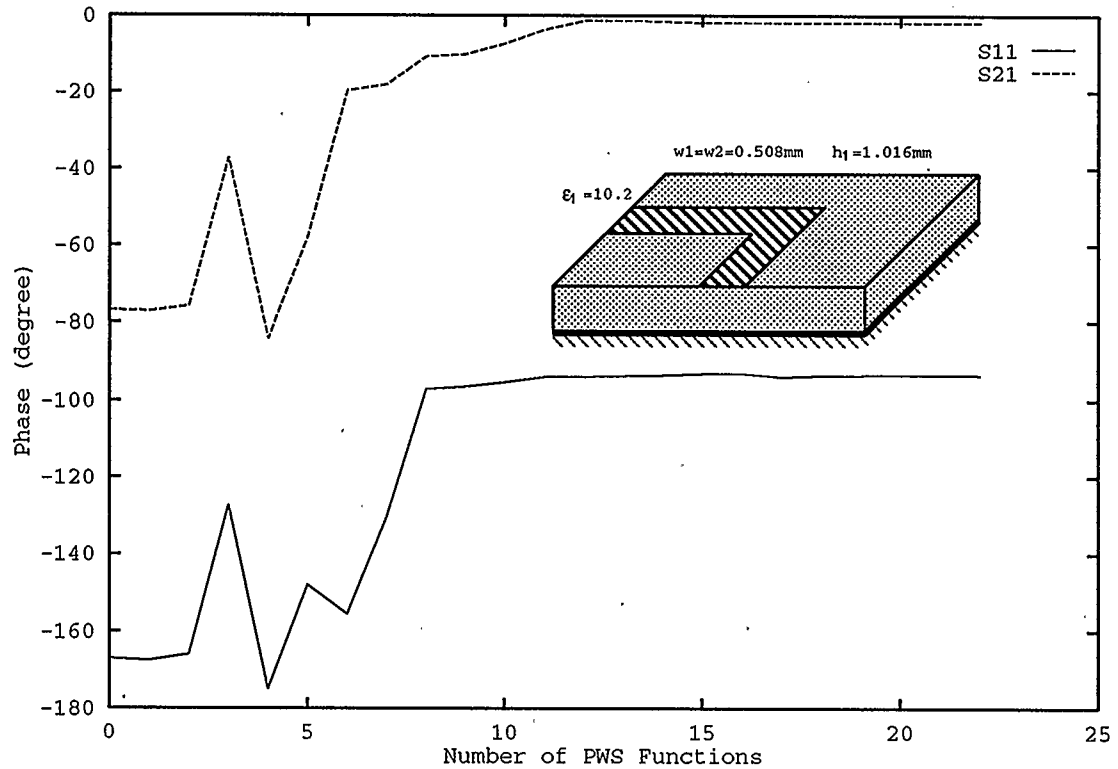


Figure 6.3: Phase convergence test for a corner (freq = 3GHz, $W_1 = W_2 = .508\text{mm}$, $h = 1.016\text{mm}$, $\epsilon_r = 10.2$).

open and pure short circuits. The lower the frequency, the larger the capacitance (due to the larger area of the load strip that is covered by the larger wavelength), but the susceptance can change in either direction. Therefore frequency and the equivalent load capacitance do not change in the same direction. Thus it is hard to predict the zero frequency response of the reflection phase.

6.2.2 Corner Circuit Parameters as Functions of Frequency

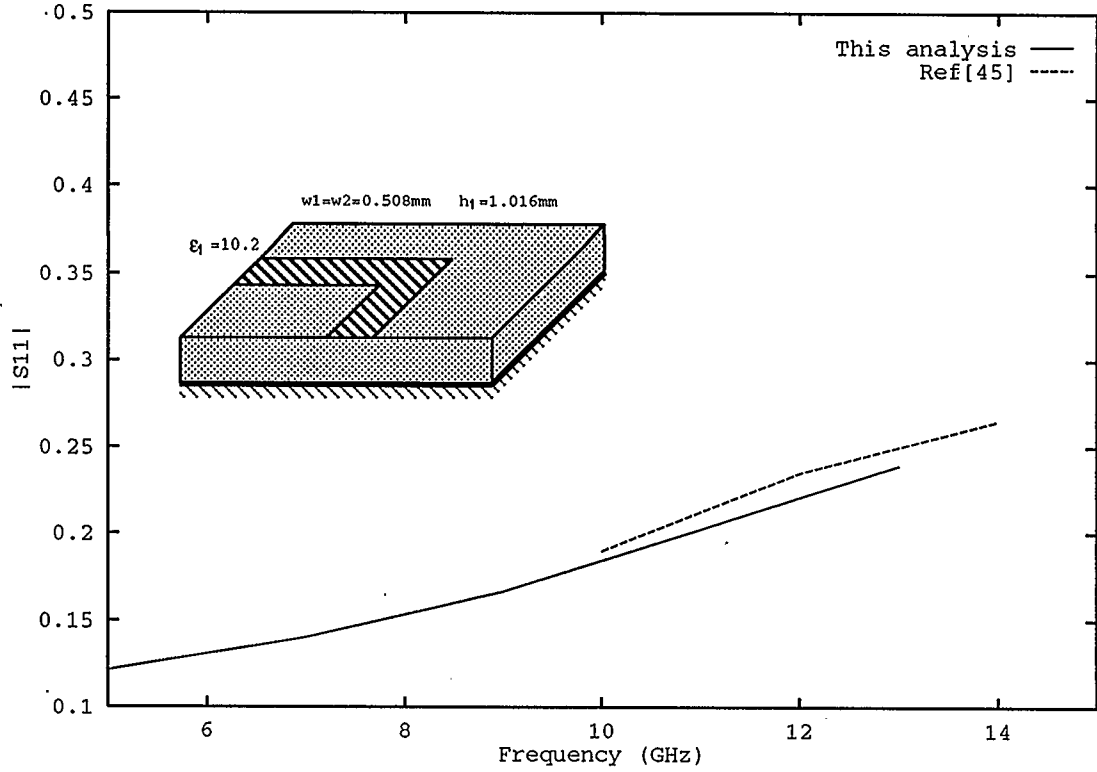


Figure 6.4: Frequency response of $|S_{11}|$ for a corner ($W_1 = W_2 = .508\text{mm}$, $h = 1.016\text{mm}$, $\epsilon_r = 10.2$).

Having tested its convergence performance, we can now use this algorithm to obtain more data. The frequency response of a corner with equal input and output strip width is analyzed.

The results are shown in Figure 6.4 through 6.7, with the magnitude results

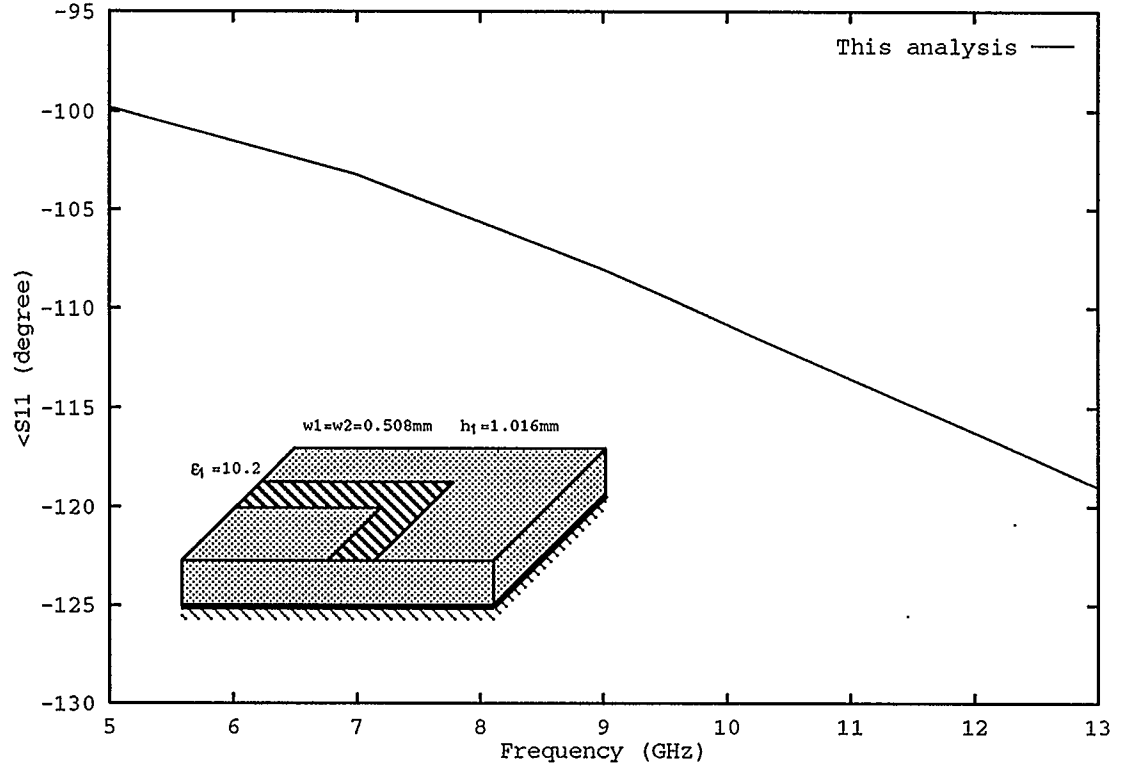


Figure 6.5: Frequency response of $\angle S_{11}$ for a corner ($W_1 = W_2 = .508\text{mm}$, $h = 1.016\text{mm}$, $\epsilon_r = 10.2$).

obtained in [46]. Good agreement between them has been achieved. The magnitude of the reflection $|S_{11}|$ and the transmission $|S_{21}|$ are as expected. The reflection has very small magnitude at low frequency, suggesting that the incident wave is not greatly affected by the existence of the corner. The transmission, on the other hand, is very high, which validates the applicability of the corner at low frequencies. As frequency goes up, however, the reflection becomes larger and the transmission

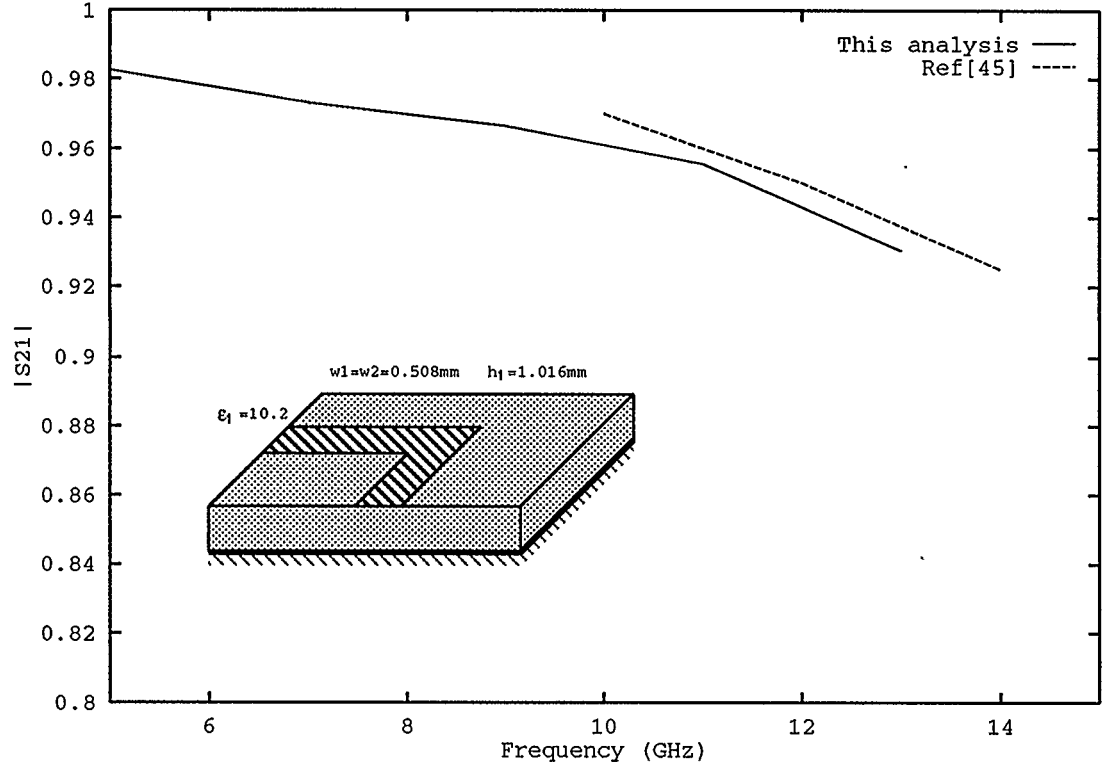


Figure 6.6: Frequency response of $|S_{21}|$ for a corner ($W_1 = W_2 = .508\text{mm}$, $h = 1.016\text{mm}$, $\epsilon_r = 10.2$).

smaller. This is because more high order modes are generated as the frequency becomes higher. High frequencies represent short wavelength, making the electrical dimensions of the circuit and the structure large, which includes the width of the strip, the size of the corner, and the thickness of the substrate. It is noted that even at the frequency of 13GHz, there is still a considerable amount of power that passes through this corner, due to the small size of the strip and the substrate. The small

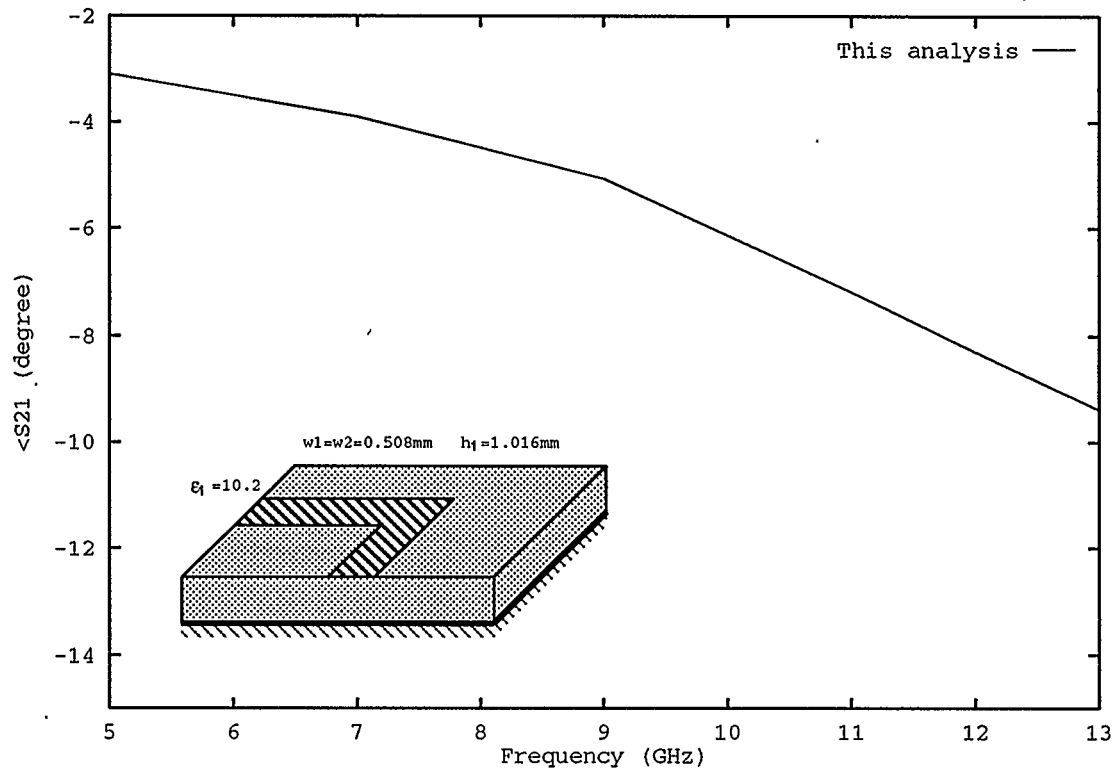


Figure 6.7: Frequency response of $\angle S_{21}$ for a corner ($W_1 = W_2 = .508\text{mm}$, $h = 1.016\text{mm}$, $\epsilon_r = 10.2$).

size also introduces a small phase shift as the wave passes the corner, as shown in Figure 6.7.

It is concluded that corners are useful in configuring the layout of the circuit. However, care must be taken not to choose large strip width and substrate thickness, because at high frequencies, the corners can impose a certain amount of blockage to the propagation of the wave on the strip, which has been taken into consideration in

the design of the circuit.

Chapter 7

Vertical Dipole Analyses

Vertical conductors in stratified medium are often seen in various applications. In microstrip circuits, vertical metallized holes are often used as a method of supplying ground contact for the circuits on the substrate surface; in VLSI, vertical conductors, which are called via holes, are used to connect strips in different layers; and coax-fed microstrip antennas are excited by the center conductors of coax-lines from the ground plane.

In this chapter, a vertical dipole is investigated in the spectral domain. The results are in good agreement with the results obtained with the spatial domain method.

7.1 Theory

7.1.1 Circuit Discussions

The vertical dipole to be analyzed is shown in Figure 7.1. Generally it is embedded in a multilayer medium. The vertical dipole is assumed to be a perfectly conducting cylinder, whose radius is far less than the shortest wavelength for any medium in the

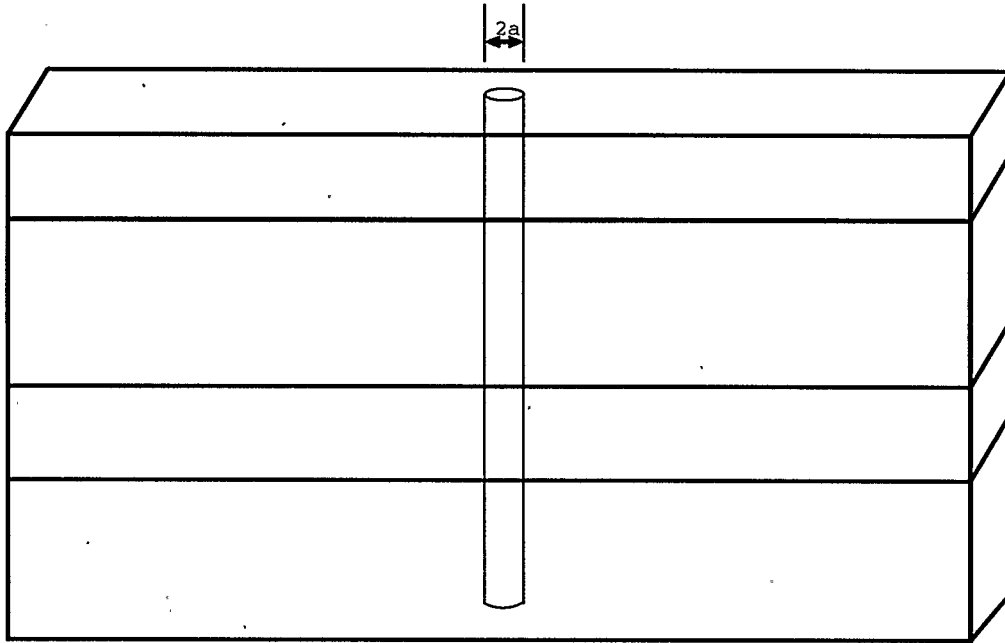


Figure 7.1: A vertical wire in a multilayer structure.

structure (It is understood that the wavelength varies from one dielectric layer to the other). The small radius means that the current flowing on the top and bottom surfaces can be neglected, thus a line current can be assumed to flow along the center of the cylinder.

Up to Chapter 6, all the horizontal dyadic Green's function's elements $G_{\mu\nu}$, where μ and ν are either x or y , have been used to some extent. They are sufficient to describe all electromagnetic behavior of all the planar structures in a multilayer medium, because no vertical source or field components need to be considered. If a vertical object or any vertical field components are to be analyzed, however, the rest

of the elements in a dyadic Green's function have to be used completely or partly. If the circuit has both vertical and horizontal objects, all the elements have to be used to provide a comprehensive analysis. An example of this kind of circuit is a microstrip line with a shorting pin, which is to be analyzed in the next chapter. In this chapter, since the circuit (a vertical dipole) has only vertical objects, and its horizontal dimensions are negligibly small, only G_{zz} is needed in the analysis.

7.1.2 Matrix Formulation

The boundary condition is to be enforced on the dipole surface. In the calculation of the z direction electric field, a generalized multilayer structure is dynamically formed to describe the source and field points relationship for the generalized Green's function (see Chapter 2 for details). Having this relationship is sufficient for the evaluation of the unshifted Green's function G_{zz} . Since the observation point is at the cylinder surface but the source current is at the center, a shift factor $e^{-ja\lambda_x}e^{-ja\lambda_y}$ has to be added to the final expression, where a is the radius of the dipole. It is noted that the circuit is rotationally symmetrical about the z axis, thus the cylindrical coordinate system is more suitable here. In the cylindrical coordinate system, the dipole surface is represented as $\rho = a$.

In this procedure, the basis current functions are still the PWS functions as in previous chapters, except that they are now z directed. Unlike the transmission line type discontinuities, the dipole has a finite structure, and does not have a traveling

wave input source. In this analysis the commonly used δ gap source in the middle is chosen as the input to the dipole. It is assumed that there is a small voltage gap in the middle of the dipole. The gap size is h , the voltage is 1.0 volt, and thus the electric field over the gap is $1/h$. To meet the boundary conditions, the vectorial summation of the electric field produced by all of the induced currents should be zero on the dipole surface, except at the feeding point, where it is equal to $-1/h$ in order to make the total tangential field zero at that point.

The z directed electric field generated by a line current $J_z(z')$ in the same direction is

$$E_z(x, y, z) = \int_{z'} dz' \int_{-\infty}^{+\infty} \int_{-\infty}^{+\infty} \tilde{G}_{zz}(\lambda_x, \lambda_y, z|z') J_z(z') e^{j\lambda_x x} e^{j\lambda_y y} d\lambda_x d\lambda_y \quad (7.1)$$

The boundary condition states that this electric field should be zero on the dipole surface. It is noted that it is independent of the variable ϕ . Converting the coordinate system into polar form gives the following expression (Appendix B):

$$E_z(\rho, z) = \int_{z'} dz' \int_0^\infty J_z(z') \tilde{G}_{zz}(\lambda, z|z') J_0(\lambda \rho) \lambda d\lambda \quad (7.2)$$

This expression is actually the famous Sommerfeld integration [1]. It is a demonstration that the Sommerfeld integration of Green's function's expressions is simply a polar coordinate version of the 2-D Fourier domain formulation.

Using PWS's as both basis and testing functions, with the above electric field expression, a MoM matrix equation can be formulated as follows:

$$\begin{bmatrix} Z_{1,1} & Z_{1,2} & \cdots & Z_{1,N-1} \\ Z_{2,1} & Z_{2,2} & \cdots & Z_{2,N-1} \\ \cdot & \cdot & & \\ \cdot & \cdot & & \\ \cdot & \cdot & & \\ Z_{N-1,1} & Z_{N-1,2} & \cdots & Z_{N-1,N-1} \end{bmatrix} \begin{bmatrix} I_1 \\ I_2 \\ \cdot \\ \cdot \\ \cdot \\ I_{N-1} \end{bmatrix} = \begin{bmatrix} b_1 \\ b_2 \\ \cdot \\ \cdot \\ \cdot \\ b_{N-1} \end{bmatrix} \quad (7.3)$$

where $I_1 \sim I_{N-1}$ are the current function coefficients to be determined in the process; N is the number of the segments the dipole is divided into (Figure 7.2); $Z_{i,j}$'s and b_i 's are reactions between testing functions and basis functions, and testing functions and the source, respectively. Their expressions are as follows:

$$Z_{i,j} = \int_0^\infty d\lambda \int_{z'} dz' \int_z dz 2\pi J_i(z) J_j(z') \lambda J_0(\lambda a) G_{zz}(\lambda, z|z')$$

$$b_i = \begin{cases} 0 & \text{if } i \neq i_{feed} \\ \frac{1}{h} \int J_i(z) dz & \text{if } i = i_{feed} \end{cases}$$

where i_{feed} is the segment where the dipole is excited.

7.1.3 Consideration on Diagonal elements

G_{zz} is the z directed electric field due to a Hertz dipole in the same direction. Since the structure is multilayer in z direction, the field in each location of interest is determined by the inverse 2-D Fourier transformation. It does not take much time

to compute G_{zz} if the observation point and the source point are not on the same plane ($z \neq z'$), because the integrand decreases exponentially with λ . If, however, these two points are on the same plane, the integral is not convergent. This is the case when one considers the elements whose base and testing functions have some vertical overlaps. There is no doubt that in reality the z direction field produced by a vertical dipole at the same plane exists and is finite. This divergency is due to the fact that the field varies as λ^{-3} as the observation point approaches the source on the same plane. In other words, the forward Fourier transform does not exist in the first place, therefore one can not expect the inverse transform to exist. An acceptable way of getting around this problem is to re-define the integral as a limit as follows:

$$E_z(\rho, 0) = \lim_{\Delta \rightarrow 0} \int_0^\infty \tilde{G}_{zz}(\lambda, \Delta) J_0(\lambda \rho) \lambda d\lambda \quad (7.4)$$

where $\Delta = z - z'$. This limit exists because any non-zero Δ is an exponential factor in the integrand and thus the convergence is guaranteed. Physically this change means that we insert an imaginary layer between the source and the observation points. If the thickness of this layer is small enough, the field obtained should be close enough to the field without the layer.

Numerically, \tilde{G}_{zz} is obtained by passing the key word “Gzz” and a pre-determined very small Δ to the generalized dyadic Green’s function in the program.

7.2 Results

For the purpose of simplicity and for comparison to the spatial domain method, the vertical dipole is assumed to be embedded in a homogeneous medium, which can be viewed as a special case of the multilayer media case. If a multilayered structure is used, much more computer time will be taken for the analysis, because the reaction coefficient matrix will no longer be Toeplitz. The Toeplitz matrix has elements that are determined only by the separation of the base and testing functions involved. Additionally, there is not a spatial domain analysis of a vertical dipole for comparison. The operation frequency is chosen to be 3GHz. A dipole length of half wavelength in free space is chosen. The effects of different dielectric constants are investigated. The results compare favorably with the spatial domain method proposed by Harrington [42].

7.2.1 Results from SDA

The results obtained using the spectral domain method are shown in Figure 7.3 and 7.4. The dielectric constant ϵ_r of the medium is chosen to be 1, 2, and 4. At the dielectric constant of 4, the dipole is actually one full wavelength in length. In other words, it has become a full wavelength dipole. This is clearly seen in the current magnitude distribution (Figure 7.3).

7.2.2 Results from the Spatial Domain Method

To compare the SDA results with the existing spatial domain method, the well known Harrington's method is used to analyze the same dipole. The results are shown in Figure 7.5 and 7.6. As can be seen, they match the spectral domain results Figure 7.3 and 7.4 very well. The major discrepancies are that the spatial method gives smoother curves on the dipole arms and more detailed sharp variations at the feeding point. This is because for the spatial method 65 segments of current were used, whereas for SDA only 20 PWS current basis were used. It is expected that with more PWS functions in the SDA method, the curves will be smoother and the results should be identical to those obtained by the spatial method. Also noted is that SDA uses PWS as the basis functions and the total number of them is even, whereas the spatial domain method uses pulse functions as the basis and the total number is odd. That is why for the spatial domain method there is a center peak for some graphs, and the SDA graphs are relatively flat at the center. The most important thing in this comparison is that the Green's function should be the same. The next subsection will compare the Green's function values obtained with different methods.

7.2.3 Comparison of the Green's Functions

As discussed in this chapter, the spectral domain Green's function G_{zz} for two points on the same plane is not convergent, nor is it Riemann integrable. A limit definition

is introduced as in Figure 7.4. This is to give some off-set in the observation point, which is equivalent to introducing a thin layer between these two points. The choice of this layer thickness is a trial-and-error process. It is found that choosing the off-set to be $10^{-3}a$ is satisfactory. Table 7.1 shows the Green's function values calculated with the two methods (freq = 3GHz, $\epsilon_r = 1$, $a = .5\text{mm}$, off-set = .0005mm).

Although there is some off-set in the observation point for the spectral domain method, the Green's function thus obtained is very close to the exact one obtained in the spatial domain (without any off-set). The relatively big difference for the imaginary part is due to the much larger real part, which is the dominant term in the complex number. Therefore this imaginary part will not make a significant contribution to the whole complex number for either the magnitude or the phase. The error due the off-set observation point becomes smaller and smaller as the separation (Δ) becomes larger and larger. Numerical truncation of the infinite integration is another source of error.

Layer Thickness (mm)	Spectral G_{zz}		Spatial G_{zz}	
	Im	Re	Im	Re
0.0000	-7.936176	382046.3	-7.899535	382046.0
0.1983	-7.936023	180739.7	-7.900444	180739.7
0.3966	-7.935623	-29767.09	-7.899521	-29767.14
0.5948	-7.934976	-77389.56	-7.897985	-77389.64
0.7931	-7.934082	-66562.48	-7.890542	-66562.50
0.9914	-7.932940	-48629.21	-7.903650	-48629.16
1.1897	-7.931551	-34510.14	-7.900283	-34510.25
1.3880	-7.929915	-24695.75	-7.891000	-24695.69
1.5862	-7.928032	-18019.85	-7.896985	-18019.82
1.7845	-7.892801	-13439.26	-7.897064	-13439.29

Table 7.1: G_{zz} values calculated using two different methods (freq = 3GHz, $\epsilon_r = 1$, a = .5mm, off-set = .0005mm).

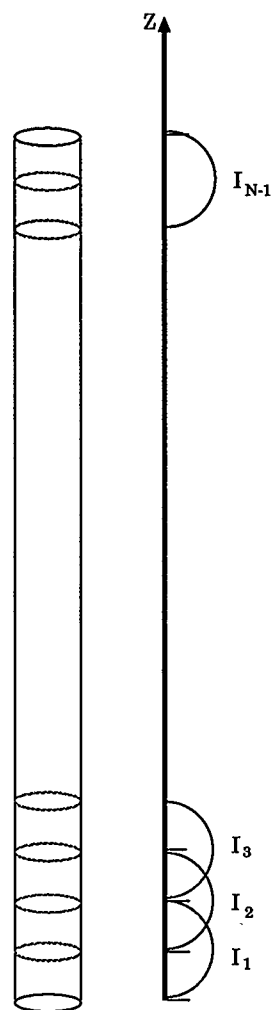


Figure 7.2: PWS functions on a vertical dipole.

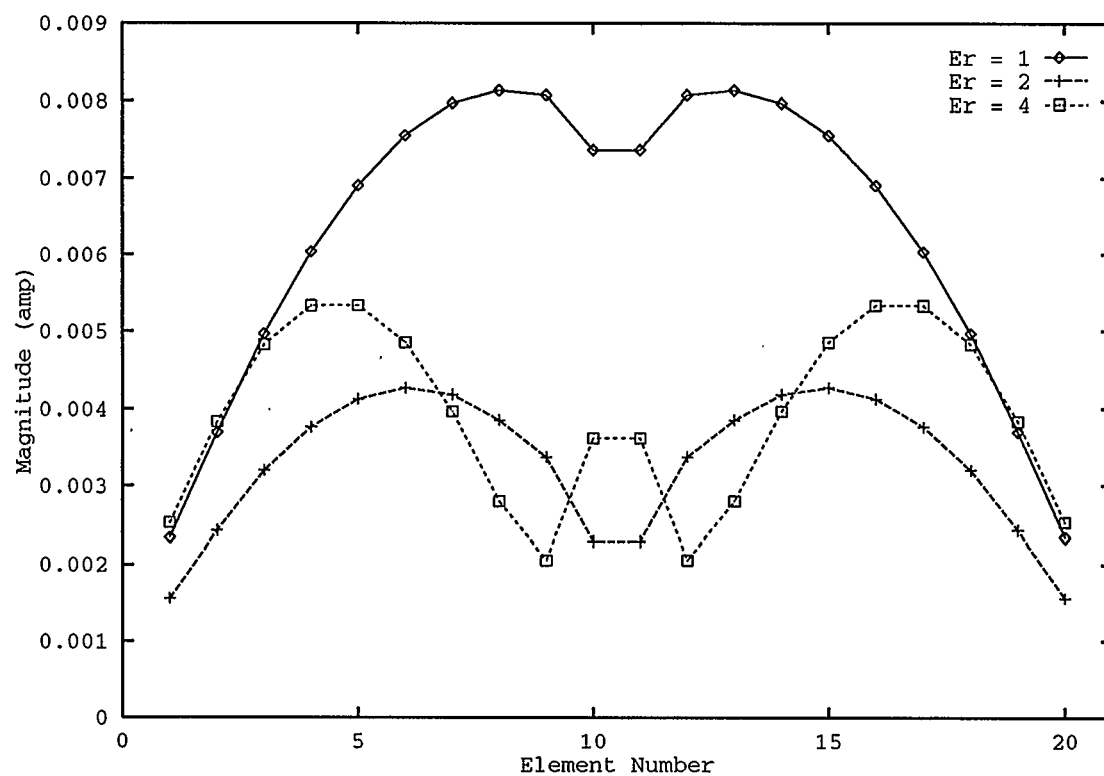


Figure 7.3: Magnitude of the current on a dipole by SDA (freq = 3GHz, $a = .5\text{mm}$, $L = 50\text{mm}$).

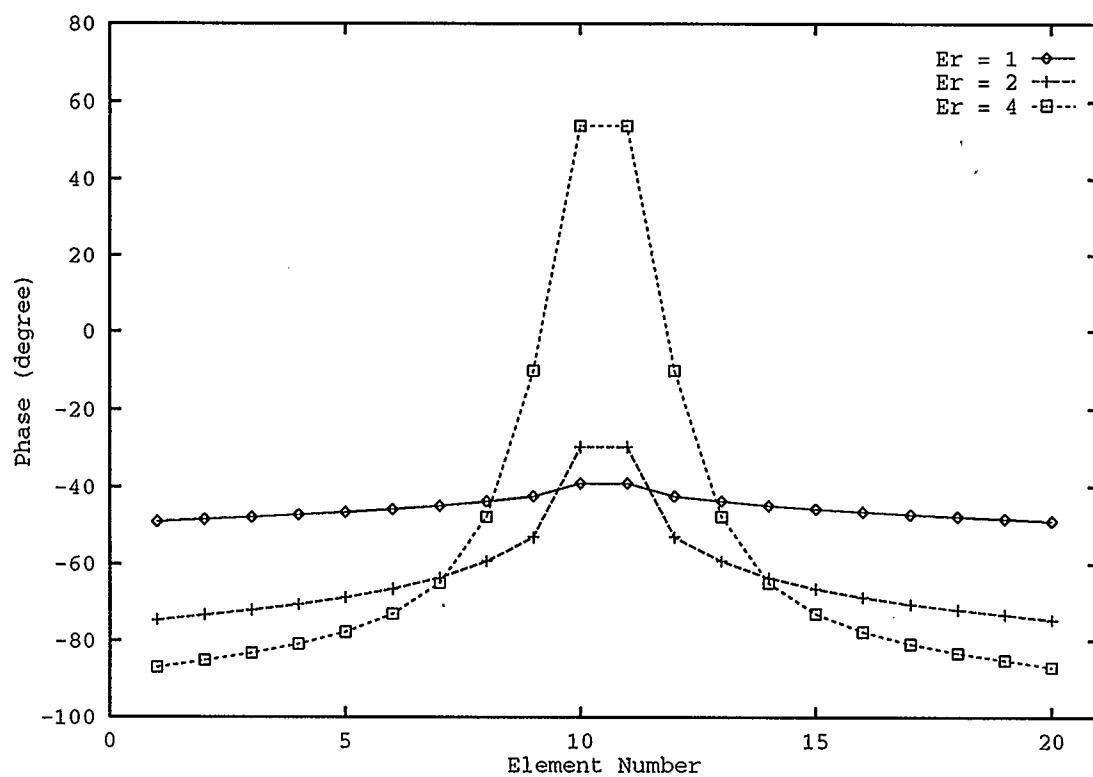


Figure 7.4: Phase of the current on a dipole by SDA (freq = 3GHz, $a = .5\text{mm}$, $L = 50\text{mm}$).

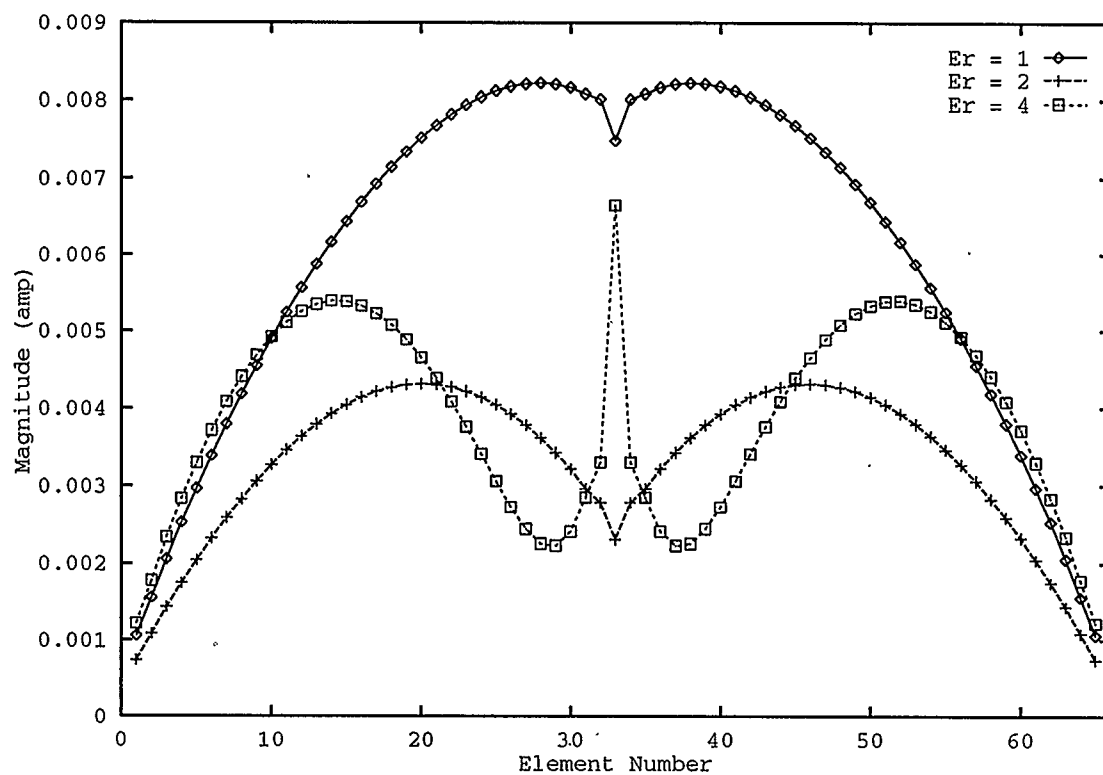


Figure 7.5: Magnitude of the current on a dipole by spatial domain method (Harrington's method [41]) (freq = 3GHz, $a = .5\text{mm}$, $L = 50\text{mm}$).

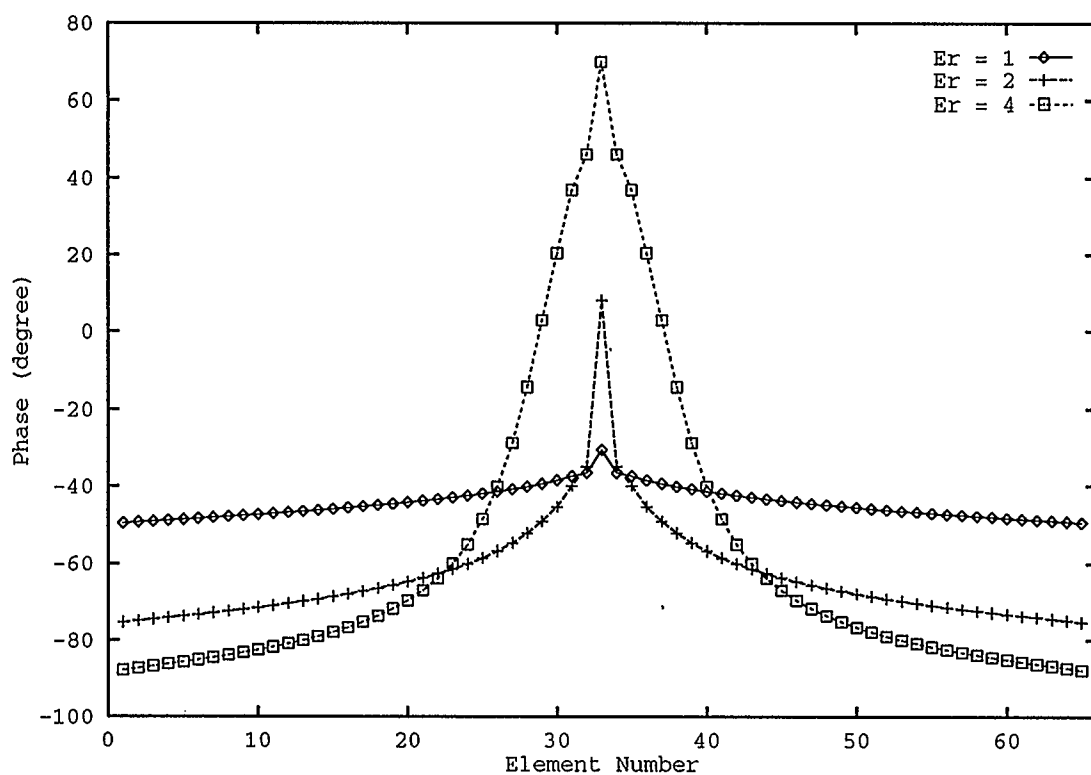


Figure 7.6: Phase of the current on a dipole by spatial domain method (Harrington's method [41]) (freq = 3GHz, $a = .5\text{mm}$, $L = 50\text{mm}$).

Chapter 8

3-D Discontinuity — Shorting Via

In microwave integrated circuits, shorting vias are usually used to ground components on the substrate surface. A microstrip transmission line with a shorting via is a good example of a 3-D discontinuity. In this chapter, the spectral domain method is applied to a circuit with a semi-infinite microstrip and a shorting via at one end.

Some research has been done on the analysis of circuits with both planar and vertical conductors. Becker et al used finite difference time domain (FDTD) method to analyze vias in a computer chip package [106]. Gu et al used an equivalent network approach to analyze vias in multilayered integrated circuits [107].

Using the spectral domain method, coax-fed microstrip dipoles are analyzed in [108]. Microstrip lines terminated with shorting vias are analyzed by Tsay and Aberle [109]. In that analysis the attached mode (the current on the strip surface) due to the existence of a shorting via is expressed with an infinite series, determined by an equivalent cavity method. This method is difficult to extend to multilayer cases. The attached mode expression in this chapter is similar to the one used in [108], where a strip loaded, coax-fed antenna was analyzed. Although this expression is simplified, it is easy to extend it to multilayer cases, and reasonable results

are obtained.

8.1 Theory

8.1.1 Circuit Discussions

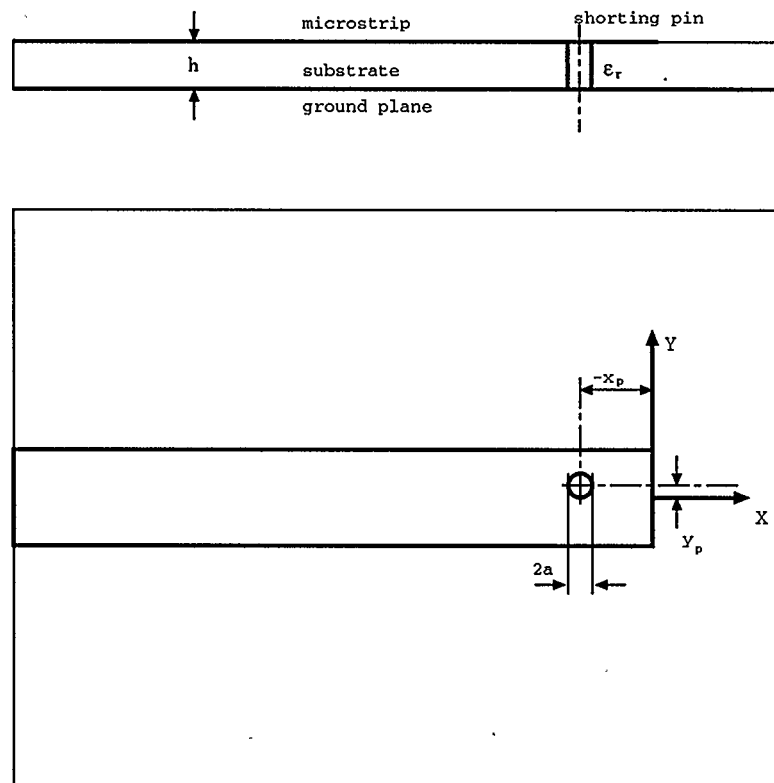


Figure 8.1: Microstrip with a shorting via.

The microstrip line with a shorting via is shown in Figure 8.1. The via is assumed to be at x_p and y_p , joining the microstrip on top of the substrate with the ground

plane on the bottom of the substrate.

As stated in Chapter 1 and 2, a full representation of a dyadic Green's function needs nine scalar elements, each of which has two subscripts as $G_{\mu\nu}$, which means the μ directed field due to a ν directed Hertz dipole. Here μ and ν should be x, y , or z . Since an assumption was made that the medium is multilayer in the z direction and homogeneous in x and y , a series of simplifications can be made. G_{xx} can be easily transformed into G_{yy} through coordinate transformation, for instance. In the numerical process, the reaction between two y elements is the same as that between two x elements, if their relative locations are the same. This is also used to save on computation time.

Although theoretically sound and clear, the analyses of 3-D circuits are numerically complicated. It needs the calculation of the reactions for each pair of the currents and the fields involved, which may need all nine elements of the dyadic Green's function. Some simplifications, however, can be made, according to the specific circuit under investigation. For instance, if the line is narrow in terms of effective wavelength, transverse current can be neglected[108]. It is also noted that the analysis can make use of the algorithm developed for the open circuit analysis, because the short circuit consists of an open circuit and a shorting via. To analyze a short circuit, one has to include the reactions involving the current on the via.

The introduction of the reactions of the current on the via with the current on the strip plays a key role in the analysis. The input is again a traveling current wave

from $x = -\infty$, which radiates into the whole structure causing induced current on all conductor surfaces (except the ground plane, which has been taken into consideration in the Green's functions.). The induced current also causes radiation. The total current has to radiate in such a way that the boundary conditions on the conductor surfaces be met. In other words, the total current distribution adjusts itself to radiating a field pattern which has zero tangential electric field on all conductor surfaces. When there is a shorting via, current is induced on its surface as well, which re-radiates into the structure. The conductor shorting via supplies a current path to the ground, and consequently causes the phase of the reflection coefficient to be different from that for an open circuit.

8.1.2 Matrix Formulation

Basis Functions

The current on the strip and the via are expressed as linear combinations of the basis functions. Due to the fact that the strip is not electrically wide, no transverse current flow is assumed on the strip. The basis functions around the discontinuity on the strip surface are again chosen to be PWS functions, with a uniform transverse distribution. The input from and the reflection to $x = -\infty$ are traveling current waves. These are the same as in the open circuit analysis.

The shorting via is assumed to carry a constant current flow along the cylinder

center, because the substrate thickness is very small comparing to the wavelength. If the substrate is thick, and consequently the via is long, the current on the via has to be expressed with multiterm z direction PWS functions, as in the case of vertical dipole analysis.

The current basis functions have to be kept continuous, in order to avoid using any electric charge as source, because any discontinuity in current flow means an accumulation of electric charge, according to the current continuity law. There is concern about the continuity if one checks at the top of the via, where the current on the via stops abruptly and forms a discontinuity in current flow. Therefore one has to add an attached mode to the strip surface to make the current flow continuous. Physically this means that the current flowing upward on the via turns onto the strip surface and joins the current on the surface. This attached mode splits from

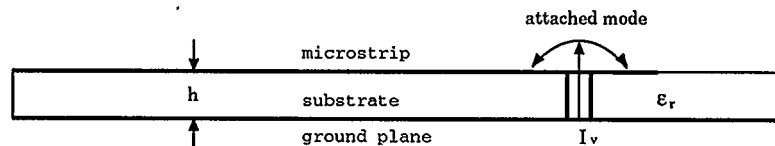


Figure 8.2: Attached mode due to the current flow on the via.

the point where the center of the via touches the strip and flows in opposite directions (Figure 8.2). It looks like a PWS function, but its two parts flow in opposite directions. The PWS function is even, but the attached mode is odd. It should be pointed out that the current from the vertical via does not necessarily stop at the at-

tached mode on the strip surface. It will continue to flow on the strip surface, which will be accounted for by the PWS functions on the strip. The current on the shorting via and the attached mode together form a base function in the determination of the whole current distribution. If there are N PWS basis functions, in addition to the reflection coefficient and the vertical current flow, there will be totally $(N + 2)$ unknowns to be determined.

Testing Functions

The testing functions are chosen to be almost the same as the basis functions. Therefore this is a quasi-Galerkin's procedure, or can be regarded as a modified Galerkin's procedure. All of the PWS functions are again used as the testing functions. Two more testing functions are needed to form a square reaction matrix for the linear equation solution. Similar to the method used in open circuit analysis, one more PWS testing function is defined on the surface at the edge of the area covered by the basis PWS functions. The last testing function is chosen to be the same as the vertical current, which is a uniform function over the length of the via. Therefore, in this formulation, all the basis functions but two have been used as the testing functions as well. One base function that is not used as the testing function is the reflected traveling wave, which is replaced by an extra PWS function on the strip surface. The other one is the via base function. Only part of it is used in the testing function. The attached mode on the strip surface is not used because the boundary condition on the strip surface has been taken care of by the PWS functions.

Formulation of Linear Equations

The electric field due to the current on the conductor surfaces is expressed as follows:

$$E_x(x, y) = \iint (G_{xx} \sum I_x + G_{xz} I_z) dx' dy' dz' \quad (8.1)$$

$$E_z(x, y) = \iint (G_{zx} \sum I_x + G_{zz} I_z) dx' dy' dz' \quad (8.2)$$

where the x directed current $\sum I_x$ includes the input and the reflected traveling waves, the PWS functions on the strip surface, and the attached mode caused by the vertical current on the shorting via; and the vertical current I_z is a uniform current flowing at the center of the via. The Green's functions are obtained from the generalized computer algorithm.

Now each of the testing functions is applied to the field expressions above, to get the inner product between the testing function and the electric field. Note that the x directed testing functions can only produce zero inner products with the z direction field. The same is true between the z direction testing function and the x direction field. Therefore each application of the testing function results in one equation. A total of $(N + 2)$ equations are formed and are shown as follows:

$$\begin{bmatrix} [Z_{pp}^{(N+1) \times N}] & [Z_{pR}^{(N+1) \times 1}] & [Z_{pV}^{(N+1) \times 1}] \\ [Z_{Vp}^{1 \times N}] & [Z_{VR}^{1 \times 1}] & [Z_{VV}^{1 \times 1}] \end{bmatrix} \begin{bmatrix} [I_p^{N \times 1}] \\ \Gamma \\ I_v \end{bmatrix} = - \begin{bmatrix} [V_{pI}^{(N+1) \times 1}] \\ [V_{VI}^{1 \times 1}] \end{bmatrix} \quad (8.3)$$

where I_p is the PWS function coefficients matrix which determines the magnitude of

the PWS functions; Γ is the reflection coefficient of the short circuit; and I_v is the magnitude of the current on the via.

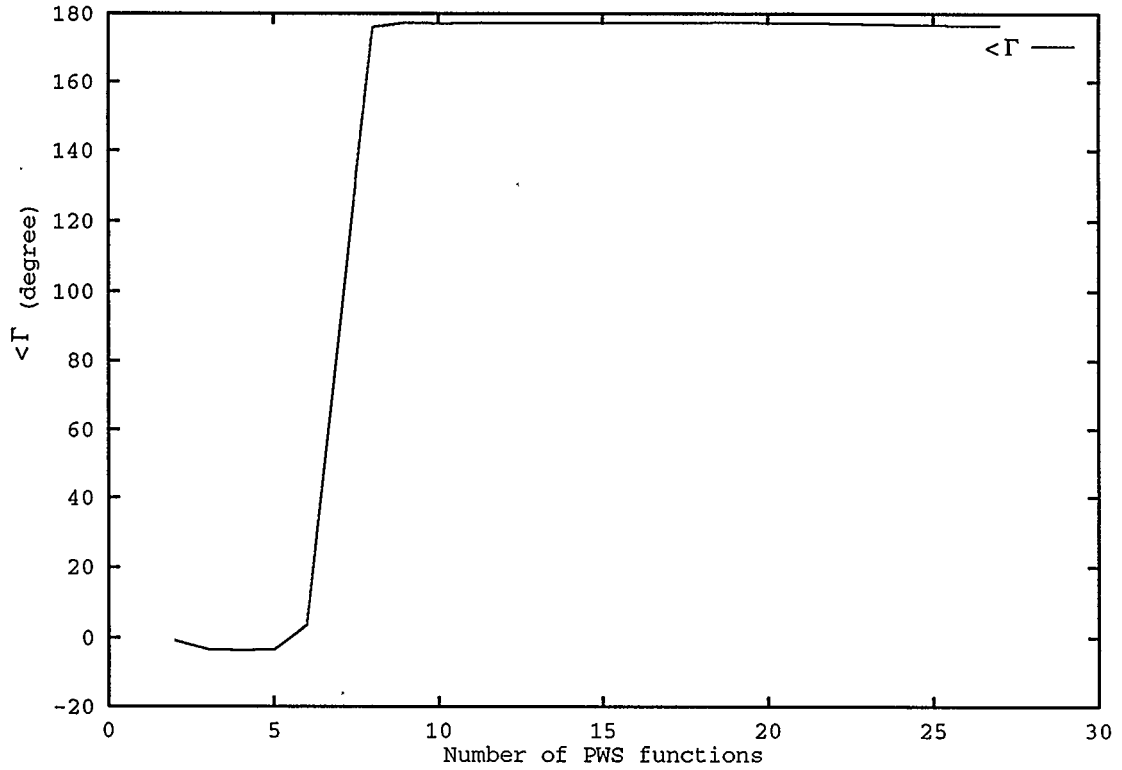


Figure 8.3: Convergence test of the reflection coefficient ($\angle\Gamma$) (freq = 2GHz, $W = 2\text{mm}$, $h = 1\text{mm}$, $a = .1W$, $x_p = -5\text{mm}$, $y_p = 0\text{mm}$, $\epsilon_r = 2.5$).

The elements in the above equations are the reactions (inner products) between electric field and the testing functions, the evaluation of which is done in the same way as in the other chapters. The numerical details will not be elaborated on here.

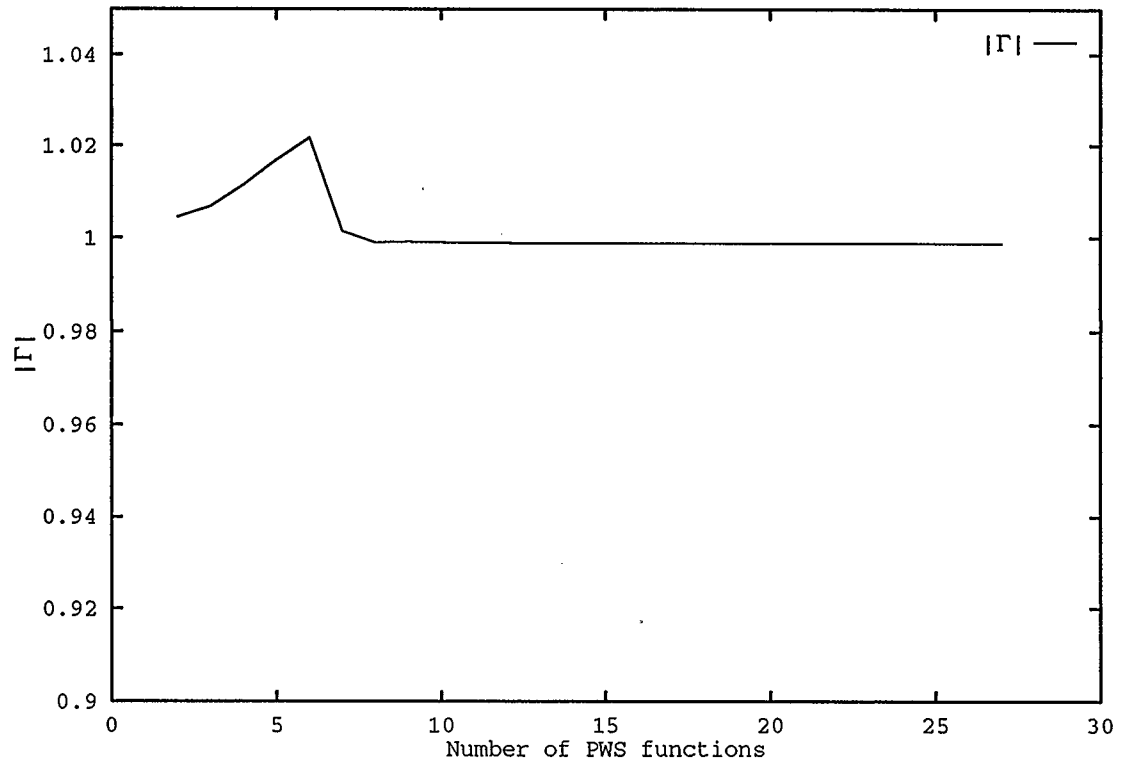


Figure 8.4: Convergence test of the reflection coefficient ($|\Gamma|$) (freq = 2GHz, $W = 2\text{mm}$, $h = 1\text{mm}$, $a = .1W$, $x_p = -5\text{mm}$, $y_p = 0\text{mm}$, $\epsilon_r = 2.5$).

8.2 Results

8.2.1 Convergence Test

The convergence of the algorithm to analyze microstrip transmission lines terminated with a shorting via is tested with an example. The frequency is chosen to be 2GHz.

The width of the strip $W = 2mm$, the height of the substrate $h = 1mm$, the dielectric constant $\epsilon_r = 2.5$, and the via radius $a = 0.1W$. The via is assumed to be at $x_p = -5mm$ and $y_p = 0mm$.

The convergence behavior of the algorithm as the number of the PWS basis functions increases is shown in Figure 8.3 and 8.4, where the phase and the magnitude of the reflection coefficient are investigated. As shown in these graphs, the convergence can be reached shortly after there are enough PWS functions to cover up the area between the cosine traveling wave and the end of the strip.

8.2.2 Frequency Response of the Short Circuit

As the frequency increases, it is expected the shorting via will demonstrate properties different from those at low frequencies. This is because that the shorting via becomes electrically longer at higher frequencies. The surface waves launched into the substrate and the radiation into free space will increase with the frequency.

Figure 8.5 shows the change of the magnitude of the reflection coefficient as the frequency changes. As the frequency sweeps from 2GHz to 16GHz, the magnitude changes from 0.998 to 0.901, suggesting that some power has been lost into the surface waves and the free space waves. It is also noted that the drop of the reflection coefficient is not as severe as in the open circuit cases. This is understandable because the short circuit is not as “open” in its structure as an open circuit, and therefore

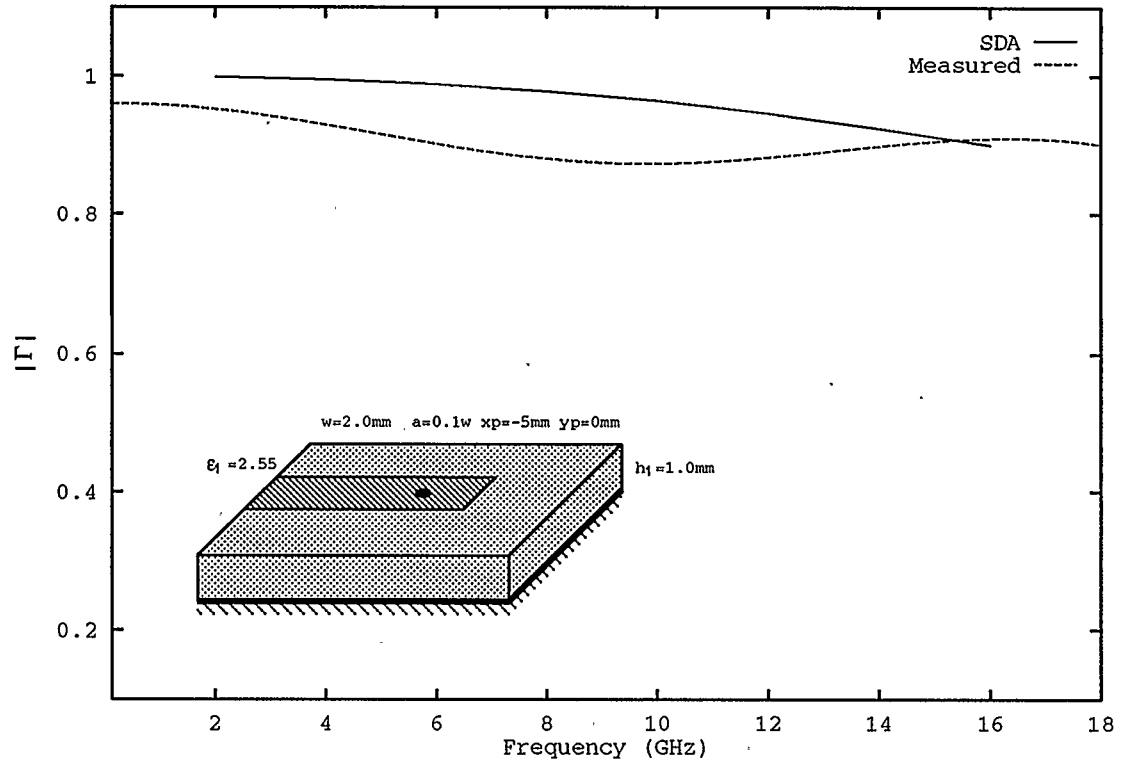


Figure 8.5: Frequency response of the reflection coefficient ($|\Gamma|$) for a shorting via ($W = 2\text{mm}$, $h = 1\text{mm}$, $a = .1W$, $x_p = -5\text{mm}$, $y_p = 0\text{mm}$, $\epsilon_r = 2.5$).

the radiation mechanism has been suppressed.

It is notable that there are some discrepancies between the SDA computed results and the measurement. It is believed that this is due to the technique used in the measurement. Since there is an open end beyond the via, a signal flow loop is formed between the open end and the via. Using time domain feature of the network analyzer can only gate on a specific object. So the measurement just measures the

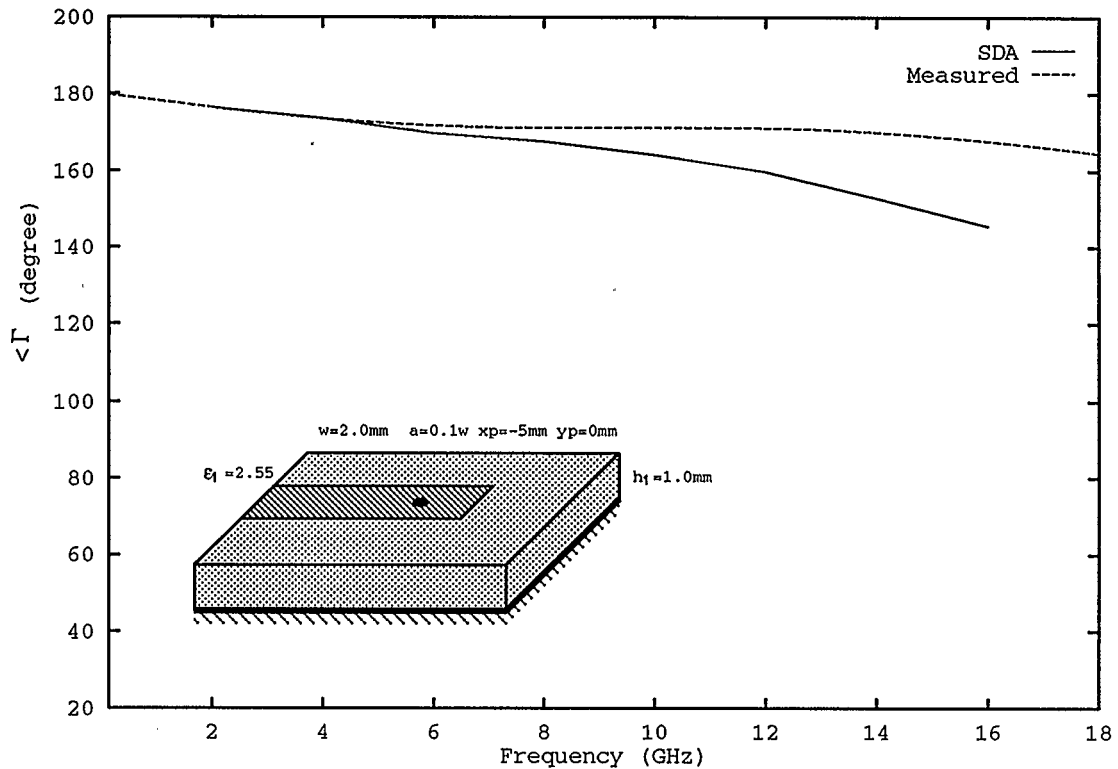


Figure 8.6: Frequency response of the reflection coefficient ($\angle \Gamma$) for a shorting via ($W = 2\text{mm}$, $h = 1\text{mm}$, $a = .1W$, $x_p = -5\text{mm}$, $y_p = 0\text{mm}$, $\epsilon_r = 2.5$).

reflection from the via, without good inclusion of the effect of the open end. The SDA method, on the other hand, gives the the combined effect of the via and the open end. In other words, the signal flow loop is included in the analysis.

The same explanation can be applied to Figure 8.6, which shows the computed and measured phase of the reflection coefficient as a function of frequency. It is noted that at low frequency ($f = 2\text{GHz}$) the phase is very close to that of an ideal short

circuit, that is, a perfect 180° . It is apparent that at D.C. this phase will be 180° . The higher the frequency, the smaller the phase. This means that as the frequency becomes higher, the reactance of the shorting via becomes larger.

Chapter 9

Measurement of Microstrip Discontinuities

Microstrip discontinuities are usually embedded in microstrip circuits. The most often seen discontinuities are corners, steps, opens, and gaps. They are all connected to transmission lines, in other words, they are embedded in a microstrip transmission line environment, which is in turn embedded in a coaxial line environment. This kind of configuration is most frequently seen, because almost all functional modules and measurement equipment use coaxial connectors as their input and output ports.

The question arises as to how one can measure embedded microstrip elements at the coaxial connectors? The procedure involved is called the de-embedding measurement. To directly measure a discontinuity is impractical, since there is no measurement equipment that can measure in microstrip without a coax-microstrip adapter. In addition, it is very difficult to manufacture highly accurate calibration standards for microstrip.

Therefore, the measurement has to be made at a pair of coaxial ports with a network analyzer. The behavior of the microstrip discontinuity can only be obtained with de-embedding techniques after the measurement has been made at coaxial connectors. Various de-embedding techniques have been studied and proposed by other

researchers [110][101][111][112]. Most of these methods make use of precise microstrip standards. Some methods, [101], for instance, have to use an automatic network analyzer with a time-domain reflection and transmission analysis feature, to which the accessibility is not guaranteed for every one.

TRL (Thru-Reflect-Line) technique was proposed by Engen and Hoer [110], and it is widely used in the measurement of non-coaxial circuits, such as microstrip transistors. In the calibration process, thru, reflection, and line are connected in turn to the network analyzer. This technique does not require the reflections to be known standards, which is a good feature for microstrip circuits measurement, where it is very difficult to build standards such as opens and shorts. To apply this technique, however, one has to use carefully fabricated fixtures that can give very good connections when the thru (T) is formed, and line (L) standard and later the DUT (Device Under Test) are inserted. For microstrip this is not easy to achieve. This method could have been used to determine the performance of microstrip discontinuities, however, it was not as another method was derived.

In this chapter, a new, simple technique is proposed for the measurement of microstrip discontinuities [113]. The method is similar to the TRL method, but it replaces the reflection component with another line of different length. The method uses a Line1-Line2-Line3 (multiline) calibration and it assumes that the two transitions (coax to microstrip) are identical. This method does not require any one-port standards, such as opens, shorts, and loads in microstrip. The de-embedding is

achieved with non-linear least squared error algorithm. The random errors in the fabrication of the circuits and in the measurement are minimized by using multiple through lines to introduce redundancy. The measurement can be made with any conventional network analyzers including those that do not have a time-domain feature.

Also in this chapter another de-embedding technique is briefly described, which makes use of the time-domain feature of automatic network analyzers [114]. Some discussions and observations are given.

9.1 Formulations

In microwave measurements, the discontinuity is often referred to as the DUT (Device Under Test), and the network surrounding it is called the intervening network. The process of determining the intervening network is called untermination. The process of obtaining the parameters of the DUT from measured data is called de-embedding [111].

9.1.1 DUT Circuit and Its Signal Flow Graph

A corner, as an example of the microstrip discontinuity circuits, is shown in Figure 9.1. The discontinuity is located between two sections of microstrip transmission line. The transmission lines are connected to the transition section which is be-

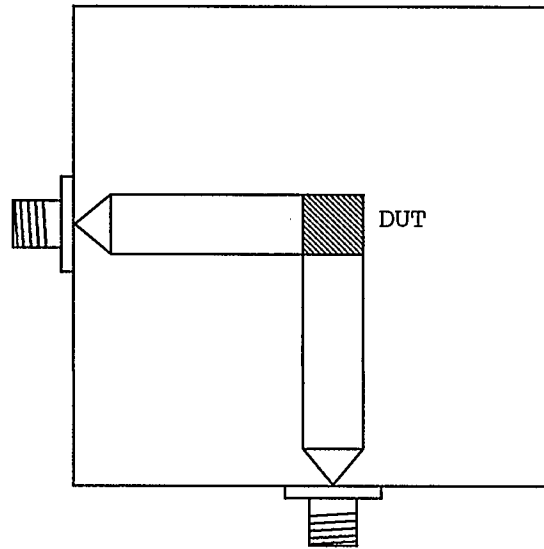


Figure 9.1: A microstrip discontinuity (corner) embedded in microstrip lines.

tween the microstrip transmission line and the coaxial line. The transition section usually consists of a coax-microstrip adapter, and/or a tapered microstrip line to have a smoother transition (match) between the microstrip transmission line and the adapter.

The signal flow graph representation of the circuit in Figure 9.1 is shown in Figure 9.2. It is noted that this is a simplified signal flow graph. The cross-talk couplings between the adapters at the two ports through substrate waves are neglected. The traveling wave is assumed to be TEM-like, with an effective propagation constant γ . The transition sections at the two ports of the circuit are modeled into two-port networks, the parameters of which, together with the effective propagation constant

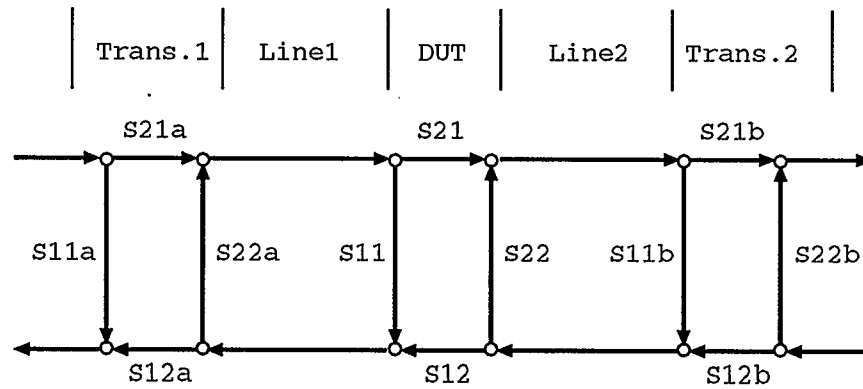


Figure 9.2: Signal flow graph for discontinuity measurement circuit.

γ , are to be determined in the unterminating process.

If the parameters of the transition network and the propagation constant γ are known, the parameters of the DUT can be easily determined from the measured data.

9.1.2 Through Lines as Standards

To determine the networks surrounding the discontinuity, standards have to be used. The number of these standards and the measurements usually depends on how complicated the intervening networks are. For most applications, simplifications can be applied to reduce the number of the unknowns, which consequently simplifies the untermination process.

The standards used in this method are simply through lines of different lengths, with the same type of transitions at the microstrip-coax adapters. The standards replace the DUT and its sections of transmission line temporarily in the measurement circuit (Figure 9.3). In reality the standards are fabricated on the same substrate and with the same connectors as the DUT.

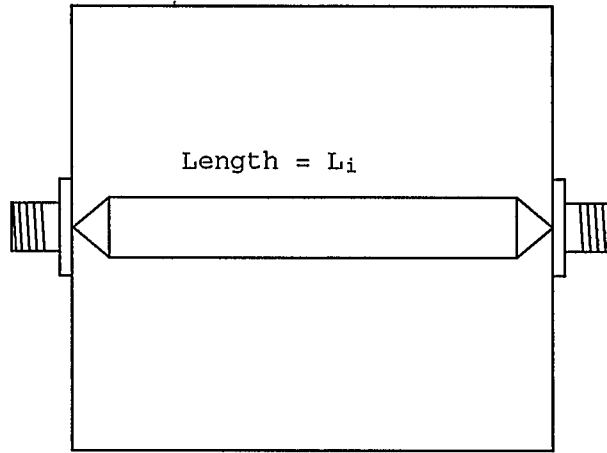


Figure 9.3: Through lines with different lengths as standards.

For most discontinuity circuits the two microstrip-coax transitions are identical (if not, another set of through lines is needed). These two networks are just placed in different orientations, which means, for instance that $S_{11a} = S_{22b} = S_{11t}$. Thus, for the transitions there are only 3 complex unknowns (S_{11t} , S_{22t} , and S_{21t}). The two transmission lines connected to the DUT have the same propagation constant γ . It is clear now that the task of the untermination process is to determine the S-parameters of the transition network (adapter) and the propagation constant of

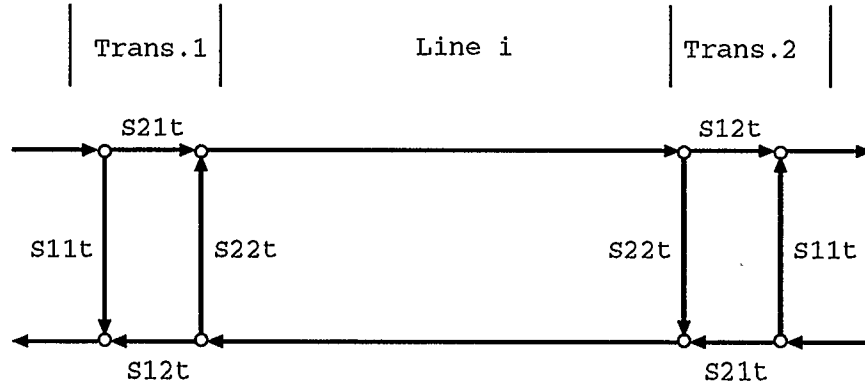


Figure 9.4: Signal flow graph for the through line standards.

the transmission line leading to the DUT. The signal flow graph of the through lines is shown in Figure 9.4.

The standards should be different from each other only in the lengths of the transmission lines. The other parameters should be kept as identical as possible.

Each of these standards can provide two independent equations in the measurement: $S_{11m}^{(i)}$, and $S_{21m}^{(i)}$, because they are symmetrical through lines. Therefore, theoretically, two of these type of standards should be enough to determine the 4 unknowns. However, due to the small differences between the physical circuits (other than the length difference) and the random errors in the measurement, two through line standards usually can not provide satisfactory results. One good feature for the proposed technique is that one can use more than two through lines in the untermination. The redundancy is used to minimize the random error effect. The results

can be obtained from a least squared error algorithm.

9.1.3 Multi-line Nonlinear Least Square Error De-embedding Techniques

As stated above, each through line can provide two independent equations from the measurement, namely,

$$S_{11m}^{(i)} = S_{11t} + \frac{S_{21t}^2 e^{-2\gamma l_i} S_{22t}}{1 - S_{22t}^2 e^{-2\gamma l_i}} \quad (9.1)$$

$$S_{21m}^{(i)} = \frac{S_{21t}^2 e^{-\gamma l_i} S_{22t}}{1 - S_{22t}^2 e^{-2\gamma l_i}} \quad (9.2)$$

$$(i = 1, 2, 3, \dots, N)$$

where S_{ijt} (i, j are either 1 or 2) are the S-parameters of the transition, γ is the propagation constant of the microstrip line, l_i is the length of i th through line, and N is the total number of the standard through lines used.

Choosing $N = 2$ will provide four independent equations. Theoretically these four equations are enough to solve for the S-parameters S_{ijt} and the propagation constant γ of the transmission line. However, if the measurement is noisy, redundancy has to be used to reduce the effect of the random noise and a least squared error undertermination results. In this case, N is chosen to be greater than 2.

Using Newton's method, the iterative root searching algorithm will be:

$$X_{4 \times 1}^{(n+1)} = X_{4 \times 1}^{(n)} - [J_{4 \times 2N}^T \cdot J_{2N \times 4}]^{-1} \cdot J_{4 \times 2N}^T \cdot F(X^{(n)})_{2N \times 1} \quad (9.3)$$

where $X_{4 \times 1}^{(n)}$ is a vertical vector whose elements are the four unknowns: $S_{11t}, S_{22t}, S_{21t}$ and γ at the n -th step in the iteration; $J_{2N \times 4}$ is the so-called Jacobi matrix, defined

as

$$J_{2N \times 4} = \begin{bmatrix} \frac{\partial f_1}{\partial x_1} & \frac{\partial f_1}{\partial x_2} & \frac{\partial f_1}{\partial x_3} & \frac{\partial f_1}{\partial x_4} \\ \frac{\partial f_2}{\partial x_1} & \frac{\partial f_2}{\partial x_2} & \frac{\partial f_2}{\partial x_3} & \frac{\partial f_2}{\partial x_4} \\ \vdots & \vdots & \vdots & \vdots \\ \frac{\partial f_{2N}}{\partial x_1} & \frac{\partial f_{2N}}{\partial x_2} & \frac{\partial f_{2N}}{\partial x_3} & \frac{\partial f_{2N}}{\partial x_4} \end{bmatrix}$$

and $F(X^{(n)})_{2N \times 1}$ is the equation value at $X^{(n)}$.

After the root vector to the equations is obtained, one can use it to de-embed the DUT with the following expression:

$$[T]_{DUT} = [T]_{line1}^{-1} [T]_{trans.f}^{-1} [T]_{measure} [T]_{trans.b}^{-1} [T]_{line2}^{-1} \quad (9.4)$$

where all $[T]$'s are the ABCD matrices of the circuit components, and particularly, $[T]_{trans.f}$ and $[T]_{trans.b}$ are the ABCD matrices for the forward and the backward transitions, respectively.

9.2 Results

9.2.1 Untermination

The first circuit studied here is a microstrip corner. The circuit parameters are as follows: substrate thickness $h = 12.7mm$, dielectric constant $\epsilon_r = 2.40$, and strip width $w = 37.0mm$.

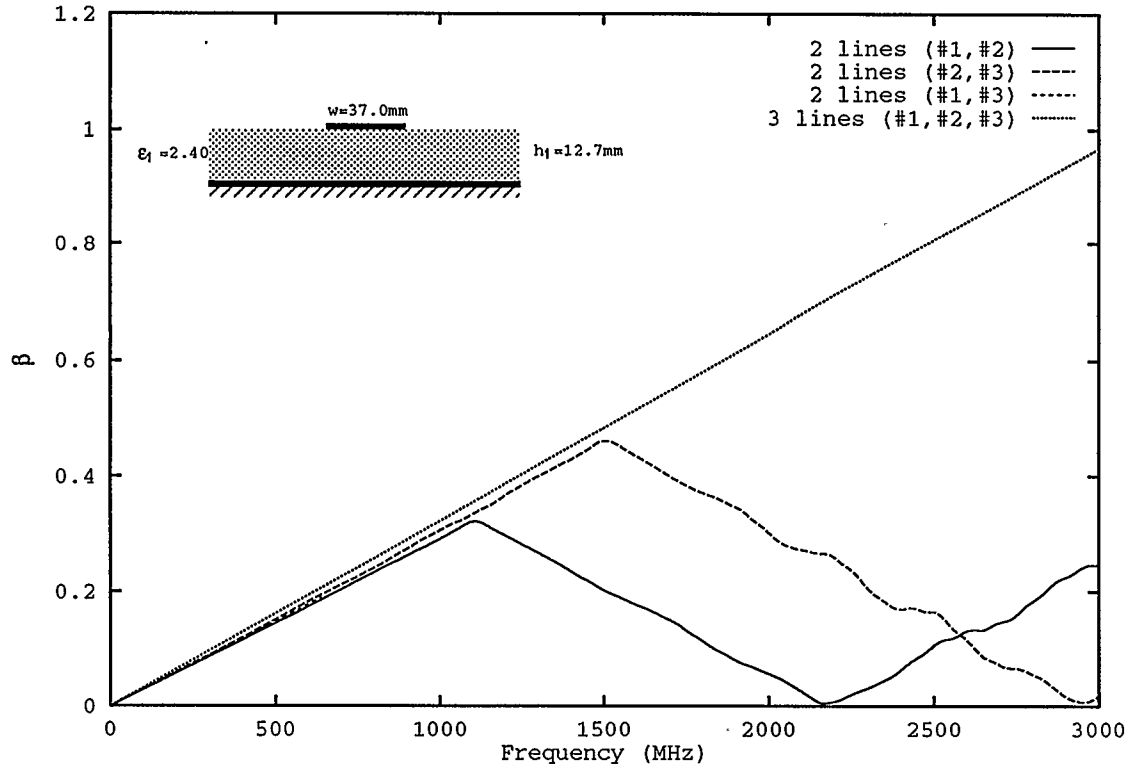


Figure 9.5: $\text{Im}(\gamma)$ of the intervening transmission line ($W = 37.0\text{mm}$, $h = 12.7\text{mm}$, $\epsilon_r = 2.4$).

The untermination process determines the four network parameters of the intervening networks, using the nonlinear least squared error techniques (Equation 9.3). Figure 9.5 is the imaginary part of the propagation constant of the transmission line. Three standard lines are measured to unterminate the intervening networks. It is known that this imaginary part is also called wave number, and is defined as:

$$\text{Im}(\gamma) = \beta = \frac{2\pi}{\lambda_e(f)} \propto \sqrt{\epsilon_e(f)} \cdot f$$

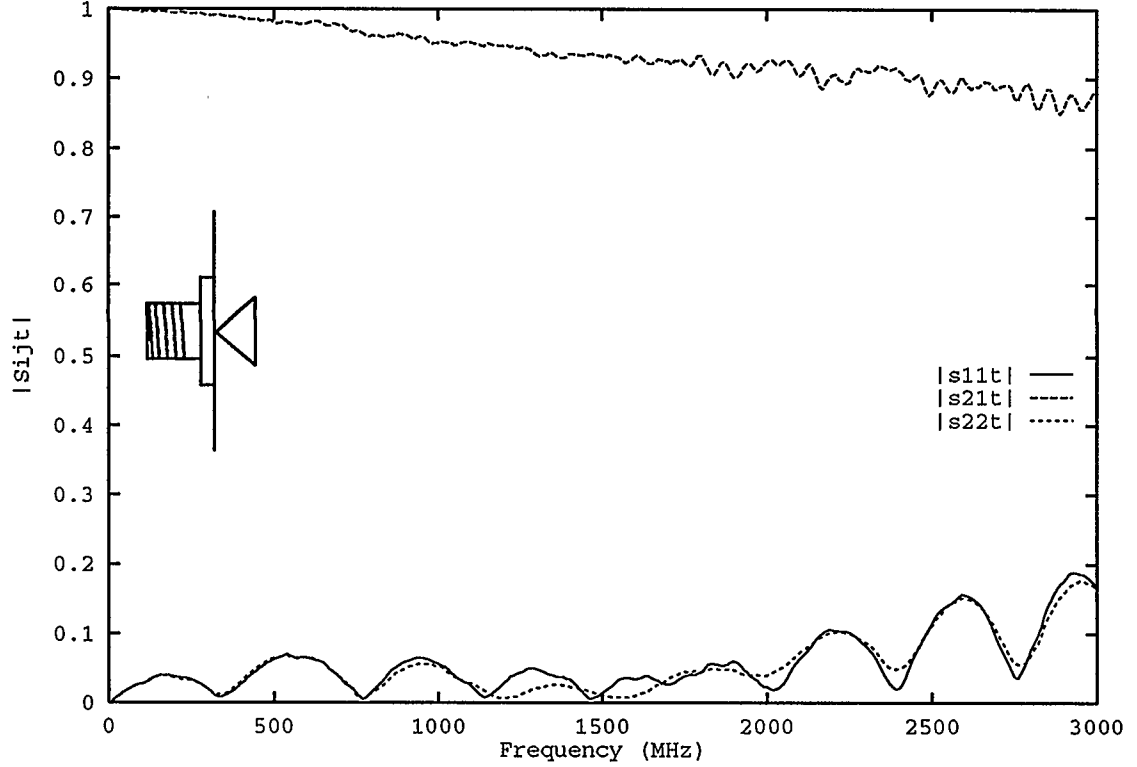


Figure 9.6: S-parameters of the coax-microstrip transition obtained with three standard lines.

Since $\sqrt{\epsilon_e(f)}$ changes very slowly with the frequency, $Im(\gamma)$ as a function of frequency is expected to be basically a linear function of frequency. As shown in Figure 9.5, the combinations of any two standard lines failed to give this result. The combination of line 1 and 3 does not even converge after around $f = 800\text{MHz}$ (It is not very visible because it overlaps with other lines). It is notable that the three line combination gives a smooth and straight line. There are still some small ripples

on the curve, but the random error effects have been greatly reduced.

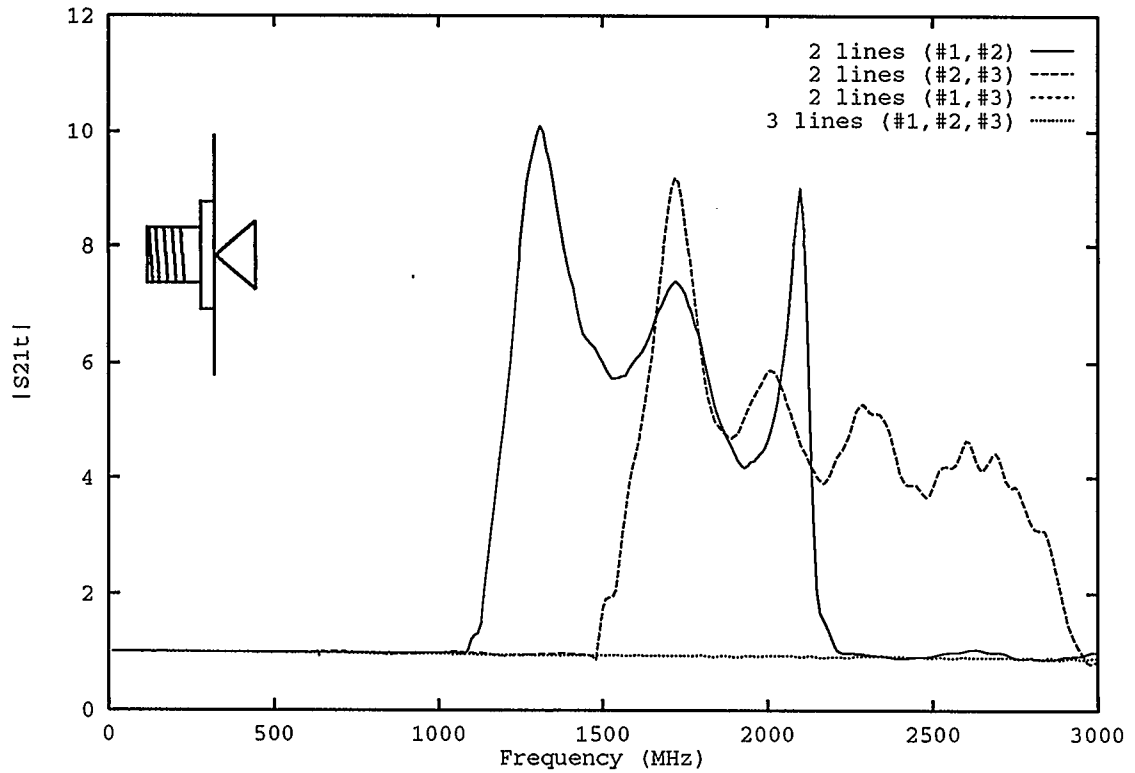


Figure 9.7: Comparison of 3-line and 2-line untermination of the coax-microstrip transition.

Figure 9.6 is the S-parameter of the transition part of the circuit determined with three standard lines ($N = 3$). If, on the other hand, only two lines are used, as shown in Figure 9.7, the results are obviously incorrect (note again The combination of line 1 and 3 does not even converge after around $f = 800\text{MHz}$). For the purpose of comparison, the three-line results for $|S_{21t}|$ is replotted in Figure 9.7. All of the

two-line combination results give some unrealistic values ($|S_{21}| > 1.0$) over certain frequency bands, while three lines gives bounded results.

It is notable from Figure 9.5 and Figure 9.7 that the data of S_{21t} blows up at the frequency where β bends down. This is due to the error in the construction of the circuits and the noise in the measurement. This argument is supported by the noiseless simulations made on computers where two through lines always gave good straight line for β and bounded S_{21t} .

9.2.2 De-embedding of the DUT

The network parameters obtained from the untermination process are then used to remove the effects of the intervening networks from the measured data, using Equation 9.4. The measured data for the corner are first transformed into the ABCD matrix format, then the matrix is left or right multiplied by the inverse of the ABCD matrices of other cascaded networks.

Figure 9.8 shows the comparison of $|S_{11}|$ between the de-embedded and unde-embedded (raw measured) results. As shown in this figure, the de-embedding process successfully removed the effects of the multiple reflections between the two connectors, which causes the data to oscillate about the real value. It is also noted that there is still room for improvement in the final data. Some ripple effects can still be seen as the plot is still not a completely smooth curve. The ripple can be due

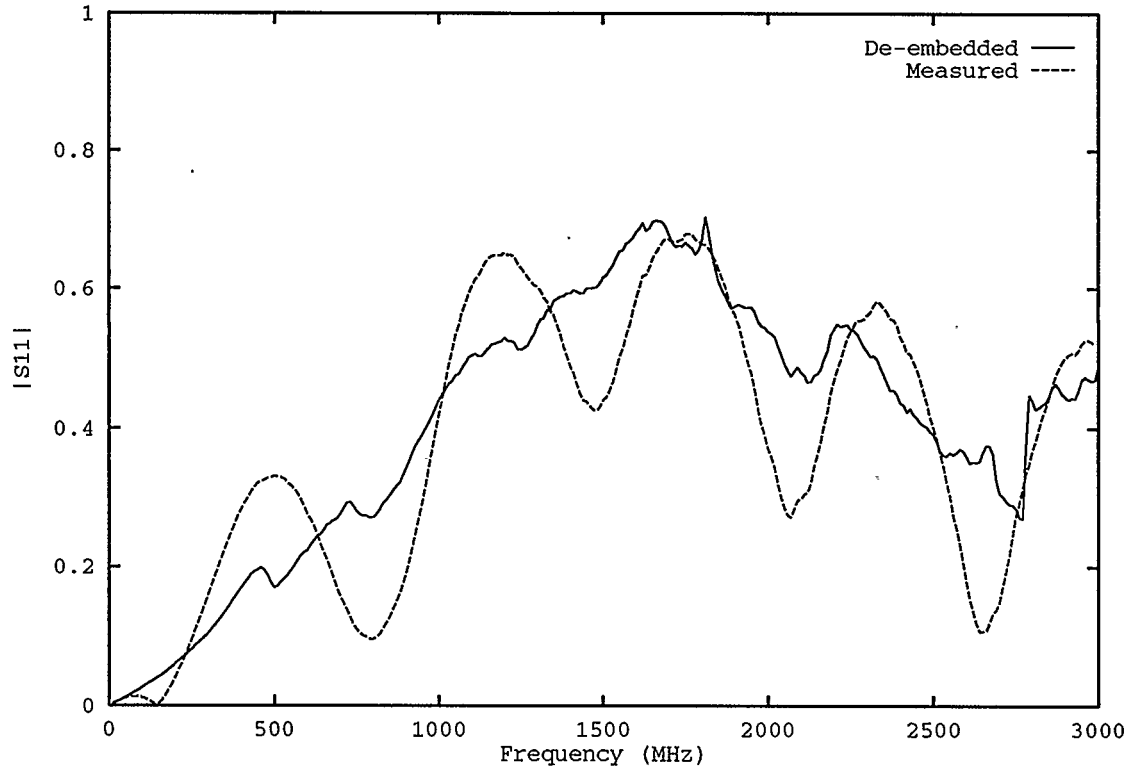


Figure 9.8: Comparison of a corner's de-embedded $|S_{11}|$ with measured data ($W_1 = W_2 = 37.0\text{mm}$, $h = 12.7\text{mm}$, $\epsilon_r = 2.4$).

to the noise in the measurements, the imperfect fabrication of the (standards and DUT) circuits, and surface waves propagation between the two transitions. It is believed that to further remove the random error effects, a multi-DUT circuit might be recommended. This way, a reasonable mean behavior may be obtainable which would provide smoother measurement results.

Figure 9.9 is the comparison of the transmission scattering parameter ($|S_{21}|$) of

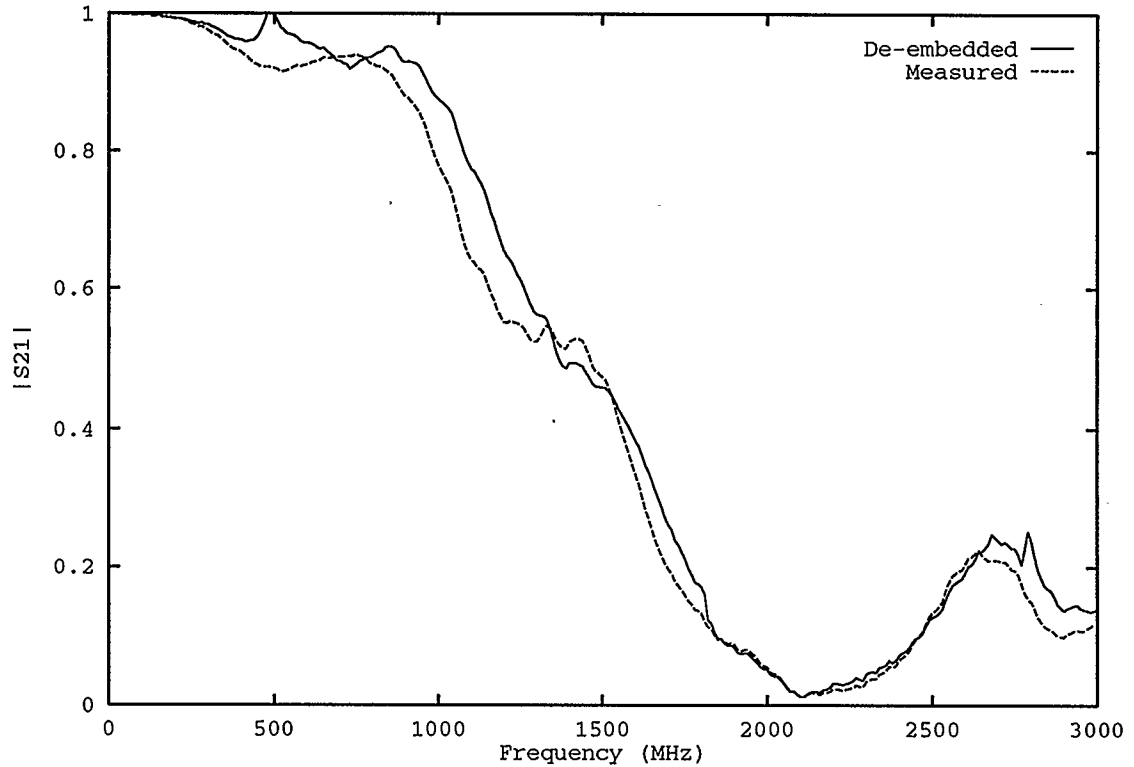


Figure 9.9: Comparison of a corner's de-embedded $|S_{21}|$ with measured data ($W_1 = W_2 = 37.0\text{mm}$, $h = 12.7\text{mm}$, $\epsilon_r = 2.4$).

the same corner. This figure shows very close agreement between the measured and de-embedded results. This is due to the relative large magnitude of the corner transmission ($|S_{21}|$) itself, and small reflection of the transitions so that the one-pass trip makes very significant contribution to the measured data. The oscillatory effects are again seen to be removed to some extent.

9.3 Other De-embedded Discontinuities

9.3.1 Open

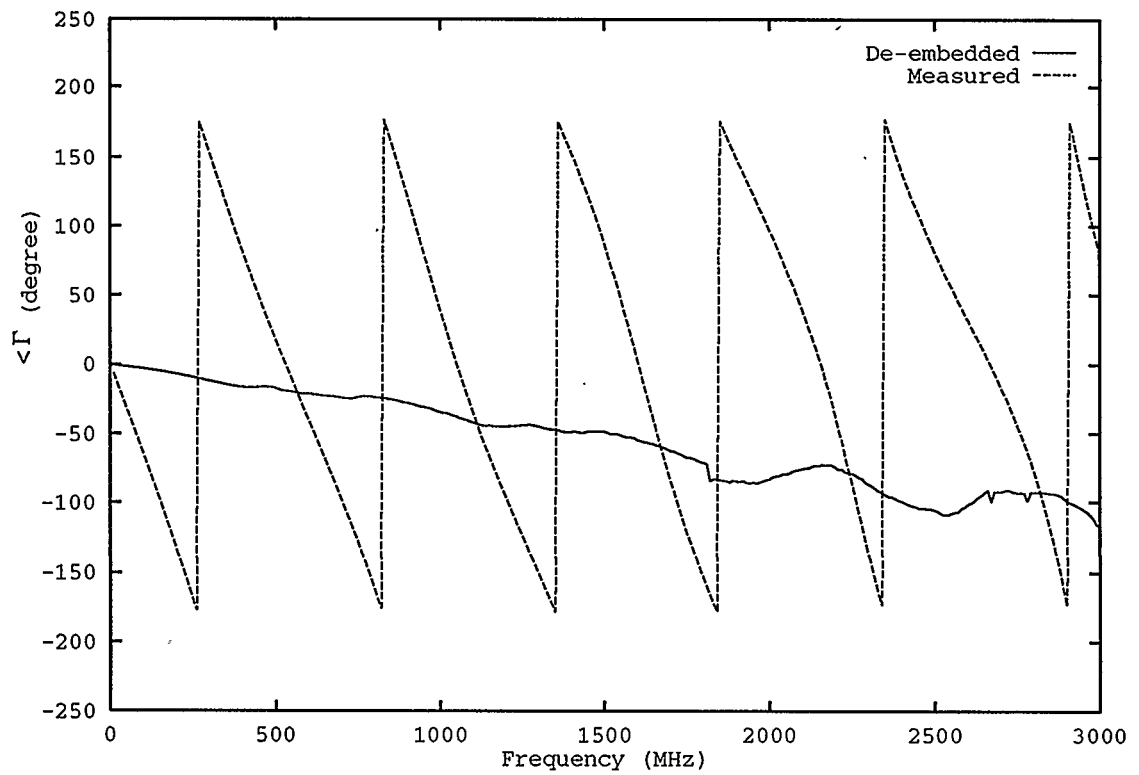


Figure 9.10: Comparison of an open circuit reflection: de-embedded and measured ($W = 37.0\text{mm}$, $h = 12.7\text{mm}$, $\epsilon_r = 2.4$).

The technique can also be applied to one-port discontinuities such as opens and shorts, because the basic idea is to solve a cascaded network problem.

Figure 9.10 shows the phase of an open circuit on the same board and with the same strip width. The rapid phase change caused by the transition and the length of the transmission line is removed and smooth phase curve results. It is noted that the phase decreases as the frequency increases. This effect has been widely observed and analyzed as an excess length effect (see Chapter 4). There are still some random error effects on the de-embedded results. If better results are required, two or more similar open circuits should be used.

9.3.2 Short

Figure 9.11 shows the phase of a short circuit on the same board and with the same strip width. The rapid phase change is again removed by the de-embedding process. Unlike the open circuit, the phase for the short does not decrease as rapidly as the open circuit. This is because the reference plane is moved next to a real short end. The only effect that changes the phase is the physical thickness of the board, which is not very sensitive to frequency. It is noted that the higher the frequency, the bigger the oscillation. This suggests that variations in the standard line transitions differed from the transition in the shorted line, especially at higher frequencies. For better accuracy at high frequencies, more precise standards may be needed.

9.3.3 Zero Length Transmission Line

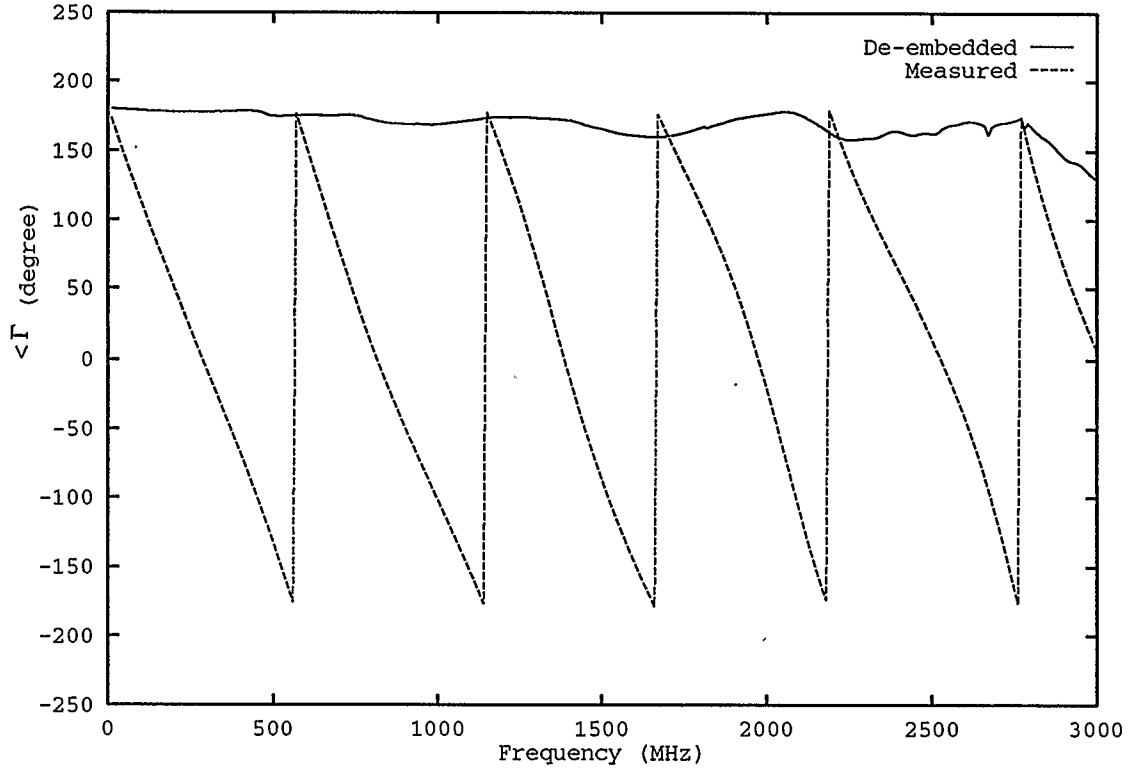


Figure 9.11: Comparison of a short circuit reflection: de-embedded and measured ($W = 37.0\text{mm}$, $h = 12.7\text{mm}$, $\epsilon_r = 2.4$).

To further investigate the proposed technique, an imaginary network is assumed to be placed at the center of a standard through line. This network is a zero length transmission line, whose S-parameters are ideal, i.e, all pass for transmission parameters and zero for reflection parameters.

Figure 9.12 and 9.13 are the de-embedded S-parameters of this imaginary network. As shown in these figures, the results are reasonably good at relatively low

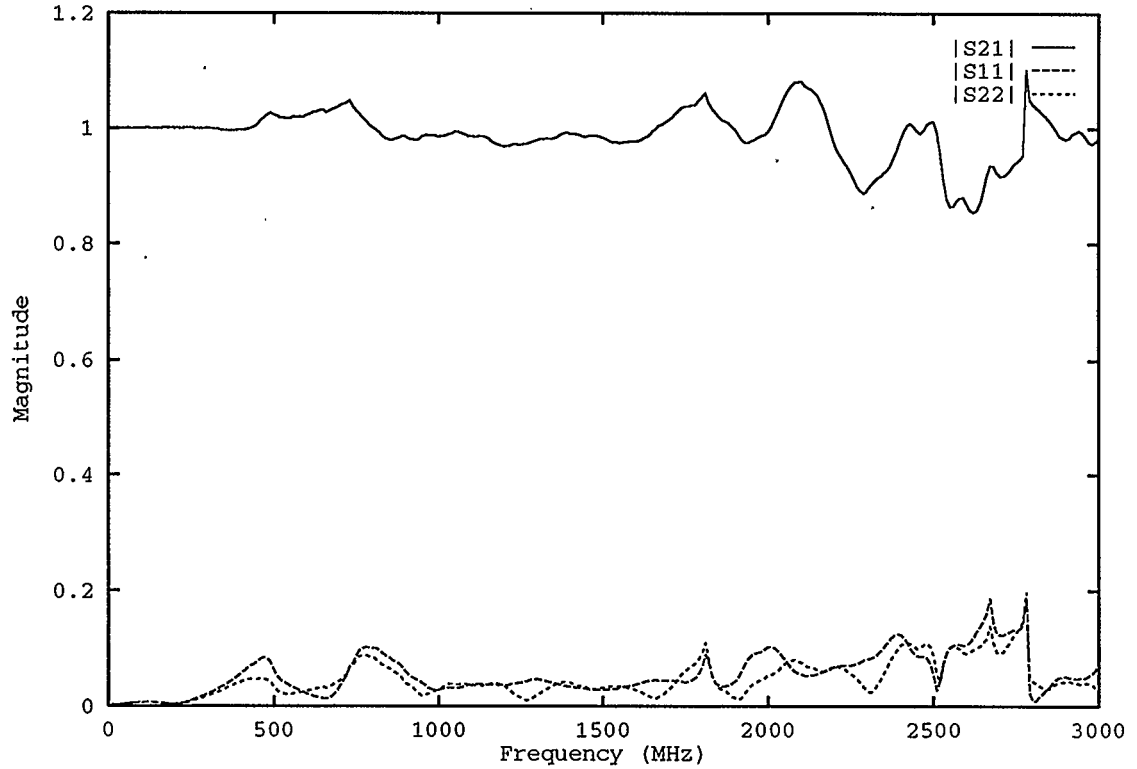


Figure 9.12: Magnitude of zero length transmission line S-parameters ($W = 37.0\text{mm}$, $h = 12.7\text{mm}$, $\epsilon_r = 2.4$).

frequency. At higher frequencies, the error becomes significant. The magnitude is not very large, compared relatively. The phases of the reflection parameters change drastically. But that of the transmission parameters are constantly small. This is because that at nearly zero reflection magnitude, the phases are hard to measure. They are basically the phases of noise, whereas for transmission parameters there is a predominant signal part that determines the phase.

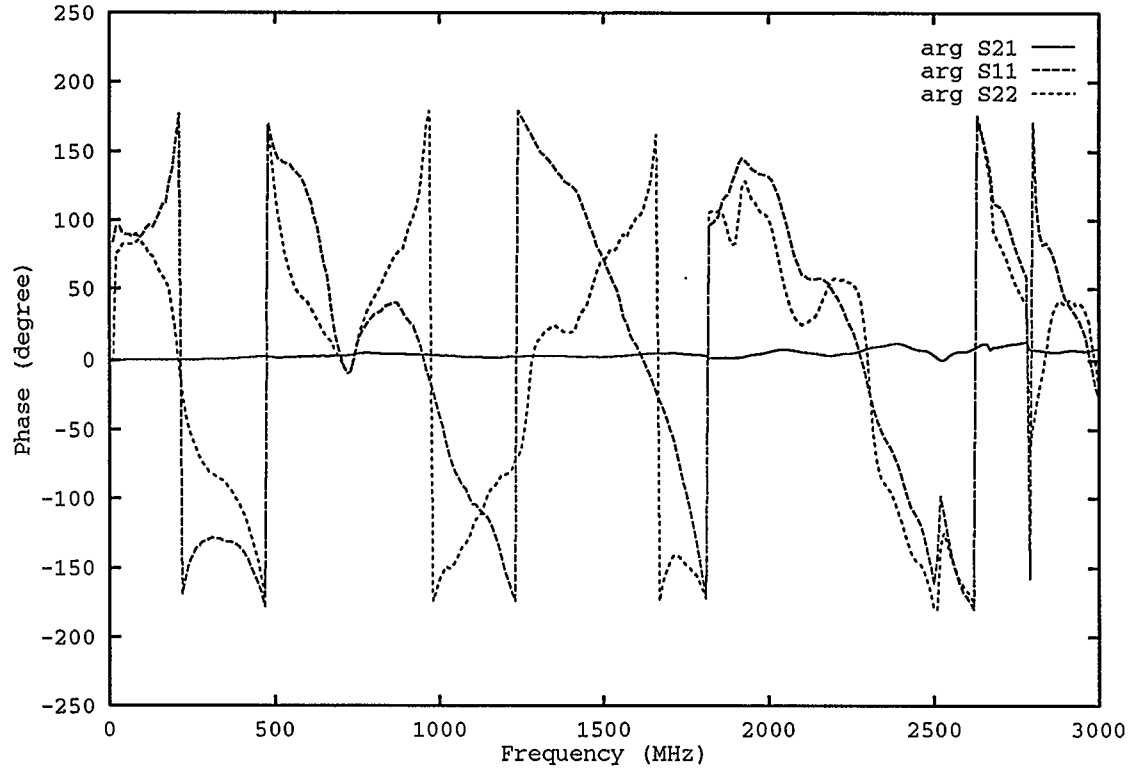


Figure 9.13: Phase of zero length transmission line S-parameters ($W = 37.0\text{mm}$, $h = 12.7\text{mm}$, $\epsilon_r = 2.4$).

9.4 Conclusions on the Multi-Line Method

The error in the zero length transmission results is not necessarily that of the DUT de-embedding. The error here is merely that between the least squared error results of the multiple through line and this particular through line where the imaginary network is assumed. The main error source is the nonidentical construction of the

transitions in the through lines . Since this construction error is random and removable, good results with minimum error could be obtained with multiple DUT circuits along with multiple through line standards. Although this technique may not be the most convenient way of measuring discontinuities, when accurate circuit measurement is required, this method can give good results. The penalty for the accuracy is the cost of the extra circuits, measurement, and numerical work.

9.5 De-embedding with Time-Domain Network Analyzers

If an automatic network analyzer with the time-domain option installed is available, one can make use of the time-domain feature to de-embed a DUT relatively easily. If the standard line and the DUT circuit are designed to be of the same length, one only has to use one standard to have the DUT de-embedded.

The method is simple and straight forward. The measurement procedure is as follows:

1. a standard through line is measured for the one-trip pass response on a HP8510 automatic network analyzer (ANA), in the inverse Fourier-transformed time domain, with low-pass time domain gate turned on [115], Since the through line is a combination of transition1-line-transition2, the measured one-trip response S_{21s}^t is

$$S_{21s}^t = S_{21st}^{[1]} e^{-\gamma l_s} S_{21st}^{[2]}, \quad (9.5)$$

where l_s is the length of the transmission line, and $S_{s21st}^{[1]}$ and $S_{s21st}^{[2]}$ are the S_{21} 's of the two transitions in the standard through line.

2. The DUT circuit is constructed in a way that the two sections of the transmission line (l_1 and l_2) are of the same length, and satisfies the relationship:

$$l_1 = l_2 = \frac{l_s}{2}.$$

3. For S_{21}^{DUT} , a one-trip pass response measurement S_{21m}^t is made on the DUT circuit. The following result is obtained:

$$S_{21m}^t = S_{21dt}^{[1]} e^{-\gamma l_1} S_{21}^{DUT} e^{-\gamma l_2} S_{21dt}^{[2]} \quad (9.6)$$

where $S_{21dt}^{[1]}$ and $S_{21dt}^{[2]}$ are the S_{21} 's of the two transitions in the DUT circuit.

S_{21}^{DUT} can be obtained simply using the expression

$$S_{21}^{DUT} = \frac{S_{21m}^t}{S_{21s}^t}$$

4. For S_{11}^{DUT} , a one-trip reflection response measurement S_{11m}^t is made on the DUT circuit, and one has

$$S_{11m}^t = (S_{21dt}^{[1]})^2 e^{-2\gamma l_1} S_{11}^{DUT} \quad (9.7)$$

Since $l_s = 2 \times l_1$, S_{11}^{DUT} can be obtained as

$$S_{11}^{DUT} = \frac{S_{11m}^t}{S_{21s}^t}$$

This time-domain de-embedding technique does not require heavy data processing. But, needless to say, one has to have access to a network analyzer with a time-domain feature, and since there is no redundancy in the measurement, the circuit must be fabricated very precisely in order to have an accurate result. A great deal of attention has to be paid to the identicalness of the four transitions in the standard through line and the DUT circuit so that the following relationship holds:

$$S_{21st}^{[1]} \approx S_{21st}^{[2]} \approx S_{21dt}^{[1]} \approx S_{21dt}^{[2]}.$$

During this dissertation research, the access to HP8510 automatic network analyzer was not possible until early 1992. So some early measurements were made on a HP8410 network analyzer at Novatel Communications, Inc., which does not have time domain feature. In addition, the cables used were not in good condition, and the circuit board was relatively thick (.5"). Therefore, the early measurements were somewhat noisy, and the frequencies at which reliable measurements could be made were only as high as up to 3GHz.

Chapter 10

Conclusions

In this dissertation, various typical microstrip discontinuities in multilayered media have been investigated. Attempts have been made to generalize the analyses. The use of the spectral domain method enables the inclusion in the analysis of all the aspects of the main concerns of microwave engineers have, namely, the power loss into the sub/superstrates (surface waves), into free space (radiation), and to the media bulk resistance (heat loss). With modified boundary conditions, it is also possible to account for the loss to the microstrip surface resistance. Due to its rigorousness, this spectral domain method is a full-wave method of analysis.

For each discontinuity type, an analysis program has been written in C++ which is intended to cover all the aspects in which microwave engineers may possibly be interested. The numerical method used is the moment method. The exact and modified Galerkin's procedure have both been used. In some instances, the convergence behavior of them is compared. It is found that the modified version is more suitable for microstrip discontinuities where the local nature of the boundary conditions needs to be emphasized. The programs are also generalized in that the user only needs to provide the description of the media, and the dimensions of the strip. A step-up procedure is used to let the user view the convergence of the process. As soon

as satisfactory convergence is reached, the user can stop the process. This step-up procedure saves time at no loss of accuracy.

The Green's function plays a key role in all analyses, because it describes the geometries and the electromagnetic properties of the whole medium. The definition of the Green's function as the response to an impulse source makes it easier to get a closed form expression in the 2-D Fourier domain. The generalization is successful in accounting for multilayer and lossy media structures with or without top and bottom conductor layers. All of the nine elements in a dyadic Green's function can be calculated, which lays a solid foundation for analyses of any possible configuration of microstrip transmission line discontinuities and microstrip antennas with or without vertical coax-feed in multilayer structures.

The infinitely long microstrip transmission line is the most basic component in all microstrip circuits. Its analysis has been generalized in Chapter 3. A careful convergence test is carried out. The algorithm is also used in the following chapters where discontinuities with semi-infinite transmission lines are studied. The two most important parameters for a transmission line, propagation constant γ (or alternatively, the effective dielectric constant $\sqrt{\epsilon_e}$) and characteristic impedance Z_0 , can be calculated for any multilayer structure. A generalized Poynting vector function is derived for the computation of the transmitted power along the transmission line in a multilayered structure. The results have been found to be in good agreement with measured data and in good agreement with quasi-static results at low frequency,

which suggests that the spectral domain method is full-band applicable, if appropriate basis functions are used. The application of the multilayer sub/superstrates can result in low dispersion transmission lines, and possibly frequency compensation is achievable.

Opens and gaps are analyzed as typical 1-D discontinuities. The moment method used, unlike the one in the infinite line analysis, is a modified Galerkin's procedure. The testing function corresponding to the traveling wave base function is changed to a PWS function local to the discontinuity. This has been shown to be able to give better convergence, because the locality of the boundary condition is emphasized. The results are found to be in good agreement with the measurements. The results are also compared with the predictions by commercial software package Touchstone. Some meaningful results have been observed. One good feature of this technique is that it can predict the loss of power into the substrate and the space at the open or the gap. Touchstone, and most other quasi-static analyses, on the other hand, assume lossless discontinuities.

The most commonly seen discontinuities in microstrip circuits are two dimensional. These 2-D discontinuities include the corner, step, bend, and Tee. To analyze them, the horizontal current flow has to be assumed to be in both x and y direction. Therefore the analysis is more involved, because the reactions are now between the base and testing functions in different directions as well as in the same directions, and transverse direction current on each branch of the discontinuity can

not be neglected. Although the analysis is more complicated for 2-D discontinuities, the basic principle remains unchanged. A corner is analyzed in Chapter 6. The moment method is applied again to reconstruct the local current distribution in the corner region.

Through the examples of a corner and many others in other chapters, a picture has become very clear as to how Green's function and the moment method solve a specific problem. Taking the corner as an example, the input is the traveling wave on branch 1. This is the only known quantity given. There are many unknown quantities in this problem: how large is the reflection on branch 1? how large is the transmission on branch 2? and how are local piece-wise-sinusoids (PWS) distributed?. Before applying the testing functions in the moment method, all we know is the expression for the EM field produced by the input current and the assumed currents (reflection, transmission, and the PWS's). When the testing functions are applied to form the inner products with the tangential electric field on the strip surface, the input and the output (unknown currents) are joined together. The PWS functions play very important roles in this joint, because the corner region is where the input current transfers the energy to the reflected wave and transfers the energy on to the output branch to finish the transmission. These basis PWS functions construct the local current distribution. The testing functions (also PWS) make sure the boundary conditions are not violated on the strip surface.

Vertical objects are often seen in microstrip circuits. For instance, in active

circuits usually screws or metalized holes are used to ground devices; microstrip antennas are usually fed with a coaxial line from the ground plane. A vertical dipole has been analyzed as an example of a vertical conducting object in a stratified medium. Good agreement has been observed with the results obtained from the spatial domain method. As a matter of fact, the spectral domain method only converts the horizontal coordinates into the Fourier domain. The vertical coordinate z remains intact. The spatial domain Green's function in a homogeneous medium is readily available [58]. However, it is difficult, if not impossible, to get a closed form expression in the spatial domain for Green's function G_{zz} in stratified media. It is even more difficult if this Green's function is for a source and a field pair in different directions. It takes much computer time to evaluate Green's function for vertical objects unless the vertical wire is a short one such as the feed pin from the coaxial line.

An example of comprehensive use of the dyadic Green's function is the analysis of the shorting pin at the end of a semi-infinite microstrip transmission line, where almost all nine elements of the dyad are used. Again the input is a traveling wave from $x = -\infty$, which reflects and radiates at the discontinuity. The moment method is used to determine the current distribution, by enforcing the boundary conditions on the conductor surface. The magnitude and the phase of the reflected wave is thus determined. This procedure can be viewed as the input wave being converted to the local currents (PWS's and the current on the pin) and the reflected wave, with the help of the testing functions enforcing the boundary conditions. In other words,

without the testing functions enforcing the boundary conditions, no currents can be excited on the pin, for the PWS's, and for the reflected wave.

Also in this dissertation, a de-embedding technique for accurate measurement of discontinuities is developed and applied successfully to some of the discontinuities. This method uses redundancy to reduce the effects of random errors in the measurement and in the fabrication of the standard lines and the DUT circuit. The most serious source of errors is believed to be the un-identicalness of the transitions between microstrip lines and the coaxial connectors. Using multiple through lines and multiple DUT circuits this error can be minimized in a least squared error sense. Thus the procedure is an over-determined, nonlinear least squared error numerical method. While this method appears to be inefficient and uneconomical, it is, however, a good choice for accurate measurements. The main advantage of this method is that one can use circuits that are not precisely fabricated. They only have a reasonably good average, and the redundancy introduced from extra circuits is used to minimize the error.

The transmission lines involved in this dissertation are all assumed to be slender strips, which makes possible the assumption that only longitudinal current flows on the strip away from the discontinuity. For electrically wide strips transverse current flow should be included in the analysis. The main drawback of the spectral domain method is the relatively long CPU time it takes to fill out the matrices of the MoM. There are two ways to speed up the process in the spectral domain: (1) one

can truncate the numerical integration early and use the asymptotic expressions to calculate the tail contribution, which can be very tedious; (2) one can consider the effects (field) of the elements (current patch) only in close proximity and neglect the field generated by the distant elements. It is not a big problem in the spatial domain, where Green's functions can be approximated with complex images [31][32]. In other words, assume that the distant elements do not exist. The error thus introduced, however, must be known a priori. These two methods, of course, can be used together to get even shorter computational time.

The analysis of more complicated configurations is possible. With the generalized Green's function, almost all possible microstrip circuits are analyzable. The only restriction is that they have to comply with the assumption that the dielectrics are isotropic, and the medium is stratified and is essentially of a planar construction. (For finite size stratified medium, it is viable to use the discrete 2-D Fourier transform to get a discrete spectral domain Green's functions).

In addition to speeding up of the numerical process, future work could also be done on other types of circuits. For instance, work can be done on a coaxial or strip line fed patch and slot antennas now used widely in indoor communications, the mutual coupling between transmission lines in multilayer structures such as VLSI, MMICs, microstrip phased arrays, and coupler designs. Also an interesting area is to extend the analysis into the discrete spectral domain, because the circuits involved are in reality finite in size. Jackson used side wall image to compute the package

effect of MMIC circuits [116]. or the combinations of different analysis techniques, such as the spatial-spectral domain approach [117], for instance, which have proved to be effective in overcoming difficulties and drawbacks if only one single technique is employed.

Bibliography

- [1] A. Sommerfeld, *Partial Differential Equations in Physics*, Academic Press, New York, 1949.
- [2] Alfredo Banos, Jr, *Dipole Radiation in the Presence of a Conducting half-space*, Pergamon Press, Oxford, 1966.
- [3] E. Yamashita and R. Mittra, "Variational method for the analysis of microstrip line", *IEEE trans. Microwave Theory and Techniques*, vol. MTT-16, pp. 251–256, Apr. 1968.
- [4] E.J. Denlinger, "A frequency dependent solution for microstrip transmission lines", *IEEE trans. Microwave Theory and Techniques*, vol. MTT-19, pp. 30–39, Jan. 1971.
- [5] T. Itoh and R. Mittra, "Spectral-domain approach for calculating the dispersion characteristics of microstrip lines", *IEEE trans. Microwave Theory and Techniques*, vol. MTT-21, pp. 496–499, July 1973.
- [6] T. Itoh and R. Mittra, "A technique for computing dispersion characteristics of shielded microstrip lines", *IEEE trans. Microwave Theory and Techniques*, vol. MTT-22, pp. 896–898, Oct. 1974.
- [7] T. Itoh, "Analysis of microstrip resonators", *IEEE trans. Microwave Theory and Techniques*, vol. MTT-22, pp. 946–952, Nov. 1974.

- [8] T. Itoh, "Generalized spectral domain method for multiconductor printed lines and its application to turnable suspended microstrips", *IEEE trans. Microwave Theory and Techniques*, vol. MTT-26, pp. 983–987, Dec. 1978.
- [9] T. Itoh, "Spectral domain immittance approach for dispersion characteristics of generalized printed transmission lines", *IEEE trans. Microwave Theory and Techniques*, vol. MTT-28, pp. 733–736, July 1980.
- [10] N. Herscovici and D.M. Pozar, "Full-wave analysis of aperture-coupled microstrip lines", *IEEE trans. Microwave Theory and Techniques*, vol. MTT-39, pp. 1108–1114, July 1991.
- [11] H-Y. Yang and N.G. Alexopoulos, "A dynamic model for microstrip-slotline transition and related structures", *IEEE trans. Microwave Theory and Techniques*, vol. MTT-36, pp. 286–293, Feb. 1988.
- [12] H-Y. Yang and N.G. Alexopoulos, "Basic blocks for high-frequency interconnects: theory and experiment", *IEEE trans. Microwave Theory and Techniques*, vol. MTT-36, pp. 1258–1264, Aug. 1988.
- [13] S-C. Wu, H-Y. Yang, N.G. Alexopoulos, and I. Wolff, "A rigorous dispersive characterization of microstrip cross and T junctions", *IEEE trans. Microwave Theory and Techniques*, vol. MTT-38, pp. 1837–1944, Dec. 1990.
- [14] S. Papatheodorou, J.R. Mautz, and R.F. Harrington, "Full-wave analysis of a strip crossover", *IEEE trans. Microwave Theory and Techniques*, vol. MTT-38,

pp. 1439–1448, Oct. 1990.

- [15] W.P. Harokopus and L.P.B. Katehi, “Electromagnetic coupling and radiation loss considerations in microstrip (M)MIC design”, *IEEE trans. Microwave Theory and Techniques*, vol. MTT-39, pp. 413–420, Mar. 1991.
- [16] U.V. Gothelf and A. Ostergaard, “Full-wave analysis of a two slot microstrip filter using a new algorithm for computation of the spectral integral”, *IEEE trans. Microwave Theory and Techniques*, vol. MTT-41, pp. 101–108, Jan. 1993.
- [17] N.I. Dib, P.B. Katehi, G.E. Ponchak, and R.N. Simons, “Theoretical and experimental characterization of coplanar waveguide discontinuities for filter applications”, *IEEE trans. Microwave Theory and Techniques*, vol. MTT-39, pp. 873–882, 1991.
- [18] T.R. Arabi, A.T. Murphy, and T.K. Sarkar, “Electric field integral equation formulation for a dynamic analysis of nonuniform microstrip multi-conductor transmission lines”, *IEEE trans. Microwave Theory and Techniques*, vol. MTT-40, pp. 1857–1869, Oct. 1992.
- [19] N.I. Dib, G.E. Ponchak, and L.P.B. Katehi, “A theoretical and experimental study of coplanar waveguide shunt stubs”, *IEEE trans. Microwave Theory and Techniques*, vol. MTT-41, pp. 38–44, Jan. 1993.
- [20] N. Faché, F. Olyslager, and D. De Zutter, “Full-wave analysis of coupled

- perfect conducting wires in a multilayered medium", *IEEE trans. Microwave Theory and Techniques*, vol. MTT-39, pp. 673–680, Apr. 1991.
- [21] F. Olyslager, D.D. Zutter, and K. Blomme, "Rigorous analysis of the propagation characteristics of general lossless and lossy multiconductor transmission lines", *IEEE trans. Microwave Theory and Techniques*, vol. MTT-41, pp. 80–88, Jan. 1993.
- [22] C.G. Hus, R.F. Harrington, K.A. Michalski, and D. Zheng, "Analysis of multiconductor transmission lines of arbitrary cross section in multilayered uniaxial media", *IEEE trans. Microwave Theory and Techniques*, vol. MTT-41, pp. 70–78, Jan. 1993.
- [23] Y. Chen and B. Beker, "Analysis of single and coupled microstrip lines on anisotropic substrates using differential matrix operators and the spectral-domain method", *IEEE trans. Microwave Theory and Techniques*, vol. MTT-41, pp. 123–128, Jan. 1993.
- [24] G. Maze-Merceur, S. Tedjini, and J. Bonnefoy, "Analysis of a cpw on electric and magnetic biaxial substrate", *IEEE trans. Microwave Theory and Techniques*, vol. MTT-41, pp. 457–461, Mar. 1993.
- [25] E. El-Sharawy and R. Jackson, "Coplanar waveguide and slot line on magnetic substrates: Analysis and experiment", *IEEE trans. Microwave Theory and Techniques*, vol. MTT-36, pp. 1071–1079, June 1988.

- [26] El-B. El-Sharawy and R.W. Jackson, "Full-wave analysis of an infinitely long magnetic surface wave transducer", *IEEE trans. Microwave Theory and Techniques*, vol. MTT-38, pp. 730–738, June 1990.
- [27] R. Mitra, Y. Rahmat-Samii, D.V. Jamnejad, and T.K. Sarkar, "A new look at the thin plate scattering problem", *Radio Sci*, vol. 8, pp. 869–875, 1973.
- [28] E. Alanen and I.V. Lindell, "Exact image method for field calculation in horizontally layered medium above a conducting ground plane", *Proc. Inst. Elec. Eng.*, vol. 133, pp. 297–304, 1986.
- [29] S. Barkeshli, P.H. Pathak, and M. Marin, "An asymptotic closed-form microstrip surface Green's function for the efficient moment method analysis of mutual coupling in microstrip antennas", *IEEE trans. Antennas and Propagation*, vol. AP-38, pp. 1374–1383, Sep. 1990.
- [30] M.I. Aksun and R. Mittra, "Derivation of closed-form Green's function for a general microstrip geometry", *IEEE trans. Microwave Theory and Techniques*, vol. MTT-40, pp. 2055–2062, Nov. 1992.
- [31] Y.L. Chow, J.J. Yang, and G.E. Howard, "Complex images for electrostatic field computation in multilayered media", *IEEE trans. Microwave Theory and Techniques*, vol. MTT-39, pp. 1120–1125, July 1991.
- [32] J.J. Yang, Y.L. Chow, G.E. Howard, and D.G. Fang, "Complex images of an electric dipole in homogeneous and layered dielectric between two ground

- planes", *IEEE trans. Microwave Theory and Techniques*, vol. MTT-40, pp. 595–600, Mar. 1992.
- [33] M. Kominami, D.M. Pozar, and D.H. Schaubert, "Dipole and slot elements and arrays on semi-infinite substrates", *IEEE trans. Antennas and Propagation*, vol. AP-33, pp. 600–607, June 1985.
- [34] D.M. Pozar, "General relations for a phased array of printed antennas derived from infinite current sheets", *IEEE trans. Antennas and Propagation*, vol. AP-33, pp. 498–504, May 1985.
- [35] D.M. Pozar, "Input impedance and mutual coupling of rectangular microstrip antennas", *IEEE trans. Antennas and Propagation*, vol. AP-30, pp. 1191–1196, Nov. 1982.
- [36] M.D. Deshpande and M.C. Bailey, "Input impedance of microstrip antennas", *IEEE trans. Antennas and Propagation*, vol. AP-30, pp. 645–650, July 1982.
- [37] D.Pozar, "Considerations for millimeter wave printed antennas", *IEEE trans. Antennas and Propagation*, vol. AP-31, pp. 740–747, Sep. 1983.
- [38] N.G. Alexopoulos and D.R. Jackson, "Fundamental superstrate (cover) effects on printed circuit antennas", *IEEE trans. Antennas and Propagation*, vol. AP-32, pp. 807–816, Aug. 1984.
- [39] T-S. Horng, S-C. Wu, H-Y. Yang, and N.G. Alexopoulos, "A generalized method for distinguishing between radiation and surface-wave losses in mi-

- crostrip discontinuities", *IEEE trans. Microwave Theory and Techniques*, vol. MTT-38, pp. 1800–1806, Dec. 1990.
- [40] M. Kahrizi, T.K. Sarkar, and Z.A. Maricevic, "Analysis of a wide radiating slot in the ground plane of a microstrip line", *IEEE trans. Microwave Theory and Techniques*, vol. MTT-41, pp. 29–37, Jan. 1993.
- [41] T.G. Livernois and P.B. Katehi, "Characteristic impedance and electromagnetic field distribution in metal-insulator-semiconductor microstrip", *IEEE trans. Microwave Theory and Techniques*, vol. MTT-38, pp. 1740–1743, Nov. 1990.
- [42] R.F. Harrington, *Field Computation by Moment Method*, Robert E. Krieger Publishing Co., Malabar, Florida, 1982.
- [43] A.R. Djordjevic, C.K. Allen, T.K. Sarkar, and Z.A. Maricevic, "Inductance of perfectly conducting foils including spiral inductors", *IEEE trans. Microwave Theory and Techniques*, vol. MTT-38, pp. 1407–1414, Oct. 1990.
- [44] R.W. Jackson and D.M. Pozar, "Full-wave analysis of microstrip open-end and gap discontinuities", *IEEE trans. Microwave Theory and Techniques*, vol. MTT-33, pp. 1036–1042, Oct. 1985.
- [45] Y. Yuan and D.P. Nyquist, "Full-wave perturbation theory based upon electric field integral equations for coupled microstrip transmission lines", *IEEE trans. Microwave Theory and Techniques*, vol. MTT-38, pp. 1576–1584, Nov. 1990.

- [46] W.P. Harokopus and P.B. Katehi, "Characterization of microstrip discontinuities on multilayer dielectric substrates including radiation losses", *IEEE trans. Microwave Theory and Techniques*, vol. MTT-37, pp. 2058–2066, Dec. 1989.
- [47] N.K. Das and D.M. Pozar, "A generalized spectral-domain Green's function for multilayer dielectric substrates with application to multilayer transmission lines", *IEEE trans. Microwave Theory and Techniques*, vol. MTT-35, pp. 326–335, Mar. 1987.
- [48] A. Farrar and A.T. Adams, "Multilayer microstrip transmission lines", *IEEE trans. Microwave Theory and Techniques*, vol. MTT-22, pp. 889–891, Oct. 1974.
- [49] J.B. Davies and D. Mirshekar-Syahkal, "Spectral domain solution of arbitrary coplanar transmission line with multilayer substrates", *IEEE trans. Microwave Theory and Techniques*, vol. MTT-25, pp. 143–146, Feb. 1977.
- [50] J.S. Gagby and D.P. Nyquist, "Dyadic Green's functions for integrated electronic and optical circuits", *IEEE trans. Microwave Theory and Techniques*, vol. MTT-35, pp. 206–210, Feb. 1987.
- [51] A. Janhsen, B. Schiek, and V. Hansen, "Fullwave analysis of planar microwave circuits by integral equation methods and bilinear transformation", *IEEE trans. Microwave Theory and Techniques*, vol. MTT-40, pp. 1581–1584, July 1992.

- [52] Y.L. Chow, J.J. Yang, D.G. Fang, and G.E. Howard, "A closed-form spatial Green's function for the thick microstrip substrate", *IEEE trans. Microwave Theory and Techniques*, vol. MTT-39, pp. 588–592, Mar. 1991.
- [53] Y.L. Chow, "An approximate dynamic Green's function in three dimensions for finite length microstripline", *IEEE trans. Microwave Theory and Techniques*, vol. MTT-28, pp. 393–397, Apr. 1980.
- [54] Y.L. Chow and I.N. El-Behery, "An approximate dynamic spatial Green's function for microstriplines", *IEEE trans. Microwave Theory and Techniques*, vol. MTT-26, pp. 978–983, Dec. 1978.
- [55] A.A. Omar and Y.L. Chow, "A solution of coplanar waveguide with air-bridge using complex images", *IEEE trans. Microwave Theory and Techniques*, vol. MTT-40, pp. 2070–2077, Nov. 1992.
- [56] J.J. Yang, G.E. Howard, and Y.L. Chow, "Complex image method for analyzing multiconductor transmission lines in multilayered dielectric media", in *1991 IEEE AP-S International Symposium Digest*, London, Ontario, June 1991.
- [57] D.C. Stinson, *Intermeditate Mathematics of Electromagnetics*, Prentice-Hall, 1976.
- [58] T. Itoh, editor, *Numerical Techniques for Microwave and Millimeter-wave passive structures*, Wiley-Interscience, 1989.

- [59] C.A. Balanis, *Advanced Engineering Electromagnetics*, John Wiley & Sons, 1989.
- [60] R.H. Jansen, "The spectral-domain approach for microwave integrated circuits", *IEEE trans. Microwave Theory and Techniques*, vol. MTT-33, pp. 1043–1056, Oct. 1985.
- [61] J.K. Kong, *Theory of Electromagnetic Waves*, Wiley, New York, 1975.
- [62] T. Itoh, editor, *Numerical Techniques for Microwave and Millimeter-Wave Passive Structures*, chapter 3, pp. 133–213, John Wiley & Sons, New York, 1989.
- [63] T.E van Deventer, P.B. Katehi, and A.C. Cangellaris, "An integral equation method for the evaluation of conductor and dielectric losses in high-frequency interconnects", *IEEE trans. Microwave Theory and Techniques*, vol. MTT-37, pp. 1964–1971, Dec. 1989.
- [64] Dietrich Marcuse, *Light Transmission Optics*, Van Nostrand Reinhold Publishing, 1972.
- [65] P.B. Katehi, *A Generalized Solution of a Class of Printed Circuit Antennas*, PhD thesis, UCLA, L.A., 1984.
- [66] Y. Chow and E. Cassagnol, *Linear Signal-flow Graphs and Applications*, Wiley, New York, 1962.

- [67] N.L. Vandenberger and P.B. Katehi, "Broadband vertical interconnects using slot-coupled shielded microstrip lines", *IEEE trans. Microwave Theory and Techniques*, vol. MTT-40, pp. 81–88, Jan. 1992.
- [68] M. Kobayashi and H. Sekine, "Closed-form expressions for the current distribution on open microstrip lines", *IEEE trans. Microwave Theory and Techniques*, vol. MTT-39, pp. 1115–1118, July 1991.
- [69] Owen Fordham, "Two layer microstrip transmission lines", Master's thesis, UCLA, 1987.
- [70] M. Hashimoto, "A rigorous solution for dispersive microstrip", *IEEE trans. Microwave Theory and Techniques*, vol. MTT-33, pp. 1131–1137, Nov. 1985.
- [71] H.C. Pocklington, "Electric oscillations in wire", *Cambridge Philos. Soc. Proc.*, vol. 9, pp. 324–332, 1897.
- [72] P.B. Katehi and N.G. Alexopoulos, "Frequency-dependent characteristics of microstrip discontinuities in millimeter-wave integrated circuits", *IEEE trans. Microwave Theory and Techniques*, vol. MTT-33, pp. 1029–1035, Oct. 1985.
- [73] N.K. Das and D.M. Pozar, "Full-wave spectral-domain computation of material, radiation, and guided wave losses in infinite multilayered printed transmission lines", *IEEE trans. Microwave Theory and Techniques*, vol. MTT-39, pp. 54–63, Jan. 1991.

- [74] J.B. Knorr and A. Tufekcioglu, "Spectral-domain calculation of microstrip characteristic impedance", *IEEE trans. Microwave Theory and Techniques*, vol. MTT-23, pp. 725–728, Sep. 1975.
- [75] I.N. Sneddon, *The Use of Integral Transforms*, McGraw-Hill, New York, 1972.
- [76] H-Y. Yang, N.G. Alexopoulos, and D.R. Jackson, "Microstrip open-end and gap discontinuities in a substrate-superstrate structure", *IEEE trans. Microwave Theory and Techniques*, vol. MTT-37, pp. 1542–1546, Oct. 1989.
- [77] I.E. Rana and N.G. Alexopoulos, "Current distribution and input impedance of printed dipoles", *IEEE trans. Antennas and Propagation*, vol. AP-29, pp. 99–105, Jan. 1981.
- [78] E.H. Newman and D.F. Forrai, "Scattering from a microstrip patch", *IEEE trans. Antennas and Propagation*, vol. AP-35, pp. 245–251, Mar. 1987.
- [79] R.F. Harrington, *Time Harmonic Electromagnetic Fields*, McGraw-Hill, New York, 1961.
- [80] Chuan-Li Chi, *Modeling Probe and Probe-Microstrip Transitions*, PhD thesis, UCLA, L.A., 1987.
- [81] N.K. Uzunoglu, N.G. Alexopoulos, and J.D. Fikioris, "Radiation properties of microstrip dipoles", *IEEE trans. Antennas and Propagation*, vol. AP-27, pp. 853–858, Nov. 1979.

- [82] M. Marin, S. Barkeshli, and P.H. Pathak, "On the location of proper and improper surface wave poles for the grounded dielectric slab", *IEEE trans. Antennas and Propagation*, vol. AP-38, pp. 570–573, Apr. 1990.
- [83] D.M. Pozar, "Input impedance and mutual coupling of rectangular microstrip antennas", *IEEE trans. Antennas and Propagation*, vol. AP-30, pp. 1191–1196, 1982.
- [84] N.G. Alexopoulos, D.R. Jackson, and P.B. Katehi, "Criteria for nearly omnidirectional radiation patterns for printed antennas", *IEEE trans. Antennas and Propagation*, vol. AP-33, pp. 195–205, Feb. 1985.
- [85] C. Hsu, R.F. Harrington, J.R. Mautz, and T.K. Sarkar, "On the location of leaky wave poles for a grounded dielectric slab", *IEEE trans. Microwave Theory and Techniques*, vol. MTT-39, pp. 346–349, Feb. 1991.
- [86] A.A. Oliner, "Leakage from higher modes on microstrip line with application to antennas", *Radio Sci.*, vol. 22, pp. 907–912, Nov. 1987.
- [87] K.A. Michalski and D. Zheng, "Rigorous analysis of open microstrip lines of arbitrary cross-section in bound and leaky regimes", *IEEE trans. Microwave Theory and Techniques*, vol. MTT-37, pp. 2005–2010, Dec. 1989.
- [88] J.M. Grimm and D.P. Nyquist, "Spectral analysis considerations relevant to radiation and leaky modes of open-boundary microstrip transmission line", *IEEE trans. Microwave Theory and Techniques*, vol. MTT-41, pp. 150–153,

Jan. 1993.

- [89] W.P. Harocopus, Jr., P.B. Katehi, W.Y. Ali-Ahmad, and G.M.Rebeiz, "Surface wave excitation from open microstrip discontinuities", *IEEE trans. Microwave Theory and Techniques*, vol. MTT-39, pp. 1098–1107, July 1991.
- [90] E.T. Copson, *An Introduction to the Theory of Functions of a Complex Variable*, Oxford University Press, London, 1957.
- [91] H-Y. Yang, A. Nakatani, and J.A. Castaneda, "Efficient evaluation of spectral integrals in the moment method solution of microstrip antennas and circuits", *IEEE trans. Microwave Theory and Techniques*, vol. MTT-38, pp. 1127–1130, July 1990.
- [92] Milton Abramowitz and Irene A. Stegun, *Handbook of Mathematical Functions*, Dover, New York, 1965.
- [93] J.C. Maxwell, *A Treatise on Electricity and Magnetism*, vol. 1, New York, 3rd edition, 1954.
- [94] C.T. Ishii, *Microwave Engineering Electromagnetics*, John Wiley & Sons, 1989.
- [95] W.J. Getsinger, "Measurement and modeling of the apparent characteristic impedance of microstrip", *IEEE trans. Microwave Theory and Techniques*, vol. MTT-31, pp. 624–632, Aug. 1983.

- [96] P.B. Kaheti and N.G. Alexopoulos, "On the modeling of electromagnetically coupled microstrip antennas—the printed strip dipole", *IEEE trans. Antennas and Propagation*, vol. AP-32, pp. 1179–1186, Nov. 1984.
- [97] M.I. Aksun and R. Mittra, "Choices of expansion and testing functions for the method of moments applied to a class of electromagnetic problems", *IEEE trans. Microwave Theory and Techniques*, vol. MTT-41, pp. 503–509, Mar. 1993.
- [98] M.M. Ney, "Method of moments as applied to electromagnetic problems", *IEEE trans. Microwave Theory and Techniques*, vol. MTT-33, pp. 972–980, Oct. 1985.
- [99] R.W. Jackson, "Full-wave, finite analysis of irregular microstrip discontinuities", *IEEE trans. Microwave Theory and Techniques*, vol. MTT-37, pp. 81–89, Jan. 1989.
- [100] Hung-Yu Yang, *Frequency Dependent Modeling of Passive Integrated Circuit Components*, PhD thesis, UCLA, 1988.
- [101] Gregor Gronau and Ingo Wolff, "A simple broad-band device de-embedding method using an automatic network analyzer with time-domain option", *IEEE trans. Microwave Theory and Techniques*, vol. MTT-37, pp. 479–483, March 1989.
- [102] EEsof, Inc., *Touchstone Reference Manual, version 1.6*, Jan. 1987.

- [103] M. Kirschning, R.H. Jansen, and N.H.L. Koster, "Accurate model for open end effect of microstrip lines", *Electronics Letters*, vol. 17, pp. 123–125, Feb. 1981.
- [104] E. Hammerstad, "Computer aided design of microstrip couplers with accurate discontinuity models", in *IEEE MTT-S International Microwave Symposium Digest*, pp. 54 – 56, June 1981.
- [105] T. Horng, W.E. Mckinzie, and N.G. Alexopoulos, "Full-wave spectral-domain analysis of compensation of microstrip discontinuities using triangular subdomain functions", *IEEE trans. Microwave Theory and Techniques*, vol. MTT-40, pp. 2137–2154, Dec. 1992.
- [106] W.D. Becker, P. Harms, and R. Mittra, "Time domain electromagnetic analysis of interconnects in a computer chip package", *IEEE trans. Microwave Theory and Techniques*, vol. MTT-40, pp. 2155–2163, Dec. 1992.
- [107] Q. Gu, Y.E. Yang, and M.A. Tassoudji, "Modeling and analysis of vias in multilayered intergrated cicuits", *IEEE trans. Microwave Theory and Techniques*, vol. MTT-41, pp. 206–214, Feb. 1993.
- [108] C-L. Chi and N.G. Alexopoulos, "An efficient numerical approach for modeling microstrip-type antennas", *IEEE trans. Microwave Theory and Techniques*, vol. MTT-38, pp. 1399–1404, Sep. 1990.
- [109] W. Tsay and J.T. Aberle, "Analysis of a microstrip line terminated with a

- shorting pin”, *IEEE trans. Microwave Theory and Techniques*, vol. MTT-40, pp. 645–651, Apr. 1992.
- [110] G.F. Engen and C.A. Hoer, ““thru-reflect-line”: An improved technique for calibrating the dual six-port automatic network analyzer”, *IEEE trans. Microwave Theory and Techniques*, vol. MTT-27, pp. 987–993, Dec. 1979.
- [111] R.F. Bauer and Jr. P. Penfield, “De-embedding and unterminating”, *IEEE trans. Microwave Theory and Techniques*, vol. MTT-22, pp. 282–288, Mar. 1974.
- [112] R. Lane, “De-embedding device scattering parameters”, *Microwave J.*, vol. 27, pp. 149–156, Aug. 1984.
- [113] M. Yang and R.H. Johnston, “De-embedding measurement of microstrip discontinuities using nonlinear least-square techniques”, in *Proceedings of 3rd Intl. Symp. on Recent Advances in Microwave Technology*, pp. 165–168, Reno, Nevada, USA, Aug. 1991. ISRAMT’91.
- [114] R.H. Johnston and M. Yang, “A comparison of microstrip discontinuity models with measured data”, in *Proceedings of 35th Midwest Symp. on Circuits and Systems*, Washington, DC, USA, Aug. 1992.
- [115] Hewlett-Packard Company, *HP8510 Automatic Network Analyzer: User’s Manual*, 1991.

- [116] R.W. Jackson, "The use of side wall images to compute package effects in mom analysis of mmic circuits", *IEEE trans. Microwave Theory and Techniques*, vol. MTT-41, pp. 406–414, Mar. 1993.
- [117] K. Wu, M. Yu, and R. Vahldieck, "Rigorous analysis of 3-D planar circuit discontinuities using the space-spectral domain approach (SSDA)", *IEEE trans. Microwave Theory and Techniques*, vol. MTT-40, pp. 1475–1483, July 1992.

Appendix A

Comparison of Decomposed and Undecomposed Traveling Wave Functions

In the analysis of the discontinuities with semi-infinite microstrip transmission lines, the traveling wave (either incident, reflected, or transmitted) is in reality an exponential function with a complex argument, i.e. $e^{\pm jk_e x}$. When an open or a gap is being analyzed, the reflection coefficient and/or the transmission will be the unknowns to be determined in the process, which makes this traveling wave one of the basis functions.

If the exponential function is not decomposed (we now call it method 1), a half PWS function will have to be added to the open end of the strip to cancel out the non-zero current there. The reflection base function will be, for instance

$$f_1^R = e^{jk_e x} - f_{hpus} \quad (x \leq 0)$$

where f_{hpus} is defined as

$$f_{hpus} = \begin{cases} \frac{\sin[k_e(h+x)]}{\sin(k_e h)} & \text{if } -h \leq x \leq 0 \\ 0 & \text{if } x < 0 \end{cases}$$

If, on the other hand, the exponential function is decomposed into sine and cosine terms, and the cosine term is terminated at $x = -\pi/(2k_e)$ (we now call it method

2), then the half PWS function is not needed and the base function for the reflection will be

$$f_2^R = \cos(k_e x) + j \sin(k_e x)$$

Theoretically both method 1 and 2 are valid basis functions for MoM. Numerically, however, the existence and speed of the convergence has to be considered. When transformed into the spectral domain, they become:

$$\tilde{f}_1^R = \frac{j}{\lambda_x - k_e} + \tilde{f}_{hpus}$$

and

$$\tilde{f}_2^R = \frac{k_e}{\lambda_x^2 - k_e^2},$$

respectively. As λ_x approaches ∞ , \tilde{f}_1^R varies only as a function of λ_x^{-1} , while \tilde{f}_2^R varies as λ_x^{-2} . Therefore, it is clear that method 2 is a better choice for the traveling wave basis functions.

Appendix B

Conversion of the 2-D Spectral Domain Green's Function into the Sommerfeld Integral

The well-known Sommerfeld integral is written in the cylindrical coordinate system. The spectral domain method is written in the Cartesian coordinates to conform with the straight edge geometry of the microstrip circuits. If there is rotational symmetry in the microstrip circuit, however, use of the cylindrical coordinate system can lead to a simpler and a faster analysis.

In Chapter 7, a vertical dipole is analyzed. Since the current is assumed to occur at the center on the axis of the dipole, and the electric field is examined at the surface of dipole, the cylindrical coordinates are recommended. The Green's function for the z direction electric field due to the Hertz dipole in the same direction is

$$E_z(x, y, z, z') = \int_{-\infty}^{+\infty} \int_{-\infty}^{+\infty} \tilde{G}_{zz}(\lambda_x, \lambda_y, z, z') e^{j\lambda_x x} e^{j\lambda_y y} d\lambda_x d\lambda_y \quad (\text{B.1})$$

On the dipole surface, the coordinates are

$$x = a \cos \phi \quad , \quad y = a \sin \phi \quad (\text{B.2})$$

Substituting the above expressions into Equation B.1, and expressing the spectral

domain variables in cylindrical form, one obtains

$$E_z(a \cos \phi, a \sin \phi, z, z') = \int_{\lambda=0}^{+\infty} \int_{\phi=0}^{2\pi} \tilde{G}_{zz}(\lambda, z, z') \lambda e^{j\lambda a \cos \phi \cos \varphi} e^{j\lambda a \sin \phi \sin \varphi} d\lambda d\varphi \quad (\text{B.3})$$

Due to the symmetry, the electric field should be ϕ independent. For convenience in getting the electric field, let $\phi = 0$. This simplifies the above expression to give

$$E_z(a, z, z') = \int_{\lambda=0}^{+\infty} \int_{\phi=0}^{2\pi} \tilde{G}_{zz}(\lambda, z, z') \lambda e^{j\lambda a \cos \varphi} d\lambda d\varphi \quad (\text{B.4})$$

It is noted that [59]

$$\begin{aligned} \int_0^{2\pi} e^{j\lambda a \cos \varphi} d\varphi &= \int_{-\pi}^{\pi} e^{j\lambda a \cos \varphi} d\varphi \\ &= \int_{-\pi}^{\pi} [\cos(\lambda a \cos \varphi) - j \sin(\lambda a \cos \varphi)] d\varphi \\ &= 2 \int_0^{\pi} \cos(\lambda a \cos \varphi) d\varphi \\ &= 2\pi J_0(\lambda a) \end{aligned}$$

where J_0 is the zero-order Bessel function. Thus

$$E_z(a, z, z') = 2\pi \int_{\lambda=0}^{+\infty} \tilde{G}_{zz}(\lambda, z, z') J_0(\lambda a) \lambda d\lambda$$

Since this is the relationship between a Hertz dipole at the center to its z direction field at the dipole surface, $E_z(a, z, z')$ actually is a Green's function for this particular problem in the spatial domain. To get the total field at z due to a known current $J_z(z')$ at the dipole center, the following expression holds:

$$E_z(a, z) = 2\pi \int_{z'} J_z(z') dz' \int_{\lambda=0}^{+\infty} \tilde{G}_{zz}(\lambda, z, z') J_0(\lambda a) \lambda d\lambda$$

This is the well-known Sommerfeld integral.